Università della Calabria

Dottorato di Ricerca in
Psicologia della Programmazione e Intelligenza Artificiale
XXV Ciclo

Settore scientifico-disciplinare: ING-INF/01

Tesi di Dottorato

INVESTIGATION OF SILICON SOLAR CELLS BY MEANS OF ELECTRO-OPTICAL NUMERICAL SIMULATIONS

Candidato
Dott. Raffaele De Rose

Tutor
Ing. Marco Lanuzza

Coordinatrice
Prof.ssa Eleonora Bilotta

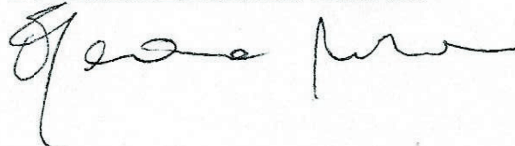

Anno Accademico 2011/2012

RAFFAELE DE ROSE

INVESTIGATION OF SILICON SOLAR CELLS BY MEANS OF ELECTRO-OPTICAL NUMERICAL SIMULATIONS

To my family

Alla mia famiglia

“There are those who look at things the way they are, and ask why?
I dream of things that never were, and ask why not?”
(*R. F. Kennedy, quoting George Bernard Shaw*)

“Ci sono coloro che guardano le cose come sono, e si chiedono perché?
Io sogno cose che non ci sono mai state, e mi chiedo perché no?”
(*R. F. Kennedy, citando George Bernard Shaw*)

ABOUT THE AUTHOR

Raffaele De Rose was born in Cosenza (CS), Italy, on October 24th, 1985.

He received the High School “Diploma di Liceo Scientifico P.N.I.” with full grade (100/100) from the “Liceo Scientifico Statale G. B. Scorza” of Cosenza (CS), Italy, in 2004.

He received the Bachelor of Science Degree in Electronic Engineering cum Laude from the University of Calabria, Rende (CS), Italy, in 2007. The thesis title was: “Data Acquisition and Elaboration Techniques on FPGA Devices” (in Italian). The advisors were Prof. Marco Lanuzza and Prof. Arrigo Palumbo.

He received the Master of Science Degree in Electronic Engineering cum Laude from the University of Calabria, Rende (CS), Italy, in 2009. The thesis title was: “Impact of Process Variations on Flip-Flops Performance and Energy Consumption” (in Italian). The advisors were Prof. Pasquale Corsonello and Prof. Marco Lanuzza.

In 2009, he started to work toward the Ph.D. degree of the Ph.D. course in “Psychology of Programming and Artificial Intelligence” (Scientific field: ING/INF01-Electronics) at the University of Calabria. His scientific tutor has been Prof. Marco Lanuzza.

From July 2010 to now, he has joined as research fellow the Advanced Research Center on Electronic Systems for Information and Communication Technologies “E. De Castro” (ARCES), University of Bologna (Cesena Campus), Italy, where he has worked on numerical simulation of silicon solar cells for his Ph.D. research activity. The scientific supervisor has been Prof. Claudio Fiegna.

From May 2011 to October 2011, he joined for a research internship the Interuniversity MicroElectronics Center (IMEC), Leuven, Belgium, where he worked on three-dimensional numerical simulation of advanced silicon-based solar cells.

His research interests include the modeling and the electro-optical numerical simulation of semiconductor devices and silicon solar cells.

NOTE SULL'AUTORE

Raffaele De Rose è nato a Cosenza (CS), Italia, il 24 Ottobre 1985.

Ha conseguito con il massimo dei voti (100/100) il Diploma di Liceo Scientifico "P.N.I." presso il Liceo Scientifico Statale G. B. Scorza di Cosenza (CS) nel 2004.

Ha conseguito con lode la Laurea Triennale in Ingegneria Elettronica (indirizzo Microelettronica) presso l'Università della Calabria, Rende (CS) nel 2007. Il titolo della tesi è stato: "Tecniche di Acquisizione ed Elaborazione di Segnali su Dispositivi FPGA". I relatori sono stati l'Ing. Marco Lanuzza e l'Ing. Arrigo Palumbo.

Ha conseguito con lode la Laurea Specialistica in Ingegneria Elettronica presso l'Università della Calabria, Rende (CS) nel 2009. Il titolo della tesi è stato: "Impatto delle Variazioni di Processo sulle Prestazioni e sul Consumo di Energia dei Flip-Flops". I relatori sono stati il Prof. Pasquale Corsonello e l'Ing. Marco Lanuzza.

Nel 2009, ha iniziato il percorso di studi per il conseguimento del titolo di Dottore di Ricerca nell'ambito del corso in "Psicologia della Programmazione e Intelligenza Artificiale" (Settore scientifico-disciplinare S.S.D.: ING/INF01-Elettronica) presso l'Università della Calabria. Il tutor scientifico è stato l'Ing. Marco Lanuzza.

Da Luglio 2010 a tutt'oggi, è stato titolare di assegno di ricerca presso il Centro di Ricerca Avanzato sui Sistemi Elettronici per l'Ingegneria dell'Informazione e delle Telecomunicazioni "Ercole De Castro" (ARCES) dell'Università di Bologna (sede di Cesena), dove ha lavorato sulla simulazione numerica di celle solari in silicio nell'ambito dell'attività di ricerca svolta durante il programma di dottorato. Il supervisore scientifico è stato il Prof. Claudio Fiegna.

Da Maggio 2011 a Ottobre 2011, ha svolto un tirocinio di ricerca all'estero presso il Centro Interuniversitario di MicroElettronica (IMEC), situato a Leuven in Belgio, dove ha lavorato sulla simulazione numerica tridimensionale di celle solari avanzate in silicio.

La sua attività di ricerca riguarda principalmente la modellistica e la simulazione numerica elettro-ottica dei dispositivi a semiconduttori e delle celle solari in silicio.

ACKNOWLEDGMENTS

Firstly, I would like to thank my supervisor Marco Lanuzza, who was the first to give me the idea of starting a Ph.D., while I was still carrying out the Master thesis. I am really thankful to him for the opportunity, the encouragement and the support.

I would also like to thank all the members of the Ph.D. course at the University of Calabria.

I would like to express my special gratitude to Prof. Claudio Fiegna from ARCES-University of Bologna for his continuous help and support during my Ph.D. studies, and for his generosity to review and examine this thesis. I am very grateful to him and to Prof. Enrico Sangiorgi (ARCES-University of Bologna) for giving me the opportunity to spend most of my Ph.D. at ARCES-University of Bologna (Cesena Campus).

I would also particularly like to thank my colleagues at ARCES-University of Bologna, Dr. Paolo Magnone, Dr. Mauro Zanuccoli, Dr. Claudio Berti and Daniele Giaffreda, for the support and the helpful discussions, and for the friendly atmosphere in the team.

The research activity concerning this thesis has been supported by several partners. For these fruitful collaborations, the following people also deserve a special mention:

- Dr. Michel Frei and Dr. Hsiu-Wu (Jason) Guo from Applied Materials Inc., Santa Clara, CA, USA;
- Dr. Giorgio Cellere, Diego Tonini and Marco Galiazzo from Applied Materials Baccini S.p.A., Treviso, Italy;
- Dr. Koen Van Wichelen, Dr. Frederic Dross, Loic Tous and Angel Uruena De Castro from the Interuniversity MicroElectronics Center (IMEC), Leuven, Belgium;
- Prof. Felice Crupi from the University of Calabria, Italy.

In particular, special thanks must go to Koen Van Wichelen for giving me the exciting opportunity to spend about six months of my Ph.D. at IMEC in Belgium, and for the fruitful discussions on the numerical simulation of solar cells.

I would like to thank the Master thesis students, Antonio Malomo, Antonio Napoletano, Giovanna Palermo, Silvia Picerno, and Alberto Vaccaro, who had the “bad-luck” to be followed by me during their thesis work. They have also been a source of major contributions in this thesis and, therefore, they are deeply acknowledged.

ABSTRACT

Solar energy is the primary source of renewable energy on earth. In fact, most of the energy forms available on our planet arise, more or less directly, from the solar energy, including fossil fuels, wind energy, hydro energy and biomass energy, with the only exceptions of nuclear energy, geothermal energy and tidal energy. Moreover, among several renewable energy sources, solar energy has both the energetic potential and the duration sufficient to match mankind future energy needs, being able, theoretically, to fully cover the world-wide energy demand, or at least an important portion.

Accordingly, photovoltaics (PV), i.e. the direct conversion of solar energy into electrical energy using the electronic properties of semiconductor materials, is one of the most promising processes for electricity generation from renewable source, as viable alternative to conventional fossil fuels. In particular, PV can be a strategic choice for Italy, whereas our country is currently strongly dependent on foreign primary energy supplies, and its geographic location, particularly in the Southern Italy, is rather favorable for the exploitation of this technology.

Nowadays, despite the significant potential of sunlight for supplying energy, solar power provides only a very small fraction (about 0.5%) of the global energy demand. In order to increase the world-wide installed PV capacity, PV solar systems must become more efficient, reliable, cost-competitive and responsive to the current demands of the market. In this regard, the improvement of PV solar cells, both in terms of reducing manufacturing costs and increasing conversion efficiency, requires a careful device and process optimization. In this context, modeling of PV devices plays a major role to aid the design of solar cells. Furthermore, solar cell modeling becomes increasingly strategic for PV industry in view of the forthcoming adoption of more complex architectures for next-generation solar cells.

This Ph.D. thesis is part of a research activity on some advanced technological solutions aimed at increasing the conversion efficiency of silicon solar cells. In particular, the main goal of this thesis is to provide a detailed investigation on the physical mechanisms that limit the conversion efficiency of silicon solar cells by means of electro-optical numerical simulations, carried out with a state-of-the-art TCAD computer program.

The first part of the thesis forms an introduction to the numerical simulation of silicon solar cells. First, a review of the device physics of solar cells is presented, starting from the simple analytical 1-D *p-n* junction model. More refined analytical models are then reported in order to include the effects of several non-idealities on the real solar cell characteristics. In addition, the theoretical efficiency limits and the main loss mechanisms of silicon solar cells are discussed. Afterward, the typical TCAD-based modeling approach for solar cells, including both electro-optical device simulations and circuit simulations, is outlined. Then, in order to

achieve realistic predictions on the performance of the simulated solar cells, the ad-hoc calibration for specific PV requirements of some of the most relevant physical models typically implemented in the adopted TCAD simulators, such as those for the intrinsic carrier density, the Auger recombination, the SRH recombination, and the surface recombination, is discussed.

The second part of the thesis reports in detail the simulation results of the performed analysis, aimed at investigating the physical mechanisms that limit the conversion efficiency of conventional silicon solar cells and of some next-generation silicon solar cells intended for industrial scale productions, such as Double Screen-Printed (DP) solar cells, Selective Emitter (SE) solar cells and Rear Point Contact (RPC) solar cells. Numerical results show that the technological solutions adopted for these next-generation silicon solar cells can be very effective to improve the solar cell performance, as compared to current industrial silicon solar cells.

Finally, a simulation methodology based on a mixed-mode simulation approach, which combines numerical device simulations and circuit simulations, is proposed to investigate the impact of the non-uniformities in the front-side metallization grid, due to the roughness and/or the interruptions of front metal lines, on the performance of silicon solar cells.

SOMMARIO

L'energia solare rappresenta la fonte primaria di energia rinnovabile sulla terra, dalla quale derivano, più o meno direttamente, la gran parte delle forme di energia disponibili sul nostro pianeta, quali i combustibili fossili, l'energia eolica, l'energia del moto ondoso, l'energia idroelettrica e l'energia da biomassa, con le sole eccezioni dell'energia nucleare, dell'energia geotermica e dell'energia delle maree. Inoltre, tra le varie fonti di energia rinnovabile, l'energia solare offre sia il potenziale energetico che la durata sufficienti per soddisfare il futuro fabbisogno energetico dell'umanità, essendo in grado, teoricamente, di coprire l'intera domanda di energia a livello mondiale, o, più realisticamente, almeno una porzione rilevante.

Di conseguenza, il fotovoltaico, cioè il processo di conversione diretta dell'energia solare in energia elettrica che sfrutta le proprietà elettroniche dei materiali semiconduttori, rappresenta uno dei processi più promettenti per la generazione di elettricità da fonte rinnovabile, come valida alternativa ai combustibili fossili convenzionali. In particolare, il fotovoltaico può essere una scelta strategica per l'Italia, considerato che il nostro paese attualmente è fortemente dipendente dalle forniture estere di energia primaria, e che la sua posizione geografica, specialmente nel Sud Italia, è particolarmente favorevole per lo sfruttamento di tale tecnologia.

Attualmente, nonostante il significativo potenziale energetico associato alla radiazione solare, l'energia solare copre solo una piccola porzione (circa lo 0.5%) della domanda globale di energia sulla terra. Al fine di poter incrementare la capacità fotovoltaica installata a livello mondiale, è necessario che i sistemi fotovoltaici diventino sempre più efficienti, affidabili e meno costosi, in risposta alle attuali esigenze del mercato. A tal riguardo, il miglioramento delle celle solari fotovoltaiche, sia in termini di riduzione dei costi di produzione che di aumento dell'efficienza di conversione, richiede un'accurata ottimizzazione dei dispositivi e del processo di produzione. In quest'ottica, la modellistica dei dispositivi fotovoltaici assume un ruolo di primo piano nel settore fotovoltaico per supportare tale processo di ottimizzazione, soprattutto in vista dell'adozione di architetture più complesse per le celle solari di nuova generazione.

Questo lavoro di tesi di dottorato si inserisce nell'ambito di un'attività di studio e di ricerca volta all'analisi di soluzioni tecnologiche avanzate, finalizzate all'incremento dell'efficienza di conversione delle celle solari in silicio. In particolare, l'obiettivo principale della tesi è quello di fornire un'analisi dettagliata dei meccanismi fisici che limitano l'efficienza di conversione delle celle solari in silicio mediante simulazioni numeriche elettro-ottiche, eseguite con un programma numerico commerciale TCAD.

La prima parte della tesi costituisce un'introduzione alla simulazione numerica di celle solari in silicio. Inizialmente, viene presentato un resoconto sulla fisica delle celle solari, a partire dall'analisi analitica del modello semplificato 1-D della giunzione *p-n* ideale. Vengono

poi presentati modelli analitici più complessi al fine di includere gli effetti di varie non-idealità sulle caratteristiche di una cella solare. In più, vengono discussi i limiti teorici di efficienza e i principali meccanismi di perdita delle celle solari in silicio. Successivamente, viene descritto l'approccio, basato sull'utilizzo di programmi numerici TCAD, tipicamente adottato per la modellistica delle celle solari, prendendo in considerazione sia le simulazioni elettro-ottiche di dispositivo, che le simulazioni di tipo circuitale. In particolare, al fine di poter ottenere una predizione realistica sulle prestazioni delle celle solari simulate, viene descritta la calibrazione ad-hoc che è stata eseguita per alcuni dei modelli fisici comunemente implementati nei simulatori TCAD, come quelli per la concentrazione intrinseca dei portatori, la ricombinazione Auger, la ricombinazione SRH e la ricombinazione superficiale, che risultano essere più critici nella simulazione delle celle solari in silicio.

La seconda parte della tesi presenta i risultati delle simulazioni eseguite al fine di individuare i meccanismi fisici che limitano l'efficienza delle celle solari in silicio convenzionali e di alcune celle solari di nuova generazione destinate alla produzione su scala industriale, quali le celle solari con architetture di metallizzazione anteriore a doppia stampa (DP), le celle solari ad emettitore selettivo (SE) e le celle solari con contatti puntuali sul lato posteriore (RPC). I risultati delle simulazioni numeriche mostrano che le soluzioni tecnologiche adottate per queste celle solari di nuova generazione consentono di incrementare in maniera significativa l'efficienza di conversione rispetto alle celle convenzionali.

Infine, viene presentata una metodologia di simulazione basata su un approccio misto, cioè che combina simulazioni elettro-ottiche di dispositivo e simulazioni circuitali, che è stata impiegata all'analisi dell'impatto delle disuniformità presenti nella griglia anteriore di metallizzazione, in particolare dovute alla rugosità delle linee metalliche e/o alla presenza di interruzioni, sulle prestazioni di una cella solare in silicio.

LIST OF ABBREVIATIONS AND SYMBOLS

List of abbreviations

1-D	One-dimensional
2-D	Two-dimensional
3-D	Three-dimensional
a-Si	Amorphous Silicon
ADEPT	A Device Emulation Program and Toolbox
Ag	Silver
Al	Aluminum
AMPS-1D	Analysis of Microelectronic and Photonic Structure in 1-Dimension
ARC	Anti-Reflective Coating
BGN	Band-Gap Narrowing
BSF	Back-Surface Field
BTE	Boltzmann Transport Equation
c-Si	Monocrystalline Silicon
CdTe	Cadmium Telluride
CIGS	Copper Indium Gallium Selenide
CIS	Copper Indium Selenide
CPV	Concentrated Photovoltaics
CVD	Chemical Vapor Deposition
Cz-Si	Czochralski Silicon
DD	Drift-Diffusion
DESSIS	Device Simulation for Smart Integrated Systems
DoE	Design of Experiments
DP	Double Screen-Printing
ESP	Electroless Silver Plating
FEM	Finite Element Method
FDTD	Finite-Difference Time-Domain
FMM	Fourier Modal Method
Fz-Si	Float-zone Silicon
GaAs	Gallium Arsenide
HDOP	Highly-Doped
HE	Homogeneous Emitter
I-*V*	Current-Voltage
LDOP	Lowly-Doped
LFC	Laser Firing Contact
mc-Si	Multicrystalline Silicon
NaOH	Dilute Caustic Soda
PDE	Partial Differential Equation
PECVD	Plasma Enhanced Chemical Vapor Deposition
PERC	Passivated Emitter and Rear Cell
PERL	Passivated Emitter Rear Locally diffused
PV	Photovoltaics

PUPHS	Purdue University Program for Heterojunction Simulation
RPA	Random-Phase Approximations
QNR	Quasi-Neutral Region
RCWA	Rigorous Coupled Wave Analysis
RPC	Rear Point Contact
RT	Ray-Tracing
SCAP1D	Solar Cell Analysis Program in 1-Dimension
SE	Selective Emitter
SEM	Scanning Electron Microscope
Si	Silicon
SiN_x	Silicon Nitride
SiO_2	Silicon Dioxide
SP	Single Screen-Printing
SQ	Shockley-Queisser
SRH	Shockley-Read Hall
SRV	Surface Recombination Velocity
TCAD	Technology Computer-Aided Design
TFSSP	Thin-Film Semiconductor Simulation Program
TMM	Transfer Matrix Method
UNSW	University of New South Wales

List of symbols

α (λ)	Absorption coefficient [cm^{-1}]
$\Delta\eta$	Efficiency degradation [$\%_{abs}$]
Δn	Excess electron density [cm^{-3}]
Δp	Excess hole density [cm^{-3}]
ε	Electromagnetic permittivity [F/cm]
ξ	Intensity of the electric field [V/m], or correlation length [µm]
ξ_m	Maximum intensity of the electric field [V/m]
η	Power conversion efficiency [%]
η_c	Quantum collection efficiency [%]
θ	Angle of incidence of the radiation [°]
λ	Wavelength of the radiation [nm]
μ_n	Electron mobility [$cm^2/V \cdot s$]
μ_p	Hole mobility [$cm^2/V \cdot s$]
ρ	Charge density [C/cm^3]
ρ_c	Specific contact resistivity [$\Omega \cdot cm^2$]
ρ_m (or ρ_f)	Metal finger resistivity [$\Omega \cdot cm$]
σ_A	Standard deviation of the finger cross-section [μm^2]
σ_H	Standard deviation of the finger height [µm]
σ_n	Electron capture cross-section [cm^2]
σ_n	Electron capture cross-section [cm^2]
σ_p	Hole capture cross-section [cm^2]
φ	Electrostatic potential [V]
φ_0	Built-in electrostatic potential [V]
Φ (λ)	Incident photon flux [$s^{-1}cm^{-2}$]
Φ_b	Barrier height at metal/semiconductor interface [eV]
Φ_F	Fermi potential [V]
Φ_n	Quasi-Fermi potential for electrons [V]
Φ_p	Quasi-Fermi potential for holes [V]
T_{bulk}	Bulk minority-carrier recombination lifetime [s]
τ_{eff}	Effective minority-carrier recombination lifetime [s]
τ_n	Recombination lifetime for electrons [s]
τ_p	Recombination lifetime for holes [s]
v	Frequency [s^{-1}]
χ	Electron affinity [eV]
A (λ)	Absorbance [%]
A_m	Finger cross-section area [μm^2]
B	Radiative recombination coefficient [cm^3/s]
CF_{rear}	Rear contact fraction [%]
C_n	Auger coefficient for electrons [cm^6/s]
C_p	Auger coefficient for holes [cm^6/s]
C_{peak}	Peak surface doping concentration [cm^{-3}]
D_n	Electron diffusion coefficient [cm^2/s]
D_p	Hole diffusion coefficient [cm^2/s]
D_{sub}	Wafer thickness [µm]

E_C	Conduction band edge energy [eV]
E_F	Fermi level [eV]
E_{Fn}	Quasi-Fermi level for electrons [eV]
E_{Fp}	Quasi-Fermi level for holes [eV]
E_g	Energy band-gap [eV]
$E_{g,eff}$	Effective 1nergy band-gap [eV]
E_{ph} (λ)	Photon energy [eV]
EQE (λ)	External quantum efficiency [%]
E_V	Valence band edge energy [eV]
F	Finger area factor
F_n	Geometric factor for electrons
F_p	Geometric factor for holes
FF	Fill factor [%]
G	Net generation rate [$cm^{-3}s^{-1}$]
G_{opt}	Optical generation rate [$cm^{-3}s^{-1}$]
H_{bb}	Busbar height [μm]
H_{fm} (or H_m)	Front finger height [μm]
I_{in}	Incident solar irradiance [W/m^2]
IQE (λ)	Internal quantum efficiency [%]
J_0 (or $J_{0,tot}$)	Saturation current density [A/cm^2]
$J_{0,b}$	Base saturation current density [A/cm^2]
$J_{0,BSF}$	BSF saturation current density [A/cm^2]
$J_{0,e}$	Emitter saturation current density [A/cm^2]
$J_{0,min}$	Minimum saturation current density [A/cm^2]
J_{depth}	Junction depth [μm]
J_{in}	Incident photon current density [A/cm^2]
J_L (or J_{ph})	Photogenerated current density [A/cm^2]
J_{mpp}	Current density at maximum power point [A/cm^2]
J_n	Electron current density [A/cm^2]
J_p	Hole current density [A/cm^2]
J_{sc}	Short-circuit current density [A/cm^2]
$J_{sc,max}$	Maximum short-circuit current density [A/cm^2]
κ_λ	Extinction coefficient (imaginary part of the refractive index)
k	Boltzmann constant [J/K]
L_{bb}	Busbar length [cm]
L_{fm} (or L_m)	Front finger length [cm]
L_n	Diffusion length for electrons [cm]
L_p	Diffusion length for holes [cm]
L_T	Transport length [cm]
m_e^*	Effective mass for electrons [g]
m_p^*	Effective mass for holes [g]
n	Electron concentration [cm^{-3}]
$\tilde{n}$	Complex refractive index
n_λ	Real part of the complex refractive index
n_i	Intrinsic carrier density [cm^{-3}]

$n_{i,eff}$	Effective intrinsic carrier density [cm^{-3}]
n_{n0}	Electron equilibrium concentration in *n*-type semiconductors [cm^{-3}]
n_{p0}	Electron equilibrium concentration in *p*-type semiconductors [cm^{-3}]
N_A	Acceptor density [cm^{-3}]
N_C	Effective density of states in the conduction band [cm^{-3}]
N_D	Donor density [cm^{-3}]
N_{dop}	Net doping density [cm^{-3}]
N_s	Surface doping concentration [cm^{-3}]
$N_{s,chem}$	Chemical surface doping concentration [cm^{-3}]
N_{sub}	Substrate doping density [cm^{-3}]
N_t	SRH trap density [cm^{-3}]
N_V	Effective density of states in the valence band [cm^{-3}]
p	Hole concentration [cm^{-3}]
P_{in}	Incident solar power [W/cm^2]
P_{mpp}	Maximum output power [W/cm^2]
p_{n0}	Hole equilibrium concentration in *n*-type semiconductors [cm^{-3}]
p_{p0}	Hole equilibrium concentration in *p*-type semiconductors [cm^{-3}]
q	Electronic charge [C]
R	Net recombination rate [$cm^{-3}s^{-1}$]
$R(\lambda)$	Reflectance [%]
R_b	Bulk semiconductor resistance [Ω]
R_{bb}	Resistance of the front busbars [Ω]
R_{bc}	Back contact resistance [Ω]
R_{ch}	Characteristic resistance of a solar cell [Ω]
$R_{ext,front}$	External front reflectivity
R_{fc}	Front contact resistance [Ω]
R_{fm} (or R_m)	Resistance of the front metal fingers [Ω]
$R_{int,back}$	Internal back reflectivity
$R_{int,front}$	Internal front reflectivity
R_s	Series resistance [Ω]
R_{sh}	Shunt resistance [Ω]
R_{sq}	Emitter sheet resistance [Ω/sq]
S	Interruption size [µm]
S_n	Surface recombination velocity for electrons [cm/s]
S_p	Surface recombination velocity for holes [cm/s]
$SR(\lambda)$	Spectral response [A/W]
v_{oc}	Normalized open-circuit voltage
t	Time [s]
$T(\lambda)$	Transmittance [%]
T	Temperature [K]
V_a	Applied bias voltage [V]
V_{mpp}	Voltage at maximum power point [V]
V_{oc}	Open-circuit voltage [V]
v_{oc}	Normalized open-circuit voltage
v_{th}	Thermal velocity [cm/s]
W_{bb}	Busbar width [mm]

W_{fm} (or W_m)	Front finger width [µm]
W_{se}	Lateral width of the SE diffusion [µm]
W_{sub}	Front contact pitch [mm]
W_{wafer}	Wafer width [cm]
x_F	Interruption position [mm]

CONTENTS

About the author................... vii

Note sull'autore................... ix

Acknowledgments................... xi

Abstract................... xiii

Sommario................... xv

List of abbreviations and symbols................... xvii

1. **Introduction**................... 1
   - 1.1. The development of PV technology................... 1
   - 1.2. The new energy paradigm based on renewable energy sources................... 3
   - 1.3. Solar cell technologies................... 5
   - 1.4. Motivation and thesis outline................... 7
   - References................... 10

2. **Physics of Solar Cells**................... 11
   - 2.1. Semiconductor device equations................... 13
     - 2.1.1. Poisson equation................... 13
     - 2.1.2. Drift-diffusion current density equations................... 13
     - 2.1.3. Continuity equations................... 14
     - 2.1.4. Equations in one-dimensional form................... 15
   - 2.2. 1-D *p-n* junction diode model................... 16
     - 2.2.1. Electrostatics of the *p-n* junction................... 16
     - 2.2.2. Ideal dark *I-V* characteristics................... 21
     - 2.2.3. Ideal illuminated *I-V* characteristics................... 26
     - 2.2.4. Electrical output parameters of a solar cell................... 28
     - 2.2.5. Optical output parameters of a solar cell................... 29
   - 2.3. Real solar cell characteristics................... 32
     - 2.3.1. Position-dependent minority-carrier lifetime................... 32
     - 2.3.2. Surface recombination................... 34
     - 2.3.3. Series and shunt resistances................... 36
     - 2.3.4. Recombination in the depletion region................... 37
     - 2.3.5. Spatially-dependent photogeneration................... 39
   - 2.4. Efficiency limits of a silicon solar cell................... 40
     - 2.4.1. Short-circuit current limits................... 40

2.4.2. Open-circuit voltage and efficiency limits................... 42
2.5. Loss mechanisms in silicon solar cells................... 45
2.5.1. Non-absorption and thermalization losses................... 45
2.5.2. Optical losses................... 47
2.5.3. Recombination losses................... 55
2.5.4. Parasitic resistive losses................... 59
2.5.5. Thermal losses (Effect of temperature)................... 64
References................... 65

3. Numerical Modeling of Solar Cells................... 67
3.1. Numerical solution of semiconductor device equations................... 67
3.1.1. Historical overview on solar cell modeling................... 68
3.1.2. Drift-diffusion transport model................... 70
3.1.3. Numerical solution method................... 74
3.2. TCAD-based numerical simulation of solar cells................... 77
3.2.1. Device editing and mesh generation................... 78
3.2.2. Optical simulation................... 80
3.2.3. Electrical simulation................... 85
3.2.4. Post-processing analysis................... 86
3.2.5. Mixed-mode simulation approach................... 91
3.3. Calibration of physical models for silicon solar cells................... 93
3.3.1. Intrinsic carrier density model................... 93
3.3.2. Auger recombination model................... 96
3.3.3. SRH recombination model................... 99
3.3.4. Surface SRH recombination model................... 103
References................... 107

4. Simulation of Conventional Silicon Solar Cells................... 111
4.1. Simulation setup................... 112
4.1.1. Device structure and mesh................... 113
4.1.2. Electro-optical simulation................... 115
4.1.3. Post-processing analysis................... 117
4.2. Simulation of screen-printed *c*-Si solar cells................... 119
4.2.1. Light *J-V* analysis................... 119
4.2.2. Dark *J-V* analysis................... 120
4.2.3. Cell losses analysis................... 121
4.3. Simulation of double screen-printed *c*-Si solar cells................... 123

4.3.1. Double screen-printing technology.................... 123
4.3.2. Simulation results.................... 125
References.................... 128

5. Simulation of High-Efficiency Silicon Solar Cells.................... 129
5.1. Simulation of selective emitter solar cells.................... 129
5.1.1. Introduction to SE solar cells.................... 130
5.1.2. Simulation setup.................... 132
5.1.3. Analysis of the effect of the lowly-doped profile.................... 134
5.1.4. Analysis of the effect of the highly-doped profile.................... 137
5.1.5. Investigation on the alignment tolerance.................... 141
5.1.6. Effect of DP process over SE design.................... 144
5.2. Simulation of rear point contact solar cells....................
147
5.2.1. Introduction to rear point contact solar cells.................... 147
5.2.2. Simulation setup.................... 149
5.2.3. Optimization of the rear point contact design.................... 154
References.................... 156

6. Simulation Methodology to Account for the Finger Non-Uniformity.................... 159
6.1. Analysis of the impact of the finger roughness.................... 160
6.1.1. Simulation methodology.................... 161
6.1.2. Simulation results.................... 165
6.2. Analysis of the impact of the finger interruptions.................... 167
6.2.1. Simulation methodology.................... 168
6.2.2. Simulation results.................... 170
References.................... 174

Conclusions.................... 175

Chapter 1

Introduction

Photovoltaics (PV), i.e. the direct conversion of sunlight into electrical energy using the electronic properties of a class of material known as semiconductors, is one of the most promising energy-conversion processes. This technology provides several attractive features, such as pollution-free operation without mechanical stress, relatively low maintenance costs and modularity. Nowadays, PV technology is a rapidly growing and important alternative to fossil energy forms for electricity generation. In future energy scenarios, PV solar cells will occupy a prominent role in global electricity generation in order to limit environmental pollution and, consequently, the impact on the climatic change.

1.1 The development of PV technology

Solar cells exploit the *photovoltaic effect* for their operation. This effect was accidentally discovered in 1839 by the French physicist Edmond Becquerel, who observed a light-dependent voltage between two electrodes immersed in an electrolyte. Nevertheless, the first modern photovoltaic device, based on semiconductors that converted light to electricity with a reasonable efficiency, was introduced only in 1954. By the early 1960s, PV technology was intensively used for space use. However, solar cells for space applications were extremely expensive devices, unsuitable for terrestrial use. The first vast oil crisis, which occurred during the 1970s, gave a first important boost to the promotion of photovoltaics as an alternative energy-generation process for terrestrial use. Consequently, solar cells research and development experienced growing interest. As a result, solar cells began to quickly increase their energy-conversion efficiency (see Fig. 1.1) and the increase of the volume of cells produced for terrestrial use led to a significant reduction in solar cell manufacturing costs. Through the 1980s and 1990s, innovative solar cell technologies and concepts were introduced and, therefore, PV industry saw a further remarkable growth. Moreover, by the early 1990s, ecological considerations acted as a main driving force in promoting PV solar energy. Nowadays, the installation of PV systems is growing very fast and the cost of PV-derived electricity is decreasing steadily. In particular, at the end of 2011, the world-wide installed capacity of solar PV systems has reached more than 69,000 megawatts (MW), representing 0.5% of global electricity demand. It is worth noting that the cumulative PV capacity (grid-connected) was only 1,200 MW at the end of 2000. Accordingly, photovoltaics is now, after

hydro and wind power, the third most important renewable energy source in terms of global installed capacity [1.1].

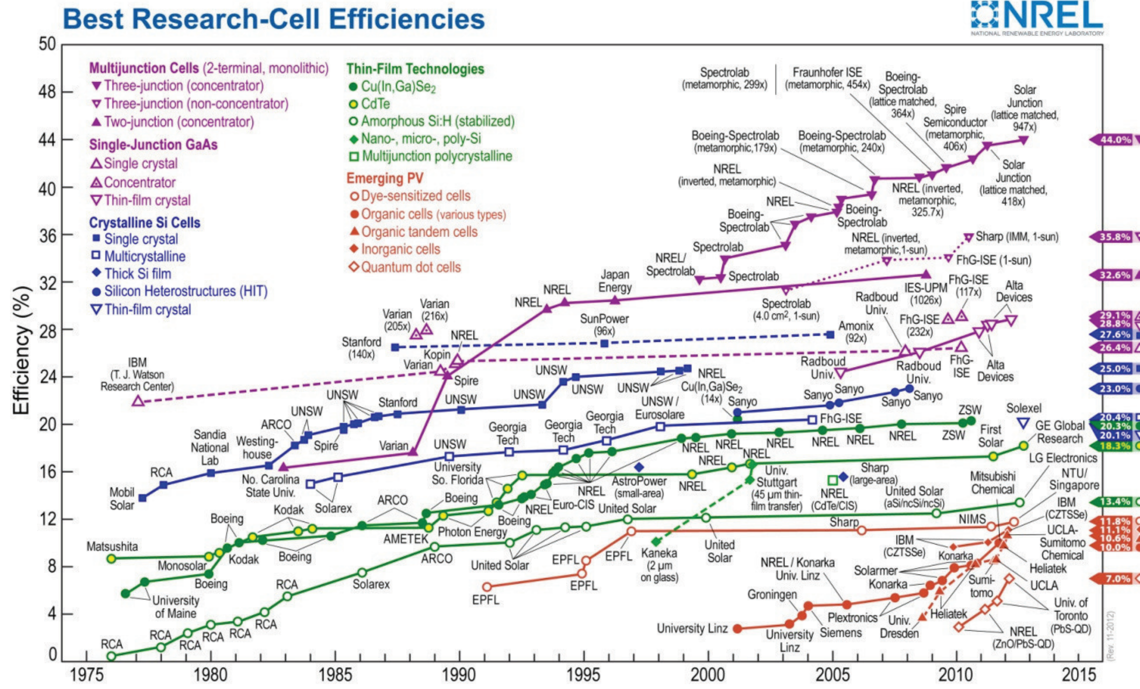

Figure 1.1. Evolution of conversion efficiency for different types of solar cells since 1975. Taken from *www.nrel.gov/pv/*.

1.2 The new energy paradigm based on renewable energy sources

The use of new kinds of renewable energy sources, more durable and less damaging to the environment compared to burning fossils, is rapidly expanding and will gradually grow in the future. Such progressive growth will be driven by the likely inability of fossils to sustain the future energy demand, which increases at the rate of + 2.5% per year world-wide, without large price increase due to progressive scarcity introduced by the rising demand, and by the growing evidence for the climate change, primarily owing to the extended use of fossils [1.2]. As a matter of fact, global carbon dioxide emissions have risen by 3.3% per year since 1950, and the average global temperature has increased by 0.3-0.6 °C since the early 1900s and by 0.2-0.3 °C over last 40 years [1.3].

Among the renewable energy sources, the sun-derived energy has both the energetic potential and the duration sufficient to match the future energy needs. Each moment, the sun, which is a source of practically unlimited energy, irradiates an enormous amount of energy into space. Only a small fraction of this energy is intercepted by the earth, resulting in about 170,000 terrawatt (TW), i.e. 170×10^{15} watt, of incident solar power. Whereas mankind consumes only about 15 TW of energy (less than 0.01% of the received solar energy) and in the future it is expected that additional 10 TW will be necessary to satisfy our energy needs, solar energy can theoretically cover the world-wide energy demand, or at least an important portion [1.4]. Despite this significant potential of sunlight for supplying energy, so far, solar power provides only a very small fraction of the global energy demand, as stated above. In order to reverse this situation, solar technologies must become more efficient, reliable, cost-competitive and responsive to the current demands of the market.

Concerning the PV technology, due to forthcoming improvements in terms of solar cell energy-conversion efficiency, reliability and production costs, it is expected that, by 2020, such technology will cover about 10% of the world-wide energy consumption. In particular, PV can be a strategic choice for Italy, whereas Italy is currently strongly dependent on foreign primary energy supplies and its geographic location, particularly in the Southern Italy, is rather favorable to the exploitation of this technology (see Fig. 1.2).

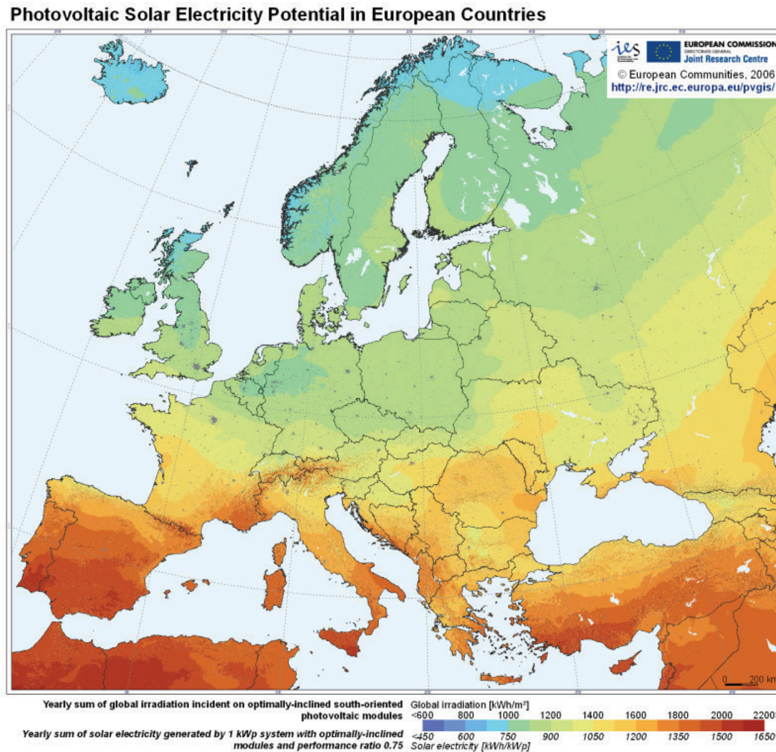

Figure 1.2. Map of the PV solar electricity potential in European countries published by the European Commission. Taken from *http://re.jrc.ec.europa.eu/pvgis/cmaps/*.

However, at the present time, an important hurdle to the development of PV technology is constituted by the limitations of the power grid. Indeed, the largest part of power supply system is currently based on a centralized and large-scale model and, hence, it is not suited to sustain an high amount of distributed electrical power. In future scenarios, the implementation of *smart grids*, able to quickly respond to the local energy demand, will lead to a further development of PV technology and other forms of distributed energy generation. Accordingly, the power grid will consist of a decentralized, distributed, downsized and modular system, where the energy mix will be supplied by small modular generation units, primarily based on renewable energy sources, such as combined-cycle gas turbines, PV panels, wind turbines and fuel cells [1.5].

1.3 Solar cell technologies

Solar cells can be fabricated on the basis of different semiconductor technologies. However, although some innovative materials represent a promising and interesting topic for the PV community, silicon (Si) is still the most widely used semiconductor for mass production PV devices and it will be also competitive for the next decades, according to the most recent roadmaps [1.6].

Current industrial solar cell manufacturing technologies can be divided in two major classes:

- *first-generation* or *wafer-based* solar cells, featuring thick silicon substrates;
- *second-generation* or *thin-film* solar cells, featuring thinner substrates.

The first-generation of solar cells is currently the most commercially widespread technology, as well as the oldest. Conventional wafer-based solar cells make use of *mono-crystalline* (*c*-Si) and *multi-crystalline* (*mc*-Si) silicon substrates with a thickness of 150-220 μm. Nowadays, these cells are produced on a very large scale, covering more than 80% of the global PV market due to their relatively high conversion efficiencies (around 18-20% for *c*-Si solar cells and 14-16% for *mc*-Si solar cells) and quite simple manufacturing process [1.6].

The second-generation includes thin-film solar cells, based on different semiconductor materials: amorphous silicon (*a*-Si), cadmium telluride (CdTe), copper indium selenide (CIS), copper indium gallium selenide (CIGS) and III-V compound semiconductors. These PV devices make use of low-cost thin substrates, thus aiming at reducing the material usage and, consequently, the production costs. So far, thin-film solar cells have shown lower performance as compared to the first-generation devices, because of a lower material quality and, hence, higher electrical losses, and of the limited capability to collect the photons from sunlight due to the thinner substrates. However, despite their lower conversion efficiencies, second-generation solar cells are expected to overtake conventional wafer-based silicon solar cells in the PV market within next decades thanks to their lower manufacturing costs and greater flexibility. Currently, these cells account for about 10-15% of the global PV market [1.6].

In addition, there exists a wide range of emerging PV technologies, including *concentrated* photovoltaics (CPV) and *third-generation* solar cells, as well as novel solar cell concepts, with a significant potential to increase the cell performance. CPV technologies, that use an optical concentrator system in order to focus the solar radiation on a small high-efficiency solar cell, are mostly being tested in pilot applications, even though they are already present in the PV market on a very small scale. Instead, the new generation (*third-generation*) of solar cells is currently the main subject of basic research into the PV field. These innovative solar cells aim at achieving high conversion efficiencies through the adoption of advanced

materials and new cell concepts, without increasing drastically the production costs. In particular, the third-generation includes non-semiconductor technologies (polymer solar cells, photo-electrochemical solar cells and organic dye-sensitized cells), tandem/multi-junction solar cells and nano-structured devices, which are expected to have a very promising future [1.7].

1.4 Motivation and thesis outline

The improvement of PV solar cells in terms of reducing costs and increasing conversion efficiency requires a careful device optimization, including the design of contacts, doping profiles and passivation layers, the choice of materials and the implementation of advanced light trapping strategies. The growing complexity of solar cell concepts and architectures has led to ever more extensive Design of Experiments (DoE), which hardly could be performed only through experimental tests. In this context, modeling of PV devices has become increasingly strategic and helpful for the PV industry in order to aid the design of solar cells, thus accelerating the optimization and, at the same time, reducing the testing costs.

Solar cell modeling, based on numerical simulation techniques and advanced models for representing the physical properties of the devices, is a powerful tool to investigate the physical mechanisms that limit the cell conversion efficiency. While numerical simulation has been extensively used by the electronics industry since the early days of computer modeling, only recently it has become widely used in the PV industry [1.8]. In particular, prior to last decade, first simulation works in the PV context relied on analytical approaches, partially supported by the aid of computer programs, and, consequently, they were mainly focused on the modeling of one-dimensional (1-D) devices. The first popular simulation tool widely used in the PV research community was PC1D [1.9], originally written at Sandia National Labs in 1982 and, then, further developed at the University of New South Wales (UNSW) in Australia, which is still the most commonly used of the commercially available solar cell modeling programs. The success of PC1D is mainly based on its speed due to the low requirement of computational resources, and on its very simple and intuitive user interface. However, its predictive capability is limited by a few assumptions. Among these limitations, the most important are the adoption of Boltzmann statistics, that is not suitable to adequately model some performance-limiting highly-doped regions of the solar cell, and the restriction to the mono-dimensional analysis, thus preventing an accurate investigation of innovative cell architectures [1.10]. In fact, during the last years, the growing interest for advanced solar cell architectures, featuring inherently two-dimensional (2-D) or even three-dimensional (3-D) geometries, and the requirement for a more accurate analysis of cell losses have driven to the adoption in the PV research community of multi-dimensional and general-purpose TCAD (Technology Computer-Aided Design) device simulators, able to solve numerically the fully coupled set of semiconductor differential equations within the drift-diffusion approximation, accounting also for the Fermi-Dirac statistics. Nowadays, one of the most commonly adopted commercial TCAD program in the PV community is Sentaurus by Synopsys [1.11], and to a smaller extent Atlas by Silvaco [1.12] as well as Microtec by Siborg Systems [1.13]. However, in order to achieve sufficiently high

prediction capabilities, several physical models and parameters of these simulators, which are usually tailored to CMOS devices, must be accurately calibrated for the specific requirements of solar cells [1.10], [1.14]. In addition to the electrical simulation, the simulation of PV devices under illumination requires an accurate modeling of light propagation and absorption inside the solar cells. To this purpose, several approaches can be adopted to calculate the optical generation rate inside the device, depending on the specific requirements about accuracy and computational effort. Among the most commonly used optical solvers in PV simulations, it is worth mentioning the Transfer Matrix Method (TMM), the Ray-Tracing (RT) method or the Finite-Difference Time-Domain (FDTD) method [1.10]. Moreover, a mixed-mode simulation approach, based on the combination of numerical device simulations and circuit simulations, can be successfully adopted for the modeling of entire large-area solar cells, thus accounting also for their full metallization geometry and their edges [1.8].

The aim of this Ph.D. thesis is to provide a contribution to the numerical simulation and modeling of *c*-Si solar cells by using a state-of-the-art TCAD computer program [1.11]. In order to achieve realistic predictions on *c*-Si solar cell performance, an ad-hoc refinement of the physical models and parameters implemented in the TCAD simulator has been performed for specific PV requirements. These fine-tuned models include the band-gap narrowing model (BGN) to account for the effective intrinsic carrier density, the Auger recombination model, the bulk Shockley-Read-Hall (SRH) lifetime model in boron-doped and aluminum-doped Czochralski silicon (*Cz*-Si) and the surface recombination velocity (SRV) model at silicon nitride (SiN_x) passivated interfaces. Afterwards, two-dimensional (2-D) and three-dimensional (3-D) numerical simulations have been performed in order to investigate the mechanisms that limit the conversion efficiency of conventional *c*-Si solar cells and of some high-efficiency *c*-Si solar cells intended for industrial scale production, such as Double Screen-Printed (DP) solar cells, Selective Emitter (SE) solar cells, and Passivated Emitter and Rear Cell (PERC) solar cells. Finally, a simulation methodology based on a mixed-mode approach, which combines numerical device simulations and circuit simulations, has been applied to evaluate the impact of non-uniformities in the front-side metallization on the performance of a *c*-Si solar cell.

In the following, the detail of the contents of this thesis is summarized.

In *Chapter 2*, a review of the device physics of solar cells is presented. Starting from the set of basic equations that describe the ideal properties of semiconductor devices in the drift-diffusion approximation, the ideal solar cell output dark and illuminated *I-V* characteristics are first discussed. Later, the effects of various non-idealities on the solar cell characteristics are introduced. Finally, the theoretical efficiency limits and the main loss mechanisms in silicon solar cells are discussed.

In *Chapter 3*, the TCAD-based numerical electro-optical simulation of solar cells is introduced. In particular, the typical approach adopted to solve numerically the basic fully

coupled set of semiconductor equations by using a discretization method is briefly explained. After that, the TCAD-based simulation flow used in this thesis is described. Finally, the calibration of the most critical physical models implemented in the TCAD simulator for specific PV requirements is discussed.

In *Chapter 4*, conventional screen-printed *c*-Si solar cells are analyzed by means of 2-D numerical electro-optical simulations. First, the adopted simulation setup, including the geometrical and physical details of the simulated structures and the implemented physical models, is described. Then, the simulation results of these conventional silicon solar cells are reported, both in terms of light and dark *I-V* analysis. Finally, the impact of more advanced front metallization architectures due to the Double Screen-Printing (DP) technology is investigated.

In *Chapter 5*, some advanced technological solutions for high-efficiency silicon solar cells are explored by means of 2-D and 3-D electro-optical numerical simulations. First, a 2-D modeling approach is adopted to investigate the impact of different doping profiles in Selective Emitter (SE) solar cells. Then, rigorous 3-D numerical simulations are performed to optimize the rear point contact geometry of a Passivated Emitter and Rear Cell (PERC) solar cell.

In *Chapter 6*, a simulation methodology based on a mixed-mode simulation approach is proposed to investigate the impact of the non-uniformities in the front-side metallization on the performance of silicon solar cells. First, the effect of the finger roughness is studied as function of the finger height, width and resistivity for both conventional Single Screen-Printing (SP) and Double Screen-Printing (DP) metallization technologies. Then, the proposed methodology is applied to evaluate the impact of the finger interruptions on the solar cell performance as function of the interruption size, interruption position, number of interruptions and finger resistivity for typical fingers realized with DP technology.

References

[1.1] European Photovoltaic Industry Association (EPIA), "Global Market Outlook for Photovoltaics until 2016", 2012.
[1.2] Agenzia nazionale per le nuove tecnologie, l'energia e lo sviluppo economico sostenibile (ENEA), "Solar thermal energy production: guidelines and future programmes of ENEA", Italy, 2001.
[1.3] Intergovernmental Panel on Climate Change (IPCC), "IPCC Fourth Assessment Report", *Cambridge University Press*, 2007.
[1.4] C. Philibert, "The present and future use of solar thermal energy as a primary source of energy", *International Energy Agency*, Paris, France 2005.
[1.5] C. Flavin and S. Dunn, "A new energy paradigm for the 21st century", *Journal of International Affairs*, Vol. 53, pp. 167-190, 1999.
[1.6] International Energy Agency (IEA), "Technology Roadmap - Solar photovoltaic energy", 2010.
[1.7] M. A. Green, "Third generation photovoltaics: Ultra-high conversion efficiency at low cost", *Progress in Photovoltaics: Research and Applications*, Vol. 9, No. 2, pp. 123-135, 2001.
[1.8] P. P. Altermatt et al., "Highly Predictive Modelling of Entire Si Solar Cells for Industrial Applications", *Proc. of 24th European Photovoltaic Solar Energy Conference* (*EU PVSEC*), pp. 901-906, 2009.
[1.9] P. A. Basore, "Numerical Modeling of Textured Silicon Solar Cells using PC-1D", *IEEE Transaction on Electron Devices*, Vol. 37, No. 2, pp. 337-343, 1990.
[1.10] R. De Rose, M. Zanuccoli, P. Magnone, E. Sangiorgi, C. Fiegna, "Open Issues for the Numerical Simulation of Silicon Solar Cells", *Proc. of 12th International Conference on Ultimate Integration on Silicon* (*ULIS*), pp. 1-4, 2011.
[1.11] Sentaurus, Synopsys, Mountain View, CA, USA.
[1.12] Atlas, Silvaco, Santa Clara, CA, USA.
[1.13] MicroTec, Siborg Systems, Waterloo, Canada.
[1.14] P. P. Altermatt, "Models for numerical device simulations of crystalline silicon solar cells – a review", *Journal of Computational Electronics*, Vol. 10, No. 3, pp. 314-330, 2011.

Chapter 2

Physics of Solar Cells

PV solar cells are fundamentally quite simple devices that directly convert the sunlight into electrical energy by exploiting the ability of semiconductor materials to absorb light and to deliver a portion of the absorbed energy to carriers of electrical current. A conventional solar cell structure is simply based on a semiconductor *p-n* junction diode that operates under solar illumination (see Fig. 2.1). When sunlight strikes the surface of a semiconductor, a certain portion of photons is transmitted and, then, absorbed into the semiconductor material, thus giving rise to photogenerated electron-hole pairs, while the remainder is reflected from the surface. Some of these photo-generated charge carriers are separated by the internal built-in electric field of the *p-n* junction before they recombine and, then, they are collected at the cell terminals, thus contributing to the cell output current in the external circuit.

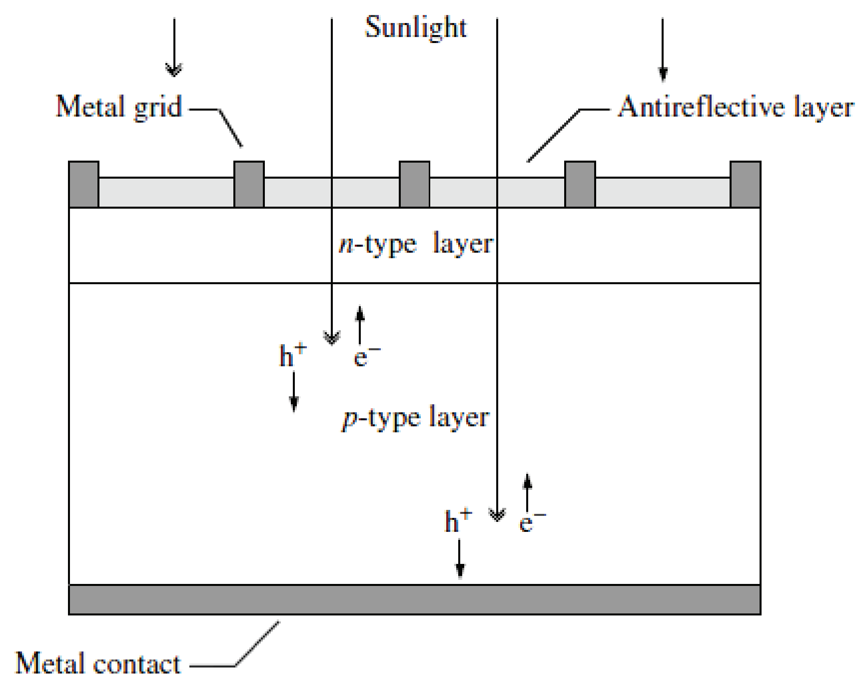

Figure 2.1. Schematic of a simple single-junction solar cell structure, where the photogeneration of electron-hole pairs is evidenced. Taken from [2.1].

In this chapter, a review of the basic physical principles that underlie the operation of solar cells is reported. Starting from the set of basic equations that describe the ideal properties of semiconductor devices in the drift-diffusion approximation, the simple 1-D diode model is

first discussed in order to analytically derive the ideal solar cell output dark and illuminated *I-V* characteristics. Afterwards, the effects of various non-idealities on the solar cell characteristics are introduced. Finally, the theoretical efficiency limits and the main loss mechanisms that affect the performance of silicon solar cells are explained.

2.1 Semiconductor device equations

A set of five basic equations, constituting the well-known drift-diffusion (DD) transport model, is capable of describing the operation of semiconductor devices under the influence of an electric field and/or light, both of which lead to a deviation from the thermal equilibrium conditions. In particular, the solution of this set of equations allows to derive the characteristics of semiconductor devices, including silicon solar cells.

2.1.1 Poisson equation

Poisson equation describes the electrostatics, by relating the divergence of the static electric field $\boldsymbol{\xi}$ to the charge density ρ:

$$\nabla \cdot \boldsymbol{\xi} = -\nabla^2 \varphi = \frac{\rho}{\varepsilon} \tag{2.1}$$

where φ is the electrostatic potential and ε is the material permittivity. The charge density in a semiconductor device is given by:

$$\rho = q\left(p - n + N_D^+ - N_A^-\right) \tag{2.2}$$

where n and p are the electron and hole densities, respectively, and N_D^+ and N_A^- are the densities of ionized donors and acceptors, respectively.

2.1.2 Drift-diffusion current density equations

It is widely known that, in a semiconductor device, electrons and holes can contribute to the current flow through drift and diffusion processes. The drift process occurs when applying an electric field $\boldsymbol{\xi}$ across the semiconductor device, while the diffusion transport is driven by a concentration gradient. Consequently, the total current densities of electrons and holes, $\boldsymbol{J_p}$ e $\boldsymbol{J_n}$, are given by:

$$\boldsymbol{J}_n = q\mu_n n\boldsymbol{\xi} + qD_n \nabla n \tag{2.3}$$

$$\boldsymbol{J}_p = q\mu_p p\boldsymbol{\xi} - qD_p \nabla p \tag{2.4}$$

where μ_n and μ_p are the electron and hole mobilities, respectively, and D_n and D_p are the electron and hole diffusion coefficients, respectively. Therefore, the first terms on the right hand side of Eqs. 2.3 and 2.4 represent the drift currents, while the second terms denote the diffusion currents. The mobilities and the diffusion coefficients are related through the Einstein relationships:

$$D_n = \mu_n \frac{kT}{q}, \qquad D_p = \mu_p \frac{kT}{q} \tag{2.5}$$

2.1.3 Continuity equations

Two additional equations, i.e. the continuity equations, are required to define the complete set of semiconductor equations. These equations relate the divergence of the current densities to the recombination and generation rates of charge carriers. Under steady-state conditions, the electron and hole continuity equations can be written as:

$$\frac{1}{q} \nabla \cdot \boldsymbol{J}_n = R_n - G_n \tag{2.6}$$

$$\frac{1}{q} \nabla \cdot \boldsymbol{J}_p = -\left(R_p - G_p\right) \tag{2.7}$$

where R and G are the net recombination and generation rates, respectively.

2.1.4 Equations set in one-dimensional form

The complete set of basic semiconductor equations is thus composed by Eqs. 2.1, 2.3, 2.4, 2.6 and 2.7. Under the one-dimensional assumption (i.e., the variations in other two spatial dimensions are neglected), the equations become:

$$\frac{d\xi}{dx} = \frac{q}{\varepsilon}\left(p - n + N_D^+ - N_A^-\right) \tag{2.8}$$

$$J_n = q\mu_n n\xi + qD_n \frac{dn}{dx} \tag{2.9}$$

$$J_p = q\mu_p p\xi - qD_p \frac{dp}{dx} \tag{2.10}$$

$$\frac{1}{q}\frac{dJ_n}{dx} = R_n - G_n \tag{2.11}$$

$$\frac{1}{q}\frac{dJ_p}{dx} = -\left(R_p - G_p\right) \tag{2.12}$$

By including the expressions of the current densities (Eqs. 2.9 and 2.10) into the continuity equations (Eqs. 2.11 and 2.12), the following transport equations can be obtained as:

$$D_n \frac{d^2 n}{dx^2} + \mu_n\xi \frac{dn}{dx} + n\mu_n \frac{d\xi}{dx} - R_n + G_n = 0 \tag{2.13}$$

$$D_p \frac{d^2 p}{dx^2} - \mu_p\xi \frac{dp}{dx} - p\mu_p \frac{d\xi}{dx} - R_p + G_p = 0 \tag{2.14}$$

These two equations are coupled through the electric field ξ defined in the Poisson equation (see Eq. 2.8). Therefore, they form a coupled set of nonlinear differential equations for which it is not possible to find general analytical solutions. However, this set of equations can be solved, with different degrees of accuracy, numerically on a computer, or analytically by making some specific assumptions, as shown in the following section for the simple 1-D diode model.

2.2 1-D *p-n* junction diode model

By adopting a simple 1-D *p-n* junction diode model for a silicon solar cell featuring a constant doping in the *p*-type and *n*-type regions and an abrupt doping step transition, and by taking into account some simplifying assumptions, the ideal solar cell output dark and illuminated *I-V* characteristics can be easily derived analytically from the set of equations presented in the previous section.

2.2.1 Electrostatics of the *p-n* junction

As already explained, a conventional solar cell is simply formed by a *p-n* junction (Fig. 2.2). When two pieces of *n*-type and *p*-type doped semiconductors are brought into contact, electrons diffuse from the region of high concentration (*n*-type side) to the region of low concentration (*p*-type side), due to the concentration gradient between the two types of material. Similarly, holes diffuse from *p*-type side to *n*-type side. As a consequence, the electrons diffusion current from the *n*-doped to the *p*-doped region creates a charge imbalance in the *n*-type side, leading to a positively charged region in that side (see Fig. 2.2). Likewise, the holes diffusion causes a negative charge in the *p*-type side. This leads to the creation of an electric field that opposes the diffusion transport, thus resulting in an equilibrium situation.

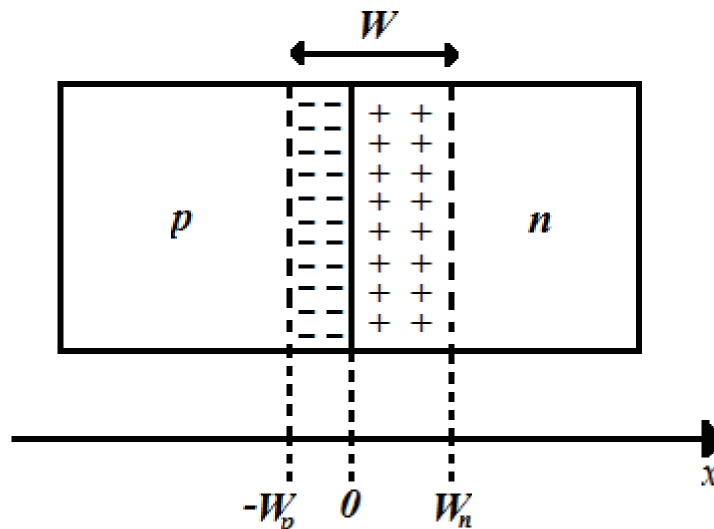

Figure 2.2. Schematic of a simple 1-D *p-n* junction. *W* represents the width of the depletion region, while W_p and W_n define the edges of the depletion region.

In terms of energy bands, the Fermi levels E_F of two separated *p*- and *n*-doped regions are different, as shown in Fig. 2.3a. Instead, the *p-n* junction in equilibrium shows a constant Fermi

level, thus causing the band bending of the conduction energy band E_C and the valence energy band E_V (see Fig. 2.3b).

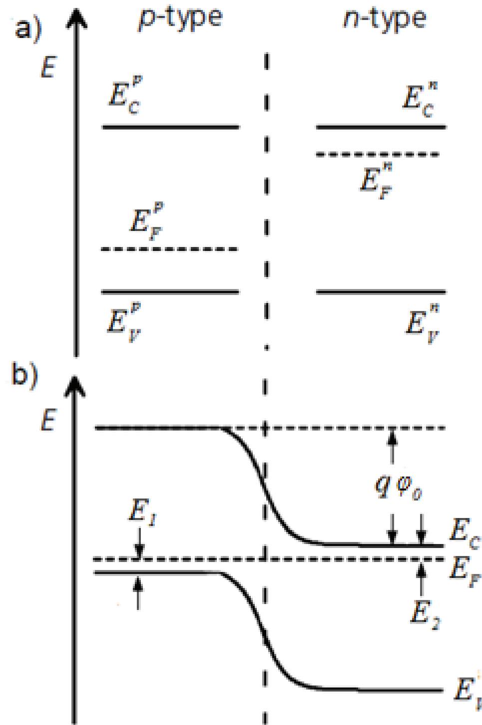

Figure 2.3. Energy-band diagrams of a) two isolated pieces of *p*-type and *n*-type semiconductors, and of b) the *p*-*n* junction at equilibrium conditions.

From Fig. 2.3b, the electrostatic potential difference across the junction, known as the built-in potential φ_0, can be expressed as:

$$q\varphi_0 = E_g - E_1 - E_2 \tag{2.15}$$

where $E_g = E_C - E_V$ is the energy band-gap between the conduction and valence band edges. E_1 and E_2 can be derived from the Boltzmann expressions of the free carrier concentrations for non-degenerate doped semiconductors at thermal equilibrium, assuming that the dopants are fully ionized [2.2]:

$$n_0 = N_D = N_C\, exp\left(- \frac{E_C - E_F}{kT} \right) \tag{2.16}$$

$$p_0 = N_A = N_V\, exp\left(- \frac{E_F - E_V}{kT} \right) \tag{2.17}$$

where N_C and N_V are the effective densities of states of the conduction and valence bands, respectively. Consequently:

$$E_1 = E_F - E_V = kT\, ln\left(\frac{N_V}{N_A}\right), \qquad E_2 = E_C - E_F = kT\, ln\left(\frac{N_C}{N_D}\right) \tag{2.18}$$

At thermal equilibrium conditions, the semiconductor mass-action law is still valid, and, by using Eqs. 2.16 and 2.17, it can be written as:

$$n_i^2 = n_0\, p_0 = N_C\, N_V\, exp\left(-\frac{E_g}{kT}\right) \tag{2.19}$$

Therefore, by including Eqs. 2.18 and 2.19 in Eq. 2.15, it is possible to express the built-in potential as:

$$\varphi_0 = \frac{kT}{q}\, ln\left(\frac{N_A N_D}{n_i^2}\right) \tag{2.20}$$

The electrostatics of the *p-n* junction is defined by Poisson equation (see Eq. 2.1). Since the space-charge region across the junction (i.e., for $-W_p < x < W_n$ in Fig.2.2) is almost completely depleted of mobile charge carriers (i.e., *p* and *n* are negligible compared to the donor and acceptor densities), a simple model for this region, based on the *depletion approximation*, can be considered by assuming rectangular charge density distributions in the device, as shown in Fig. 2.4a. In this way, the device can be divided into two types of regions: the *quasi-neutral regions* (QNRs) where the charge density is assumed to be zero throughout (i.e., for $x \leq -W_p$ and $x \geq W_n$ in Fig. 2.2), and the *depletion region* where the carrier densities are assumed to be negligible and, therefore, the only contribution to the charge density comes from the ionized dopants. Accordingly, Poisson equation in the depletion region is given by:

$$\frac{d\xi}{dx} = -\frac{d^2\varphi}{dx^2} = -\frac{q}{\varepsilon} N_A \qquad \text{if } -W_p < x < 0 \tag{2.21}$$

$$\frac{d\xi}{dx} = -\frac{d^2\varphi}{dx^2} = \frac{q}{\varepsilon} N_D \qquad \text{if } 0 < x < W_n \tag{2.22}$$

On the contrary, in the QNRs, Poisson equation becomes:

$$\frac{d\xi}{dx} = -\frac{d^2\varphi}{dx^2} = 0 \qquad \text{if } -W_p \le x \text{ and } x \ge W_n \tag{2.23}$$

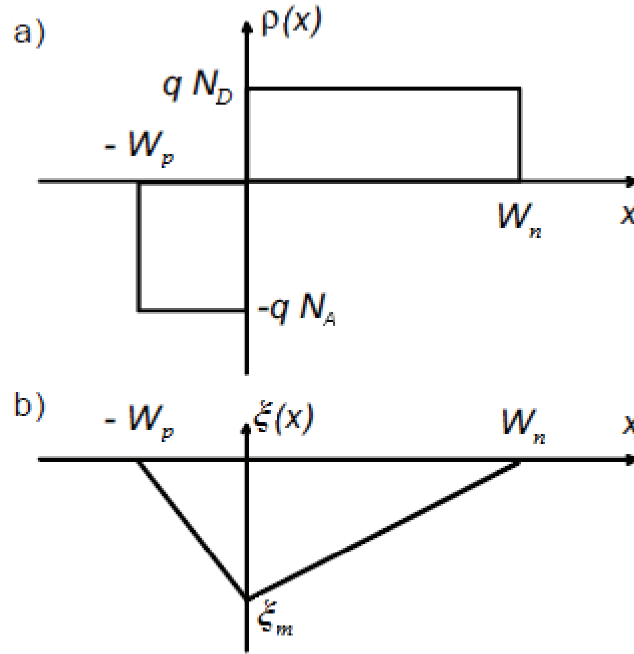

Figure 2.4. a) Charge density distributions in the *p-n* junction under the depletion approximation. b) Corresponding electrical field profile.

Therefore, the electric field in the depletion region can be found by integrating Poisson equation, expressed in Eqs. 2.21 and 2.22, from $x = 0$ to the edges of this region, thus obtaining:

$$\xi(x) = -\frac{qN_A}{\varepsilon}\left(x + W_p\right) \qquad \text{if } -W_p < x < 0 \tag{2.24}$$

$$\xi(x) = \frac{qN_D}{\varepsilon}\left(x - W_n\right) \qquad \text{if } 0 < x < W_n \tag{2.25}$$

$$\xi_m = \frac{qN_D W_n}{\varepsilon} = \frac{qN_A W_p}{\varepsilon} \qquad \text{in } x = 0 \tag{2.26}$$

where ξ_m is the maximum intensity of the electric field in $x = 0$ (see Fig. 2.4b). Fig. 2.4b shows the linear dependence of the electrical field on the position in the depletion region, while the electric filed vanishes in the QNRs, according to the assumed charge density distributions.

By integrating Eqs. 2.24 and 2.25 along x, the electrostatic potential in the depletion region can be found as:

$$\varphi_p(x) = \frac{qN_A}{2\varepsilon} x(2W_p + x) \qquad \text{if } -W_p < x < 0 \tag{2.27}$$

$$\varphi_n(x) = \frac{qN_D}{2\varepsilon} x(2W_n - x) \qquad \text{if } 0 < x < W_n \tag{2.28}$$

Consequently, the potential difference at the depletion region edges is given by:

$$\varphi_0 = \varphi_n(W_n) - \varphi_p(-W_p) = \frac{q}{2\varepsilon}\left(N_D W_n^2 + N_A W_p^2\right) = \frac{1}{2}\xi_m W \tag{2.29}$$

where $W = W_n + W_p$ is the width of the depletion region (see Fig. 2.2). Moreover, the electrical neutrality of the device can be expressed as:

$$W_p N_A = W_n N_D \tag{2.30}$$

By combining Eqs. 2.29 and 2.30, the width of the depletion region can be defined as:

$$W = \sqrt{\frac{2\varepsilon}{q}\left(\frac{N_A + N_D}{N_A N_D}\right)\varphi_0} \tag{2.31}$$

An external applied bias voltage V_a disturbs the equilibrium conditions, shifting the potential barrier and, consequently, the potential difference across the *p-n* junction, that becomes (φ_0 - V_a). Accordingly, Eq. 2.31 changes as:

$$W = \sqrt{\frac{2\varepsilon}{q}\left(\frac{N_A + N_D}{N_A N_D}\right)(\varphi_0 - V_a)} \tag{2.32}$$

2.2.2 Ideal dark *I-V* characteristics

In order to derive the ideal *I-V* characteristics of a *p-n* junction, the minority-carrier densities at the edges of the depletion region as a function of bias have to be found. At thermal equilibrium conditions (zero bias), their values are already known [2.2]:

$$p_{n0} = p_{p0}\, exp\left(-\frac{q\varphi_0}{kT} \right) \approx \frac{n_i^2}{N_D} \tag{2.33}$$

$$n_{p0} = n_{n0}\, exp\left(-\frac{q\varphi_0}{kT} \right) \approx \frac{n_i^2}{N_A} \tag{2.34}$$

where p_{p0} and n_{n0} are the majority-carrier concentrations in the quasi-neutral regions, respectively. Under low-injection conditions, i.e. the minority-carrier densities are negligible as compared to the majority-carrier ones on both sides ($n_n >> p_n$ and $p_p >> n_p$), the majority-carrier concentrations can be expressed as:

$$n_n(W_n) = n_{n0} = N_D, \qquad p_p(-W_p) = p_{p0} = N_A \tag{2.35}$$

Under this assumption, the expressions for the minority-carrier concentrations at the edges of the depletion region (see Fig. 2.5) are given by [2.2]:

$$p_n(W_n) = p_{n0}\, exp\left(\frac{qV_a}{kT} \right) = \frac{n_i^2}{N_D} exp\left(\frac{qV_a}{kT} \right) \tag{2.36}$$

$$n_p(-W_p) = n_{p0}\, exp\left(\frac{qV_a}{kT} \right) = \frac{n_i^2}{N_A} exp\left(\frac{qV_a}{kT} \right) \tag{2.37}$$

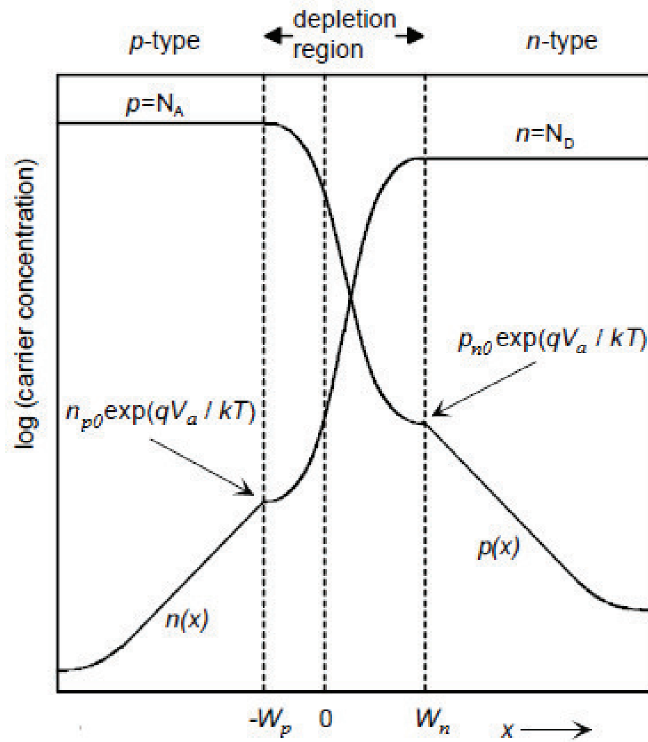

Figure 2.5. Electron and hole carrier concentrations across the dark forward-biased *p-n* junction. Taken from [2.3].

Therefore, the concentrations of the minority carriers at the edges of the depletion region increase exponentially with the applied bias voltage.

Moreover, it is possible to demonstrate that, if a uniformly doped region of semiconductor material is quasi-neutral (i.e., the charge density is approximately zero) and minority-carrier flows are not irrelevant, the minority-carrier transport in this quasi-neutral region is predominantly diffusive. Therefore:

$$J_n = qD_n \frac{dn}{dx} \qquad \text{(in } p\text{-type quasi-neutral region)} \qquad (2.38)$$

$$J_p = -qD_p \frac{dp}{dx} \qquad \text{(in } n\text{-type quasi-neutral region)} \qquad (2.39)$$

Basically, it happens that the small number of minority carriers compared to majority carriers shields them from the effect of an electric field [2.2].

The calculation of the quantitative expression for the ideal dark *I-V* characteristics of the *p-n* junction requires the solution of the transport equations for electrons and holes (see Eqs. 2.13 and 2.14). As already discussed, both these two equations contain the electrical field ξ, thus forming a coupled set of differential equations, where the unknowns are the carrier concentrations n and p, and the electrical field. Therefore, if the spatial dependence of the electric field and of the carrier concentrations is known, the current densities can be easily calculated from Eqs. 2.9 and 2.10.

Through the approximations discussed in Section 2.2.1, it has been found that the electric field vanishes in the QNRs of the *p-n* junction and, hence, the transport Eqs. 2.13 and 2.14 decouple in these regions. As a consequence, the carrier transport is purely diffusive and, therefore, the minority-carrier concentrations can be calculated separately for both quasi-neutral regions from the following decoupled linear differential equations:

$$D_n \frac{d^2 n_p}{dx^2} - R_n + G_n = 0 \qquad \text{(in } p\text{-type quasi-neutral region)} \qquad (2.40)$$

$$D_p \frac{d^2 p_n}{dx^2} - R_p + G_p = 0 \qquad \text{(in } n\text{-type quasi-neutral region)} \qquad (2.41)$$

Furthermore, under low-injection conditions, the perturbation of the majority-carrier concentrations due to generation and recombination mechanisms can be neglected [2.3]. Consequently, the recombination rate of minority carriers on both sides of the *p-n* junction is proportional to the excess minority-carrier concentrations, as given by:

$$R_n = \frac{n_p - n_{p0}}{\tau_n} \qquad \text{(in } p\text{-type quasi-neutral region)} \qquad (2.42)$$

$$R_p = \frac{p_n - p_{n0}}{\tau_p} \qquad \text{(in } n\text{-type quasi-neutral region)} \qquad (2.43)$$

where τ_n and τ_p are the minority-carrier lifetimes of electrons and holes, respectively, assumed to be independent of carrier concentrations. Therefore, transport equations become:

$$D_n \frac{d^2 n_p}{dx^2} - \frac{n_p - n_{p0}}{\tau_n} + G_n = 0 \qquad \text{(in } p\text{-type quasi-neutral region)} \qquad (2.44)$$

$$D_p \frac{d^2 p_n}{dx^2} - \frac{p_n - p_{n0}}{\tau_p} + G_p = 0 \qquad \text{(in } n\text{-type quasi-neutral region)} \tag{2.45}$$

In dark conditions, $G = 0$, then, Eqs. 2.42 and 2.43 in the QNRs reduce to homogeneous differential equations:

$$\frac{d^2 \Delta n}{dx^2} - \frac{\Delta n}{L_n^2} = 0 \qquad (x \leq -W_p) \tag{2.46}$$

$$\frac{d^2 \Delta p}{dx^2} - \frac{\Delta p}{L_p^2} = 0 \qquad (x \geq W_n) \tag{2.47}$$

$$L_n = \sqrt{D_n \tau_n}, \qquad L_p = \sqrt{D_p \tau_p} \tag{2.48}$$

where L_n and L_p are the diffusion length of electrons in the p-type side and holes in the n-type side, respectively.

For the solution of Eqs. 2.46 and 2.47, the two following boundary conditions have to be considered:

1) at $x \rightarrow \infty$, by assuming that there are no recombination losses at the surface of both quasi-neutral regions (i.e., n-type and p-type regions are of infinite dimensions), n_p and p_n are finite, therefore:

$$\frac{dn}{dx}\Big|_{x \to -\infty} = 0, \qquad \frac{dp}{dx}\Big|_{x \to \infty} = 0 \tag{2.49}$$

2) at $x = W_n$ and $x = -W_p$, the boundary conditions are given by Eqs. 2.36 and 2.37, respectively.

These boundary conditions give the following particular solutions [2.3]:

$$n_p(x) = n_{p0} + n_{p0}\left[exp\left(\frac{qV_a}{kT}\right) - 1\right] exp\left(\frac{W_p + x}{L_n}\right) \tag{2.50}$$

$$p_n(x) = p_{n0} + p_{n0}\left[exp\left(\frac{qV_a}{kT}\right) - 1\right] exp\left(\frac{W_n - x}{L_p}\right) \tag{2.51}$$

From Eqs. 2.50 and 2.51, it is possible to note that the excess carrier concentrations for electrons in the *p*-type QNR and holes in the *n*-type QNR decay exponentially from position $x = -W_p$ and $x = W_n$, respectively, with the diffusion lengths as characteristic lengths (see Fig. 2.5).

Once the minority-carrier density distributions are known, the minority-carrier diffusive current densities in the QNRs can be easily calculated from Eqs. 2.38 and 2.39:

$$J_n(x) = \frac{qD_n n_{p0}}{L_n}\left[exp\left(\frac{qV_a}{kT}\right) - 1\right] exp\left(\frac{W_p + x}{L_n}\right) \qquad (2.52)$$

$$J_p(x) = \frac{qD_p p_{n0}}{L_p}\left[exp\left(\frac{qV_a}{kT}\right) - 1\right] exp\left(\frac{W_n - x}{L_p}\right) \qquad (2.53)$$

Instead, considering the current flows in the depletion region, the continuity equations in this region are given by:

$$\frac{1}{q}\frac{dJ_n}{dx} = R - G = -\frac{1}{q}\frac{dJ_p}{dx} \qquad (2.54)$$

By assuming that no recombination losses occur in the depletion region, it follows that, in dark conditions (i.e., $G = 0$), both the current densities are essentially constant across the depletion region. Consequently, the total current density can be found from Eqs. 2.52 and 2.53 as:

$$J_{tot} = J_n(-W_p) + J_p(W_n) = J_0\left[exp\left(\frac{qV_a}{kT}\right) - 1\right] \qquad (2.55)$$

where

$$J_0 = \frac{qD_n n_{p0}}{L_n} + \frac{qD_p p_{n0}}{L_p} = qn_i^2\left[\frac{D_n}{L_n N_A} + \frac{D_p}{L_p N_D}\right] \qquad (2.56)$$

is the dark saturation current density of the *p-n* junction. Eq. 2.55, also known as the *Shockley equation*, represents the ideal dark *I-V* characteristics of the *p-n* junction.

2.2.3 Ideal illuminated *I-V* characteristics

The ideal illuminated *I-V* characteristics are generally derived by considering, for mathematical simplicity, the case of a spatially-uniform generation rate G of electron-hole pairs inside the device. This assumption strongly simplifies the mathematical treatment, without altering the most important conclusions.

Therefore, in illuminated conditions (i.e., $G \neq 0$), the transport equations (Eqs. 2.44 and 2.45) in the QNRs become inhomogeneous differential equations:

$$\frac{d^2 \Delta n}{dx^2} - \frac{\Delta n}{L_n^2} = -\frac{G_n}{D_n} \qquad (x \leq -W_p) \qquad (2.57)$$

$$\frac{d^2 \Delta p}{dx^2} - \frac{\Delta p}{L_p^2} = -\frac{G_p}{D_p} \qquad (x \geq W_n) \qquad (2.58)$$

Since the terms G_n / D_n and G_p / D_p are constant, the solutions of Eqs. 2.57 and 2.58 can be found by applying the superposition principle, i.e., by adding particular solutions of the inhomogeneous differential equations to the general homogeneous solutions, as explained in [2.3]. By following this approach, the minority-carrier densities in the QNRs under illumination can be calculated as:

$$n_p(x) = n_{p0} + G\tau_n + \left[n_{p0}\left(exp\left(\frac{qV_a}{kT}\right) - 1 \right) - G\tau_n \right] exp\left(\frac{W_p + x}{L_n}\right) \qquad (2.59)$$

$$p_n(x) = p_{n0} + G\tau_p + \left[p_{n0}\left(exp\left(\frac{qV_a}{kT}\right) - 1 \right) - G\tau_p \right] exp\left(\frac{W_n - x}{L_p}\right) \qquad (2.60)$$

Then, the corresponding diffusive current densities become:

$$J_n(x) = \frac{qD_n n_{p0}}{L_n}\left[exp\left(\frac{qV_a}{kT}\right) - 1 \right] exp\left(\frac{W_p + x}{L_n}\right) - qGL_n\, exp\left(\frac{W_p + x}{L_n}\right) \qquad (2.61)$$

$$J_p(x) = \frac{qD_p p_{n0}}{L_p}\left[exp\left(\frac{qV_a}{kT}\right) - 1 \right] exp\left(\frac{W_n - x}{L_p}\right) - qGL_p\, exp\left(\frac{W_n - x}{L_p}\right) \qquad (2.62)$$

In the depletion region, neglecting again the recombination losses, the effect of the uniform photogeneration of electron-hole pairs gives a change in the total current density equal to qGW [2.2]. Consequently, in illuminated conditions, the total current density is given by:

$$J_{tot} = J_n\left(-W_p\right) + J_p\left(W_n\right) - qGW = J_0\left[exp\left(\frac{qV_a}{kT}\right) - 1\right] - J_L \tag{2.63}$$

where J_L is the photogenerated current, expressed as:

$$J_L = qG\left(W + L_n + L_p\right) \tag{2.64}$$

Eq. 2.63 represents the ideal illuminated *I-V* characteristics of a solar cell (see Fig. 2.6). It is worth noting in Fig. 2.6 that the illuminated *I-V* curve is simply the dark curve shifted down from the first quadrant to the fourth quadrant by the photogenerated current density J_L.

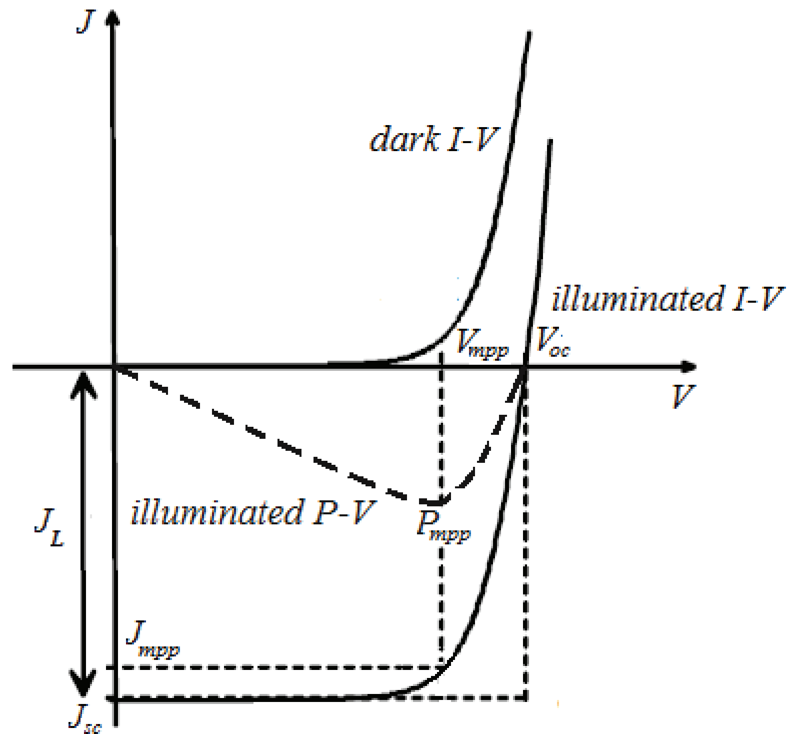

Figure 2.6. Typical dark and illuminated *I-V* curves of a solar cell. The dashed line represents the illuminated *P-V* curve.

2.2.4 Electrical output parameters of a solar cell

The following electrical output parameters are typically used to characterize the performance of a solar cell:

- the *photogenerated current density* J_L (or J_{ph}) under illumination, typically expressed in mA/cm^2;
- the *short-circuit current density* J_{sc}, typically expressed in mA/cm^2, that denotes the current density at zero voltage (see Fig. 2.6); ideally (i.e., zero recombination), the J_{sc} is equal to the photogenerated current density;
- the *open-circuit voltage* V_{oc}, typically expressed in mV, that represents the voltage at zero current (see Fig. 2.6); by setting J_{tot} = 0 in Eq. 2.63, the relationship between the V_{oc} and the dark saturation current density J_0 can be found as:

$$V_{oc} = \frac{kT}{q} ln\left(\frac{J_L}{J_0} + 1\right) \tag{2.65}$$

- the *maximum output power* P_{mpp}, typically expressed in mW/cm^2, which is given by the product $V_{mpp} \cdot J_{mpp}$, where V_{mpp} and J_{mpp} denote the voltage and the current density at the maximum power point, respectively (see Fig. 2.6);
- the *fill factor FF*, typically expressed as a percentage, which is defined as the ratio of the maximum output power to the theoretical maximum output power:

$$FF = \frac{P_{mpp}}{V_{oc}J_{sc}} = \frac{V_{mpp}J_{mpp}}{V_{oc}J_{sc}} \tag{2.66}$$

Graphically, the *FF* can be calculated as the ratio of the two rectangular areas shown in Fig. 2.6. Ideally, the *FF* is a function only of the open-circuit voltage. A typical empirical expression, that relates *FF* and V_{oc}, is given by:

$$FF = \frac{v_{oc} - ln\left(v_{oc} + 0.72\right)}{v_{oc} + 1} \tag{2.67}$$

where v_{oc} is the normalized open-circuit voltage, defined as $V_{oc}/(kT/q)$.

- the *power conversion efficiency* η, typically expressed as a percentage, which is defined as the ratio of the maximum output power to the incident solar power P_{in} (that is typically equal to 1000 W/m^2):

$$\eta = \frac{P_{mpp}}{P_{in}} = \frac{V_{mpp} J_{mpp}}{P_{in}} = \frac{V_{oc} J_{sc} FF}{P_{in}} \tag{2.68}$$

2.2.5 Optical output parameters of a solar cell

The electrical figures of merit defined in Section 2.2.4 are not sufficient to fully characterize the performance of a solar cell. The following optical output parameters can help to understand in more detail which are the dominant loss mechanisms that limit the conversion efficiency in a solar cell, including the optical losses:

- the *reflectance* $R(\lambda)$, given by:

$$R(\lambda) = \frac{P_R(\lambda)}{P_{in}(\lambda)} \tag{2.69}$$

where P_R is the reflected portion of the incident solar power;

- the *transmittance* $T(\lambda)$, given by:

$$T(\lambda) = \frac{P_T(\lambda)}{P_{in}(\lambda)} \tag{2.70}$$

where P_T is the transmitted portion of the incident solar power;

- the *absorbance* $A(\lambda)$, given by:

$$A(\lambda) = \frac{P_A(\lambda)}{P_{in}(\lambda)} \tag{2.71}$$

where P_A is the absorbed portion of the incident solar power.

It is worth noting that, for the optical conservation law, $R(\lambda) + T(\lambda) + A(\lambda) = 1$.

- the *spectral response SR* (λ), typically expressed in A/W, which is defined as the ratio of the current generated by the solar cell under short-circuit conditions J_{sc} (λ) to the incident irradiance I_{in} (λ), as a function of the wavelength λ of the radiation:

$$SR(\lambda) = \frac{J_{sc}(\lambda)}{I_{in}(\lambda)} \tag{2.72}$$

- the *external quantum efficiency EQE* (λ), representing the probability that carriers are generated and collected at the cell terminals under illumination, which is defined as the ratio of the number of carriers collected by the solar cell under short-circuit conditions to the number of incident photons of a given energy:

$$EQE(\lambda) = \frac{\eta_{sc}(\lambda)}{\eta_{in}(\lambda)} = \frac{J_{sc}(\lambda)}{J_{in}(\lambda)} \tag{2.73}$$

where η_{sc} (λ) is the rate of carriers collected by the solar cell under short-circuit conditions, η_{in} (λ) is the incident photon rate (i.e., the number of incident photons per unit time), J_{sc} (λ) is the short-circuit current density, and J_{in} (λ) is the incident photon current density, respectively, as a function of the wavelength λ of the radiation.
The incident photon flux Φ (λ) (i.e., the number of photons per time and area unit) is given by:

$$\Phi(\lambda) = \frac{I_{in}(\lambda)}{E_{ph}(\lambda)} = \frac{I_{in}(\lambda)}{h\nu} \tag{2.74}$$

where E_{ph} (λ) is the photon energy as a function of the wavelength λ of the radiation. The collection rate of carriers under short-circuit conditions is given by $J_{sc} \cdot A/q$, while the incident photon rate is $\Phi(\lambda) \cdot A$, where A is the area of the solar cell. Therefore, Eq. 2.73 can be rewritten as:

$$EQE(\lambda) = \frac{J_{sc}(\lambda)/q}{I_{in}(\lambda)/E_{ph}(\lambda)} = SR(\lambda)\frac{E_{ph}(\lambda)}{q} \tag{2.75}$$

Eq. 2.75 thus relates the external quantum efficiency and the spectral response.

- the *internal quantum efficiency IQE* (λ), which is defined as the ratio of the number of carriers which contribute to the cell output current under short-circuit conditions to the number of photons that are not reflected by the cell:

$$IQE(\lambda) = \frac{EQE(\lambda)}{1 - R(\lambda)} \tag{2.76}$$

- the *quantum collection efficiency* η_c (λ), which is defined as the ratio of the number of carriers collected by the solar cell under short-circuit conditions to the total number of photogenerated electron-hole pairs inside the device:

$$\eta_c(\lambda) = \frac{J_{sc}(\lambda)}{J_{ph}(\lambda)} = \frac{EQE(\lambda)}{1 - R(\lambda) - T(\lambda)} \tag{2.77}$$

It is worth noting that, while *EQE* includes the effect of all the optical losses, such as transmission and reflection losses, *IQE* takes into account only the transmission losses, as evidenced in Eq. 2.76, thus reporting about the efficiency whereby photons that are not reflected by the solar cell generate carriers which are then collected at the cell terminals. On the contrary, η_c does not account for the effect of both optical loss mechanisms (according to Eq. 2.77), thus referring to the efficiency whereby the solar cell collects the carriers, once generated in the device.

2.3 Real solar cell characteristics

The ideal characteristics allow to account for the basic physical mechanisms occurring inside a solar cell. However, a real device can generally exhibit strong deviations from the ideal behavior. For deriving the ideal solar cell characteristics, some important simplifying assumptions have been made above, such as:

- the *depletion approximation*, whereby the device has been divided into two types of regions: the quasi-neutral regions and the depletion region;
- *low-injection conditions*, leading to majority carrier concentrations equal to the dopant densities in the quasi-neutral regions (according to Eq. 2.35); it is worth noting that this assumption is not still valid when the device is illuminated by concentrated sunlight or at high forward bias voltages;
- minority-carrier lifetimes assumed to be constant, i.e. independent of carrier concentrations (according to Eqs. 2.42 and 2.43);
- the cell has been assumed wide enough so that surface recombination losses have been neglected;
- zero parasitic resistive losses due to series and shunt resistances;
- zero recombination losses in the depletion region;
- spatially-uniform photogeneration of electron-hole pairs inside the device.

In the following, the effects of various non-idealities on the solar cell characteristics are briefly discussed.

2.3.1 Position-dependent minority-carrier lifetime

In Eqs. 2.42 and 2.43, the minority-carrier lifetimes τ_n and τ_p have been assumed to be constant. In a real device, these lifetimes depend on the doping density and, consequently, on the carrier concentration. Therefore, they are typically position-dependent. In particular, τ_n and τ_p are determined by the dominant recombination mechanisms inside the device, such as:

- *radiative* or *band-to-band recombination*, whose recombination lifetimes can be expressed as:

$$\tau_n^R = \frac{1}{Bp_{p0}} = \frac{1}{BN_A}, \qquad \tau_p^R = \frac{1}{Bn_{n0}} = \frac{1}{BN_D} \tag{2.78}$$

where B is the radiative recombination rate coefficient;

- *Shockley-Read-Hall* (*SRH*) or *trap-assisted recombination*, whose minority-carrier lifetimes in case of a single-trap can be written as:

$$\tau_n^{SRH} = \frac{1}{N_t \sigma_n v_{th}}, \qquad \tau_p^{SRH} = \frac{1}{N_t \sigma_p v_{th}} \tag{2.79}$$

where N_t is the trap concentration, v_{th} is the thermal velocity, σ_n and σ_p are the electrons and holes capture cross-section of the trap (which is proportional to the carrier capture probability), respectively;

- *Auger recombination*, whose minority-carrier lifetimes for low-injection conditions are given by:

$$\tau_n^A = \frac{1}{C_p p_{p0}^2} = \frac{1}{C_p N_A^2}, \qquad \tau_p^A = \frac{1}{C_n n_{n0}^2} = \frac{1}{C_n N_D^2} \tag{2.80}$$

where C_n and C_p are the Auger recombination rate constants for electrons and holes, respectively.

SRH and Auger recombinations are typically the two dominant recombination mechanisms in silicon solar cells. Therefore, the effective minority-carrier lifetimes for electrons in the *p*-type region and for holes in the *n*-type region, respectively, can be expressed as:

$$\frac{1}{\tau_n} = \frac{1}{\tau_n^{SRH}} + \frac{1}{\tau_n^A}, \qquad \frac{1}{\tau_p} = \frac{1}{\tau_p^{SRH}} + \frac{1}{\tau_p^A} \tag{2.81}$$

In particular, due to the inverse quadratic dependence of the Auger lifetime on doping density (see Eq. 2.80), Auger recombination typically dominates in heavily-doped regions, while SRH mechanism generally determines the lifetimes in lightly-doped regions. Moreover, if low-injection conditions are not satisfied, the recombination rates for electrons and holes, R_n and R_p (see Eqs. 2.42 and 2.43), depend on both the electron and hole concentrations. Consequently, the coupled set of semiconductor differential equations have to be solved numerically [2.3].

2.3.2 Surface recombination

Another important assumption, which has been made in the discussion of the ideal solar cell characteristics, has concerned the thickness of the cell. In particular, it has been assumed that the cell extended to an infinite distance on either side of the *p-n* junction in order to neglect surface recombination losses. Thereby, the boundary conditions of Eq. 2.49 have been considered. Obviously, a real device has finite dimensions, as shown in Fig. 2.7. Therefore, the recombination at the cell surfaces has to be taken into account.

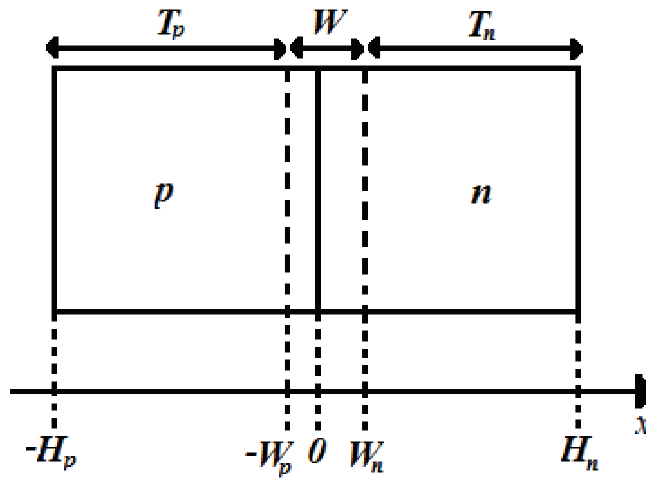

Figure 2.7. Schematic of the 1-D basic solar cell of finite dimensions.

This modifies the boundary conditions of Eq. 2.49 as:

$$D_n \frac{dn}{dx}\bigg|_{x\to -H_p} = S_n(n-n_0)\bigg|_{x\to -H_p}, \qquad D_p \frac{dp}{dx}\bigg|_{x\to H_n} = S_p(p-p_0)\bigg|_{x\to H_n} \tag{2.82}$$

where S_n and S_p are the electrons and holes surface recombination velocities (SRV), respectively. By applying these new boundary conditions and, then, by performing the same steps as in Section 2.2.2, a modified expression of the dark saturation current density J_0 can be derived as:

$$J_0 == qn_i^2\left[\frac{D_n}{L_n N_A}F_n + \frac{D_p}{L_p N_D}F_p\right] \tag{2.83}$$

where F_n and F_p are the geometric factors for electrons and holes, respectively, given by [2.2]:

$$F_n = \frac{sinh\left(\frac{T_n}{L_p}\right) + \frac{S_p L_p}{D_p} cosh\left(\frac{T_n}{L_p}\right)}{cosh\left(\frac{T_n}{L_p}\right) + \frac{S_p L_p}{D_p} sinh\left(\frac{T_n}{L_p}\right)}, \qquad F_p = \frac{sinh\left(\frac{T_p}{L_e}\right) + \frac{S_e L_e}{D_e} cosh\left(\frac{T_p}{L_e}\right)}{cosh\left(\frac{T_p}{L_e}\right) + \frac{S_e L_e}{D_e} sinh\left(\frac{T_p}{L_e}\right)} \tag{2.84}$$

where $T_n = H_n - W_n$ and $T_p = H_p - W_p$ are the widths of *n*-doped and *p*-doped quasi-neutral regions, respectively (see Fig. 2.7). It is worth noting that a lower value of J_0 and, hence, a higher V_{oc} (according to Eq. 2.65) can be reached when both cell surfaces exhibit low recombination velocities.

The effect of the surface recombination on the saturation current density can be highlighted by plotting the geometric factor as a function of T/L for different values of SL/D, as shown in Fig. 2.8. It can be observed that, for $L < T$ (i.e., $T/L > 1$), the surfaces do not contribute to the saturation current density. Moreover, it is possible to note that a thin quasi-neutral region of width T in combination with a high surface recombination velocity S can result in a very high J_0 and, consequently, a low V_{oc}. On the other hand, a good surface passivation, leading to lower surface recombination velocities, can limit J_0 in a thin device. This is particularly important for thin-film solar cells.

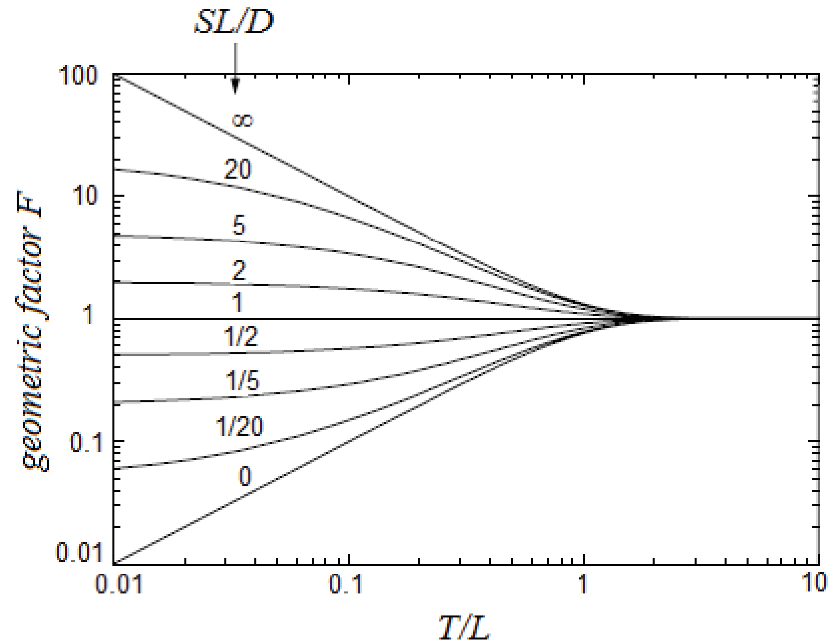

Figure 2.8. Geometric factor F as a function of the ratio of the width of the quasi-neutral region T to the minority-carrier diffusion length L for different $S{\cdot}L/D$ ratios, where S is the surface recombination velocity and D is the diffusion constant. Taken from [2.3].

2.3.3 Series and shunt resistances

In a real device, parasitic resistive losses due to a *series resistance* R_s and a *shunt* (or *parallel*) *resistance* R_{sh} have to be considered. Accounting for these, the illuminated *I-V* cell characteristics (see Eq. 2.63) become:

$$J(V) = J_0\left[exp\left(\frac{q(V - J(V)R_s)}{kT}\right) - 1\right] + \frac{V - J(V)R_s}{R_{sh}} - J_L \tag{2.85}$$

where V is the voltage at the cell terminals.

The series resistance of a solar cell consists of the resistance of the front metal grid, the contact resistances, and the bulk and emitter resistances, while shunt resistance is typically related to crystal defects and impurity precipitates, as well as leakage currents across the *p-n* junction around the edges of the cell.

The influence of these resistive components on the dark and illuminated *I-V* characteristics is shown in Fig. 2.9. In particular, focusing on the dark characteristics (Figs. 2.9c and 2.9d), it is worth noting that a high series resistance causes a deviation from the ideal dark *I-V* curve at high current densities, while a low shunt resistance influences the dark *I-V* curve at small current densities.

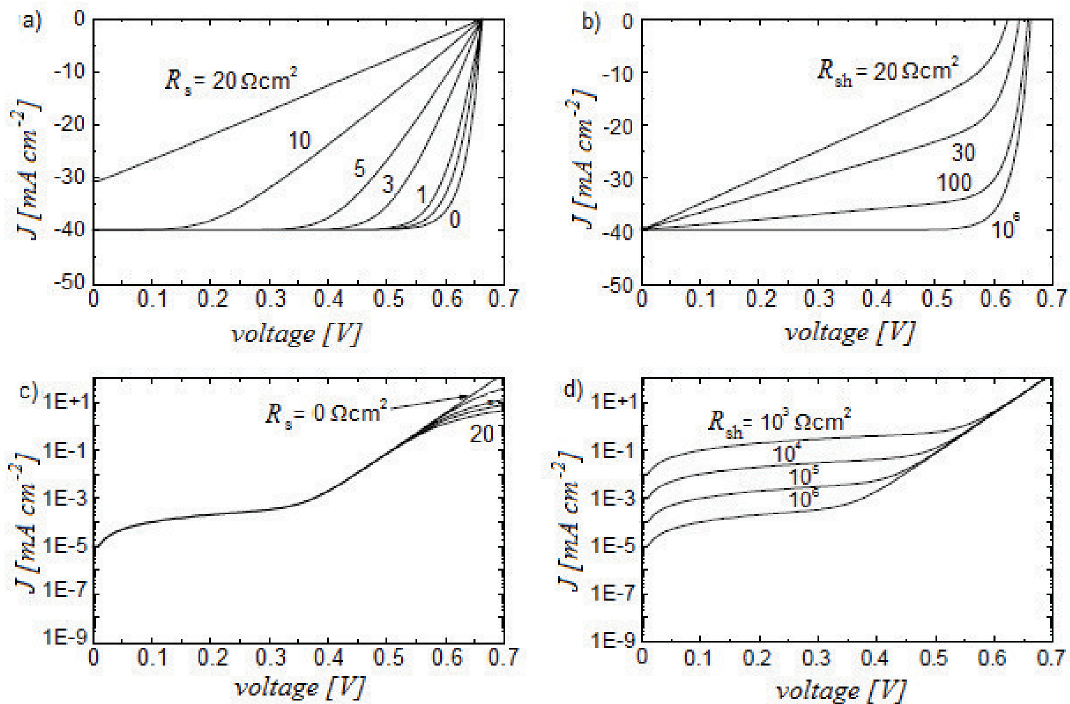

Figure 2.9. Influence of series resistance R_s and shunt resistance R_{sh} on the *I-V* cell characteristics: a) illuminated curves for different R_s; b) illuminated curves for different R_{sh}; c) dark curves (logarithmic scale) for different R_s; d) dark curves (logarithmic scale) for different R_{sh}. Taken from [2.3].

2.3.4 Recombination in the depletion region

In the calculation of the ideal cell *I-V* characteristics, it has been assumed that there are no recombination losses in the depletion region. Actually, in real devices, SRH recombination in this region represents a significant loss mechanism. By taking into account the simplified case of a single recombination trap within the forbidden gap, and by assuming that the SRH recombination rate is constant across the depletion region, an analytical expression for the recombination current in such region is given by [2.3]:

$$J_W = J_{02}\left[exp\left(\frac{qV_a}{2kT}\right)-1\right] \tag{2.86}$$

By including such depletion-region recombination current in Eq. 2.55, the dark *I-V* characteristics of the solar cell become:

$$J = J_{01}\left[exp\left(\frac{qV_a}{kT}\right)-1\right]+J_{02}\left[exp\left(\frac{qV_a}{2kT}\right)-1\right] \tag{2.87}$$

The corresponding illuminated *I-V* characteristics can be obtained from Eq. 2.85, thus taking into account also the effect of the parasitic resistances:

$$J(V)=J_{01}\left[exp\left(\frac{q(V-J(V)R_s)}{kT}\right)-1\right]+J_{02}\left[exp\left(\frac{q(V-J(V)R_s)}{2kT}\right)-1\right]+\frac{V-J(V)R_s}{R_{sh}}-J_L \tag{2.88}$$

This expression describes the non-ideal illuminated *I-V* characteristics of a solar cell.

In addition to the recombination in the depletion region, a non-ideal behavior of the solar cell can be related to other nonidealities effects, e.g. to injection-dependent surface recombination losses. In the boundary conditions of Eq. 2.82, the surface recombination velocities have been implicitly assumed to be independent of minority-carrier concentration. However, in [2.4], it was demonstrated that the non-ideal behavior of some high-efficiency silicon solar cells can be related to the surface recombination velocity at rear passivated interfaces that strongly depends on the excess minority-carrier concentration.

In practice, an *i*-th nonideal effect can be generally described in the dark forward-biased *I-V* characteristics of the cell by means of a dark current component, expressed in the exponential form as:

$$J_i = J_{0i}\left[exp\left(\frac{qV_a}{nkT}\right)-1\right] \tag{2.89}$$

where n is known as the ideality factor. Therefore, in general, a real dark *I-V* curve of a solar cell can be approximated by several exponential terms, revealing the presence of various dark current components.

Typically, the illuminated *I-V* characteristics of a real solar cell are analytically described through the well-known "*two-diode model*", given by:

$$J(V)=J_{01}\left[exp\left(\frac{q(V-J(V)R_s)}{n_1kT}\right)-1\right]+J_{02}\left[exp\left(\frac{q(V-J(V)R_s)}{n_2kT}\right)-1\right]+\frac{V-J(V)R_s}{R_{sh}}-J_L \tag{2.90}$$

Fig. 2.10 shows the equivalent circuit of Eq. 2.90, composed by two diodes in parallel with different ideality factors n_1 and n_2, and different saturation current densities J_{01} and J_{02} representing the recombination current terms, the photocurrent generator J_L, and the series and shunt resistances R_s and R_{sh}. By varying n_1, n_2, J_{01}, J_{02}, R_s and R_{sh} parameters, a wide range of experimentally measured or simulated *I-V* characteristics can be fitted [2.5]. Typically, n_1 characterizes the recombination in the quasi-neutral regions and, hence, it is close to 1, while $1.5 < n_2 < 3$ is used to represent the recombination in the depletion region and other non-ideal recombination effects.

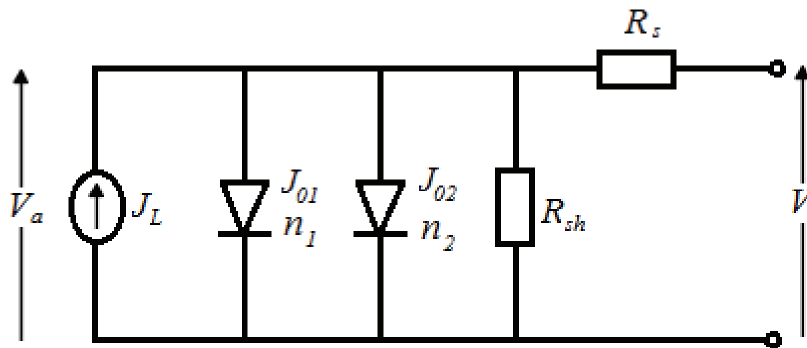

Figure 2.10. Equivalent circuit of a solar cell described by means of the two-diode model (according to Eq. 2.90).

2.3.5 Spatially-dependent photo-generation

In Section 2.2.3, the *I-V* characteristics of a solar cell under illumination have been derived under the assumption of a spatially-uniform photogeneration of electron-hole pairs inside the device. However, in a real device, the absorption of photons from sunlight and, consequently, the electron-hole pairs generation rate are spatially-dependent. In particular, an incident photon of wavelength λ is absorbed with a probability $\alpha(\lambda)$ per unit length, where $\alpha(\lambda)$ is the wavelength-dependent *absorption coefficient* of the semiconductor material. Each absorbed photon creates one electron-hole pair. Therefore, the one-dimensional optical generation rate $G_\lambda(x)$ of electron-hole pairs per unit volume is given by:

$$G_\lambda(x) = \alpha(\lambda) \cdot \Phi_\lambda(x) \tag{2.91}$$

where $\Phi_\lambda(x)$ is the photon flux at depth x. In steady-state conditions, the photon continuity equation can be expressed as:

$$\frac{d\Phi_\lambda(x)}{dx} = -G_\lambda(x) = -\alpha(\lambda) \cdot \Phi_\lambda(x) \tag{2.92}$$

The solution of this differential equation leads to an exponential decay of the photon flux inside the device, according to the well-known *Beer-Lambert law*

$$\Phi_\lambda(x) = \Phi_\lambda(0) \cdot exp\left[- \alpha(\lambda) \cdot x\right] \tag{2.93}$$

The optical generation rate is then obtained from Eq. 2.91 as:

$$G_\lambda(x) = \Phi_\lambda(0) \cdot \alpha(\lambda) \cdot exp\left[- \alpha(\lambda) \cdot x\right] \tag{2.94}$$

The total optical generation rate per unit volume can be calculated by integrating Eq. 2.94 over the wavelength range as:

$$G(x) = \int_\lambda G_\lambda(x)\, d\lambda \tag{2.95}$$

Therefore, by following the same procedure described in Section 2.2.2, the electron and hole current densities can be still calculated analytically for the generation rate given by Eq. 2.95, as shown in [2.6].

2.4 Efficiency limits of a solar cell

In the following, the theoretical upper limits of the main electrical output parameters of a solar cell, already defined in Section 2.2.4, are estimated on the basis of some simple assumptions.

2.4.1 Short-circuit current limits

For the estimation of the upper limit of the short-circuit current density, ideal conditions have to be considered, i.e., each photon incident on the solar cell having an energy greater than the energy band-gap E_g creates an electron-hole pair that contributes to the output current. Therefore, in order to calculate the theoretical maximum short-circuit current density $J_{sc,max}$, the photon flux Φ (λ) in sunlight must be calculated from the solar spectral energy distribution (see Fig. 2.11), by dividing the total energy content at each wavelength λ by the energy of an individual photon ($E_{ph} = hv = hc/\lambda$) at the same wavelength. $J_{sc,max}$ is then derived by integrating the flux distribution from low wavelengths up to the maximum wavelength for which electron-hole pairs can be generated in the semiconductor device (i.e., $\lambda_g = hc/E_g$):

$$J_{sc,max} = q \int_0^{\lambda_g} \Phi(\lambda)\, d\lambda = q \int_{E_g}^{\infty} \Phi(E)\, dE \tag{2.96}$$

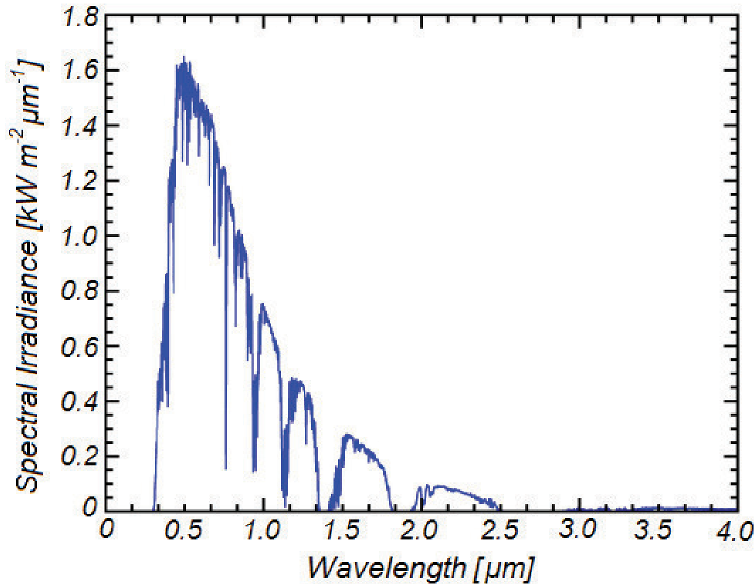

Figure 2.11. Conventional AM1.5G solar spectrum with an incident power of 1000 W/m^2.

The resulting upper limits of the J_{sc} as a function of the energy band-gap E_g of the solar cell material are shown in Fig. 2.12. The curve has been calculated by neglecting the external reflectance at the top interface, and by assuming direct illumination with a conventional AM1.5G solar spectrum with an incident power of 1000 W/m^2 (according to Fig. 2.11) [2.7]. It is worth noting in Fig. 2.12 that, as long as E_g decreases, the theoretical $J_{sc,max}$ increases because more incident photons have the energy required to create an electron-hole pair. For *c*-Si solar cells (E_g = 1.12 eV), the calculated theoretical upper limit on J_{sc} is around 43.8 mA/cm^2.

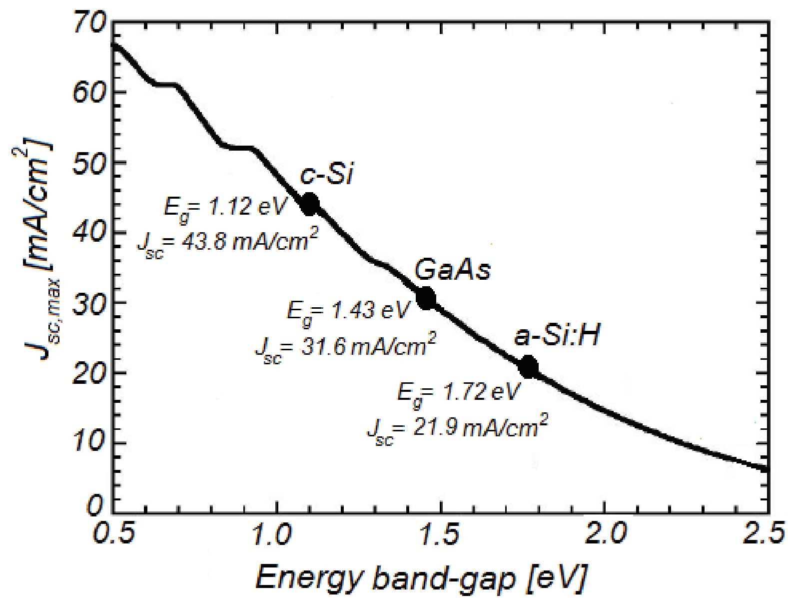

Figure 2.12. Dependence of the short-circuit current density J_{sc} on the energy band-gap E_g, calculated by neglecting the external reflectance at the top interface, and by assuming direct illumination with a conventional AM1.5G solar spectrum with an incident power of 1000 W/m^2 at T = 300 K. All photogenerated electron-hole pairs are assumed to be collected at the cell terminals.

2.4.2 Open-circuit voltage and efficiency limits

The theoretical upper limit for the open-circuit voltage of a solar cell is obviously determined by the energy band-gap E_g. A simplified empirical approach for calculating the upper limit on the V_{oc} and, consequently, on the efficiency has been proposed by Green in [2.2]. This approach is based on the calculation of the lower limit of the dark saturation current density J_0 by assigning empirical values to the semiconductor parameters in Eq. 2.56. By considering also the semiconductor mass-action law (see Eq. 2.19), the following estimation of the minimum value of J_0 as a function of E_g has been derived by Green [2.2]:

$$J_{0,min} = 1.5 \times 10^5 \; exp\left(-\frac{E_g}{kT}\right) \qquad \left[A/cm^2\right] \tag{2.97}$$

The corresponding upper limits of the V_{oc} as a function of E_g, which can be obtained by including Eq. 2.97 in Eq. 2.65, is shown in Fig. 2.13. For *c*-Si solar cells, this empirical upper limit gives a maximum expected V_{oc} of about 700 mV. The corresponding maximum fill factor *FF* (about 0.84) can be estimated through the simple empirical expression of Eq. 2.67 [2.2].

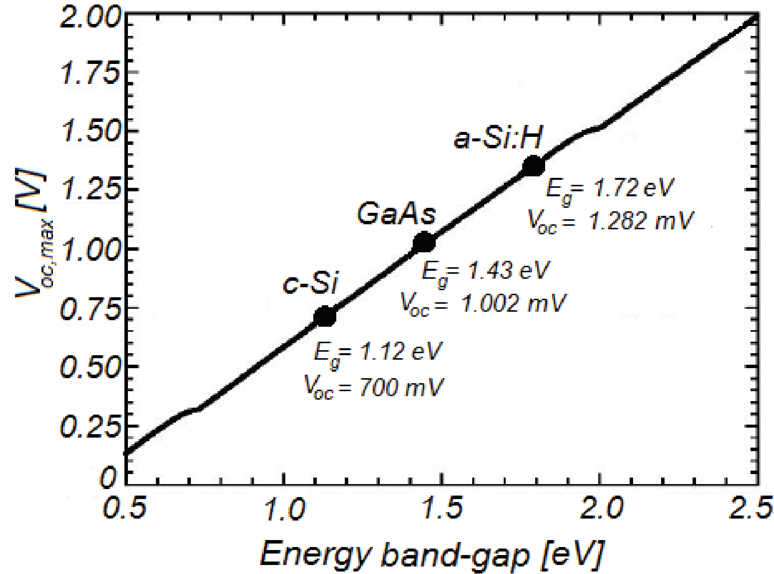

Figure 2.13. Dependence of the open-circuit voltage V_{oc} on the energy band-gap E_g, calculated by neglecting the external reflectance at the top interface, and by assuming direct illumination with a conventional AM1.5G solar spectrum with an incident power of 1000 W/m^2 at T = 300 K. The corresponding dark saturation current density J_0 is in agreement with the lower limit proposed by Green in [2.2] (according to Eq. 2.97). All photogenerated electron-hole pairs are assumed to be collected at the cell terminals.

It is worth noting in Fig. 2.13 that the maximum V_{oc} decreases with decreasing E_g. This trend is opposite from that observed for the maximum J_{sc}. Therefore, it is expected an optimum energy band gap in terms of conversion efficiency. This is confirmed in Fig. 2.14, where the upper limit of the conversion efficiency, calculated by combining the estimated upper limits on J_{sc}, V_{oc} and FF, is shown as a function of the energy band-gap E_g.

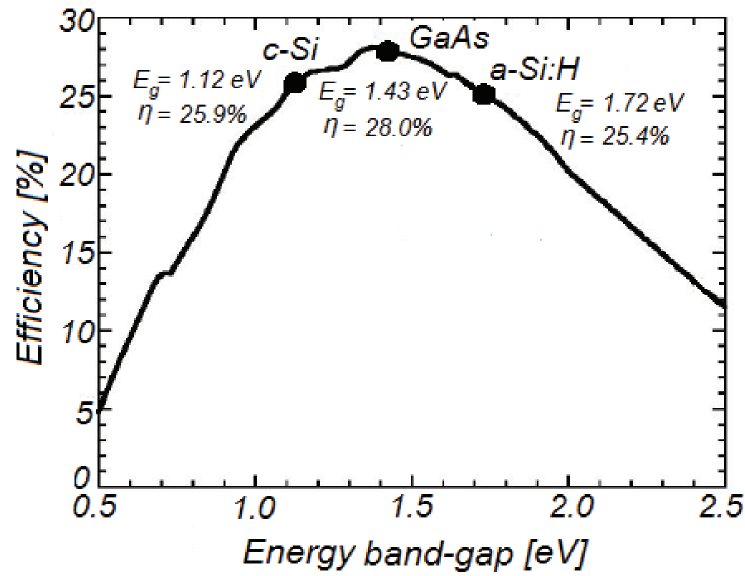

Figure 2.14. Dependence of the conversion efficiency η on the energy band-gap E_g, calculated by neglecting the external reflectance at the top interface, and by assuming direct illumination with a conventional AM1.5G solar spectrum with an incident power of 1000 W/m^2 at T = 300 K. All photogenerated electron-hole pairs are assumed to be collected at the cell terminals.

According to Fig. 2.14, the highest efficiency occurs for an energy band-gap in the range 1.4-1.5 eV. For *c*-Si solar cells, the estimated upper limit of the efficiency is around 25.9%. Gallium arsenide (GaAs) is the semiconductor material that shows an energy band-gap closer to the optimum value (i.e., E_g = 1.43 eV).

The main limitation of the approach proposed by Green for estimating the efficiency upper limit is related to its empirical nature. In order to find a theoretical upper limit for the efficiency of a conventional *p-n* junction silicon solar cell, a more rigorous approach based on the principle of detailed balance (i.e., the incoming energy is balanced by the outgoing energy) was first discussed by Shockley and Queisser in 1961 for an ideal solar cell in which the only recombination mechanism of electron-hole pairs is radiative [2.8]. By assuming also that each incident photon having an energy larger than E_g gives rise to only one electron-hole pair, while all photons with an energy below E_g are lost, a theoretical maximum conversion efficiency of about 30%, known as the *Shockley-Queisser* (*SQ*) *limit* or *detailed balance limit*, was found for a single-junction *c*-Si ($E_g \approx$ 1.1 eV) solar cell. In particular, the SQ limit for any type of single-junction solar cell places the maximum solar conversion efficiency around 33.7%, as shown in

Fig. 2.15. It is worth noting that the SQ limit only applies to conventional single-junction solar cells with the assumption that the sunlight is not concentrated. Therefore, it does not represent the ultimate limit that can be reached with PV devices. Actually, the theoretical thermodynamic limit for the ideal case of a black-body solar cell (i.e., a device that absorbs all radiation incident on it and emits radiation with a spectral distribution depending on its temperature) is much higher, corresponding to a maximum conversion efficiency of about 86% [2.9]. Different strategies have been proposed to exceed the SQ limit in real PV devices, based on reducing thermalization and non-absorption losses inside the solar cell [2.10], and/or using CPV devices that make use of concentrated sunlight [2.11]. In the extreme, it has been already shown that a multi-junction solar cell with an infinite number of layers can theoretically reach the thermodynamic efficiency limit of 86% using concentrated sunlight [2.12].

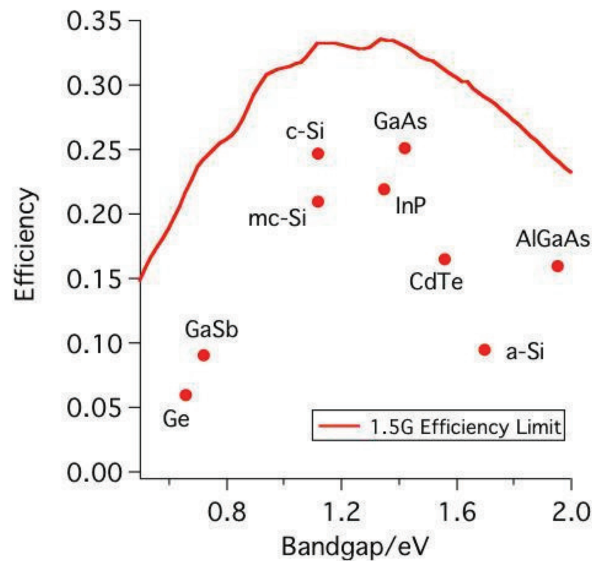

Figure 2.15. Limiting conversion efficiency curve as a function of the energy band-gap, according to the SQ limit, for a conventional single-junction solar cell under AM1.5G solar spectrum. The points represent the best experimental single-junction solar cells fabricated to date. Taken from *http://www.physics.usyd.edu.au/app/solar/research/*.

2.5 Loss mechanisms in solar cells

Real PV devices show a conversion efficiency well below the theoretical limits discussed in the previous section, due to different loss sources, such as:

- *Non-absorption* ($E_{ph} < E_g$) and *thermalization losses* ($E_{ph} > E_g$);
- *Optical losses* (*reflection*, *transmission* and *area losses*);
- *Collection* or *recombination losses*;
- *Parasitic resistive losses*;
- *Thermal losses*.

In the following, the various loss mechanisms occurring in a solar cell, as well as some techniques aiming at reducing such losses, are briefly discussed.

2.5.1 Non-absorption and thermalization losses

As already discussed above, the upper limit for the efficiency of a conventional single-junction *c*-Si solar cell, defined by the Shockley-Queisser limit, is relatively low (around 30%) as compared to the theoretical thermodynamic limit (about 86%). This large difference arises from the fact that a single-junction cell features only a single energy band-gap, whereas the solar spectrum contains photons with a wide range of energies. As a consequence, a large amount of the incident solar energy is lost due to non-absorption and thermalization effects, which account for about 56% loss of photon energy [2.10].

Non-absorption losses are related to the photons in the long-wavelength region of the solar spectrum having energy lower than the energy band-gap (i.e., $E_{ph} < E_g \rightarrow \lambda_{ph} > \lambda_g$), which are then not absorbed in the semiconductor material (see Fig. 2.16).

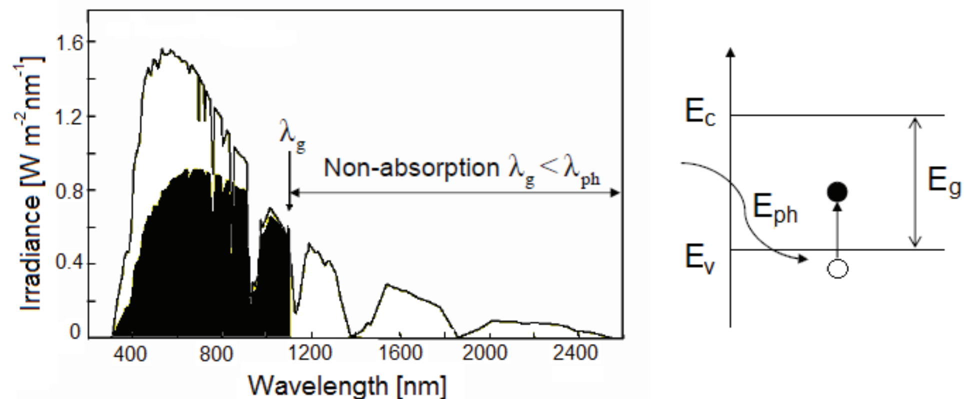

Figure 2.16. Description of non-absorption losses in the solar cell due to the photons in the long-wavelength region of the solar spectrum having energy lower than the energy band-gap (i.e., $E_{ph} < E_g \rightarrow \lambda_{ph} > \lambda_g$). Taken from *http://ocw.tudelft.nl/*.

On the contrary, thermalization losses are related to the photons in the short- and medium-wavelength regions of the solar spectrum having energy higher than the band-gap energy (i.e., $E_{ph} > E_g \rightarrow \lambda_{ph} < \lambda_g$), which can be then absorbed in the semiconductor device, thus giving rise to photogenerated electron-hole pairs (see Fig. 2.17). In this case, the photon energy in excess with respect to the energy band-gap, i.e., E_{ph}-E_g, increases the kinetic energy of the photogenerated carriers (referred to as "hot" carriers) and, therefore, it is lost in the form of heat due to lattice scattering (through phonon emission).

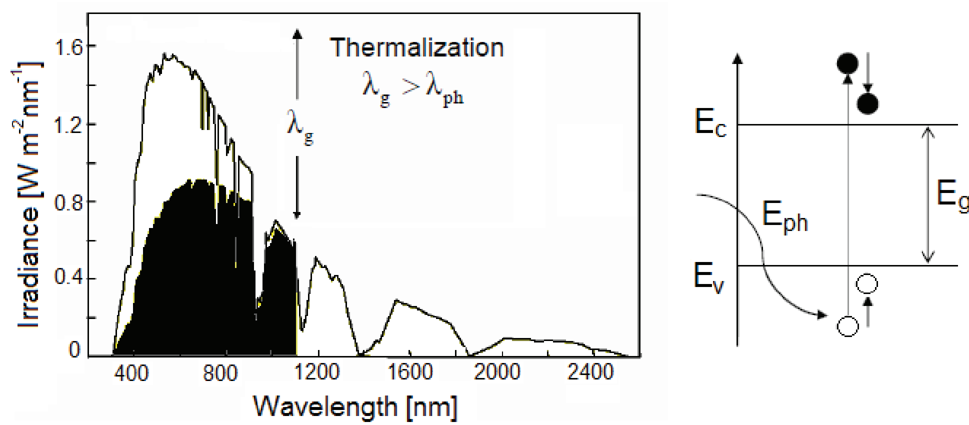

Figure 2.17. Description of thermalization losses in the solar cell due to the photons in the short- and medium-wavelength regions of the solar spectrum having energy higher than the band-gap energy (i.e., $E_{ph} > E_g \rightarrow \lambda_{ph} < \lambda_g$). Taken from *http://ocw.tudelft.nl/*.

As already mentioned in Section 2.4.2, different concepts have been proposed to reduce thermalization and non-absorption losses. These concepts are based on splitting of the solar spectrum to be absorbed in a multiple band-gap device (e.g. *tandem* or *multi-junction* solar cells, *intermediate band* solar cells, *quantum-well* solar cells), or collecting hot carriers before thermalization (*hot carrier* solar cells), or adapting the solar spectrum to one host material (e.g. up- and down-conversion of photon energy) [2.10].

2.5.2 Optical losses

The main optical losses in a solar cell include the reflection, transmission and area losses. These losses reduce the photon absorption inside the device and, consequently, they principally affect the short-circuit current density of a solar cell.

Reflection losses normally occur at the top surface of a solar cell, which receives the incident sunlight. When photons strike the top surface, a certain fraction is transmitted and, then, can be absorbed into the semiconductor material, thus giving rise to photogenerated electron-hole pairs, while the remainder is reflected from the top surface. In general, an absorbing material is characterized by a complex *refractive index* $\tilde{n} = n_\lambda - i\kappa_\lambda$, where both the two components are function of the wavelength of the incident light, as shown in Fig. 2.18 for silicon. The real part n indicates the phase speed, while the imaginary part κ, also called *extinction coefficient*, determines the amount of absorption losses when the electromagnetic wave propagates through the material. The reflectance in case of normal incidence can be then expressed as:

$$R(\lambda) = \frac{(n_\lambda - 1)^2 + {\kappa_\lambda}^2}{(n_\lambda + 1)^2 + {\kappa_\lambda}^2} \tag{2.98}$$

By including in Eq. 2.98 the appropriate values for bare silicon, it is possible to estimate that reflection losses account for more than 30% of the incident light in the wavelength range of interest.

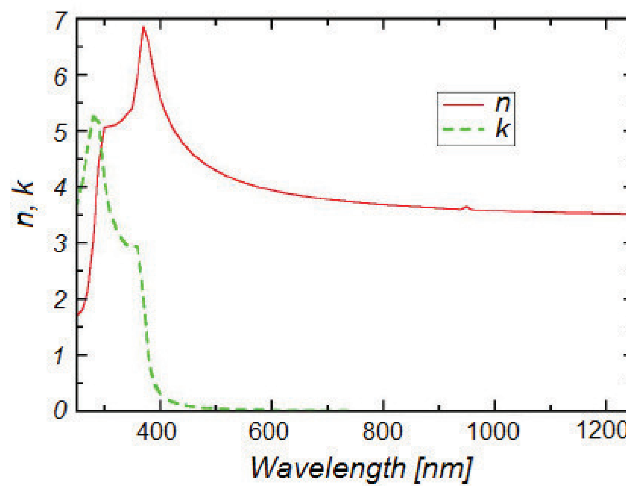

Figure 2.18. Real and imaginary parts of the refractive index for silicon as a function of the wavelength λ of the radiation.

Different techniques are commonly used in solar cells to reduce reflection losses at the top surface as much as possible and, consequently, to enhance the photon absorption inside the device. A common approach is based on the use of a quarter-wavelength anti-reflective coating (ARC) layer on the top surface. The operating principle of such layer is illustrated in Fig. 2.19. The basic idea is to design the ARC layer in such a way that the light at a given wavelength reflected from the second interface arrives back at the first interface 180° out of phase with that reflected from the first interface, thus resulting in destructive interference. To this purpose, the refractive index and the thickness of the ARC layer must be properly chosen in order to achieve lower reflection losses.

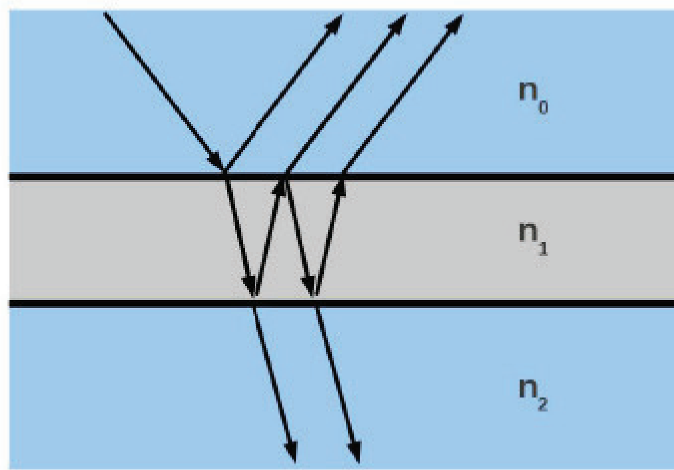

Figure 2.19. Schematic of a simple intermediate anti-reflective coating (ARC) layer featuring a refractive index n_1. The refractive indices of the uppermost material (air or glass) and the underlying absorbing material (silicon) are n_0 and n_2, respectively.

According to Fresnel's formula, the expression for the reflectance in case of a material covered by a transparent ARC layer of thickness t_1 is given by [2.2]:

$$R = \frac{r_1^2 + r_2^2 + 2r_1 r_2 \cos 2\theta}{1 + r_1^2 r_2^2 + 2r_1 r_2 \cos 2\theta} \tag{2.99}$$

where r_1 and r_2 are given by:

$$r_1 = \frac{n_0 - n_1}{n_0 + n_1}, \qquad r_1 = \frac{n_1 - n_2}{n_1 + n_2} \tag{2.100}$$

where n_0 denotes the refractive index of the uppermost material (air or glass), n_1 the refractive index of the intermediate ARC layer, and n_2 the refractive index of the underlying absorbing material (silicon), while the incident angle θ is given by:

$$\theta = \frac{2\pi\, n_1 t_1}{\lambda} \tag{2.101}$$

The reflectance at a given wavelength λ_0 has its minimum value when the optical path in the ARC layer, that is the product of its refractive index n_1 and its thickness t_1, is equal to a quarter of the wavelength (i.e., $n_1 t_1 = \lambda_0/4$). Therefore:

$$R_{min} = \left(\frac{n_1^2 - n_0 n_2}{n_1^2 + n_0 n_2} \right)^2 \tag{2.102}$$

In particular, the reflectance can be zero if the refractive index of the ARC layer is the geometric mean of those of the two surrounding materials:

$$n_1^2 = n_0 n_2 \rightarrow n_1 = \sqrt{n_0 n_2} \tag{2.103}$$

For a silicon solar cell ($n_{Si} \approx 3.8$) in air ($n_{air} \approx 1$), the optimum refractive index for the ARC layer is then about $n_{ARC} \approx 1.95$. However, solar cells are typically encapsulated under glass, or in a material of a similar refractive index to glass ($n_0 \approx 1.5$). In this case, the optimum value for the refractive index of the ARC layer increases to about 2.3. Fig. 2.20 shows the reflectance curves as a function of wavelength in case of a bare Si solar cell both in air and under glass, and in case of a Si solar cell covered with an optimal ARC layer with a refractive index of 2.3, whose thickness has been designed to produce minimum reflection at $\lambda_0 = 600$ nm. In general, a well-designed ARC layer can reduce the external top reflection losses down to 10%, as compared to over 30% for bare silicon. Different non-crystalline and amorphous materials can be used as transparent ARC layer, typically deposited through CVD (chemical vapor deposition). The most widely used material as ARC in commercial silicon solar cells is the silicon nitride (SiN_x), that ensures also a good surface passivation, as well as an excellent adhesion with *n*-type silicon material. It is worth noting that this technique fully works only for a single wavelength with direct incidence and, therefore, it is not really effective over most of the solar spectrum. However, it has been already demonstrated that the use of a stack with multiple ARC layers can be more effective within a more extended portion of the spectrum, thus leading to a further reduction of the reflection losses down to 4% [2.2].

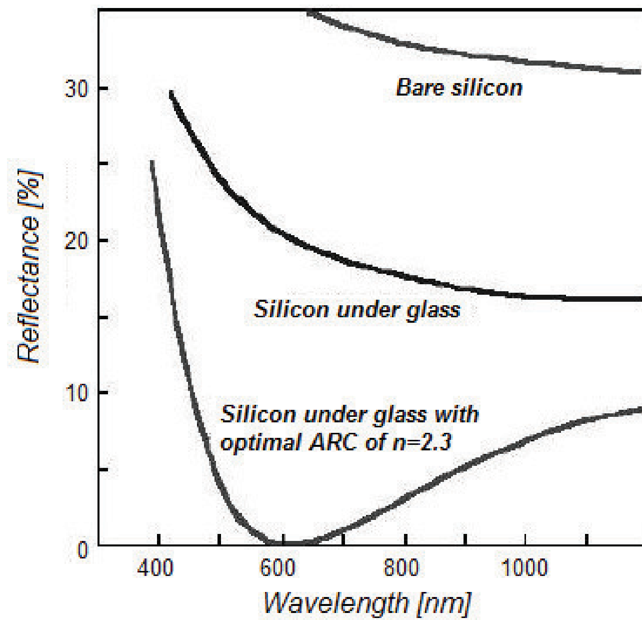

Figure 2.20. Reflectance as a function of wavelength for bare silicon, silicon under glass, and silicon under glass with an optimal ARC layer of refractive index 2.3. The thickness of the ARC layer has been chosen in order to produce minimum reflection at λ_0 = 600 nm.

Another typical approach, which is applied in standard industrial Si solar cells to reduce reflection losses, is based on the use of textured surfaces. These are produced on the surface of the silicon wafer by means of a selective (anisotropic) chemical etching process, that etches at different rates in different directions through the crystal structure. In particular, this process exposes certain planes within the crystal. Small pyramids are then formed by the intersection of these crystal planes. In terms of Miller indices, the silicon surface in textured cells is normally aligned parallel to a (100) plane, and the pyramids are formed by the intersection of (111) planes. Dilute caustic soda (NaOH) or acid solutions are commonly used for the selective etching [2.2].

Surface texturing contributes significantly to the improvement of the light trapping in the solar cell by giving rise to multiple bounces of the light within the absorbing material, thus leading to enhance the probability of photon absorption. In Fig. 2.21a, an ideal texturing scheme with regular pyramids is depicted. However, in real processes, it is not practically possible to obtain such periodic geometry because of the difficulty in controlling the etching process. A more realistic texturing scheme featuring a randomized geometry is then reported in Fig. 2.21b. Nevertheless, it is shown that a random-pyramids scheme allows to achieve better absorption performance as compared to the case of regular geometry [2.13]. Other alternative texturing schemes have been proposed to reach even better performance, such as the inverted-pyramids geometry [2.14].

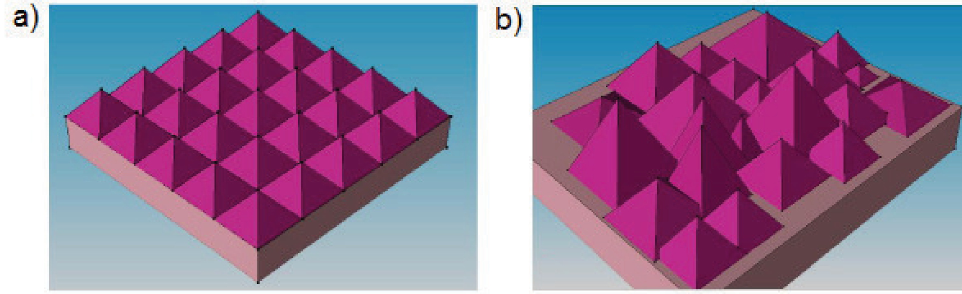

Figure 2.21. a) Ideal texturing scheme with periodic geometry. b) Realistic texturing scheme with random geometry.

Although the surface texturing can be highly beneficial to increase the photon absorption in a solar cell, there are some disadvantages to be considered associated with the use of textured surfaces. Some of these drawbacks occur in the cell manufacturing process, e.g. during the handling and the front contact metallization processes. In addition, the texturing process increases the number of defects on the surface of the silicon wafer, thus leading to higher surface recombination losses [2.2].

Moreover, it is worth pointing out that, in order to strongly reduce reflection losses in a solar cell, the two considered techniques (i.e., the anti-reflective coating and the surface texturing) can be successfully combined. As a consequence, reflection losses can be limited to a few percent.

Transmission losses refer to that part of the light that, despite of an energy greater than the energy band-gap, passes through the solar cell and, therefore, it is not absorbed due to the cell finite thickness. As already discussed above, when the sunlight strikes the top surface of the cell, a portion is reflected due to the different refractive indices at the interface, and the remainder is transmitted into the absorbing material. The transmitted light passing through the semiconductor is attenuated. As known, the attenuation of the light propagating through a simple homogeneous infinite layer of absorbing material leads to an exponential decay of the light intensity I for a given wavelength, according to the *Beer-Lambert law*, described mathematically as:

$$I_\lambda(x) = I_\lambda(0)\, exp\left[-\alpha_\lambda(x - x_0)\right] \tag{2.104}$$

where I (0) is the intensity of the light at the interface ($x = x_0$), and α_λ is the wavelength-dependent *absorption coefficient* of the material. The absorption coefficient is related to the extinction coefficient κ of the material (i.e. the imaginary part of the complex refractive index) through the following relationship:

$$\alpha = \frac{4\pi\,\kappa}{\lambda} \tag{2.105}$$

This parameter is very important in solar cell design, because it defines, how far below the top cell surface, the light of a given wavelength is absorbed. Therefore, it determines the entity of the transmission losses depending on the thickness of the solar cell. The distance α^{-1} corresponding to a light attenuation by a factor 1/e is typically defined as attenuation length. In direct band-gap semiconductors, like GaAs, where the absorption process mostly consists of direct transitions of electrons from the valence to the conduction band (see Fig. 2.22a), the absorption coefficient is quite high for all the wavelengths corresponding to photon energies greater than E_g (in particular, $E_g \approx 1.4$ eV in GaAs), as shown in Fig. 2.23. This means that photons having energy higher than the band-gap are absorbed within the first few microns of a direct band-gap semiconductor. On the contrary, in indirect band-gap semiconductors, like Si, photon energies much larger than the energy band-gap are required to allow direct transitions of electrons from the valence to the conduction band. Nevertheless, in silicon, photons at lower energies can be absorbed by involving a third particle (i.e., a phonon), that provides the crystal momentum required for the transition (see Fig. 2.22b). As a consequence, the probability of the light absorption by this indirect process is much less than the direct band-gap case. Therefore, as shown in Fig. 2.23 for Si ($E_g = 1.12\ eV$), in indirect band-gap semiconductors, the absorption coefficient is quite high only at low wavelengths (typically for $\lambda < 0.5\mu m$) corresponding to photon energies much higher than E_g for which the direct absorption process is possible, while at higher wavelengths (i.e., $\lambda > 0.8\mu m$) corresponding to photon energies slightly higher than E_g, the absorption coefficient decreases very rapidly due to the indirect absorption process. This means that low-wavelength photons, having energy much higher than E_g, are absorbed within the first few microns of an indirect band-gap semiconductor, while high-wavelength photons, having energy slightly higher than E_g, have to pass a considerable distance prior to be absorbed into the material. Therefore, a portion of these high-wavelength photons might not be absorbed within the volume of the solar cell due to its finite thickness, thus giving rise to transmission losses.

Transmission losses are then strongly dependent on the type of semiconductor material, and on the thickness of the device. Obviously, indirect band-gap semiconductors require more thick substrates than direct-gap materials to achieve good absorption performance. Moreover, it is worth noting that transmission losses can be extremely critical in thin-film technologies, for which direct band-gap materials are more appropriate, and different strategies must be used to limit these losses [2.2].

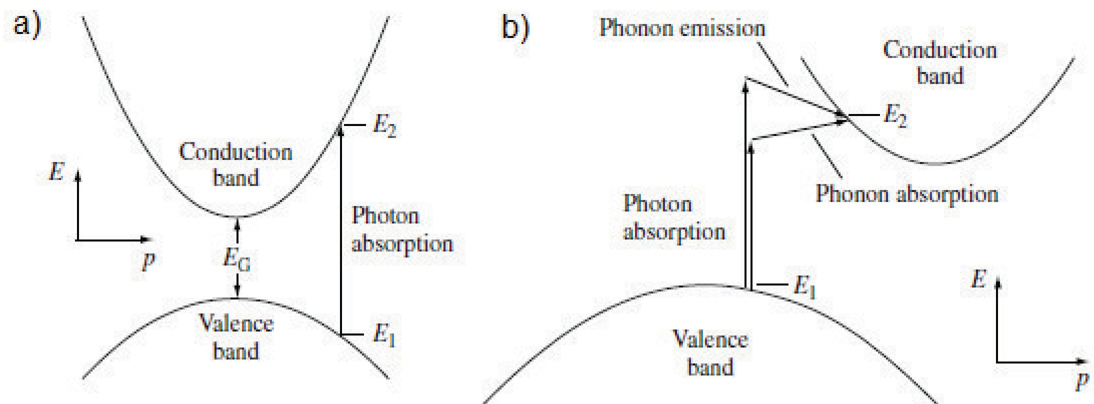

Figure 2.22. Photon absorption in a) direct band-gap semiconductors and in b) indirect band-gap semiconductors. Taken from [2.1].

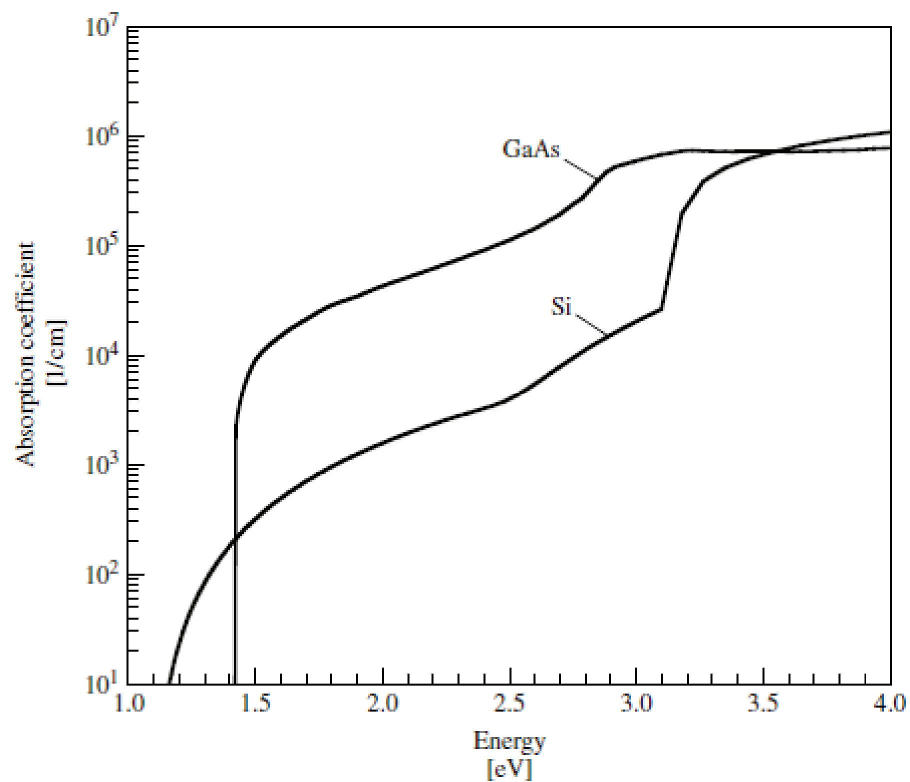

Figure 2.23. Absorption coefficient as a function of photon energy for Si (indirect band-gap) and GaAs (direct band-gap) at $T = 300$ K. Taken from [2.1].

Area losses refer to the shadowing losses due to the front metal coverage. In fact, in order to collect the photogenerated carriers and, then, to deliver them to the external load, electrical contacts have to be made on both *p*- and *n*-type sides of a solar cell. Consequently, a fraction of the incident light is blocked on the side of the cell exposed to radiation, that is normally the front side. Standard industrial screen-printed *c*-Si solar cells feature a conventional H-pattern front contact grid, as shown in Fig. 2.24, typically leading to area losses of 5-10% of the incoming light, depending on the front contact geometry. Different strategies have been proposed to reduce the front shadowing losses. Some of these are based on reducing the fingers and busbars width, e.g. the double screen-printed technique [2.15]. Other approaches aim at removing the electrical contacts from the front exposed side, such as the interdigitated back contact solar cells [2.16], where both the contacts are placed at the back side of the cell, and the buried contact solar cells [2.17], where the front contacts are buried in the substrate.

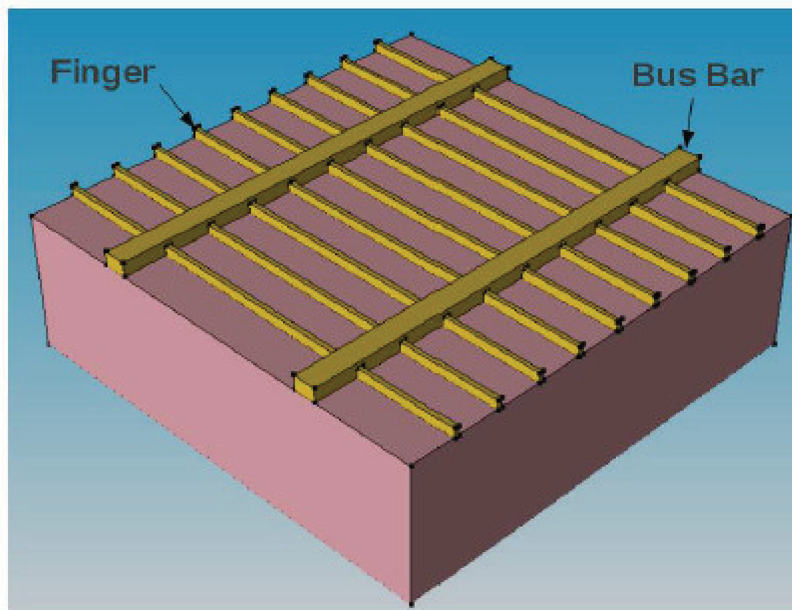

Figure 2.24. Typical H-pattern front contact grid in a silicon solar cell.

2.5.3 Recombination losses

Recombination, or *collection*, losses refer to the loss of photogenerated carriers that recombine before to be collected at the cell contacts. It has been already discussed that the generation of electron-hole pairs by incident photons occurs in the entire volume of the device. In order to be collected at the device terminals and, hence, to contribute to the cell output current, these photogenerated carriers need to be separated by the built-in electric field of the *p-n* junction before they recombine. The carriers generated near the depletion region are separated out very quickly by the electric field present in the depletion region. Conversely, carriers generated well away from the depletion region, i.e., in the bulk and near the cell surfaces, have a lower probability of getting separated and, consequently, a higher probability of recombining before they complete the trip from the point of generation to the cell terminals [2.2]. Therefore, a certain fraction of the photogenerated carriers is lost and, hence, it does not contribute to the output current flow.

Recombination losses strongly affect the cell performance, particularly the open-circuit voltage, and to a lesser extent the short-circuit current density. Various mechanisms can contribute to these losses (see Fig. 2.25), such as *radiative or band-to-band* recombination, *Shockley-Read-Hall (SRH) or trap-assisted* recombination, *Auger* recombination and *surface SRH* recombination.

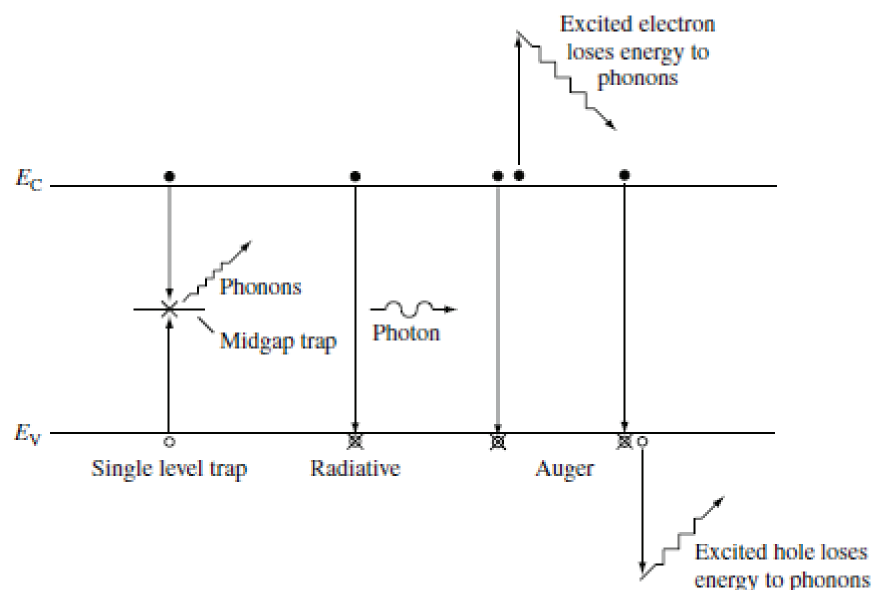

Figure 2.25. Volume recombination processes in semiconductors. Taken from [2.1].

Radiative or band-to-band recombination (see Fig. 2.25) takes place when an electron from the conduction band recombines with a hole in the valence band with the emission of a photon; this mechanism has a high probability of occurring in direct band-gap semiconductors, whereas in indirect band-gap semiconductors, like silicon, it is quite negligible.

Shockley-Read-Hall (SRH) or trap-assisted recombination is due to impurities and defects present in the semiconductor material, that introduce allowed energy levels within the forbidden energy gap (see Fig. 2.25). These additional energy levels act as a capture trap for electrons and holes, thus leading to recombination. SRH recombination is then a two-step process. A single-level trap model is usually adopted for crystalline silicon, according to Fig. 2.25, while materials having a larger defect density, like the amorphous silicon (*a*-Si), typically require an extension of the SRH model in order to account for a more complex energy level distribution of defects.

Auger recombination is the reverse process of the impact ionization. It occurs when the electron recombining with the hole gives the excess energy to a second electron which relaxes back to its original energy level by emitting phonons (see Fig. 2.25). Therefore, this mechanism involves three particles (electron-electron-hole, or hole-hole-electron). Auger recombination is primarily effective in highly-doped materials (particularly, for doping concentrations above 1×10^{18} cm^{-3}).

Surface SRH recombination is related to the large number of defects present at surfaces, due to the abrupt termination of the crystal structure. Similarly to the defects present in the volume of a semiconductor material, these defects at surfaces act as recombination centers for the minority carriers, thus leading to SRH recombination.

In general, each recombination mechanism can be described with a characteristic lifetime, as already seen in Section 2.3.1. Therefore, the effective minority-carrier lifetime τ_{eff} of a semiconductor material can be expressed as [2.18]:

$$\frac{1}{\tau_{eff}} = \frac{1}{\tau^{SRH}} + \frac{1}{\tau^{A}} + \frac{1}{\tau^{R}} + \frac{2S}{d} \tag{2.106}$$

where τ^{SRH} is the SRH lifetime, τ^{A} the Auger lifetime, τ^{R} the radiative lifetime, S the surface recombination velocity (SRV), and d the thickness of the device. Recombination losses then occur both in the volume (or bulk) and at the surfaces of a solar cell. Radiative recombination losses are negligible in silicon since it has an indirect band-gap. Auger recombination effects are significant in the heavily-doped region of the cell, such as the emitter region (see Fig. 2.26), while they are very low in the lightly-doped base region of the device (see Fig. 2.26), where the recombination is typically dominated by the SRH mechanism. In particular, it has already been discussed in Section 2.3.4 that the SRH recombination can be particularly effective in the

depletion region of the cell, resulting in an additional dark recombination current component and, consequently, in a further decrease of the V_{oc}. In addition, surface recombination represents a very important loss mechanism on both sides of a silicon solar cell, as already mentioned in Section 2.3.2. A significant effect of surface recombination also occur at metal-semiconductor contact interfaces, which provide very large recombination sites and, hence, feature very high surface recombination velocities.

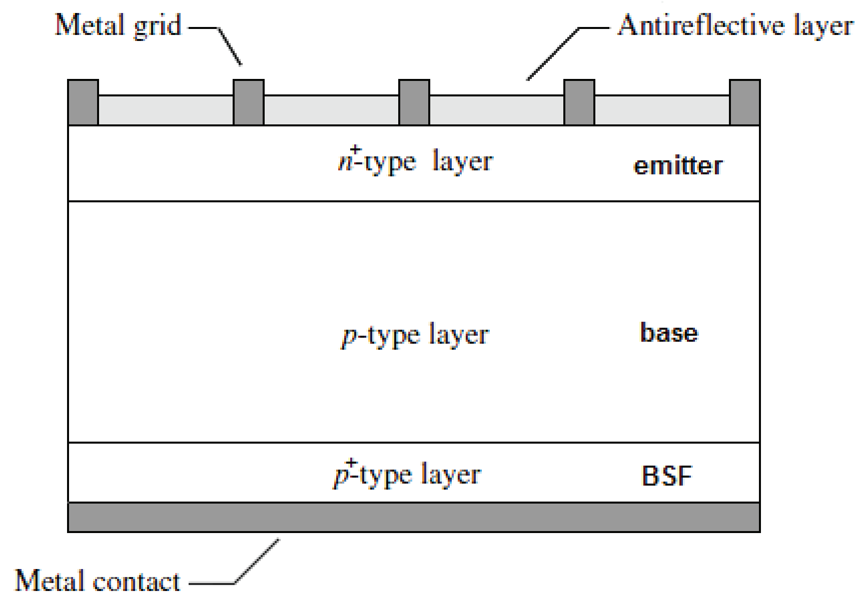

Figure 2.26. Schematic of a silicon solar cell, where the emitter, base and BSF regions are depicted.

Many different strategies can be implemented to reduce recombination losses in the different regions of a solar cell. In order to limit SRH recombination losses in the base region of the cell, a high-purity semiconductor substrate with low impurities and defects is required. To this purpose, float-zone silicon (*Fz*-Si) substrates are more suitable than Czochralski silicon (*Cz*-Si) substrates. Indeed, a highly pure material features a larger minority-carrier lifetime and, consequently, a larger diffusion length for the minority carriers, according to Eq. 2.48. A larger diffusion length means a greater distance traveled by the minority carriers before they get recombine, thus resulting in a higher probability that these carriers are collected at the cell terminals. Regarding Auger recombination losses, these can be primarily limited with a careful design of the highly-doped emitter in the solar cell. Finally, a good surface passivation is required to reduce the effects of the surface recombination on both sides of the solar cell. Bare silicon features typical values of SRV around 1×10^5 cm/s. In order to reduce this SRV, a dielectric layer (typically silicon nitride SiN_x or silicon dioxide SiO_2) is usually deposited on the top surface, acting as passivating layer, as well as anti-reflective coating. Moreover, since the rear side of conventional silicon solar cells is usually fully covered by a metal contact and,

consequently, it features a very high SRV (around 1×10^6 *cm/s*), a good rear surface passivation is also required. This is normally accomplished by designing a back-surface field (BSF) region in contact with the metal at the rear surface of the cell (see Fig. 2.26). BSF consists of a region highly doped with the same type of dopant than the base region, aiming at creating, at the junction between the high- and low-doped regions, a built-in electric field (similarly to a *p-n* junction). This electrical field acts as a barrier to minority-carrier flow to the back surface, and it also aids to separate the carriers photogenerated by long-wavelength photons close to the contacted rear side. As a consequence, the minority-carrier concentration is kept at high levels in the base region. Therefore, the BSF has a net effect of passivating the rear surface through the so-called "field-effect passivation", thus resulting in lower effective back SRVs and, hence, higher V_{oc}. Another solution for a good rear surface passivation is based on the use of passivating layers also at the rear side of the cell between the metal contact and the semiconductor material. This concept is typically adopted in rear point contact silicon solar cells, such as the PERC (Passivated Emitter and Rear Cell) and PERL (Passivated Emitter Rear Locally diffused) solar cells [2.13].

2.5.4 Parasitic resistive losses

Solar cells generally show parasitic series and shunt resistance losses. The effect of these resistive components on the *I-V* characteristics of a solar cell has been already discussed in Section 2.3.3, and shown in Fig. 2.9. Parasitic resistive losses mainly affect the fill factor of a solar cell. However, very high values of R_s, and very low values of R_{sh} can also reduce J_{sc} and V_{oc}, respectively, as depicted in Figs. 2.27 and 2.28.

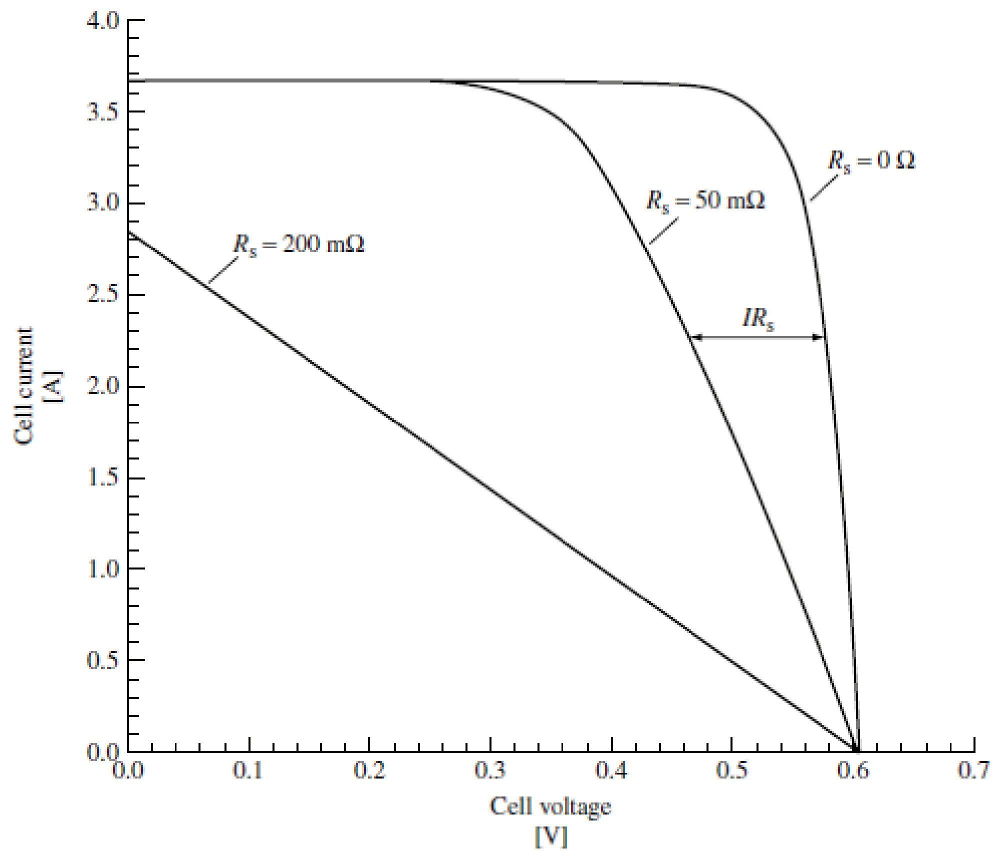

Figure 2.27. Effect of the series resistance R_s on the *I-V* characteristics of a solar cell. Taken from [2.1].

The impact of the series resistance on the *FF* can be analytically described through the following approximate expression proposed by Green in [2.2]:

$$FF = FF_0\left(1-\frac{R_s}{R_{ch}}\right) \tag{2.107}$$

where FF_0 denotes the ideal *FF* in the absence of parasitic resistances, and $R_{ch} = V_{oc}/I_{sc}$ is defined as the *characteristic resistance* of a solar cell.

A corresponding expression for the effect of the shunt resistance on the FF is given by [2.2]:

$$FF = FF_0\left[1 - \frac{(v_{oc} + 0.7)}{v_{oc}}\frac{FF_0 R_{ch}}{R_{sh}}\right] \tag{2.108}$$

where v_{oc} is the normalized open-circuit voltage, defined as $V_{oc}/(kT/q)$. The approximated expressions defined by Eqs. 2.107 and 2.108 are particularly accurate under the assumption that $v_{oc} > 10$, $R_s/R_{ch} < 0.4$ and $R_{sh}/R_{ch} > 2.5$ [2.2].

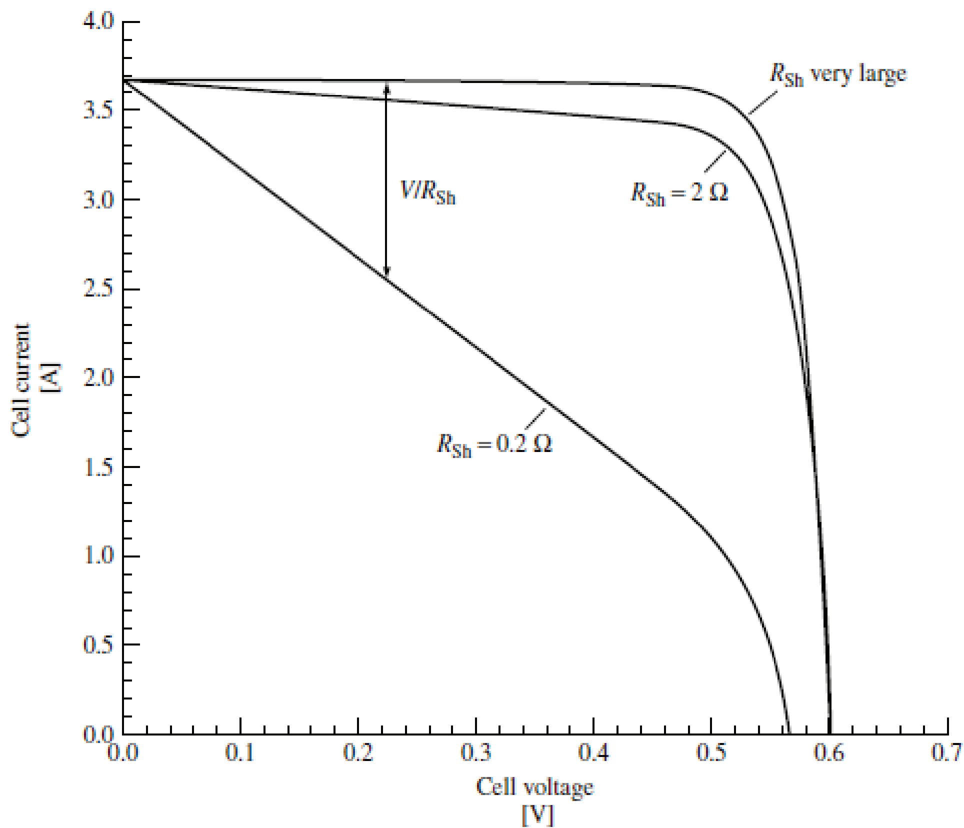

Figure 2.28. Effect of the shunt resistance R_{sh} on the *I-V* characteristics of a solar cell. Taken from [2.1].

There are several physical mechanisms responsible for these parasitic resistive effects. The shunt or parallel resistance R_{sh} is caused by the current leakage across the *p-n* junction around the edges of the cell (due to poor edge isolation), and in the regions which present crystal imperfections and impurity precipitates.

The total series resistance R_s is generally given by the sum of several contributions (see Fig. 2.29), such as the bulk resistance of the front metal fingers R_{fm} and busbars R_{bb}, the contact resistance between the front metal contacts and the semiconductor R_{fc}, the emitter or diffused

layer sheet resistance R_{sq}, the bulk semiconductor resistance R_b and the contact resistance between the back metal contact and the semiconductor R_{bc} [2.19].

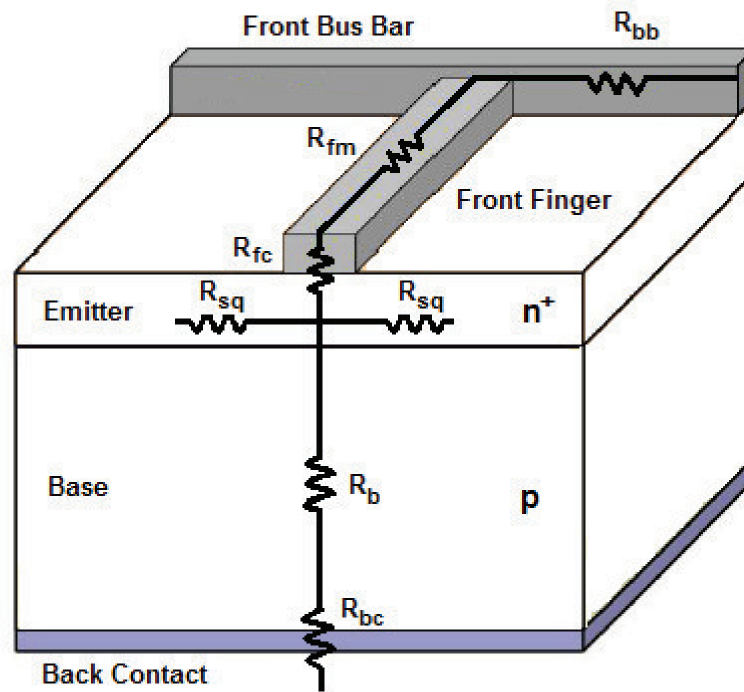

Figure 2.29. Contributions to the total series resistance in silicon solar cells.

The *bulk semiconductor resistance* R_b is defined by the substrate doping and it is generally relatively low due to the typical high conductivity of the substrate in a silicon solar cell.

The *emitter sheet resistance* R_{sq} (typically expressed in Ω/square), which is related to the lateral flow of the current in the thin emitter layer, is one of the most dominant component of the series resistance in a solar cell. It is mainly affected by the doping concentration in the emitter region, the thickness (or the junction depth) of the emitter layer and the distance between the adjacent front fingers, also called front finger pitch. In fact, a larger front finger pitch leads to a larger resistive path for the carriers through the emitter prior to be collected at the contact. The emitter resistance is also affected by the surface texturing due to the increase of the surface lateral area. A typical approach used to limit the emitter resistance requires the co-optimization of the emitter doping profile (both in terms of doping concentration and junction depth) and the front finger pitch [2.20].

The *contact resistance* depends on the nature of the metal/semiconductor contact, i.e., ohmic or rectifying (Schottky). In conventional silicon solar cells, ohmic contacts are typically obtained at the front side by depositing a metal onto a highly-doped semiconductor region, such as the emitter. In fact, in this case, although the barrier height between the metal and the semiconductor can be still significant, a narrow charge region created by the heavy surface

doping allows tunneling of carriers through the metal/semiconductor junction. It is worth noting that the heavy surface doping also helps to reduce the surface recombination at the metal/semiconductor contact. On the contrary, for lowly-doped semiconductors, the conduction mechanism at the metal/semiconductor contact is dominated by thermionic emission over the barrier [2.19]. The resistance of a metal/semiconductor contact is usually defined by a *specific contact resistivity* ρ_c (expressed in $\Omega{\cdot}cm^2$). In metal/lowly-doped semiconductor contacts, where the thermionic emission is dominating, ρ_c is a strong function of the barrier height and it is independent on the surface doping density. Conversely, in metal/highly-doped semiconductor contacts, ρ_c is a function of the surface doping level and, in particular, it decreases with increasing surface doping density [2.19]. In a conventional solar cell (see Fig. 2.29), the contact resistance of the front fingers is calculated taking into account that the lateral current flow from the thin diffused layer (i.e., the emitter) into the front metal contacts takes place over a distance which is not necessarily equal to the contact width. Therefore, the concept of the transfer length has to be applied and, consequently, a general expression for the front contact resistance is given by [2.19]:

$$R_{fc} = \frac{\rho_c}{L_T L_{fm}} coth\left(\frac{W_{fm}}{L_T}\right) \qquad (2.109)$$

where L_{fm} and W_{fm} are the length and width of the front fingers, respectively, and $L_T = \sqrt{\rho_c / R_{sq}}$ is the transport length. It is worth noting that Eq. 2.109 only applies when the current flows laterally from a thin diffused layer into the contact. For contacts into which the current flows vertically, like the back contact of a conventional solar cell, the effective area is simply equal to the total contact area. Accordingly, in conventional screen-printed silicon solar cells, where the back side is fully covered by a full-area contact (as depicted in Fig. 2.29) and, then, its entire contacted area is active, the effect of the back contact resistance R_{bc} is negligible. This is no longer true in more advanced silicon solar cells, like the rear point contact solar cells (PERC- and PERL-type solar cells), where only a fraction of the back side is contacted and, consequently, the back contact resistance becomes significant. Therefore, the contact resistance losses strongly depend on the contacted area, and on the surface doping concentration (that affects the specific contact resistivity at the metal/semiconductor interface when tunneling occurs). Some strategies to reduce the contact resistance losses can be thus based on increasing the contacted area (at the expense of increasing the shadowing losses on the illuminated side and the surface recombination losses), and/or the surface doping concentration of the semiconductor.

The front metal fingers R_{fm} and busbars R_{bb} resistances can be expressed, respectively, as [2.21]:

$$R_{fm} = \frac{1}{3}\rho_m \frac{L_{fm}}{H_{fm}W_{fm}}, \qquad R_{bb} = \frac{1}{6}\rho_m \frac{L_{bb}}{H_{bb}W_{bb}} \tag{2.110}$$

where ρ_m is the resistivity of the metal, L_{fm}, H_{fm}, and W_{fm} are the front finger length, height and width, respectively, and L_{bb}, H_{bb}, W_{bb} are the busbar length, height and width, respectively. According to Eq. 2.110, these resistances mainly depend on the chosen metal and on the geometry of fingers and busbars.

Different techniques can be used for the deposition of front and back metal contacts in a solar cell. Conventional silicon solar cells commonly adopt screen-printed contacts on both sides: silver (Ag) is typically used for the front fingers and busbars, while aluminum (Al) is used for the back contact. Standard screen-printed front fingers features a width in the range of 80-120 µm, while busbars typically have a width of 1.5-2.5 mm. In order to achieve a finer front metal grid structure, other metallization techniques, such as photolithography or sputtering, can be used instead of the standard screen-printing technology. However, such techniques are usually expensive and, hence, not properly suitable for solar cell manufacturing. Alternatively, the electroplating technique based on the use of a highly-conductive metal (e.g. copper) can be used to reduce both metal and contact resistances of the front fingers, thus allowing to contact high sheet resistance emitters [2.22].

2.5.5 Thermal losses (Effect of temperature)

The operating temperature of a solar cell can significantly vary during its operation. It has been already discussed in Section 2.5.1 that a lot of photons absorbed in a solar cell have energy in excess than that required for the generation of an electron-hole pair. This excess energy is released in the form of heat and, therefore, it causes a rise of the operating temperature. Obviously, the operating temperature of a solar cell also depends on the ambient temperature. An approximate empirical expression for the operating temperature of a cell is proposed by Green in [2.2]:

$$T_{cell}(°C) = T_{ambient}(°C) + 0.3 \times I\left(mW/cm^2\right) \tag{2.111}$$

where $T_{ambient}$ is the ambient temperature and I the intensity of the incident sunlight.

The temperature affects some of the most important semiconductor parameters (e.g., the energy band-gap, the minority-carrier lifetime, the diffusion length, the intrinsic carrier density) and, consequently, the performance of a solar cell. The short-circuit current density is not strongly affected by the temperature [2.2]. In particular, it tends to slightly increase with increasing temperature due to the increased light absorption, since the band-gap of a semiconductor material generally decreases with the temperature [2.6]. On the contrary, the open-circuit voltage (and, hence, the fill factor, according to Eq. 2.67) significantly decreases with increasing operating temperature due to the increase of the saturation current density J_0. An approximate expression for the variation of V_{oc} in response to a change of the operating temperature is derived by Green in [2.2]:

$$\frac{dV_{oc}}{dT} = -\frac{V_{g0} - V_{oc} + \gamma(kT/q)}{T} \tag{2.112}$$

where $V_{g0} = E_{g0}/q$ (E_{g0} is the zero temperature band-gap of the semiconductor material), and γ is a temperature-dependent parameter which includes the temperature dependencies of the semiconductor parameters determining J_0 in Eq. 2.56. Therefore, Eq. 2.112 predicts an approximately linear decrease of the V_{oc} with increasing temperature. By substituting typical values for a silicon solar cell ($V_{g0} \approx 1.2$ V, $V_{oc} \approx 0.6$ V, $\gamma \approx 3$, $T = 300$ K), a variation equal to $dV_{oc}/dT = -2.3\ mV/°C$ can be estimated [2.2]. The considerable decrease of the V_{oc} and, hence, of the *FF*, results in a corresponding decrease of the efficiency of a silicon solar cell with increasing operating temperature.

References

[2.1] A. Luque and S. Hegedus, "Handbook of Photovoltaic Science and Engineering", 1st Edition, *John Wiley & Sons*, 2003.
[2.2] M. A. Green, "Solar Cells: Operating Principles, Technology and System Applications", *Prentice Hall*, 1982.
[2.3] J. O. Schumacher, "Numerical simulation of silicon solar cells with novel cell structures", *PhD dissertation*, Faculty of Physics, University of Konstanz, 2000.
[2.4] A. G. Aberle et al., "High-efficiency silicon solar cells: fill factor limitations and non-ideal diode behavior due to voltage-dependent rear surface recombination velocity", *Progress in Photovoltaics: Research and Applications*, Vol. 1, No. 2, pp. 133-143, 1993.
[2.5] M. Haouari-Merbah, M. Belhamel, I. Tobias, J. M. Ruiz, "Method of extraction and analysis of solar cell parameters from the dark current-voltage curve", *Proc. of Spanish Conference on Electron Devices*, pp. 275-277, 2005.
[2.6] S. M. Sze and K. K. Ng, "Physics of Semiconductor Devices", *John Wiley & Sons*, third edition, New Jersey, 2007.
[2.7] M. Zanuccoli, "Advanced Numerical Simulation of Silicon-Based Solar Cells", *PhD dissertation*, ARCES – University of Bologna, 2012.
[2.8] W. Shockley and H. J. Queisser, "Detailed Balance Limit of Efficiency of *p-n* Junction Solar Cells", *Journal of Applied Physics*, Vol. 32, No. 3, pp. 510-519, 1961.
[2.9] M. A. Green, "Third Generation Photovoltaics: Advanced Solar Energy Conversion", *Springer Series in Photonics*, 2003.
[2.10] C. S. Solanki and G. Beaucarne, "Advanced solar cell concepts", *Energy for Sustainable Development*, Vol. 11, No. 3, pp. 17-23, 2007.
[2.11] R. M. Swanson, "The Promise of Concentrators", *Progress in Photovoltaics: Research and Applications*, Vol. 8, No. 1, pp. 93-111, 2000.
[2.12] A. De Vos, "Detailed balance limit of the efficiency of tandem solar cells", *Journal of Physics D: Applied Physics*, Vol. 13, No. 5, pp. 839-846, 1980.
[2.13] M. A. Green, "Silicon Solar Cells: Advanced Principles & Practice", *Centre for Photovoltaic Devices and Systems*, University of New South Wales, 1995.
[2.14] A. W. Smith and A. Rohatgi, "Ray tracing analysis of the inverted pyramid texturing geometry for high efficiency silicon solar cells", *Solar Energy Materials and Solar Cells*, Vol. 29, No. 1, pp. 37-49, 1993.
[2.15] M. Galiazzo et al., "Double Printing of Front Contact Ag in c-Si Solar Cells", *Proc. of 25th European Photovoltaic Solar Energy Conference* (*EU PVSEC*), pp. 2338-2340, 2010.
[2.16] E. Van Kerschaver and G. Beaucarne, "Back-contact Solar Cells: A Review", *Progress in Photovoltaics: Research and Applications*, Vol. 14, No. 2, pp. 107-123, 2006.
[2.17] Y. H. Cho et al., "Advanced buried contact solar cell structure", *Solar Energy Materials and Solar Cells*, Vol. 48, No. 1-4, pp. 173-177, 1997.
[2.18] R. K. Ahrenkiel, "Recombination processes and lifetime measurements in silicon photovoltaics", *Solar Energy Materials and Solar Cells*, Vol. 76, No. 3, pp. 243-256, 2003.
[2.19] D. K. Schroder and D. L. Meier, "Solar Cell Contact Resistance – A Review", *IEEE Transactions on Electron Devices*, Vol. 31, No. 5, pp. 637-647, 1984.
[2.20] R. De Rose et al., "2-D Numerical Analysis of the Impact of the Highly-Doped Profile on Selective Emitter Solar Cell Performance", *Proc. of 37th IEEE Photovoltaic Specialists Conference* (*PVSC*), pp. 2556-2559, 2011.
[2.21] A. Goetzberger, J. Knobloch, B. Voss, "Crystalline Silicon Solar Cells", *John Wiley & Sons*, 1998.
[2.22] C. Allebé et al., "Large-Area PERC Cells with a Ti-Cu Based Metallization Leading to Efficiencies Above 19.5%", *Proc. of 26th European Photovoltaic Solar Energy Conference* (*EU PVSEC*), pp. 2276-2279, 2011.

Chapter 3

Numerical Modeling of Solar Cells

Numerical modeling is a powerful tool for emulating real phenomena and natural systems by means of mathematical calculations. Nowadays, it has become a viable and strategic alternative to time-consuming and costly experiments in a wide variety of research fields and scientific disciplines, such as astrophysics, physics and chemistry of materials, biology, nanosciences, biomedical engineering and genomics, mechanical engineering and aeronautics, environmental and atmosphere sciences, civil and computer engineering, etc. In particular, computer simulations are widely used to investigate phenomena and systems too complex to be described by simple analytical models. This is also what is happening in the PV research field at the moment, where the increasing complexity of novel device structures, and the development of innovative cell technologies have pushed for a more extensive application of the numerical simulations.

This chapter deals with the numerical electro-optical simulation of solar cells. After a brief introduction to the numerical solution of the basic set of semiconductor differential equations within the drift-diffusion approximation, the TCAD-based simulation flow adopted in this thesis is described, focusing on both electrical and optical simulation of solar cells. Finally, the calibration of the most relevant physical models implemented in the TCAD simulator for specific PV requirements is discussed.

3.1 Numerical solution of semiconductor device equations

Analytical solutions of semiconductor device equations, as discussed in the previous chapter, provide an intuitive and simple understanding of solar cell performance. However, they are limited in accuracy due to the many simplifying assumptions that have been made to obtain them. On the contrary, numerical device simulations lead to more accurate analysis of solar cell designs and operating conditions, for which simple analytical models are inadequate. In particular, numerical models allow to account for the spatial variation of semiconductor parameters (e.g. non-uniform doping), more complex recombination mechanisms, high-level injection conditions, 2-D and 3-D effects, etc.

3.1.1 Historical overview on solar cell modeling

Although numerical modeling has been applied to silicon solar cells since the early days of computer modeling, only recently it has become widely used in the PV industry and research community [3.1]. However, first efforts in solar cell modeling date back to the 1960's at Bell Labs [3.2], [3.3], where an iterative procedure for the analytical solution of the coupled set of semiconductor device equations was developed and, then, applied for cell analysis. In the 1970's, a research group at North Carolina State University developed more refined one-dimensional solution methods for solar cells [3.4], [3.5]. The first attempts for a full-scale modeling of solar cells were also made, by combining the one-dimensional numerical solution with a circuit of resistors, in order to account for the losses in the metallization [3.6]. In the early 1980's, the first solar cell computer program, called SCAP1D (Solar Cell Analysis Program in 1-Dimension), was developed by Lundstrom at Purdue University as part of his PhD thesis [3.7]. SCAP1D software was soon extended to two dimensions, as SCAP2D [3.8]. Several other solar cell programs were developed at Purdue University at later times for the modeling of thin-film solar cells, such as TFSSP (Thin-Film Semiconductor Simulation Program) [3.9], PUPHS (Purdue University Program for Heterojunction Simulation), and PUPHS2D [3.10]. Later, thanks to the improvement of the computer capacity, several computer codes were specifically written for the purpose of solar cell modeling, like PC1D [3.11], [3.12], AMPS-1D [3.13], and ADEPT [3.14]. The basic design of these computer programs is very similar. The fully coupled set of non-linear partial differential semiconductor equations is formulated in a normalized form in order to simplify the calculations. Then, finite difference or finite element methods are used to discretize the equations on a mesh grid. Finally, by assuming properly discretized boundary conditions, these equations are solved iteratively using a generalized Newton method in order to obtain the carrier concentrations and the electrostatic potential at each mesh point.

The software ADEPT (A Device Emulation Program and Toolbox) [3.14] was developed at Purdue University for simulating solar cells in two and three dimensions. In particular, ADEPT has been mainly applied to examine solar cells made of other materials than crystalline silicon, such as heterostructure solar cells.

AMPS-1D (Analysis of Microelectronic and Photonic Structure in 1-Dimension) [3.13] was engineered at the Pennsylvania State University under the sponsorship of the Electric Power Research Institute (EPRI) as a very general and versatile simulation tool for analyzing transport in microelectronic and photonic structures. It is a 1-D device simulation program which has been successfully applied to examine a wide variety of solar cell structures, including homo-junction, hetero-junction and multi-junction devices.

PC1D [3.11], [3.12] is a one-dimensional FEM (Finite Element Method) solar cell simulator, which was originally written at Sandia National Labs in 1982 and, then, further developed at the University of New South Wales (UNSW) in Australia. It has strongly influenced the PV community and, today, it can be still considered the most widely used among the commercially available programs for the simulation of silicon solar cells. Its popularity is mainly due on its speed and its very simple and intuitive user interface. Moreover, it includes PV specific doping-dependent models for recombination processes and material parameters. It also contains a simplified model to account for the effect of surface texturing on the electron-hole pairs photogeneration. In the 1990's, PC1D was continuously improved [3.15]-[3-17], and more recently its extension to two dimensions, called PC2D, has been presented [3.18]. Despite its success in the PV research community, PC1D shows some aspects that limit its predictive capability. Among these limitations, it is worth mentioning the adoption of Boltzmann statistics, which is not suited to adequately model some performance-limiting highly-doped regions of the solar cell, such as the emitter and the back-surface field (BSF) regions, and the restriction to the mono-dimensional analysis, which prevents an accurate investigation of innovative cell structures [3.19]. Furthermore, it is worth pointing out that the more recent version PC2D, even though it allows to extend the analysis to two dimensions, features a very coarse limiting mesh (with a grid of 20×20 identical rectangular elements), which cannot provide adequate spatial resolution for most purposes in solar cell modeling.

During the last years, the growing interest for advanced cell architectures, and the consequent requirement for more accurate 2-D or 3-D simulations have pushed for the application in the PV research community of multi-dimensional and general-purpose TCAD (Technology Computer-Aided Design) device simulators, able to solve numerically the fully coupled set of semiconductor differential equations within the drift-diffusion approximation, accounting also for the Fermi-Dirac statistics. In the early 1990's, a device simulator called SIMUL became very popular in the electronics industry for developing and optimizing CMOS technologies, due to its improved numerical and meshing methods [3.20], [3.21]. It was also used at the University of New South Wales (UNSW) in Australia to investigate high-efficiency silicon solar cells [3.22], thus contributing significantly to reach the new world record efficiency in 1994 [3.23]. Its subsequent versions, called first DESSIS (Device Simulation for Smart Integrated Systems), and later Sentaurus, became widely used in PV research institutes only in the late 1990's. Nowadays, the TCAD modeling software Sentaurus by Synopsys [3.24], and to a smaller extent Atlas by Silvaco [3.25] as well as MicroTec by Siborg Systems [3.26], have become widely used in the PV industry in order to aid the design of new solar cell technologies, thus accelerating their optimization, and reducing the testing costs.

3.1.2 Drift-diffusion transport model

In general, the semi-classical charge transport in semiconductor devices is described by the Boltzmann Transport Equation (BTE). BTE is an integro-differential equation based on both statistical and classical laws of dynamics whose direct analytical solution is a very difficult task for realistic devices. This difficulty arises from the non-homogeneous device structures, the complicated models for collision mechanisms, and the complexity of the band structure. For this reason, BTE is commonly solved numerically through direct statistical methods (Monte Carlo method), or drastic approximation methods (methods of moments). Therefore, depending on the type of devices under investigation and on the required accuracy of simulations, several different approaches can be chosen for the numerical device simulations, starting from BTE.

The Monte Carlo method is the most general approach for the solution of BTE, but, due to its high computational requirements, it is not typically used for routine simulations of semiconductor devices. The most widely used transport model for semiconductor device modeling is the drift-diffusion (DD) model, which has been already described in Chapter 2. This model is obtained from BTE by solving it through the approximation method based on the moments of BTE. It is the simplest charge transport model in which the current densities only depend on the instantaneous electric field and carrier concentrations, as shown in Eqs. 2.3 and 2.4. It is worth pointing out that DD model allows only isothermal analysis and, hence, it is mostly adopted for low-power density devices with long active regions. However, DD approach can be extended to more accurate transport models, such as the thermodynamic and the hydrodynamic models. Thermodynamic (or non-isothermal) model allows to account for electrothermal and self-heating effects under the assumption that charge carriers are in thermal equilibrium with the lattice and, therefore, it is better suitable for high-power density devices. Instead, hydrodynamic (or energy balance) model accounts for carrier heating at high fields and, consequently, it is better suitable for devices with small submicron active regions.

Solar cell modeling typically adopts the conventional DD transport model. As already discussed in Chapter 2, the DD model is defined by the three governing equations for charge transport in semiconductor devices, i.e., the Poisson equation (see Eq.2.1) and the electrons and holes continuity equations (see Eqs. 2.6 and 2.7), where, in the drift-diffusion approximation, the electrons and holes current densities are given by Eqs. 2.3 and 2.4, respectively. The electrons and holes current densities can be also expressed by means of the electrons and holes quasi-Fermi potentials Φ_n and Φ_p, respectively, as given by [3.27]:

$$\boldsymbol{J}_n = -nq\mu_n \nabla \Phi_n + qD_n \nabla n \tag{3.1}$$

$$\boldsymbol{J}_p = -pq\mu_p \nabla \Phi_p - qD_p \nabla p \qquad (3.2)$$

Under the assumption of Boltzmann statistics, the carrier concentrations can be expressed as:

$$n = N_C \; exp\left(\frac{E_{Fn} - E_C}{kT} \right) \qquad (3.3)$$

$$p = N_V \; exp\left(\frac{E_V - E_{Fp}}{kT} \right) \qquad (3.4)$$

where $E_{Fn} = -q\Phi_n$ and $E_{Fp} = -q\Phi_p$ are the quasi-Fermi energies for electrons and holes, respectively. E_C and E_V are the conduction and valence band edges, which can be defined, respectively, as:

$$E_C = -\chi - q(\varphi - \varphi_{ref}), \qquad E_V = -\chi - E_{g,eff} - q(\varphi - \varphi_{ref}) \qquad (3.5)$$

where χ denotes the electron affinity, $E_{g,eff}$ the effective energy band-gap, and φ the electrostatic potential, which is calculated from an arbitrarily defined reference potential φ_{ref}. This reference potential is typically set to the Fermi potential of the intrinsic semiconductor. Therefore, Eqs. 3.3 and 3.4 become:

$$n = n_{i,eff} \; exp\left(\frac{q(\varphi - \Phi_n)}{kT} \right) \qquad (3.6)$$

$$p = n_{i,eff} \; exp\left(\frac{q(\Phi_p - \varphi)}{kT} \right) \qquad (3.7)$$

where $n_{i,eff}$ is the effective intrinsic density (Eq. 2.19).
The quasi-Fermi potentials can be thus expressed as:

$$\Phi_n = \varphi - \frac{kT}{q} ln\left(\frac{n}{n_{i,eff}} \right) \qquad (3.8)$$

$$\Phi_p = \varphi + \frac{kT}{q} ln\left(\frac{p}{n_{i,eff}}\right) \tag{3.9}$$

TCAD solvers typically allow to account for the Fermi-Dirac statistics, that becomes mandatory for high values of carrier concentrations (i.e. above 1×10^{19} cm^{-3}) in the active regions of a semiconductor device. For Fermi-Dirac statistics, Eqs. 3.3 and 3.4 are replaced by [3.27]:

$$n = N_C F_{1/2}\ exp\left(\frac{E_{Fn} - E_C}{kT}\right) \tag{3.10}$$

$$p = N_V F_{1/2}\ exp\left(\frac{E_V - E_{Fp}}{kT}\right) \tag{3.11}$$

where $F_{1/2}$ is the Fermi integral of order 1/2. As a consequence, Eqs. 3.6 and 3.7 become:

$$n = n_{i,eff} \cdot \gamma_n\ exp\left(\frac{q(\varphi - \Phi_n)}{kT}\right) \tag{3.12}$$

$$p = n_{i,eff} \cdot \gamma_p\ exp\left(\frac{q(\Phi_p - \varphi)}{kT}\right) \tag{3.13}$$

where γ_n and γ_p are functions of the electron and hole quasi-Fermi energies, respectively:

$$\gamma_n = \frac{n}{N_C} exp\left(-\frac{E_{Fn} - E_C}{kT}\right) \tag{3.14}$$

$$\gamma_p = \frac{p}{N_V} exp\left(-\frac{E_V - E_{Fp}}{kT}\right) \tag{3.15}$$

In addition to the basic equations of the DD model, boundary conditions must be introduced in order to fully define the mathematical problem. At device contacts, by default, the reflective ideal Neumann conditions are typically assumed for the current densities [3.27]:

$$\boldsymbol{J}_n \cdot \hat{n} = 0, \qquad \boldsymbol{J}_p \cdot \hat{n} = 0 \tag{3.16}$$

where $\hat{n}$ is the unit normal vector to the boundary interface.

For metal/semiconductor contacts, an ohmic behavior can be assumed at highly-doped interfaces. This implies that no barrier is at such interface and, therefore, the quasi-Fermi level of the metal is equal to the semiconductor quasi-Fermi level. In general, an ohmic boundary condition assumes charge neutrality and equilibrium conditions at contacts:

$$n = n_0, \qquad p = p_0 \tag{3.17}$$

$$n_0 - p_0 = N_D - N_A \tag{3.18}$$

$$n_0 p_0 = n_{i,eff}^2 \tag{3.19}$$

where n_0 and p_0 are the electrons and holes equilibrium concentrations. Under the assumption of Boltzmann statistics, the electrostatic potential is then given by [3.27]:

$$\varphi = \Phi_F + \frac{kT}{q} asinh\left(\frac{N_D - N_A}{2n_{i,eff}}\right) \tag{3.20}$$

where Φ_F is the Fermi potential at the contact which is equal to the externally applied voltage if the contact is not resistive.

If electrons and holes recombination velocities v_n and v_p are specified at contacts, equilibrium conditions are no longer valid and, consequently, the boundary conditions of Eq. 3.16 become:

$$\boldsymbol{J}_n \cdot \hat{n} = qv_n(n - n_0), \qquad \boldsymbol{J}_p \cdot \hat{n} = -qv_p(p - p_0) \tag{3.21}$$

It is worth pointing out that the application of Schottky contacts instead of ohmic contacts leads to modify the boundary conditions expressed in Eqs. 3.20 and 3.21, as explained in [3.27], by including the effect of the barrier height due to the difference between the metal workfunction and the electron affinity of the semiconductor. Furthermore, if the contact is resistive, the Fermi potential Φ_F at contacts cannot be still considered equal to the externally applied voltage and, therefore, it has to be carefully computed [3.27].

3.1.3 Numerical solution method

Finite Element Method (FEM) is a widely applied technique to numerically solve mathematical problems which are described by partial differential equations (PDEs), such as the three governing equations in the DD model, i.e., the Poisson equation (see Eq.2.1), and the electrons and holes continuity equations (see Eqs. 2.6 and 2.7). FEM approach is based on the discretization of the device through a grid mesh. A comprehensive review of the most widely used discretization methods of PDEs for semiconductor device simulation is reported in [3.28]. One of these is the well-known '*box discretization*' method, well described in [3.29]. This method provides the discretization of a symmetry element of the device by dividing it into boxes. Rectangular or more computationally efficient triangular boxes are typically used in a 2-D simulation domain. Then, the PDEs are integrated over a "control box volume", as shown in Fig. 3.1, where the Gauss theorem is applied, and, then, the resulting terms are discretized to a first-order approximation. For an arbitrary i-th vertex in a triangular 2-D discretization mesh, a control box Ω_i is built by choosing box boundaries as the perpendicular bisectors of the lines connecting adjacent vertices (according to Fig. 3.1).

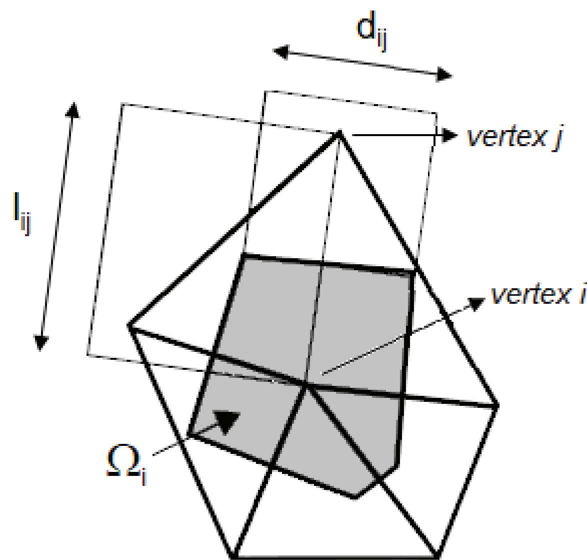

Figure 3.1. Example of the box discretization method for the numerical solution of PDEs in a triangular mesh. The highlighted area represents the volume Ω_i of the control box for an arbitrary i-th vertex.

In general, a PDE can be expressed in the following form:

$$\nabla \boldsymbol{\Gamma}(\boldsymbol{r}) = \Sigma(\boldsymbol{r}) \tag{3.22}$$

where $\boldsymbol{\Gamma}(\boldsymbol{r})$ is a position-dependent vector field, and $\Sigma(\boldsymbol{r})$ is a position-dependent scalar field. By considering the Poisson equation, the electric field $\boldsymbol{\xi}$ is a conservative field and, consequently, the Gauss theorem can be applied to integrate Eq. 3.22 over the control box volume Ω_i:

$$\int_{\Omega_i} \left[\nabla \boldsymbol{\Gamma}(\boldsymbol{r}) - \Sigma(\boldsymbol{r})\right] dV = \int_{\partial\Omega_i} \boldsymbol{\Gamma}(\boldsymbol{r})\, d\hat{n}(\boldsymbol{r}) - \int_{\Omega_i} \Sigma(\boldsymbol{r}) dV = 0 \tag{3.23}$$

where $\hat{n}$ is the unit normal vector to the box boundaries. Therefore, the discretized PDE can be written as:

$$\sum_{j \neq i} \Gamma_{ij}\, d_{ij} - \Sigma_i\, V_i = 0 \tag{3.24}$$

where Γ_{ij} is the projection of the vector field $\boldsymbol{\Gamma}(\boldsymbol{r})$ onto the edge l_{ij} from vertex i to vertex j (see Fig. 3.1), d_{ij} is the length of the perpendicular bisector on the same edge (see Fig. 3.1), Σ_i is the value of the scalar field $\Sigma(\boldsymbol{r})$ at vertex I, and V_i represents the area of the box Ω_i in two dimensions, or the box volume in three dimensions.
By applying Eq. 3.24 to Eq. 2.1, the Poisson equation become:

$$\sum_{j \neq i} \xi_{ij}\, d_{ij} - \rho_i\, V_i = 0 \tag{3.25}$$

The electric field ξ in Eq. 3.25 can be expressed in terms of the potential difference φ_{ij} between vertices i and j along l_{ij}, therefore:

$$F_i^{\phi} = -\sum_{j \neq i} \frac{d_{ij}}{l_{ij}} \varphi_{ij} - V_i\left(p_i - n_i + N_i\right) = 0 \tag{3.26}$$

Similarly, the discretized forms of the electrons and holes continuity equations can be derived, as shown in [3.30]:

$$F_i^{n} = -\sum_{j \neq i} \frac{d_{ij}}{l_{ij}} \mu_{ij}^{n}\left[n_j B(\varphi_{ji}) - n_i B(\varphi_{ij})\right] + V_i\left(R_i - G_i\right) = 0 \tag{3.27}$$

$$F_i^{p} = -\sum_{j \neq i} \frac{d_{ij}}{l_{ij}} \mu_{ij}^{p}\left[p_j B(\varphi_{ij}) - p_i B(\varphi_{ji})\right] + V_i\left(R_i - G_i\right) = 0 \tag{3.28}$$

where B denotes the Bernoulli function:

$$B(x) = \frac{x}{exp(x) - 1} \tag{3.29}$$

and the mobility μ_{ij} is assumed to be constant on the box edge perpendicular to l_{ij}.

Therefore, the three governing equations in the DD model are discretized at each vertex of the grid mesh, thus giving rise to a system of 3N non-linear equations in 3N unknowns, where N is the total number of mesh vertices. The unknowns at each vertex are the carrier concentrations n and p, and the electrostatic potential φ. This non-linear system is typically solved through the iterative Newton method by following the procedure developed in [3.31]. In particular, the Newton procedure iteratively computes a new solution starting from the previous one until suitable convergence criteria are fulfilled [3.27].

3.2 TCAD-based numerical simulation of solar cells

In this thesis, numerical simulations of *c*-Si solar cells have been performed by using the TCAD Sentaurus suite by Synopsys [3.24], which is a general-purpose framework featuring a wide variety of tools for device editing, mesh generation, process simulation, device simulation, optical simulation, data analysis, data visualization, etc. This software includes a multi-dimensional FEM device simulator with a comprehensive set of physical models, combined with an extensive set of optical simulators. For this reason, it is particularly suitable for accurate analysis of innovative solar cell structures.

The typical TCAD-based tool flow adopted for the electro-optical numerical simulation of solar cells is described in Fig. 3.2.

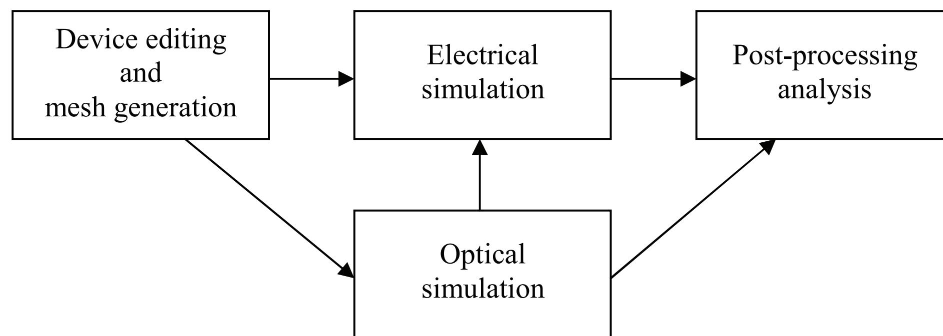

Figure 3.2. Typical TCAD-based tool flow for the electro-optical numerical simulation of solar cells.

It includes a device editor, like Sentaurus Structure Editor [3.32], that allows to create 1-D, 2-D or 3-D simulation domains with the desired geometry, by choosing the appropriate materials (semiconductors, dielectrics and metals), and by specifying the doping properties of semiconductor materials. Once the structure is created, a fine grid mesh has to be defined and generated with an appropriate tool, like Sentaurus Mesh [3.33]. The generated mesh and the doping properties are thus stored in a file, which is passed to the electro-optical simulator, like Sentaurus Device [3.27]. This simulator, first, computes the photo-generation rate inside the device and, then, uses it to perform the electrical simulation under illuminated conditions. Finally, the electrical and optical figures of merit of solar cells are extracted from the outputs of the electro-optical simulation through apposite post-processing analysis tools, like Inspect [3.34] in TCAD Sentaurus suite.

In the following, each of these steps to be performed for the electro-optical simulation of solar cells is discussed in more detail. Moreover, it is worth pointing out that TCAD Sentaurus provides a compact platform with a user-friendly graphical interface, called Sentaurus Workbench [3.35], which integrates the available tools into one environment, aiming at automating and speeding up the execution of fully parameterized simulation experiments.

3.2.1 Device editing and mesh generation

As discussed in Section 3.1.3, the numerical solution of the fully coupled set of semiconductor differential equations requires the creation of a discretization grid mesh, which must be adapted to the geometry of the device. Solar cells are large-area semiconductor devices, featuring dimensions in the order of centimeters. As a consequence, the simulation of the entire 3-D device would require a very huge computational effort. However, the structure of solar cells is highly symmetric. Therefore, the simulation domain can be reduced to only a small repetitive portion of the structure, that is typically half of the symmetry element in two dimensions, and a quarter of the symmetry element in three dimensions (Fig.3.3a).

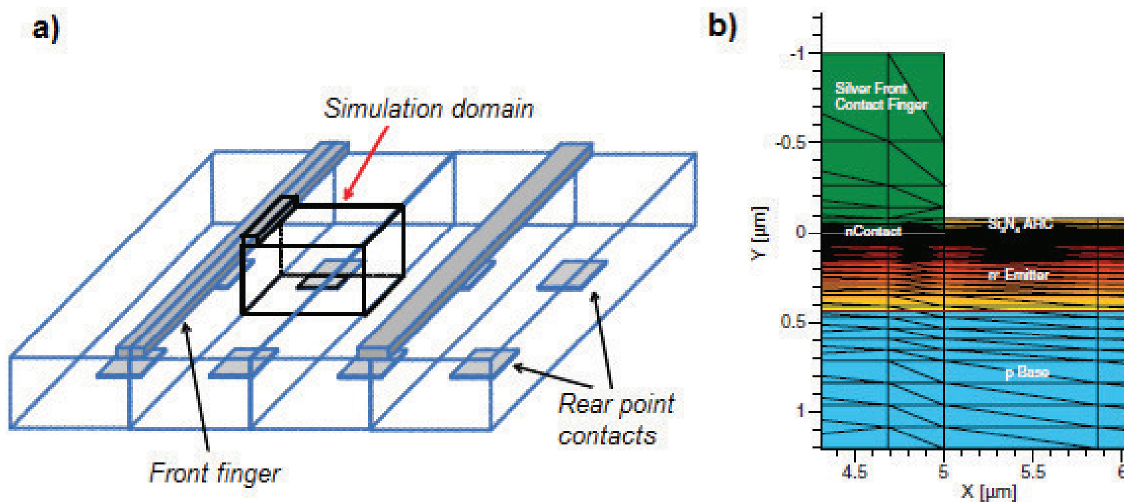

Figure 3.3. a) Example of selecting the cell simulation domain in three dimensions. b) Example of discretization mesh grid in a 2-D simulation domain.

Once the simulation domain of the device is carefully drawn with the description of the various regions in terms of boundaries, material types, location of electrical contacts and doping properties, the discretization grid mesh must be defined. Meshing is one of the most important aspects in determining the simulation efficiency and accuracy. Fig. 3.3b shows an example of mesh in a 2-D simulation domain. It is worth noting that the grid mesh is not typically regular and uniform because it must be refined in the regions where the parameters vary strongly with distance, otherwise the discretization errors become too large. In particular, a fine mesh is necessary at material interfaces, *p-n* junctions and contacts. The general practice for meshing is to apply a relatively coarse mesh to the whole structure first and, then, to add mesh refinements to specific regions. Although meshing strategies can differ considerably for different applications, there are some common useful guidelines, such as that to gradually increase or decrease the mesh size when adding the mesh refinements in order to avoid abrupt changes. In solar cells, accurate mesh refinements are commonly required in the following regions:

- in the region underneath the front contact finger, where the shadowing effect occurs;
- at the top of the structure in order to properly resolve the optical generation rate close to the front surface, where the blue part of the sunlight is absorbed within a few nanometers;
- in the regions adjacent to junctions, such as the emitter and the BSF region, where there is a significant doping gradient;
- near the metal contacts at the front-side and in some cases, depending on cell design, also at the rear (e.g. in rear point contact cells), where current crowding occurs.

Theoretically, the finer the mesh, the more accurate the simulation results. However, practically, a good mesh is obtained when it is sufficiently refined to provide the required accuracy in a reasonable simulation time. On the other hand, it is worth pointing out that an overrefined mesh may lead to a very long simulation time without improving the accuracy. Indeed, as the accuracy improves quickly with the total number of nodes in the mesh and, then, saturates, the simulation time increases superlinearly with the number of nodes. Therefore, a good trade-off between accuracy and simulation runtime has to be reached.

3.2.2 Optical simulation

The simulation of PV devices under illumination requires an accurate modeling of light propagation and optical carrier generation within the absorbing material. As discussed in Chapter 2, the photogeneration rate of electron-hole pairs is coupled to the transport equations. Accordingly, the computation of the spatial distribution of the optical generation rate is mandatory to solve the set of semiconductor device equations for a device operating under illumination. As shown in Fig. 3.4, the optical simulator takes as input the geometry of the different device regions (ARC, metals, semiconductor), accounting for the different optical properties of the materials. Then, it calculates the optical generation rate G_λ (**r**) as a function of the wavelength λ of the radiation, by ramping the wavelength of incident sunlight from the blue region of the spectrum (close to 0.3 μm) to the infrared region (typically up to 1.2 μm). In PV optical simulations, the radiation is typically modeled thorough the conventional AM1.5G solar spectrum with an incident power of 1000 W/m^2, also known as one-sun solar spectrum (see Fig. 2.11). In addition to the optical generation rate due to photon absorption of a given wavelength λ, the spatial distribution of the total optical generation rate G (**r**) is typically extracted from a full-spectrum computation (see Fig. 3.4), i.e. by summing the optical generation rates due to photons of all the wavelengths in the solar spectrum. The optical simulation provides also the optical response of the device (i.e., reflectance, transmittance and absorbance) as a function of the wavelength λ of the radiation (see Fig. 3.5).

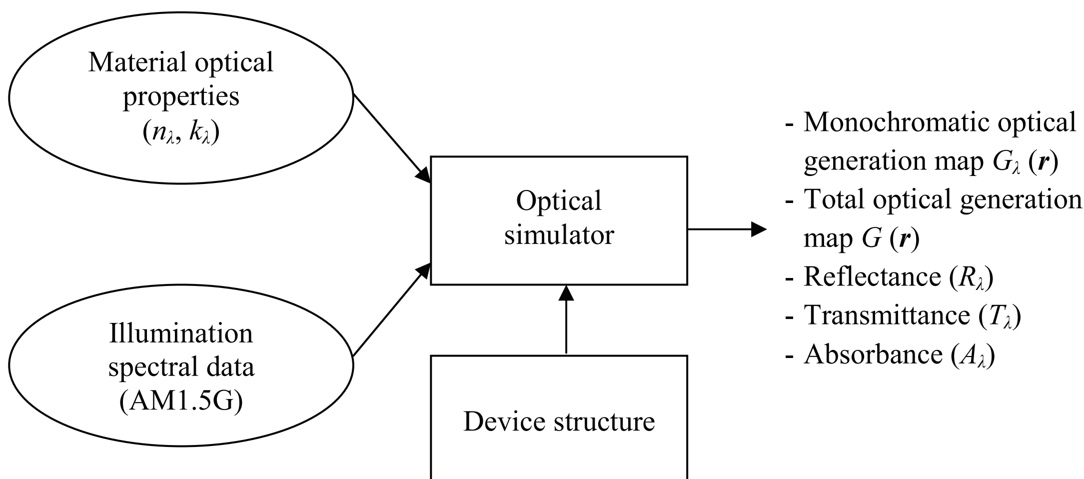

Figure 3.4. Typical TCAD-based tool flow for the optical simulation of solar cells.

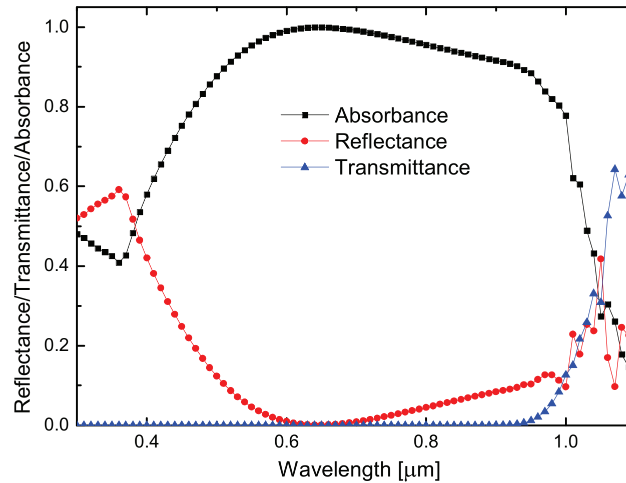

Figure 3.5. Example of simulated reflectance, transmittance and absorbance curves for a conventional silicon solar cell.

The solution of the optical problem in electro-optical simulations for a given excitation source can be performed by means of several methods, which lead to different trade-offs between accuracy and computational effort. Among these, it is worth mentioning the Ray-Tracing (RT) method based on the geometrical optics, the Transfer Matrix Method (TMM), and the more rigorous methods based on the solution of the Maxwell's equations, such as the Finite-Difference Time-Domain (FDTD) and the Rigorous Coupled Wave Analysis (RCWA) methods. Depending on the specific application, these optical solvers can be used alternatively or in mutual combination in order to exploit the potentials provided by different approaches.

The *Transfer Matrix Method* (TMM) accounts for the coherent propagation of monochromatic plane waves with arbitrary angles of incidence and polarization states through a planar-layered media by using a transfer matrix approach [3.27]. Each parallel layer is assumed to be homogeneous, isotropic and optically linear. On one hand, TMM is particularly suited to design the anti-reflective coating (ARC) layers commonly adopted on the top surface of solar cells to reduce the reflection losses and, consequently, to enhance the photon absorption inside the device. On the other hand, due to its limitation to planar devices, TMM cannot properly deal with actual solar cell structures, featuring textured surfaces at the top surface. However, an extension of this method for the modeling of light propagation in such textured structures can be obtained by appropriately transforming them into planar-layered media with equivalent optical properties [3.27].

The *Ray-tracing* (RT) method is a very fast solver, well suited both for 2-D and 3-D geometries. It is based on the geometrical optics, that describes light propagation in terms of rays. These light rays are assumed to propagate in a rectilinear path through a homogeneous medium, while at the interfaces between two dissimilar media (i.e., featuring different refractive indices) they follow the reflection, transmission and refraction rules defined by the well-known

Snell law for the plane waves [3.36]. Therefore, each ray can be considered as a local plane wave traveling in a particular direction with its polarization vector perpendicular to the direction of propagation, where the length of the polarization vector denotes the amplitude and the square of its length represents the intensity. This is a significant simplification of the optical problem that fails to account for optical phenomena such as diffraction and interference. However, geometrical optics is an excellent approximation that works when the wavelength of the radiation is much smaller than the feature size of structures with which the light interacts.

RT solvers typically uses a recursive algorithm which starts with a source ray and builds a binary tree that tracks the transmission and reflection of light rays at interfaces between media featuring different refractive indices. Indeed, at such interfaces, incident rays split into reflected and transmitted rays and, then, the latter ones may be absorbed in the absorbing material, thus giving rise to photogenerated electron-hole pairs.

In the PV community, different in-house RT programs have been developed, like TEXTURE [3.37], the RT solver in PC1D [3.12], SUNRAYS [3.38], RAYN [3.39], SONNE [3.40], RAYSIM [3.41], and, more recently, DAIDALOS [3.42]. RT solvers are also provided in TCAD modeling software, like Sentaurus [3.27] and Atlas [3.25]. All these programs have been successfully adopted for the optical modeling in 2-D or 3-D dimensions of first-generation wafer-based silicon solar cells with textured surfaces, whose geometrical features are relatively larger than the wavelength of the sunlight radiation. However, it is worth noting that, in most cases, the size of the smallest features in the front textured surfaces can be comparable to the wavelengths of sunlight. Consequently, this results in a source of error for RT solvers, which are based on the geometrical optics. Likewise, second-generation thin-film solar cells featuring rough interfaces and more advanced third-generation nano-structured solar cells cannot be handled by RT solvers. As a consequence, the modeling of light propagation in such devices requires more rigorous optical solvers based on the solution of Maxwell's equations, thus able to treat the near field optical problem.

Finite-Difference Time-Domain (FDTD) technique is one of the most popular numerical methods for computational electromagnetics based on the solution of Maxwell's equation in the time domain [3.27], [3.43]. In particular, Maxwell's equations in differential form are solved in a linearized form by means of central finite differences. FDTD is widely applied in many different areas, such as electromagnetic propagation, antennas and waveguides design. This optical method allows to handle structures featuring size comparable, or even much smaller, than the wavelength of the radiation. However, it is extremely CPU- and memory-intensive and, therefore, it is not particularly suited for large-area 2-D or 3-D structures, such as most of solar cells.

Another rigorous solver of the Maxwell's equations is the *Rigorous Coupled Wave Analysis* (RCWA) method, also known as Fourier Modal Method (FMM), based on a Fourier

modal expansion in terms of spatial harmonics of the electromagnetic field and of the permittivity. Originally developed for the modeling of light propagation in waveguides and diffraction gratings [3.44], [3.45], RCWA has been recently applied to the optical simulations of advanced solar cell structures, such-as thin-film solar cells featuring rough surfaces and nano-structured devices [3.46], [3.47]. Several alternative implementations of the RCWA have been proposed in literature [3.48], [3.49]. In particular, a computationally efficient and numerically stable RCWA-based solver has been presented in [3.47], [3.50].

An example of comparison between RT, FDTD and RCWA methods has been reported in [3.19], with the aim to put in evidence the limitations of the conventional RT technique with respect to the more rigorous electromagnetic solvers. In particular, the absorbance of a 2-μm-thick *c*-Si slab featuring ideal flat surfaces has been calculated in the wavelength range 350 □ 850 nm. Since the layer thickness is quite comparable to the wavelength of the radiation, light diffraction and interference play a fundamental role in such test structure. Therefore, the absorbance calculated by the RT method inside the device is affected by a considerable error and, consequently, it differs significantly from those computed by FDTD and RCWA simulators, especially at larger wavelengths (see Fig. 3.6a). It is worth noting that the absorbance curves calculated by means of FDTD and RCWA, respectively, are quite similar, featuring a set of maxima and minima at larger wavelengths, due to the interference effects related to the finite thickness of the silicon layer. For this particular example, by assuming the standard AM1.5G illumination spectrum, the total absorbed energy integrated over the whole spectral distribution is essentially the same for all the considered optical methods (less than 1% of relative error). However, if the thickness of the silicon layer is further reduced (see Fig. 3.6b), the total absorbed energy computed by the RT method starts to be significantly overestimated as compared to that calculated by the electromagnetic solvers.

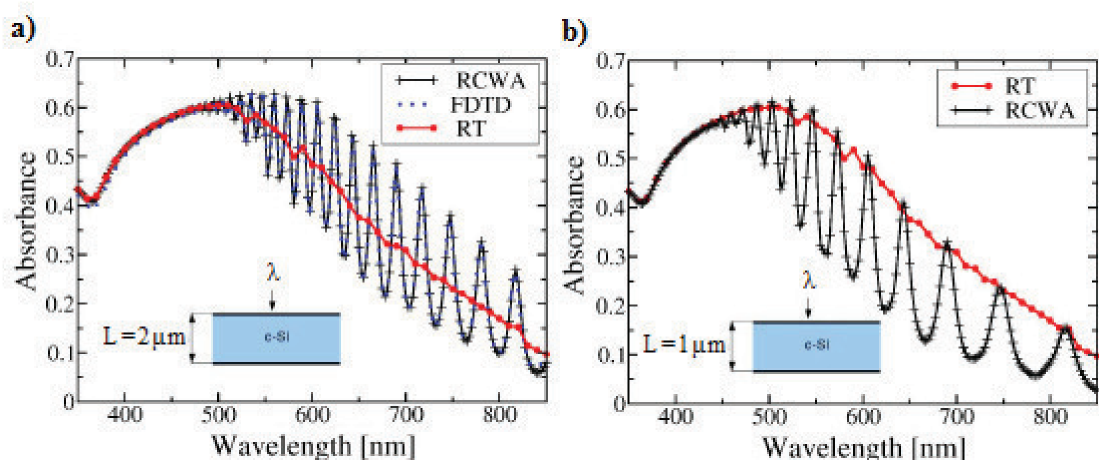

Figure 3.6. Absorbance curves for the a) 2-μm-thick and b) 1-μm-thick *c*-Si slabs, calculated by means of Ray-Tracer (RT), Finite Difference Time Domain (FDTD) and Rigorous Coupled Wave Analysis (RCWA) methods.

Regarding the computational effort, while a monochromatic simulation takes only few seconds by using a RT solver, the adoption of a FDTD simulator typically increases the simulation time by two orders of magnitude, hence resulting in prohibitively large computational times when full-spectrum calculations are performed. RCWA-based electromagnetic simulators are generally much faster than FDTD ones, providing thus a more acceptable trade-off between accuracy and computational time.

3.2.3 Electrical simulation

The electrical characteristics of a solar cell are generally simulated by means of a tool able to solve numerically the drift-diffusion transport model accounting for the Fermi-Dirac statistics (see Section 3.1.2). As illustrated in Fig. 3.7, the electrical simulator takes as input a file including the 1-D, 2-D or 3-D grid mesh and the doping properties of the solar cell from the device editor. Then, it performs voltage sweeps and calculates the output current density in absence or in presence of the incident sunlight, thus providing the dark and illuminated *J-V* characteristics of the solar cell. It is worth noting that the simulation results critically depend on the setting of the boundary conditions at device interfaces (e.g., at contacts and at passivated surfaces) and of the physical models and parameters implemented in the device simulator (according to Fig. 3.7). Since most of the commercial TCAD-based simulation programs are tailored to CMOS devices, a realistic electrical simulation of solar cells requires an ad-hoc refinement of several physical models, such as those for the intrinsic carrier density, the Auger recombination, the surface recombination at passivated surfaces, the minority carrier mobility, the trap-assisted recombination, etc. The calibration of the most relevant physical models implemented in the TCAD simulator for specific PV requirements is discussed in Section 3.3. Furthermore, the simulation accuracy is affected by the setup of the numerical solver and of the voltage ramp. In general, an accurate choice of the numerical solution method and a gradual ramping of the voltage can ensure a good trade-off between accuracy and simulation run-time, and, at the same time, prevent convergence problems in solving the equations of the DD model.

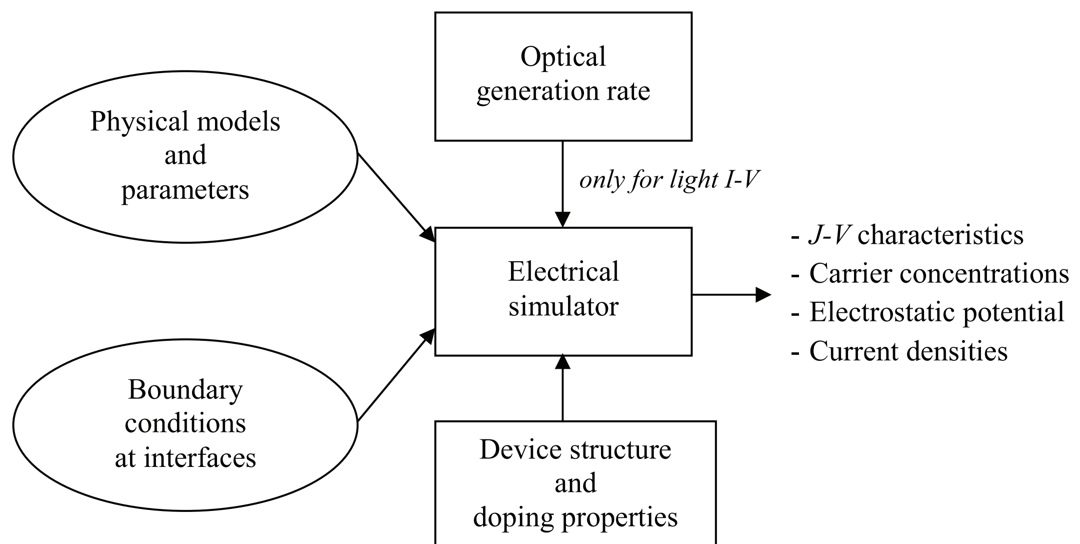

Figure 3.7. Typical TCAD-based tool flow for the electrical simulation of solar cells.

3.2.4 Post-processing analysis

The outputs from electro-optical simulations must be processed for the extraction of electrical and optical parameters of interest for a solar cell. First of all, the output current densities from the electrical simulation have to be rescaled by defining an appropriate area factor, which converts the current density unit under illumination to mA/cm^2 (that is the unit commonly adopted in PV applications). For example, in case of a 2-D structure, by default, a device simulator computes the current *I'* in units of A/μm. Therefore, the current *I* in units of A is given by:

$$I = I' \cdot L_z \tag{3.30}$$

where L_z denotes the width of the device in the z-direction, which is assumed to be the third non-simulated dimension. For 2-D structures, the default value of L_z is 1 μm. The current density *J* is then defined as:

$$J = \frac{I}{A_{surf}} \tag{3.31}$$

where A_{surf} represents the surface area of the solar cell, given by:

$$A_{surf} = W_x \cdot L_z \tag{3.32}$$

where W_x is the total width of the 2-D simulation domain along the horizontal axis. Therefore, by considering Eqs. 3.30 and 3.32, Eq.3.31 can be rewritten as:

$$J = \frac{I'}{W_z} \; \left[A/\mu m^2 \right] \tag{3.33}$$

The current density is then converted in units of mA/cm^2 by multiplying the output current *I'* by an area factor of $10^{11}/W_x$, as explained in the following expression:

$$J\left[mA/cm^2 \right] = \frac{I'}{W_z} \left[A/\mu m^2 \right] \times 10^{11} \left[\frac{\mu m^2}{A} \frac{mA}{cm^2} \right] \tag{3.34}$$

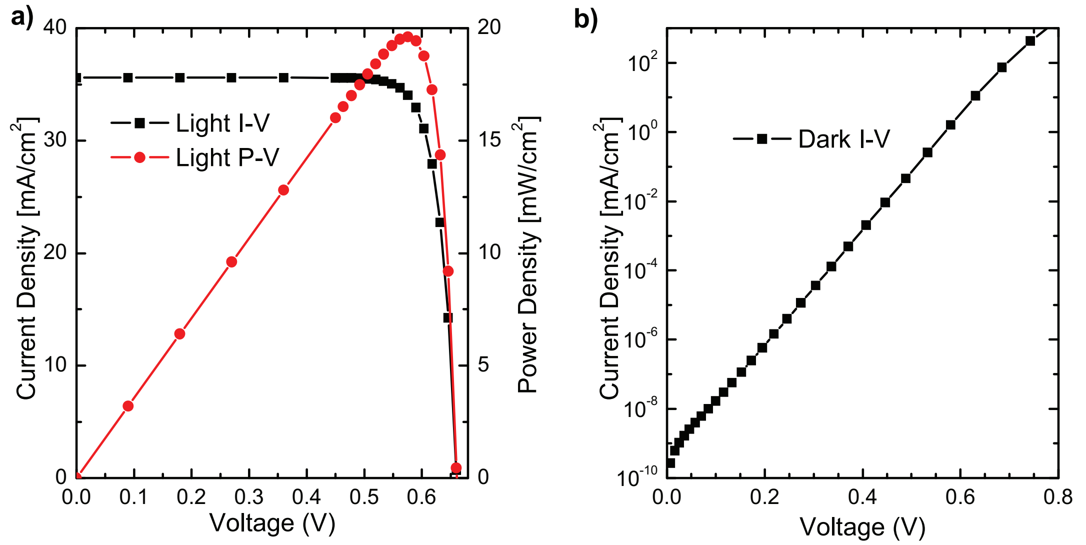

Figure 3.8. Example of post-processed a) light *J-V* and *P-V* curves, and b) dark *J-V* curve for a conventional silicon solar cell.

An example of a post-processed light *J-V* curve is illustrated in Fig. 3.8a. The power density of the solar cell can be then calculated in units of mW/cm^2 as $P = J{\cdot}V$ (see Fig. 3.8a). Therefore, the main electrical figures of merit of the solar cell operating under illumination, such as J_{sc} [mA/cm^2], V_{oc} [mV], P_{mpp} [mW/cm^2], FF [%] and η [%], can be extracted from the post-processed *J-V* and *P-V* characteristics, by considering an incident power of 100 mW/cm^2 for the conventional AM1.5G spectrum. In addition, the photogenerated current density of the illuminated solar cell is typically calculated by integrating the optical generation rate over all the simulated device. For instance, in case of a 2-D structure, the photogenerated current density $J_{ph}(\lambda)$ due to photon absorption of a given wavelength λ is obtained as:

$$J_{ph}(\lambda) = \frac{q\int_{\Omega} G_{opt}(x,y,\lambda) L_z dA}{A_{surf}} = \frac{q\int_{\Omega} G_{opt}(x,y,\lambda) dA}{W_x} \tag{3.35}$$

where Ω denotes the considered 2-D simulation domain. Eq. 3.35 gives the total number of the photogenerated electron-hole pairs due to photons of wavelength λ per unit time. Similarly, the total photogenerated current density J_{ph}, due to photon absorption of all the wavelengths in the solar spectrum, is given by:

$$J_{ph} = \frac{q\int_{\Omega} G_{opt}(x,y) dA}{W_x} \tag{3.36}$$

where G_{opt} (x,y) represents the spatial distribution of the total optical generation rate inside the 2-D simulation domain, computed by the optical simulator as the integral of the wavelength-dependent optical generation rate in the wavelength range of interest.

It is worth pointing out that the simulated *J-V* and *P-V* characteristics typically do not take into account all the parasitic resistive losses occurring in a solar cell, which are already discussed in Section 2.5.4. In particular, the simulated curves must be usually corrected by means of a further post-processing, aiming at including the effect of the front metal fingers and busbars resistances, the front contact resistance and the shunt resistance. Moreover, the shadowing effect due to the front busbars can be also accounted for by properly scaling the output current density.

An example of a post-processed forward-biased dark *J-V* curve is also reported in Fig. 3.8b. In PV simulations, dark *I-V* characteristics are typically simulated with the aim of performing a detailed dark loss analysis through which understanding the impact of the various recombination mechanisms in the different regions of the solar cell [3.51], [3.52]. Indeed, it is a common practice to extrapolate the value of the dark saturation current density J_{01}, representing the first recombination current term in the two-diode equivalent circuit model of the solar cell (see Section 2.3.4), from the simulated *J-V* curve as the *y*-intercept of the linear fitting curve computed in the region where the ideality factor is close to 1 (see Fig. 3.9).

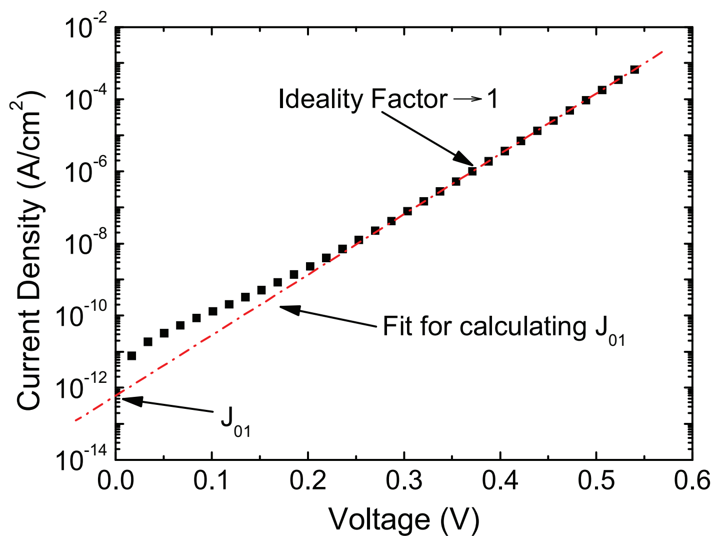

Figure 3.9. Example of extraction of the dark saturation current density J_{01} from a simulated *J-V* curve, as the *y*-intercept of the linear fitting curve computed in the region where the ideality factor is close to 1.

Then, the calculated J_{01} is usually separated into contributions due to different recombination mechanisms (i.e., SRH, Auger, surface recombination at passivated and contacted interfaces), evaluated in the different regions of the simulated device (i.e., emitter, base, BSF). In particular, each recombination current component is computed by integrating the corresponding

recombination rate in a specific region of the device, namely, through a volume integral for the calculation of bulk recombination components, or through a surface integral for the calculation of surface recombination components at interfaces. In this way, it is possible to evaluate what is the dominant recombination component that limits the conversion efficiency of the solar cell.

It is worth noting that, similarly to J_{01}, all the six parameters describing the standard two-diode equivalent circuit model in dark conditions (see Fig. 3.10a) can be extracted from the simulated forward-biased dark *I-V* curve. A typical extraction method uses separate least-squares fitting to three different zones in the *I-V* curve [3.53], as shown in Fig. 3.10b. In the first zone, corresponding to lowest values of current and voltage, the fitting is used to evaluate the shunt resistance (R_{sh}). The middle zone allows to extract the parameters of the second diode (I_{02} and n_2). Finally, the parameters of the first diode (I_{01} and n_1) and the series resistance (R_s) are determined at high voltage and current values.

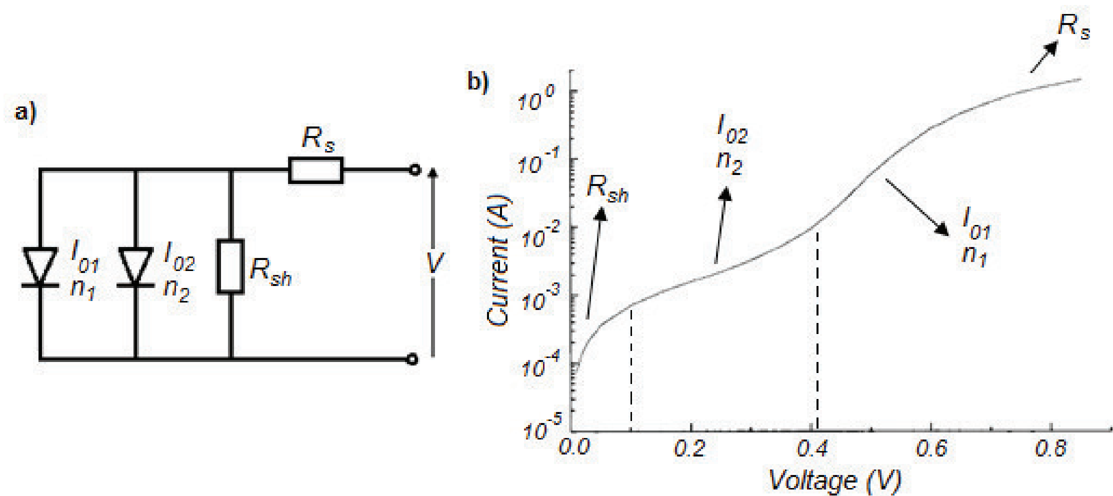

Figure 3.10. a) Equivalent two-diode circuit model of a solar cell in dark conditions. b) Extraction of the six parameters describing the two-diode model from a dark *I-V* curve.

The post-processing also involves the calculation of the optical figures of merit of the solar cell. In particular, according to the definitions given in Section 2.2.5, the computation of the incident photon current density J_{in} (λ), the photogenerated current density J_{ph} (λ), and the short-circuit current density J_{sc} (λ) as a function of the wavelength λ of the radiation (see Fig. 3.11a) is required to create the curves of quantum efficiency (external and internal) and spectral response (see Fig. 3.11b).

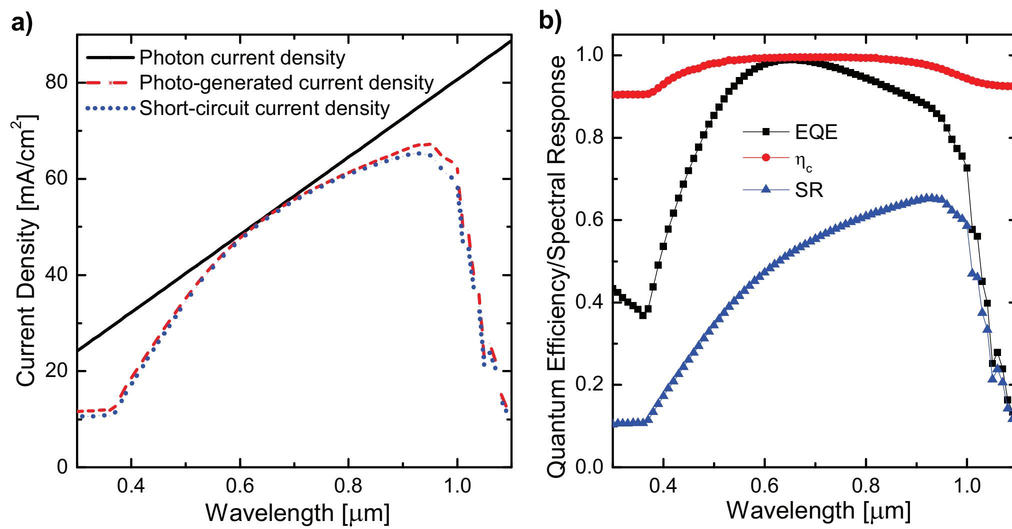

Figure 3.11. Example of simulated a) photon current density, photogenerated current density, and short-circuit current density as a function of the wavelength of the radiation, and of simulated b) external quantum efficiency (*EQE*), collection efficiency (η_c), and spectral response (*SR*) for a conventional silicon solar cell.

3.2.5 Mixed-mode simulation approach

The electro-optical numerical simulation of entire large-area solar cells would require a very large discretization mesh that cannot be handled by state-of-the-art computers. Therefore, as discussed in Section 3.2.1, the device simulation is restricted to a small symmetry element representing an irreducible section of the solar cell. However, it is worth noting that this limited simulation domain cannot model all the losses occurring in the solar cell. In particular, losses arising from the resistance of the front metal grid, and recombination losses at the cell edges cannot be included in the device simulation. Therefore, these losses are typically accounted for by using a mixed-mode simulation approach, based on a combination of device simulations and circuit simulations [3.54]. The flow diagram describing the mixed-mode approach is illustrated in Fig. 3.12. In a first step, the device simulation of a 2-D or 3-D representative portion of the cell is performed (Fig. 3.12a). This simulation takes into account all the losses occurring in the device volume, and at the passivated and contacted interfaces. The simulated *I-V* curve is then tabulated, and used as an input to the circuit simulation. The equivalent circuit of the entire solar cell consists of a distributed resistive network, where repetitive device portions, each modeled as voltage-controlled current sources through the tabulated *I-V* curves, are arranged like “tiles” and connected by ohmic resistances, which represent the front metallization (Fig. 3.12b). It is worth noting that, for symmetry reason, the size of the circuit network to be simulated can be limited to only half of the front metal grid in order to represent the *I-V* characteristics of the entire solar cell [3.1]. In this way, the effects of non-uniformities in the solar cell (Fig. 3.12c), due to the semiconductor regions contacting the busbar, the crystal grains with low lifetimes, the cell edges and corners, or the resistance variation along the metal fingers, can be modeled in the circuit simulation by inserting specific circuital elements at appropriate locations. In particular, it has been demonstrated that losses in the perimeter region of the cell can strongly affect the fill factor [3.55].

It is worth noting that the full-scale modeling of entire solar cells by means of a “tiling” circuit network can induce discretization errors in the simulation, depending on the choice of the boundary conditions of the repetitive simulation domain considered in the device simulation. In particular, these boundary conditions have to be chosen such that the current flows only through the metallization, i.e., the currents within the semiconductor across the boundaries of these simulation domains are negligible. However, this condition is usually fulfilled, because these boundaries are typically chosen considering the symmetry of the device [3.1].

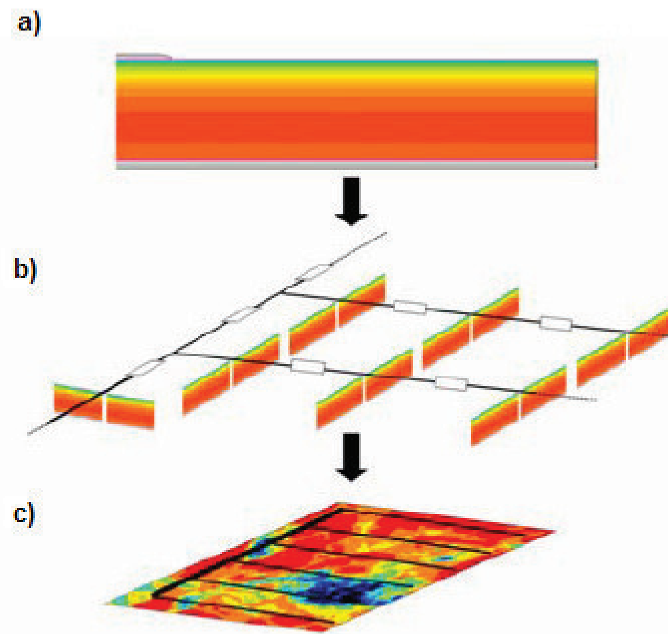

Figure 3.12. Flow diagram of the mixed-mode simulation approach: a) 2-D or 3-D device simulation of a representative portion of the solar cell; b) circuit simulation of a distributed resistive network in order to account for the front metallization and the cell edges; c) analysis of the effects of the non-uniformities in the solar cell. Taken from [3.54].

In this thesis, a simulation methodology based on a mixed-mode simulation approach has been applied in order to investigate the effects of the finger non-uniformities in the front-side metallization on the performance of a *c*-Si solar cell (see Chapter 6).

3.3 Calibration of physical models for silicon solar cells

The results of the device simulations critically depend on physical models implemented in the TCAD simulator that are usually tailored to CMOS devices. Since the behavior of solar cells is significantly different from most of the other electronic devices (e.g., unlike the binary-logic devices, solar cells are strongly influenced by minority carrier densities and recombination losses), an accurate simulation of silicon solar cells requires an ad-hoc refinement of the most relevant physical models, such as those for the intrinsic carrier density, the Auger recombination, the trap-assisted SRH recombination, and the SRH surface recombination at passivated surfaces.

3.3.1 Intrinsic carrier density model

The intrinsic carrier density n_i is a fundamental quantity in semiconductor physics, and it plays a very significant role in the simulation of solar cells in the presence of optical excitation. In particular, n_i strongly influences minority carrier densities and, consequently, the recombination losses which limit the conversion efficiency of solar cells. Therefore, the exact quantification of n_i is of primary importance for the simulation of PV devices.

The intrinsic carrier density for undoped semiconductors depends on the effective densities of states of the conduction and valence bands (N_C and N_V), and on the energy band-gap (E_g), as given by:

$$n_i(T) = \sqrt{N_C(T) N_V(T)}\, exp\left(-\frac{E_g(T)}{2kT}\right) \tag{3.37}$$

The temperature-dependent band-gap can be expressed as:

$$E_g(T) = E_g(0) - \frac{\alpha T^2}{T + \beta} \tag{3.38}$$

where α and β are material-dependent parameters, and $E_g(0)$ represents the band-gap at $T = 0$ K, given by:

$$E_g(0) = E_{g0} + \Delta E_{g0} \tag{3.39}$$

where E_{g0} and ΔE_{g0} depend on the specific band-gap narrowing (BGN) model.

Therefore, the effective band-gap $E_{g,eff}$ results from the band-gap (Eq. 3.38) decreased by the doping-dependent BGN, which occurs in the semiconductor when relatively high dopant concentrations introduce additional states near the edge of the majority carrier band:

$$E_{g,eff}(T) = E_g(T) - E_{bgn} \tag{3.40}$$

where $E_{bgn} = \Delta E_{g0} + \Delta E_{g,Fermi}$ is determined by the selected BGN model in the simulator, and strongly depends on the adopted carrier statistics [3.27], [3.56].

Accordingly, from Eqs. 3.37 and 3.40, the effective intrinsic carrier density $n_{i,eff}$, including the dependence on the doping-dependent BGN, can be expressed as:

$$n_{i,eff}(T) = n_i \, exp\left(\frac{E_{bgn}}{2kT}\right) \tag{3.41}$$

Prior to 1990, the most commonly adopted value for crystalline silicon at $T = 300$ K was $n_i = 1.45\times10^{10}$ cm^{-3}, which led to significant deviations between the measured results and the theoretically predicted results. A value of $n_i = 1.08\times10^{10}$ cm^{-3} was suggested by Green in 1990 [3.57]. Shortly after, Sproul and Green [3.58] measured $n_i = 1.00\times10^{10}$ cm^{-3}, which is still the most widely accepted value of n_i within the silicon community. However, recent investigations [3.56] reinterpreted the Sproul and Green experiment by means of numerical simulations, demonstrating that their measurements were influenced by the band-gap narrowing (BGN), although at relatively low doping densities. This reassessment of the intrinsic carrier density in *c*-Si was based on a quantum-mechanical model for BGN, proposed by Schenk in [3.59]. On the basis of this study, $n_i = 9.65\times10^{9}$ cm^{-3} was obtained for undoped silicon at $T = 300$ K. This value is quite consistent with the experimental value of $n_i = 9.70\times10^{9}$ cm^{-3} obtained by Misiakos and Tsamakis using capacitance measurements [3.60].

Different empirical doping-dependent BGN models, such as Bennett-Wilson [3.61], del Alamo [3.62], [3.63], Slotboom [3.64]-[3.66], and Jain-Roulston [3.67], are typically available in commercial TCAD simulators like Sentaurus [3.27]. However, all these doping-dependent models do not depend on carrier concentrations. It is worth noting that high carrier concentrations, due to optical excitation or high electric field injection, can also cause a BGN effect, known as plasma-induced BGN. Therefore, in order to correctly model this additional BGN effect in PV devices where the optical excitation leads to large carrier injections, in this thesis, the simulations have been carried out by adopting the theoretical BGN model proposed by Schenk [3.59] in combination with Fermi-Dirac statistics. This BGN model was derived

from a finite-temperature full random-phase approximation (RPA), where both carrier-carrier and carrier-dopant interactions were taken into account. In particular, unlike the empirical BGN models, the Schenk model allows to account for the influence of the BGN also at relatively low doping densities ($N_{dop} < 1\times10^{17}$ cm^{-3}).

In Fig. 3.13, the effective intrinsic carrier density accounting for BGN in *p*-type silicon is reported as function of the doping density for different BGN models (Bennett-Wilson, Slotboom, delAlamo, Schenk) available in the TCAD simulator. The default implementation of Bennett and Schenk models provides $n_{i,eff} = 1.075\times10^{10}$ cm^{-3} at very low doping levels, whereas the Slotboom and delAlamo models employ a correction factor, leading to higher values of $n_{i,eff}$ at such doping densities, i.e., 1.180×10^{10} and 1.412×10^{10} cm^{-3}, respectively. Fig. 3.13 also reports the $n_{i,eff}$ values calculated by a revised Schenk BGN model, implemented in a tabular format in the device simulator [3.27], where the band-gap model parameter E_{g0} is adjusted to a slightly larger value in order to achieve an intrinsic carrier concentration of 9.65×10^{9} cm^{-3} at 300 K and low doping density, according to the reassessment of n_i proposed in [3.56]. It is worth noting that a more physically meaningful adjustment of the intrinsic carrier density would require the correction of the effective masses of electron m_e^* and holes m_p^*, which influence in turn the effective densities of states in Eq. 3.37. However, this option could be rather intricate for the holes effective mass m_p^*, considering that there are two degenerate heavy-hole branches and a light split-off branch in the *E-k* relation of the valence band. Therefore, the variation of the band-gap model parameters, even though not fully physically meaningful, is typically more convenient for the calibration of the intrinsic carrier density in TCAD simulators [3.1].

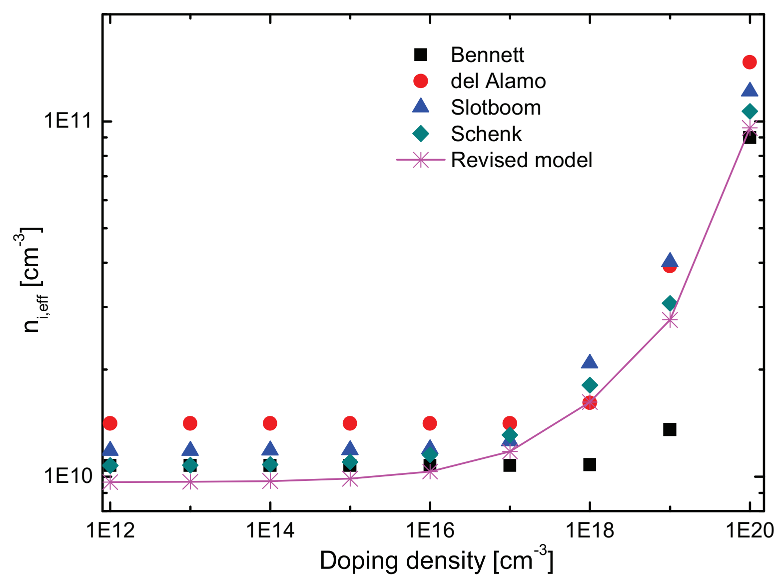

Figure 3.13. Effective intrinsic carrier density versus doping density for different BGN models.

3.3.2 Auger recombination model

The rate of the band-to-band Auger recombination is expressed as:

$$R_{Auger} = \left(np - n_{i,eff}^2\right)\left[C_n(T,n)n + C_p(T,p)p\right] \tag{3.42}$$

where the temperature-dependent Auger coefficients are given by:

$$C_n(T,n) = \left[A_{A,n} + B_{A,n}\left(\frac{T}{T_0}\right) + C_{A,n}\left(\frac{T}{T_0}\right)^2\right]\left[1 + H_n exp\left(-\frac{n}{N_{0,n}}\right)\right] \tag{3.43}$$

$$C_p(T,p) = \left[A_{A,p} + B_{A,p}\left(\frac{T}{T_0}\right) + C_{A,p}\left(\frac{T}{T_0}\right)^2\right]\left[1 + H_p exp\left(-\frac{p}{N_{0,p}}\right)\right] \tag{3.44}$$

where T_0 = 300 K. The default values of the parameters shown in Eqs. 3.43 and 3.44 for silicon are listed in [3.27]. In Eqs. 3.43 and 3.44, the first terms describe the dependence of C_n and C_p on the temperature, while the second terms account for the dependence of C_n and C_p on carrier concentrations. The corresponding minority-carrier lifetimes related to Auger recombination have been already expressed in Eq. 2.80, where C_n and C_p have been assumed as constants. The inverse quadratic dependence of the Auger lifetime on doping density implies that Auger recombination dominates at high dopant densities (typically, above 1×10^{18} cm^{-3}), e.g. in the highly-doped emitters of solar cells.

The Auger coefficients C_n and C_p were already determined in the 1970s by Dziewior and Schmid [3.68] at relatively high dopant densities ($N_{dop} > 1\times10^{18}$ cm^{-3}). At such dopant densities, the measured Auger lifetimes can be well reproduced assuming non-interacting free particles, as shown in Fig. 3.14 for *n*-type silicon (C_n = 2.8×10^{-31} cm$^6\cdot$s^{-1}, as reported by Dziewior and Schmid) [3.69]. This means that, at high N_{dop}, C_n and C_p are assumed to be independent of carrier concentrations and, consequently, the second terms in Eqs. 3.43 and 3.44 are equal to unity.

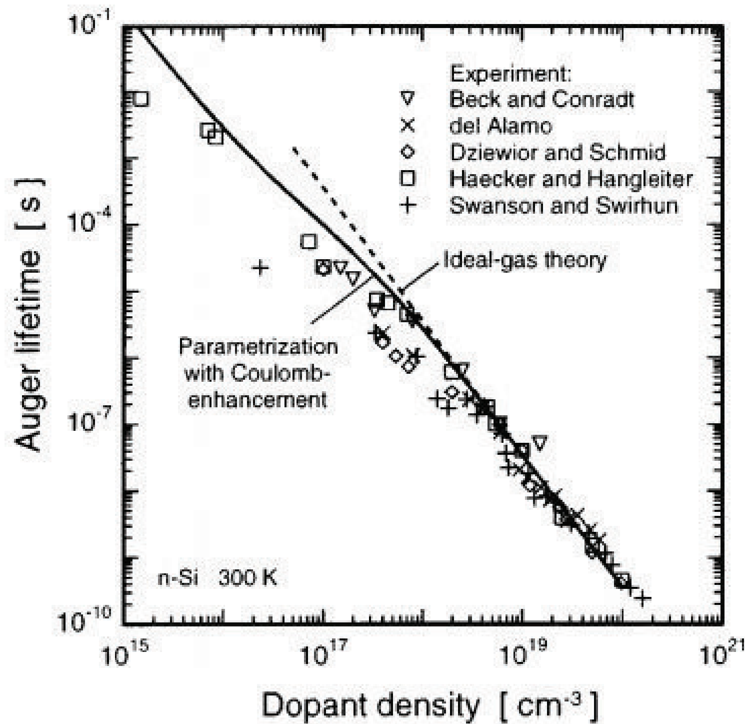

Figure 3.14. Measure Auger lifetimes at low-injection conditions as a function of dopant density in *n*-type silicon. Note that, at Ndop < 1×10^{18} cm^{-3}, the lifetimes are lower than the ideal-gas limit (dashed line) due to Coulomb enhancement. Taken from [3.69].

At lower doping densities ($N_{dop} \leq 1\times10^{18}$ cm^{-3}), the Auger recombination is enhanced by Coulomb interactions between particles [3.69]. This leads to an underestimation of the Auger recombination rate and, accordingly, to an overestimation of the measured Auger lifetime at lower N_{dop} by using Eq. 2.80 with the values of C_n and C_p extracted by Dziewior and Schmid at high dopant densities (see Fig. 3.14). The effect of this Coulomb enhancement on the Auger coefficients is modeled in Eqs. 3.43 and 3.44 through the carrier concentration-dependent second terms, representing the Coulomb enhancement factors, which become larger than unity at lower N_{dop}. This means that the recombination rate in solar cells may also depend on Auger recombination at dopant densities below 10^{18} cm^{-3}, e.g. in the base region. Instead, as stated above, the effect of Coulomb interactions between particles is practically negligible at high N_{dop}. This is due to the "screening" effect [3.1]. Electrons and holes generally attract each other through their Coulomb force. At high carrier density, electron-hole pairs are efficiently screened by the large amount of other electrons and holes. For that reason, at high N_{dop}, electrons and holes can be treated as an ideal gas, independent of dopant density. On the contrary, at lower carrier densities, electron-hole pairs are not sufficiently screened and, therefore, the Coulomb attraction between electrons and holes increases the probability that they recombine.

A few different parameterizations of the Auger recombination model have been proposed in literature taking into account this Coulomb enhancement effect. However, uncertainties still exist especially at low dopant densities and in the transition between low and high-injection

regimes. In particular, a very comprehensive parameterization of Auger recombination in crystalline silicon has been proposed by Kerr and Cuevas in [3.70]. Unfortunately, this widely used parameterization is difficult to implement in numerical device modeling because of its complex polynomial expression [3.1].

In this thesis, the parameterization proposed by Altermatt in [3.1] for Eqs. 3.43 and 3.44 has been adopted. The considered values for the parameters of Eqs. 3.43 and 3.44 are reported in Table 3.1. This parameterization well reproduces the coefficients C_n e C_p extracted by Dziewor and Schmid at high dopant densities, whereas it is rather uncertain at lower dopant densities, probably leading to slightly underestimate the Auger recombination losses in the lowly-doped base region of solar cells. However, it is generally known that the minority-carrier lifetime in the base region of a silicon solar cell is mostly limited by the SRH recombination. Therefore, it is expected that this underestimation of the Auger recombination in the base region influences the simulations only marginally.

Symbol	**Electrons**	**Holes**	**Unit**
A	2.8×10^{-31}	7.91×10^{-32}	$cm^{-6}\cdot s^{-1}$
B	0	-1.239×10^{-32}	$cm^{-6}\cdot s^{-1}$
C	0	3.231×10^{-32}	$cm^{-6}\cdot s^{-1}$
H	8	8	*1*
N_0	2.5×10^{17}	2.5×10^{17}	cm^{-3}

Table 3.1. Adopted set of parameters for Eqs. 3.43 and 3.44.

3.3.3 SRH recombination model

Trap-assisted recombination through allowed energy levels within the forbidden energy gap due to the presence of defects in the semiconductor is described by means of the Shockley-Read-Hall (SRH) theory, whose recombination rate is given by:

$$R_{SRH} = \frac{np - n_{i,eff}^2}{\tau_p \left(n + n_{i,eff} exp\left[\frac{E_{trap}}{kT} \right] \right) + \tau_n \left(p + n_{i,eff} exp\left[-\frac{E_{trap}}{kT} \right] \right)} \tag{3.45}$$

where τ_n and τ_p are the minority-carrier lifetimes for electrons and holes, respectively, and E_{trap} is the difference between the defect level and the intrinsic level. By default, $E_{trap} = 0$ in crystalline silicon. In general, the minority-carrier lifetimes τ_n and τ_p are doping-dependent and temperature-dependent. The doping dependence of the SRH lifetimes is modeled in Sentaurus simulator through the Scharfetter relation [3.27]:

$$\tau_{SRH}\left(N_{dop}\right) = \tau_{min} + \frac{\tau_{max} - \tau_{min}}{1 + \left(\frac{N_{dop}}{N_{ref}} \right)^{\gamma}} \tag{3.46}$$

where N_{dop} is the bulk doping concentration, and τ_{max}, τ_{min}, N_{ref}, and γ are the tuning parameters of the model. The default values for silicon are: $\tau_{min} = 0$ *s*, $\tau_{max} = 10$ µs for electrons and $\tau_{max} = 3$ µs for holes, $N_{ref} = 1\times10^{16}$ cm^{-3}, and $\gamma = 1$ both for electrons and holes. According to Eq. 3.46, the SRH lifetimes decrease with increasing doping concentration.

The temperature dependence is described by a power-law [3.27]:

$$\tau_{SRH}\left(T\right) = \tau_0 \left(\frac{T}{300K} \right)^{\alpha} \tag{3.47}$$

where τ_0 is the SRH lifetime at 300 K, and $\alpha = -1.5$ for silicon by default, thus leading to a decrease of the SRH lifetimes with rising temperature.

In addition to doping and temperature dependences, the SRH lifetime strongly depends on the injection conditions, e.g. in *p*-type silicon $\tau_{SRH} = \Delta n / R_{SRH}$ where Δn is the excess minority-carrier density. In particular, in *p*-type silicon, $\tau_{SRH} = \tau_n$ at low-injection conditions, i.e., only the electrons limit the SRH rate, while at high-injection conditions $\tau_{SRH} = \tau_n + \tau_p$ because electrons

and holes exist in similar densities. Such injection-dependence of τ_{SRH} has not been always considered in lifetime measurements, but it may significantly affect the performance of solar cells [3.1].

Different parameterizations based on the Scharfetter relation for the doping-dependent SRH lifetime have been reported in literature. In silicon solar cells, the SRH mechanism typically dominates the bulk recombination occurring in the lightly-doped base region. Therefore, the bulk lifetime τ_{bulk} can be considered approximately equal to τ_{SRH} and, consequently, doping-dependent. Nevertheless, high-purity boron-doped *p*-type float-zone (*Fz*) silicon materials, free of interstitial oxygen and other contaminations, show no lifetime degradation with increasing doping density [3.1], [3.71]. Hence, in such materials, τ_n and τ_p can be assumed as doping-independent in Eq. 3.45. On the contrary, in boron-doped oxygen-contaminated *p*-type Czochralski (*Cz*) silicon materials, the minority-carrier τ_{SRH} is strongly degraded due to the presence of metastable *Cz*-specific boron-oxygen (B-O) defects, that are activated as recombination centers by carrier injection or illumination. Therefore, this SRH lifetime degradation is particularly important in *Cz*-Si solar cells, where a considerable reduction of conversion efficiency can be observed under illumination. A parameterization of the degraded SRH lifetime in boron-doped *Cz*-Si is reported in [3.54]:

$$\tau_n\,[\mu s] = 4.02024\times 10^{45}\cdot[B_s]^{-0.824}\cdot[O_i]^{-1.748}\cdot m,\quad \tau_p\,[\mu s] = 10\tau_n,\quad E_t\,[eV] = E_C - 0.41 \qquad (3.48)$$

where $[B_s] = N_A$ is the substitutional boron density in cm^{-3}, $[O_i]$ the interstitial oxygen density in cm^{-3}, and m is a processing-dependent improvement factor between 2 and 4. Note that the asymmetric ratio τ_p/τ_n = 10 results in a strongly injection-dependent SRH lifetime. However, this lifetime degradation can be permanently reduced, or even fully reversed, by applying appropriate high-temperature annealing steps (using conventional tube or rapid thermal processes) into the process sequence, thus leading to transform the metastable defects into inactive recombination centers. An empirical fitting of the measured doping-dependent minority-carrier lifetime in boron-doped *Cz*-Si for both states, degraded and non-degraded (or annealed), was reported by Glunz *et al.* in [3.71], where the simple empirical expression used in the PC1D program [3.17] was adopted to describe the doping dependence of the bulk lifetime:

$$\begin{aligned} \tau_{bulk}(N_A) &= \tau_0 && for\ N_A < N_{onset}, \\ \tau_{bulk}(N_A) &= \tau_0\left(\frac{N_A}{N_{onset}}\right)^{\alpha} && for\ N_A > N_{onset} \end{aligned} \qquad (3.49)$$

For the degraded state, the best fitting was achieved by Glunz *et al.* through the following parameter set: τ_0 = 1047 μs, N_{onset} = 1.25×10^{15} cm^{-3}, and α = -1.779. For the non-degraded state, Glunz *et al.* proposed τ_0 = 1136 μs, N_{onset} = 2.97×10^{15} cm^{-3}, and α = -1.407 as best fitting parameters. Moreover, $\tau_n = \tau_p$ can be assumed in the non-degraded state, in agreement with measurements [3.51].

In this thesis, the bulk SRH lifetime in the boron-doped *Cz*-Si base region of the simulated solar cells has been modeled according to the empirical fitting proposed by Glunz *et al.* in [3.71] for the non-degraded state. To this purpose, the parameters of the Scharfetter relation (Eq. 3.46) implemented in Sentaurus for modeling the doping-dependent SRH lifetime have been tuned in order to reproduce the Glunz's empirical fitting [3.19]. Fig. 3.15 reports the bulk SRH lifetime versus boron doping concentration for the empirical fitting suggested by Glunz *et al.* (for both degraded and non-degraded states), and for the default parameterization implemented in Sentaurus. The bulk lifetime curve provided by the revised Scharfetter relation is also reported in Fig. 3.15, highlighting a good agreement with the Glunz's empirical fitting for N_{dop} > 3×10^{15} cm^{-3}.

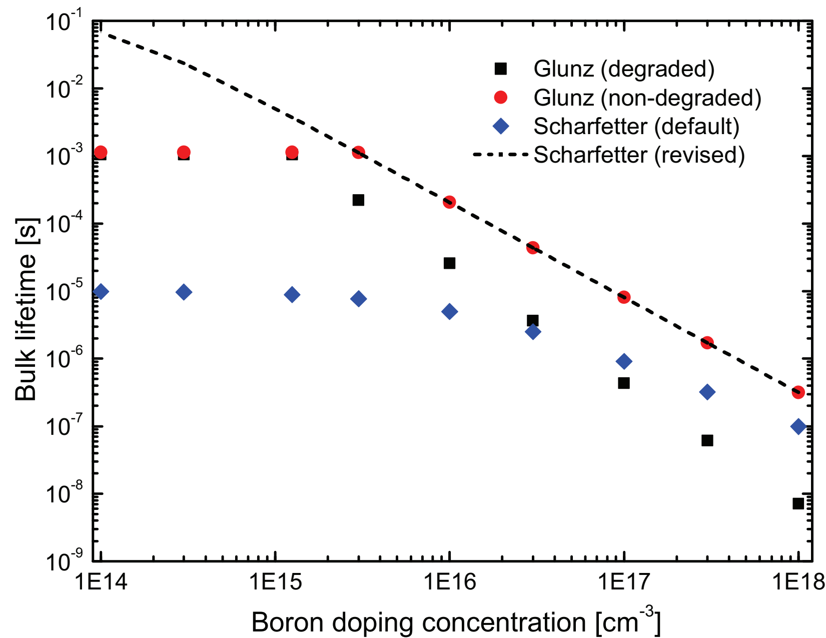

Figure 3.15. SRH bulk lifetime versus boron doping concentration for different SRH recombination models.

Similarly to boron-doped *Cz*-Si, aluminum-doped *p*-type *Cz*-Si shows a degradation of the bulk lifetime due to the SRH recombination, probably caused by the formation of aluminum-oxygen (Al-O) recombination-active defect complexes [3.54]. This leads to an increase of the dark saturation current density in Al-doped *Cz*-materials. A parameterization of the degraded

SRH lifetime as a function of the Al acceptor density N_A has been proposed for simulation purposes by Altermatt *et al.* in [3.54]:

$$\frac{1}{\tau_{SRH}[\mu s]} = 2.8339 \times 10^{-24} \cdot N_A^{1.5048} \cdot f \tag{3.50}$$

where f is a processing-dependent factor, which must be accurately set in order to reproduce the measured dark saturation current density. For Al-doped *Cz*-Si wafers, typically $f = 1$. However, it has been demonstrated that the SRH lifetimes measured in highly Al-doped *p*-type silicon (Al-p^+) regions, such as the Al-alloyed back surface fields (BSF) of industrial-type silicon solar cells fabricated by means of screen-printing and firing of an aluminum paste, are much larger (of about three orders of magnitude) than the lifetimes expected from the extrapolation of the lifetime data measured in Al-doped *Cz*-Si wafers [3.54], [3.72]. As matter of fact, standard Al-p^+ BSFs of solar cells typically show measured $J_{0,BSF}$ values between 600 fA/cm^2 and 900 fA/cm^2, while applying Eq. 3.50 with $f = 1$ to simulations of the Al-BSFs results in far too high $J_{0,BSF}$ values [3.54], [3.72]. Therefore, in order to correctly reproduce the measured values of the dark saturation current density in screen-printed Al-p^+ BSF regions, lower values of the factor f (in the range of 1×10^{-3}-1×10^{-2}) must be used in Eq. 3.50. In this thesis, the doping-dependent SRH lifetime in the screen-printed Al-p^+ BSF of the simulated solar cells has been modeled according to Altermatt's parameterization (Eq. 3.50), where the factor f has been set to reproduce typical measured $J_{0,BSF}$ values. However, it is worth pointing out that a more accurate modeling of the recombination in highly aluminum-doped *Cz*-Si has been recently proposed by Rüdiger *et al.* in [3.73] and [3.74], accounting also for the effect of incomplete ionization of Al acceptor atoms.

3.3.4 Surface SRH recombination model

The surface SRH recombination model at interfaces between two different materials or regions uses a formula similar to that adopted for the bulk SRH recombination, as given by:

$$R_{Surf} = \frac{np - n_{i,eff}^2}{S_p^{-1}\left(n + n_{i,eff} exp\left[\frac{E_{trap}}{kT}\right]\right) + S_n^{-1}\left(p + n_{i,eff} exp\left[-\frac{E_{trap}}{kT}\right]\right)} \qquad (3.51)$$

where S_n and S_p are the minority-carrier surface recombination velocities (SRVs) for electrons and holes, respectively, and E_{trap} is the difference between the defect level and the intrinsic level.

In general, the surface recombination velocities depend on the doping concentration at the surface. In Sentaurus simulator, this doping dependence of SRV is expressed according to [3.27]:

$$S = S_0\left[1 + S_{ref}\left(\frac{N_s}{N_{ref}}\right)^{\gamma}\right] \qquad (3.52)$$

where N_s is the doping concentration at the surface, and S_0, S_{ref}, N_{ref}, γ and E_{trap} are the tuning parameters of the model. By default, in silicon, both for electrons and holes, S_0 is set to 1×10^3 cm/s, S_{ref} to 1×10^{-3}, N_{ref} to 1×10^{16} cm^{-3}, $\gamma = 1$, and $E_{trap} = 0$ eV.

Several parameterizations and experimental data for the doping-dependent SRV have been reported in literature by different authors. Cuevas *et al.* in [3.75] reported experimental data for the minority-carrier SRV of highly-doped *n*-type silicon, i.e., S_p, extracted from photo-conductance decay (PCD) measurements of the emitter saturation current density ($J_{0,e}$) corresponding to different phosphorous diffusions, considering the cases of oxide-passivated, unpassivated and contacted surfaces. They observed that S_p remains essentially constant for unpassivated and for contacted Si surfaces, at about 2×10^5 cm/s and 3×10^6 cm/s, respectively, while, for the passivated case, S_p was found to increase almost linearly with the surface doping concentration for $N_s > 1\times10^{16}$ cm^{-3}. Accordingly, the following simple approximate expression for the doping-dependent SRV at silicon dioxide-passivated surfaces was proposed in [3.75]:

$$S_p \approx 10^{-16} N_s, \qquad for\ N_s > 1\times10^{18}\,cm^{-3} \qquad (3.53)$$

It is worth noting that the extraction of the SRV from the measured $J_{0,e}$ values at different N_s is particularly challenging, because the SRV needs to be separated from losses occurring in the bulk of the emitter by applying theoretical models. Therefore, this extraction procedure is model-dependent. In particular, it strongly depends on the adopted statistics and on the assumed models for the band-gap narrowing, the intrinsic carrier density, the minority-carrier mobility, and lifetime. The parameterization proposed in [3.75] was obtained by assuming the Boltzmann statistics to model the highly-doped *n*-type silicon, thus leading to adopt effective parameters in the applied models in order to compensate for the incorrect statistics, e.g. in the apparent band-gap narrowing model. However, it has been shown that such adjustments can lead to various inconsistencies in the modeling [3.69]. A reassessment of the $J_{0,e}$ measurements made by Cuevas *et al.* was reported by Altermatt *et al.* in [3.69], by using the Fermi-Dirac statistics and improved physical models and parameters for recombination mechanisms, mobility and BGN (in particular, the quantum-mechanical BGN model developed by Schenk [3.59] was adopted). Thereby, a more rigorous parameterization for the doping-dependent SRV of n^+-emitters was extracted from the considered $J_{0,e}$ measurements:

$$S_p = S_{p1}\left(\frac{N_s}{N_{p1}}\right)^{\gamma_{p1}} + S_{p2}\left(\frac{N_s}{N_{p2}}\right)^{\gamma_{p2}} \tag{3.54}$$

According to Eq. 3.54, Altermatt *et al.* show that SRV increases more gradually at low than at high surface doping concentrations, unlike the linear increase suggested by Eq. 3.53. The values of the parameters in Eq. 3.54 for several experimental data set corresponding to different surface passivation conditions are given in Table I of [3.69]. In particular, for silicon nitride (SiN_x) passivated n^+-silicon planar surfaces, S_{p1} = 1700 cm/s, $N_{p1} = 1\times10^{19}$ cm^{-3}, γ_{p1} = 0.565, S_{p2} = 5 cm/s, $N_{p2} = 1\times10^{19}$ cm^{-3}, and γ_{p2} = 4.

A similar parameterization for the doping-dependent SRV at SiN_x-passivated n^+-silicon surfaces has been proposed more recently by Kimmerle *et al.* in [3.76]. This parameterization has been extracted from $J_{0,e}$ measurements of highly phosphorous-doped emitters by means of an analytical model, assuming also an Auger-limited lifetime in the bulk of the emitter and a dependence of the SRV on the chemical phosphorus concentration at the surface. In fact, the calculated SRVs show a power-law dependence on the chemical phosphorous surface concentration $N_{s,chem}$, as given by:

$$S_p = S_{p0}\left(\frac{N_{s,chem}}{10^{19}\,cm^{-3}}\right)^{\gamma} \tag{3.55}$$

where S_{p0} = (47 ± 12)×10^{2} cm/s, and γ = 0.99 ± 0.06. Note that Eq. 3.55 is similar to Eq. 3.54, where the first term has been neglected by Kimmerle *et al.* because they evaluated data only for $N_s > 4\times10^{19}$ cm^{-3}.

In this thesis, according to the applied model for BGN (already discussed in Section 3.3.1) and to the adoption of the Fermi-Dirac statistics, the doping-dependent SRV at SiN_x-passivated n^+-silicon surfaces has been modeled through the parameterization proposed by Kimmerle *et al.* in [3.76]. In Fig. 3.16, the SRVs at SiN_x-passivated n^+-silicon surfaces are reported as function of the surface doping concentration for the parameterizations provided by Altermatt *et al.* (according to Eq. 3.54) and Kimmerle *et al* (according to Eq. 3.55), and for the default parameterization implemented in Sentaurus (see Eq. 3.52). It is worth noting that Kimmerle's parameterization is plotted only for $N_s > 4\times10^{19}$ cm^{-3}. As shown in Fig. 3.16, the default parameterization leads to strongly underestimate the SRV at high surface doping concentrations (above 1×10^{20} cm^{-3}) as compared to the other proposed parameterizations. According to Eq. 3.54, Altermatt's parameterization shows a quick increase of the SRV for $N_s > 5\times10^{19}$ cm^{-3}. On the contrary, Kimmerle's parameterization shows a less steep increase, thus leading to obtain lower values of SRV for $N_s > 1\times10^{20}$ cm^{-3} as compared to those provided by Altermatt. This is mainly due to the additional firing step applied in the experiments made by Kimmerle *et al.*, thus allowing a better hydrogen passivation of the surfaces [3.76].

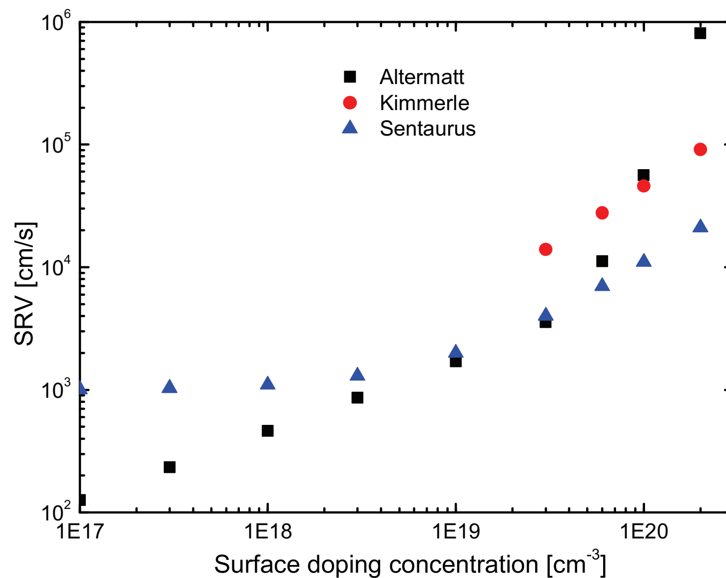

Figure 3.16. Surface recombination velocity versus surface doping concentration at SiN_x-passivated n^+-silicon surfaces for different SRV models.

It is worth pointing out that both the considered parameterizations have been extracted for planar surfaces and, consequently, need to be modified for representing textured surfaces. Indeed, it has been clearly demonstrated in [3.69] that textured surfaces cause larger surface

recombination velocities, as shown in Fig. 3.17. This increase can be partially attributed to the larger surface area of textured surfaces as compared to planar surfaces. In addition, the texturing process increases the defect density on the surface of a textured wafer. The electrical device simulations performed in this work do not take into account the surface texturing. Therefore, it is expected that the update of the SRV model for representing textured surfaces may lead to a decrease of the performance of the simulated devices, due to an increase of the surface recombination losses.

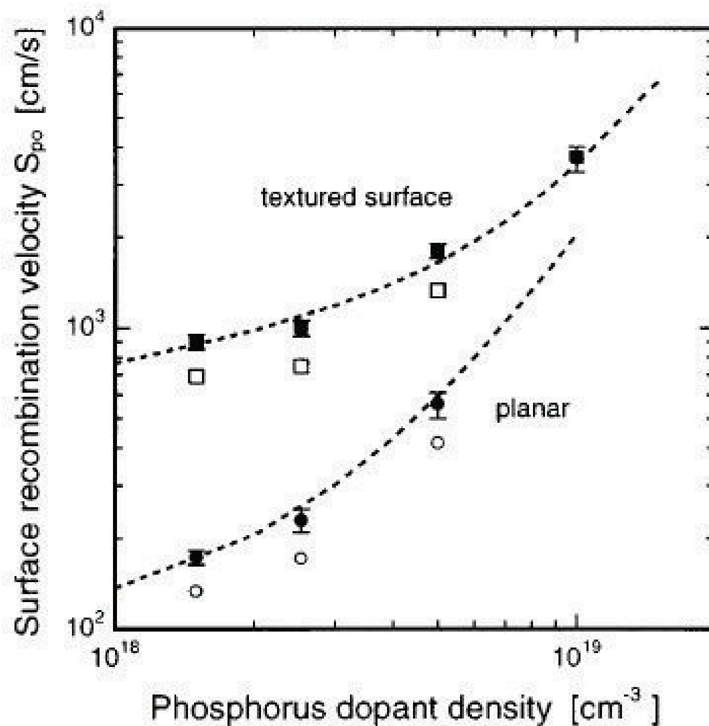

Figure 3.17. Surface recombination velocity versus surface doping density at passivated n^+-silicon planar and textured surfaces. Taken from [3.69].

References

[3.1] P. P. Altermatt, “Models for numerical device simulations of crystalline silicon solar cells – a review”, *Journal of Computational Electronics*, Vol. 10, No. 3, pp. 314-330, 2011.

[3.2] H. Gummel, “A Self-Consistent Iterative Scheme for One-Dimensional Steady State Transistor Calculations”, *IEEE Transactions on Electron Devices*, Vol. 11, pp. 455-465, 1964.

[3.3] D. Scharfetter and H. Gummel, “Large-Signal Analysis of a Silicon Read Diode Oscillator”, *IEEE Transactions on Electron Devices*, Vol. 16, No. 10, pp. 64-77, 1969.

[3.4] E. D. Graham and J. R. Hauser, “Effects of base doping and width on the J-V characteristics of the n^+–n–p^+ structure”, *Solid-State Electronics*, Vol. 15, No. 3, pp. 303-310, 1972.

[3.5] J. R. Hauser and P. M. Dunbar, “Performance limitations of silicon solar cells”, *IEEE Transactions on Electron Devices*, Vol. 24, No. 4, pp. 305-321, 1977.

[3.6] C. R. Fang and J. R. Hauser, “Comparison of theoretical and experimental solar cell performance”, *Proc. of 13th IEEE Photovoltaic Specialists Conference* (*PVSC*), pp. 1318-1326, 1978.

[3.7] M. S. Lundstrom, “Numerical Analysis of Silicon Solar Cells”, *Ph.D. Thesis*, School of Electrical Engineering, Purdue University, Indiana, USA, 1980.

[3.8] J. L. Gray, “Two-Dimensional Modeling of Silicon Solar Cells”, *Ph.D. Thesis*, School of Electrical Engineering, Purdue University, Indiana, USA, 1982.

[3.9] J. L. Gray, “A computer model for the simulation of thin-film silicon-hydrogenalloy solar cells”, *IEEE Transactions on Electron Devices*, Vol. 36, pp. 906-912, 1989.

[3.10] P. D. DeMoulin and M. S. Lundstrom, “Projections of GaAs solar-cell performance limits based on two-dimensional numerical simulation”, *IEEE Transactions on Electron Devices*, Vol. 36, pp. 897-905, 1989.

[3.11] P. A. Basore, D. T. Rover, A. W. Smith, “PC-1D version 2: enhanced numerical solar cell modeling”, *Proc. of 20th IEEE Photovoltaic Specialists Conference* (*PVSC*), pp. 389-396, 1988.

[3.12] P. A. Basore, “Numerical Modeling of Textured Silicon Solar Cells using PC-1D”, *IEEE Transaction on Electron Devices*, Vol. 37, No. 2, pp. 337-343, 1990.

[3.13] J. K. Arch et al., “Computer analysis of the role of *p*-layer quality, thickness, transport mechanisms, and contact barrier height in the performance of hydrogenated amorphous silicon *p-i-n* solar cells”, *Journal of Applied Physiscs*, Vol. 69, No. 10, pp. 7057-7066, 1991.

[3.14] J. L. Gray, “A General Purpose Numerical Device Simulator for Modeling Solar Cells in One-, Two-, and Three-Dimension”, *Proc. of 22nd IEEE Photovoltaic Specialists Conference* (*PVSC*), pp. 436-438, 1991.

[3.15] P. A. Basore, “PC-1D version 3: Improved speed and convergence”, *Proc. of 22nd IEEE Photovoltaic Specialists Conference* (*PVSC*), pp. 299-302, 1991.

[3.16] P. A. Basore, “PC1D version 4 for Windows: from analysis to design”, *Proc. of 25th IEEE Photovoltaic Specialists Conference* (*PVSC*), pp. 377-381, 1996.

[3.17] D. A. Clugston and P. A. Basore, “PC1D version 5: 32-bit solar cell modeling on personal computers”, *Proc. of 26th IEEE Photovoltaic Specialists Conference* (*PVSC*), pp. 207-210, 1997.

[3.18] P. A. Basore and K. Cabanas-Holmen, “PC2D: A Circular-Reference Spreadsheet Solar Cell Device Simulator”, *IEEE Journal of Photovoltaics*, Vol. 1, No. 1, pp. 72-77, 2011.

[3.19] R. De Rose, M. Zanuccoli, P. Magnone, E. Sangiorgi, C. Fiegna, “Open Issues for the Numerical Simulation of Silicon Solar Cells”, *Proc. of 12th International Conference on Ultimate Integration on Silicon* (*ULIS*), pp. 1-4, 2011.

[3.20] G. Heiser, C. Pommerell, J. Weis, W. Fichtner, “Three-dimensional numerical semiconductor device simulation: algorithms, architectures, results”, *IEEE Transaction on Computer-Aided Design of Integrated Circuits and Systems*, Vol. 10, No. 10, pp. 1218-1230, 1991.

[3.21] S. Müller, K. Kells, W. Fichtner, “Automatic rectangle-based adaptive mesh generation without obtuse angles”, *IEEE Transaction on Computer-Aided Design of Integrated Circuits and Systems*, Vol. 11, No. 7, pp. 855-863, 1992.

[3.22] A. G. Aberle et al., "Two-dimensional minority carrier flow in high-efficiency silicon solar cells at short-circuit, open-circuit and maximum power point operating conditions", *Solar Energy Materials and Solar Cells*, Vol. 34, No. 1-4, pp. 149-160, 1994.
[3.23] J. Zhao et al., "Twenty-four percent efficient silicon solar cells with double layer antireflection coatings and reduced resistance loss", *Solar Energy Materials and Solar Cells*, Vol. 66, No. 26, pp. 3636-3638, 1995.
[3.24] Sentaurus, Synopsys, Mountain View, CA.
[3.25] Atlas, Silvaco, Santa Clara, CA.
[3.26] MicroTec, Siborg Systems, Waterloo, Canada.
[3.27] Sentaurus Device User Guide, Synopsys, Mountain View, CA.
[3.28] S. Selberherr, "Analysis and simulation of semiconductor devices", *Springer-Verlag*, 1984.
[3.29] J. F. Bürgler, "Discretisation and grid adaption in semiconductor device modeling", *PhD thesis*, ETH-Zürich, 1990.
[3.30] G. Heiser, "Design and implementation of a three-dimensional general purpose device simulator", *PhD thesis*, ETH-Zürich, 1991.
[3.31] R. E. Bank and D. J. Rose, "Global approximate Newton methods", *Numerische Mathematik*, Vol. 37, No. 2, pp. 279-295, 1981.
[3.32] Sentaurus Structure Editor User Guide, Synopsys, Mountain View, CA.
[3.33] Mesh Generation Tools User Guide, Synopsys, Mountain View, CA.
[3.34] Inspect User Guide, Synopsys, Mountain View, CA.
[3.35] Sentaurus Workbench User Guide, Synopsys, Mountain View, CA.
[3.36] K. K. Sharma, "OPTICS: Principles and Applications", *Academic Press*, *Elsevier*, 2006.
[3.37] A. W. Smith, A. Rohatgi, S. C. Neel, "Texture: a ray tracing program for the photovoltaic community", *Proc. of 21st IEEE Photovoltaic Specialists Conference* (*PVSC*), pp. 426-431, 1990.
[3.38] R. Brendel, "Sunrays: A versatile ray tracing program for the photovoltaic community", *Proc. of 12th European Photovoltaic Solar Energy Conference* (*EU PVSEC*), pp. 1339-1342, 1994.
[3.39] J. Schumacher, S. Sterk, B. Wagner, W. Warta, "Quantum efficiency analysis of high efficiency solar cells with textured surfaces", *Proc. of 13th European Photovoltaic Solar Energy Conference* (*EU PVSEC*), pp. 96-99, 1995.
[3.40] C. Zechner et al., " Two- and three-dimensional optical carrier generation determination in crystalline silicon solar cells.", *Solar Energy Materials and Solar Cells*, Vol. 51, No. 3-4, pp. 255-267, 1998.
[3.41] J. E. Cotter, "RaySim 6.0: a free geometrical ray tracing program for silicon solar cells", *Proc. of 31st IEEE Photovoltaic Specialists Conference* (*PVSC*), pp. 1165-1168, 2005.
[3.42] H. Holst, P. P. Altermatt, R. Brendel, "DAIDALOS: A Plug-in Based Framework for Extendable Ray Tracing", *Proc. of 25th European Photovoltaic Solar Energy Conference* (*EU PVSEC*), pp. 2150-2153, 2010.
[3.43] K. S. Kunz and R. J.Luebbers, "The Finite Difference Time Domain Method for Electromagnetics" *CRC-Press*, 1993.
[3.44] M. G. Moharam and T. K. Gaylord, "Rigorous coupled-wave analysis of planar-grating diffraction", *Journal of the Optical Society of America*, Vol. 71, No. 7, pp. 811-818, 1981.
[3.45] P. Lalanne and E. Silberstein, "Fourier-modal methods applied to waveguide computational problems", *Optics Letters*, Vol. 25, No. 15, pp. 1092-1094, 2000.
[3.46] M. Agrawal et al., "Comprehensive experimental and numerical optimization of surface morphology of transparent conductive oxide films for tandem thin film photovoltaic cells", *Proc. of 35th IEEE Photovoltaic Specialists Conference* (*PVSC*), pp. 301-304, 2010.
[3.47] M. Zanuccoli, "Advanced Numerical Simulation of Silicon-Based Solar Cells", *PhD dissertation*, ARCES – University of Bologna, 2012.

[3.48] J. J. Hench and Z. Strakos, “The RCWA method – A case study with open questions and perspectives of algebraic computations”, *Electronic Transactions on Numerical Analysis*, Vol. 31, pp. 331-357, 2008.
[3.49] M. Agrawal, “Photonic Design for Efficient Solid State Energy Conversion”, *PhD dissertation*, Stanford University, CA, USA, 2008.
[3.50] I. Semenikhin et al., “Efficient implementation of the Fourier modal method (RCWA) for the optical simulation of optoelectronics devices”, *Proc. of 14th International Workshop on Computational Electronics* (*IWCE*), pp. 1-4, 2010.
[3.51] S. Steingrube et al., “Loss analysis and improvements of industrially fabricated Cz-Si solar cells by means of process and device simulations”, *Energy Procedia*, Vol. 8, pp. 263-268, 2011.
[3.52] C. Allebé et al., “Large-Area PERC Cells with a Ti-Cu Based Metallization Leading to Efficiencies Above 19.5%”, *Proc. of 26th European Photovoltaic Solar Energy Conference* (*EU PVSEC*), pp. 2276-2279, 2011.
[3.53] M. Haouari-Merbah, M. Belhamel, I. Tobias, J. M. Ruiz, “Method of extraction and analysis of solar cell parameters from the dark current-voltage curve”, *Proc. of Spanish Conference on Electron Devices*, pp. 275-277, 2005.
[3.54] P. P. Altermatt et al., “Highly Predictive Modelling of Entire Si Solar Cells for Industrial Applications”, *Proc. of 24th European Photovoltaic Solar Energy Conference* (*EU PVSEC*), pp. 901-906, 2009.
[3.55] P. P. Altermatt et al., “Spatially resolved analysis and minimization of resistive losses in high-efficiency Si solar cells”, *Progress in Photovoltaics: Research and Applications*, Vol. 4, No. 6, pp. 399-414, 1996.
[3.56] P. P. Altermatt et al., “Reassessment of the intrinsic carrier density in crystalline silicon in view of band-gap narrowing”, *Journal of Applied Physiscs*, Vol. 93, No. 3, pp. 1598-1604, 2003.
[3.57] M. A. Green., “Intrinsic carrier concentration, effective densities of states and effective mass in silicon”, *Journal of Applied Physiscs*, Vol. 67, No. 6, pp. 2944-2954, 1990.
[3.58] A. B. Sproul and M. A. Green., “Improved value for the silicon intrinsic carrier concentration from 275 to 375 K”, *Journal of Applied Physiscs*, Vol. 70, No. 2, pp. 846-854, 1991.
[3.59] A. Schenk, “Finite-temperature full random-phase approximation model of band gap narrowing for silicon device simulation”, *Journal of Applied Physiscs*, Vol. 84, No. 7, pp. 3684-3695, 1998.
[3.60] K. Misiakos and D. Tsamakis, “Accurate measurements of the silicon intrinsic carrier density from 78 to 340 K”, *Journal of Applied Physiscs*, Vol. 74, No. 5, pp. 3293-3297, 1993.
[3.61] H. S. Bennett and C. L. Wilson, “Statistical comparisons of data on band-gap narrowing in heavily doped silicon: Electrical and optical measurements,” *Journal of Applied Physics*, Vol. 55, No. 10, pp. 3582-3587, 1984.
[3.62] J. del Alamo, S. Swirhun, R. M. Swanson, “Simultaneous Measurement of Hole Lifetime, Hole Mobility and Bandgap Narrowing in Heavily Doped n-Type Silicon,” *International Electron Devices Meeting (IEDM) Technical Digest*, pp. 290–293, 1985.
[3.63] J. A. del Alamo and R. M. Swanson, “Measurement of Steady-State Minority-Carrier Transport Parameters in Heavily Doped n-Type Silicon,” *IEEE Transactions on Electron Devices*, Vol. 34, No. 7, pp. 1580-1589, 1987.
[3.64] J. W. Slotboom and H. C. de Graaff, “Measurements of Bandgap Narrowing in Si Bipolar Transistors,” *Solid-State Electronics*, Vol. 19, No. 10, pp. 857-862, 1976.
[3.65] J. W. Slotboom and H. C. de Graaff, “Bandgap Narrowing in Silicon Bipolar Transistors,” *IEEE Transactions on Electron Devices*, Vol. 24, No. 8, pp. 1123-1125, 1977.
[3.66] D. B. M. Klaassen, J. W. Slotboom and H. C. de Graaff, “Unified Apparent Bandgap Narrowing in n- and p-Type Silicon,” *Solid-State Electronics*, Vol. 35, No. 2, pp. 125-129, 1992.
[3.67] S. C. Jain and D. J. Roulston, “A Simple Expression for Band Gap Narrowing (BGN) in Heavily Doped Si, Ge, GaAs and GexSi1-x Strained Layers,” *Solid-State Electronics*, Vol. 34, No. 5, pp. 453-465, 1991.

[3.68] J. Dziewor and W. Schmid, "Auger coefficients for highly doped and highly excited silicon", *Applied Physiscs Letters*, Vol. 31, No. 5, pp. 346-348, 1977.
[3.69] P. P. Altermatt et al., "Numerical modeling of highly doped Si:P emitters based on Fermi-Dirac statistics and self-consistent material parameters", *Journal of Applied Physiscs*, Vol. 92, No. 6, pp. 3187-3197, 2002.
[3.70] M. J. Kerr and A. Cuevas, "General parameterization of Auger recombination in crystalline silicon", *Journal of Applied Physiscs*, Vol. 91, No. 4, pp. 2473-2480, 2002.
[3.71] S. W. Glunz et al., "Minority carrier lifetime degradation in boron-doped Czochralski silicon", *Journal of Applied Physiscs*, Vol. 90, No. 5, pp. 2397-2404, 2001.
[3.72] J. Schmidt et al., "Recombination lifetimes in highly aluminum-doped silicon", *Journal of Applied Physiscs*, Vol. 106, No. 9, pp. 93707-4, 2009.
[3.73] M. Rüdiger et al., "Effect of incomplete ionization for the description of highly aluminum-doped silicon", *Journal of Applied Physiscs*, Vol. 110, No. 2, pp. 24508-7, 2011.
[3.74] M. Rüdiger et al., "Accurate modeling of aluminum-doped silicon", *Energy Procedia*, Vol. 8, pp. 527-532, 2011.
[3.75] A. Cuevas et al., "Surface recombination velocity of highly doped n-type silicon", *Journal of Applied Physiscs*, Vol. 80, No. 6, pp. 3370-3375, 1996.
[3.76] A. Kimmerle et al., "Modelling carrier recombination in highly phosphorus-doped industrial emitters", *Energy Procedia*, Vol. 8, pp. 275-281, 2011.

Chapter 4

Simulation of Conventional Silicon Solar Cells

Conventional screen-printed *c*-Si solar cells, first developed in the 1970's, represent the best established and most mature solar cell manufacturing technology for terrestrial use. Moreover, these cells are currently produced on a large scale with well over 50% PV market share. This is mainly due to the their relatively high conversion efficiencies and quite simple manufacturing process, leading to much lower production costs as compared to more innovative solar cell technologies.

A state-of the-art industrial screen-printed silicon solar cell is simply based on a n^+-p-p^+ structure (see Fig. 4.1a) featuring a thick (150-220 μm) boron-doped *p*-type substrate with a shallow homogeneously phosphorous-doped front-side n^+-emitter, and a full-area Al-alloyed p^+-BSF (back-surface field). The front metallization consists of a conventional H-pattern contact grid (see Fig. 4.1b), while the rear-side is fully covered by the back contact. Moreover, the non-metallized front surface is covered with a thin anti-reflective coating (ARC) layer. The typical solar cell processing sequence consists of: saw damage removal from the starting *p*-type wafer by wet chemical etching; chemical texturing of the top surface; junction formation by phosphorous ($POCl_3$) diffusion; edge junction isolation by plasma etching; deposition of the front ARC silicon nitride (SiN_x) layer by PECVD (Plasma Enhanced Chemical Vapor Deposition); screen-printing of the front silver (Ag) metal paste through a suitable H-patterned screen, and of the full-area rear aluminum (Al) metal paste; drying and firing of the metal contacts with the formation of an Al-alloyed p^+-BSF at rear side.

This chapter deals with the analysis of conventional screen-printed *c*-Si solar cells by means of 2-D numerical electro-optical TCAD-based simulations. The geometrical and physical details of the simulated solar cells, the adopted physical models, and the simulation methodology are first explained, according to what already discussed in Chapter 3. Then, the simulation results of conventional screen-printed *c-Si* solar cells are reported. Finally, the impact of improved front metallization architectures due to double screen-printing technology is investigated by means of numerical simulations.

4.1 Simulation setup

The structure of a 2-busbar 12.5×12.5 cm^2 conventional screen-printed *c*-Si solar cell (see Fig. 4.1) featuring a full-area back contact is highly symmetric. Therefore, the simulation domain can be limited to only a two-dimensional (2-D) representative portion of the cell, which is half of the 2-D symmetry element shown in Fig. 4.1a, consisting of a cross-section perpendicular to the front metallization grid. Accordingly, the 2-D simulation domain has a lateral size equal to the half of the front contact pitch (W_{sub}), i.e., the distance between two adjacent front contact fingers, thus extending horizontally from the middle of the front contact finger to the midpoint between two front contact fingers, while the height of the simulated structure is equal to the cell thickness (D_{sub}). It is worth noting that the 2-D approach allows to account for the shadowing losses underneath the front metallization, and to distinguish the front-side passivated and metallized areas. Moreover, the effect of the lateral carrier transport inside the emitter region and the current crowding at front contacts can be accurately modeled through a 2-D simulation.

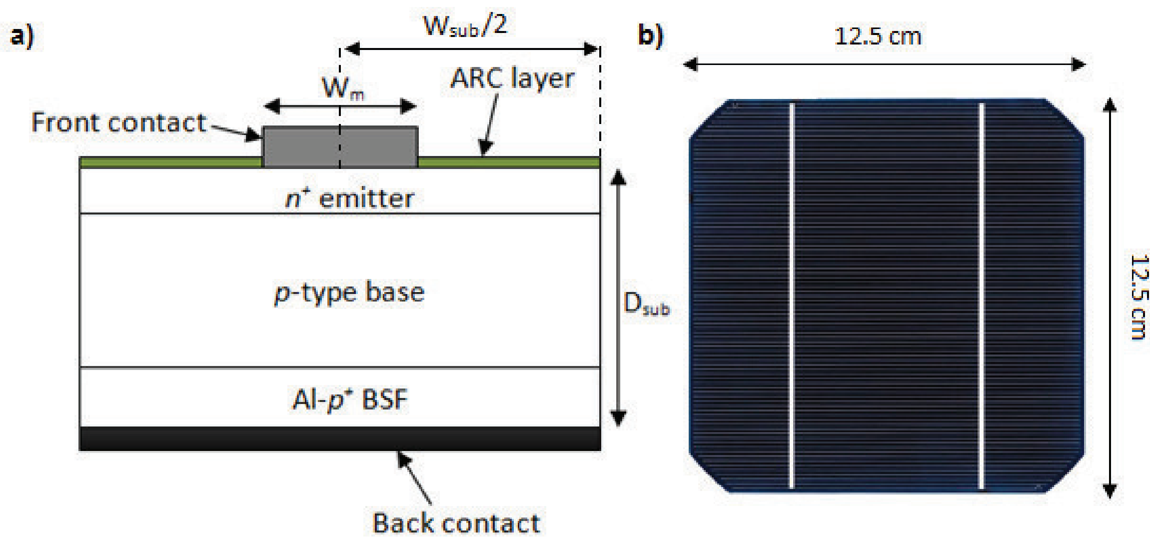

Figure 4.1. a) 2-D cross-section of a typical conventional screen-printed *c*-Si solar cell. b) Top view of the front metallization featuring a H-pattern contact grid.

4.1.1 Device structure and mesh

A 2-D planar *c*-Si homogeneous emitter (HE) solar cell (according to Fig. 4.1a) has been simulated with the following characteristics: a 1.5 Ω·cm (N_{sub} = 10^{16} cm^{-3}), 180-µm-thick boron-doped *p*-type substrate with a full-area metallized aluminum-alloyed back-surface field (Al-p^+ BSF) modeled with a typical industrial 10-µm-deep doping profile (see Fig. 4.2a) [4.1]; a front surface covered with a 70-nm-thick silicon nitride (SiN_x) anti-reflective coating (ARC) layer; a silver front finger with a width (W_m) of 100 µm.

In order to reproduce the typical "kink-and-tail" shape of the experimental phosphorous-doped ($POCl_3$) emitter profiles in silicon solar cells [4.2], [4.3], the simulated HE doping profile has been modeled by an analytical double error function (i.e., two error function-like curves with different peak position and depth) with a peak (chemical) phosphorous surface concentration (C_{peak}) of 4×10^{20} cm^{-3} and a junction depth (J_{depth}) of 0.35 µm (see Fig. 4.2b). Furthermore, a cut-off at an activation limit of ~2×10^{20} cm^{-3} [4.4] has been taken into account in order to calculate the electrically active concentration profile from the generated doping profile, as shown in Fig. 4.2b, assuming also full dopant ionization below the activation limit and, therefore, neglecting shifts between the carrier and the dopant profiles [4.5]. Accordingly, the corresponding emitter sheet resistance (R_{sq}), extracted from the electrically active profile of the simulated HE solar cell, is equal to 75 Ω/sq.

Moreover, in order to achieve a good accuracy in the simulations, several accurate mesh refinements have been performed:

- along the horizontal axis in the region underneath the front contact finger, in order to account for the shadowing effect;
- along the vertical axis at the top of the structure, in order to properly resolve the optical generation rate within a few nanometers of the cell;
- along the vertical axis in the regions adjacent to the junctions at the top and bottom of the cell, in order to accurately reproduce the doping gradient in the vertical direction;
- along the horizontal and vertical axes in the region around the front contact finger, in order to account for the current crowding.

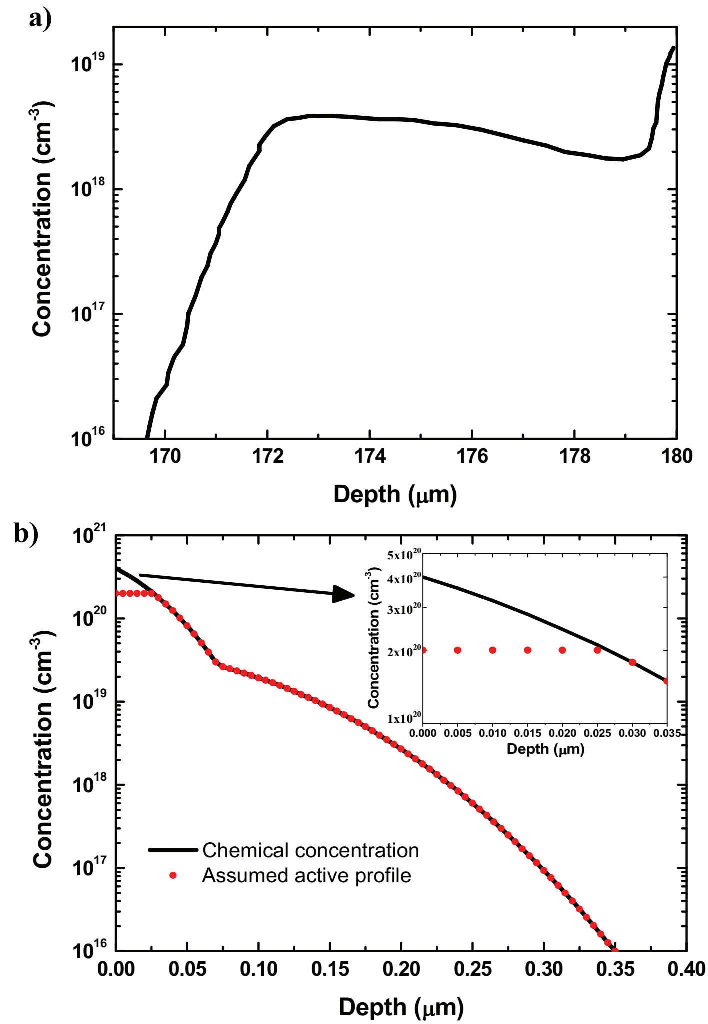

Figure 4.2. a) Typical industrial 10-μm-deep Al-p^+ BSF doping profile. b) Analytical double error function-like phosphorus concentration profile, and calculated electrically active concentration profile for the simulated 75-Ω/sq HE cell. The active profile has been obtained assuming the cut-off at an activation limit of ~$2x10^{20}$ cm^{-3}, and neglecting shifts between the carrier and the dopant profile below the activation limit.

4.1.2 Electro-optical simulation

The optical simulation of *c*-Si solar cells provides to the electrical simulator implemented in the TCAD Sentaurus suite [4.6] the 2-D map of the optical generation rate inside the solar cell (see Fig. 4.3a), taking into account an ideal shadowing under front metal fingers. In particular, the optical generation profile (see Fig. 4.3b) has been calculated with a mono-dimensional simulation of plane-waves propagation in silicon, assuming direct illumination with a standard AM1.5G spectrum (1000 W/m^2), and a random pyramids-textured SiN_x-passivated front surface. Then, the TCAD electrical simulator uses the calculated optical generation rate to compute the light *J-V* characteristics of the illuminated solar cell by ramping the bias voltage.

In order to achieve realistic predictions on *c*-Si solar cell performance, an ad-hoc calibration of the physical models and parameters implemented in the TCAD simulator has been performed, as already discussed in Section 3.3. These fine-tuned models include the band-gap narrowing (BGN) model proposed by Schenk to account for the effective intrinsic carrier density [4.7], the Auger recombination model with the parameterization adopted by Altermatt in [4.8], the mobility model proposed by Klaassen [4.9], [4.10], and the bulk Shockley-Read-Hall (SRH) lifetime model in boron-doped *Cz*-Si according to Glunz's empirical fitting in [4.11], and in Al-p^+ *Cz*-Si according to Altermatt's parameterization [4.1]. The band-gap model parameters have been adjusted to achieve an intrinsic carrier density of 9.65×10^9 cm^{-3} at 300 K and low doping density [4.12]. According to the adopted SRH lifetime model in the boron-doped *Cz*-Si base [4.11], the bulk minority-carrier lifetime has been set to about 206 µs for the considered substrate doping. Fermi-Dirac statistics has been implemented to adequately model the highly-doped regions, such as the emitter and the BSF regions. According to the applied model for BGN and to Fermi-Dirac statistics, the parameterization proposed by Kimmerle *et al.* in [4.5] for the surface recombination velocity (SRV) at SiN_x-passivated front surfaces has been adopted, thus assuming an Auger-limited lifetime in the bulk of the emitter, and a chemical phosphorus surface concentration dependence for the SRV. Finally, the SRV at the metallized surfaces has been set to 10^6 cm/s. The main geometrical and physical parameters of the simulated HE solar cell are summarized in Table 4.1.

It is worth noting that, unlike the optical simulation, the electrical simulation does not account for the surface texturing because the simulated devices feature planar front surfaces. Moreover, some of the adopted models, as the SRV model, have been extracted for planar surfaces, as already explained in Section 3.3.4. Therefore, it is expected that the implementation of the texturing in the electrical simulations, and the corresponding update of the physical models for representing textured surfaces, may lead to a decrease of the performance of the simulated devices, mainly due to an increase of the surface recombination losses and to an increased emitter resistance.

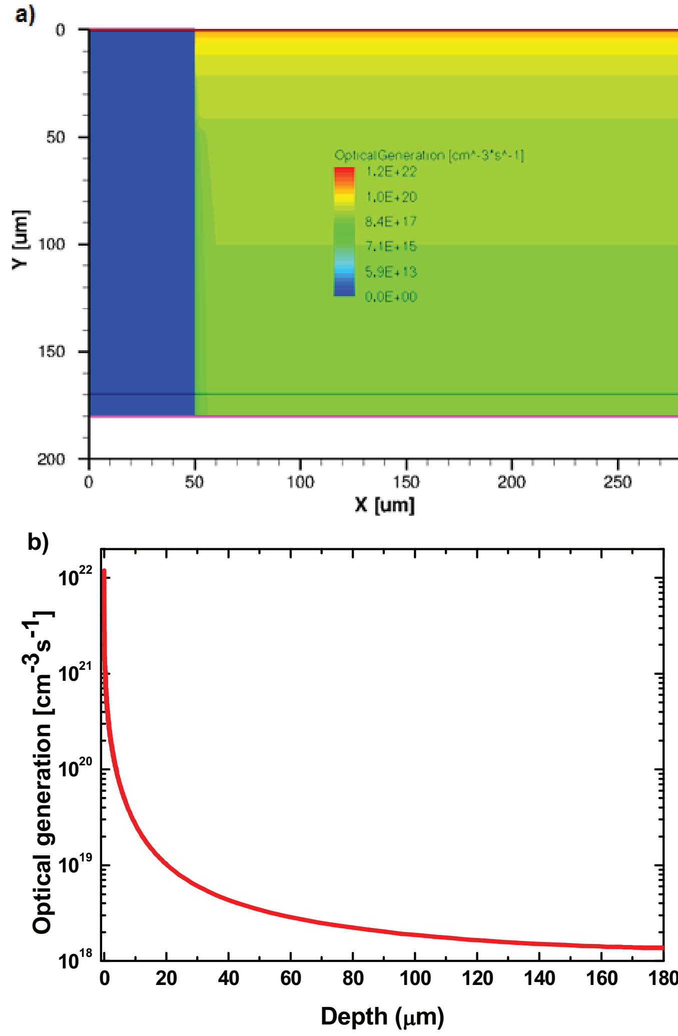

Figure 4.3. a) 2-D map of the optical generation rate in a conventional solar cell. b) Corresponding 1-D optical generation profile.

Parameter	Value	Units
Wafer width (W_{wafer})	12.5	cm
Cell thickness (D_{sub})	180	μm
Front contact pitch (W_{sub})	1.4 – 2.4	mm
Substrate doping (N_{sub})	1×10^{16} (~1.5 Ω-cm)	cm^{-3}
Emitter sheet resistance (R_{sq})	75	Ω/sq
Bulk lifetime (τ_{bulk})	206	μs
Front passivation SRV	surface concentration dependent [4.5]	cm/s
Front/back contact SRV	1×10^{6}	cm/s
Front Ag finger resistivity (ρ_m)	3×10^{-6}	Ωcm
Front Ag/Si contact resistivity (ρ_c)	2×10^{-3}	Ωcm^2
Shunt resistance (R_{sh})	56.5	Ω
Finger length (L_m)	3.05	cm
Finger width (W_m)	100	μm
Finger height (H_m)	34	μm
Finger area factor (F)	0.6	-
Busbar width (W_{bb})	0.15	cm

Table 4.1. Geometrical and physical parameters of the simulated solar cells.

4.1.3 Post-processing analysis

After the device simulation, a post-processing analysis has been performed on the simulated *J-V* characteristics for the extraction of the main electrical and optical figures of merit of a solar cell. According to Section 3.2.4, the output current densities from the electrical simulation have been rescaled by defining a suitable area factor. Afterwards, the simulated current has been corrected by accounting for the front busbars shadowing, according to:

$$I_1 = J \cdot W_{wafer} \cdot W_{wafer} - J_{sc} \cdot W_{wafer} \cdot \left(W_{bb} \cdot N_{bb}\right) \tag{4.1}$$

where J is the output current density from the 2-D simulation, W_{wafer} is the width of the cell wafer (equal to 12.5 cm, according to Fig. 4.1b and Tab. 4.1), J_{sc} is the simulated current density at $V = 0$, W_{bb} is the busbar width, and N_{bb} is the number of busbars. In particular, two front busbars featuring a width W_{bb} of 0.15 cm have been considered, leading to a further area loss of about 2.4%.

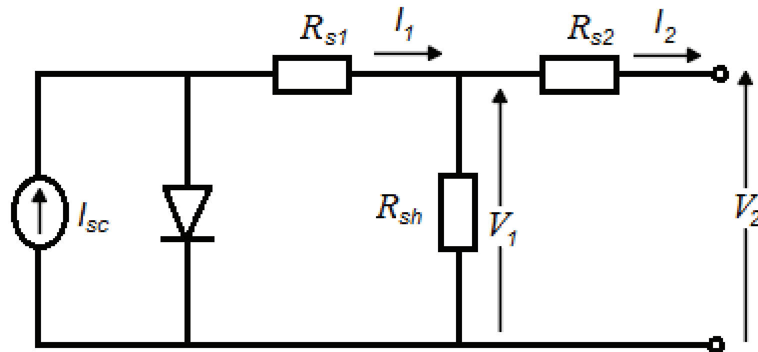

Figure 4.4. Equivalent one-diode circuit model of the simulated solar cells for the post-processing analysis.

Then, the current has been further corrected by accounting for the shunt resistance R_{sh}, according to:

$$I_2 = I_1 - \frac{V_1}{R_{sh}} \tag{4.2}$$

where I_1 is the simulated current already corrected for the busbar shadowing (Eq. 4.1), V_1 is the output voltage from 2-D simulations, and I_2 is the corrected output current (see Fig. 4.4). It is worth noting in Fig. 4.4 that the output of the 2-D simulation includes the effect of the emitter and bulk resistances (represented by R_{s1}), while the effect of the parasitic series resistance R_{s2} due to the bulk resistance of the front metal fingers R_{fm}, and to the front contact resistance R_{fc}, is

not accounted for in the simulation. Accordingly, the output voltage has been corrected, according to:

$$V_2 = V_1 - R_{s2} \cdot I_2 = V_1 - \left(R_{fm} + R_{fc}\right) \cdot I_2 \tag{4.3}$$

where the finger resistance R_{fm} and the front contact resistance R_{fc} have been calculated, respectively, through the following expressions [4.13]:

$$R_{fm} = \frac{1}{3}\rho_m \frac{L_m}{F \cdot H_m \cdot W_m} \frac{1}{2N_{bb} \cdot N_{finger}} \tag{4.4}$$

$$R_{fc} = \frac{\rho_c}{2L_T \cdot L_m} coth\left(\frac{W_m}{2L_T}\right) \frac{1}{2N_{bb} \cdot N_{finger}} \tag{4.5}$$

where ρ_m = 3×10^{-6} Ω·cm is the finger metal resistivity, L_m = 3.05 cm the considered finger length in the 2-busbar 12.5×12.5 cm^2 solar cell, H_m = 34 μm the finger height, W_m = 100 μm the finger width, F = 0.6 is a correction factor which takes into account the non-rectangular shape of the finger cross-section, N_{finger} is the number of the front fingers, ρ_c = 2×10^{-3} Ω·cm^2 the specific front contact resistivity, and $L_T = \sqrt{\rho_c / R_{sq}}$ the transport length, which is function of both ρ_c and the emitter sheet resistance R_{sq} [4.14]. It is worth noting in Eq. 4.5 that the front contact resistance is calculated by considering the metal finger composed of two parallels metals featuring a width of W_m/2, which account for the current coming from the two sides of the finger. Since the parallel of two identical resistances is considered, an additional factor equal to 1/2 has been introduced in Eq. 4.5 with respect to Eq. 2.109. The parameters of the front metallization grid have been chosen according to experimental values reported in [4.13], [4.15], and [4.16], for single screen-printed silver front fingers. The effect of the full-area back contact is not accounted for because it is a "vertical" contact (i.e., in which the current flows vertically) and, then, its entire area is active, thus resulting in a negligible back contact resistance [4.14]. The front busbar resistance (see Eq. 2.110) has been also neglected.

The main electrical output parameters of a solar cell operating under illumination, such as J_{sc}, V_{oc}, FF, and η, have been then extracted from the post-processed J-V and P-V characteristics. Moreover, the quantum collection efficiency η_c (see Eq. 2.77) curve of the simulated solar cells has been also calculated within the wavelength range 300-1200 nm.

In addition, a detailed dark loss analysis has been performed by extrapolating the different J_0 components from the simulated dark J-V characteristics, as already discussed in Section 3.2.4.

4.2 Simulation of screen-printed *c*-Si solar cells

The results of the light and dark *J-V* simulations of the conventional screen-printed *c*-Si HE solar cell described in Section 4.1 are reported below. Furthermore, the impact of the different loss mechanisms affecting the cell performance is investigated.

4.2.1 Light *J-V* analysis

The considered 75-Ω/sq HE solar cell has been simulated under illumination at different front contact pitch (W_{sub}) values, ranging from 1.4 to 2.4 mm with a step of 200 μm (see Tab. 4.1), in order to highlight the tradeoff between the emitter resistance and the illuminated area. The simulation results of such analysis in terms of J_{sc}, V_{oc}, FF, and η, are reported in Fig. 4.5. As expected, the increase of W_{sub}, leading to larger illuminated areas and, hence, higher photogenerated currents, results in an increasing trend of both J_{sc} (Fig. 4.5a) and V_{oc} (Fig. 4.5b). An opposite trend can be observed in Fig. 4.5c, where a steep decrease of the FF is shown with increasing W_{sub}, owing to the increase of the emitter resistance. The efficiency trade-off between the illuminated area and the emitter resistance can be observed in Fig. 4.5d, where the efficiency versus W_{sub} curve shows a typical bell shape. On one hand, for lower W_{sub}, η increases with W_{sub} due to the increase of both J_{sc} and V_{oc}. On the other hand, for higher W_{sub}, the emitter resistance losses dominate and, consequently, the efficiency decreases. In particular, the simulated 75-Ω/sq HE solar cell shows a maximum efficiency of 18.22% at W_{sub} = 2.2 mm (Fig. 4.5d), corresponding to a J_{sc} = 35.83 mA/cm^2, a V_{oc} = 628.3 V, and a FF = 80.91.

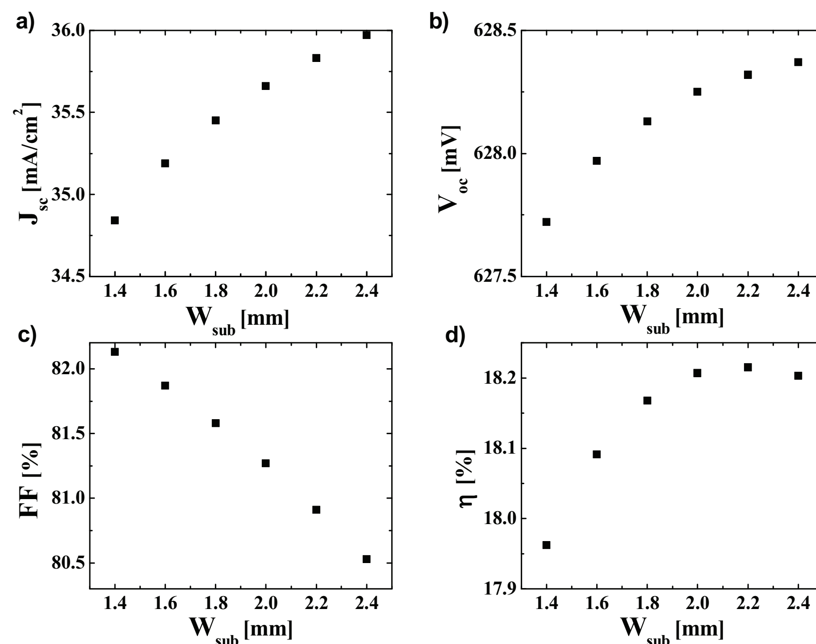

Figure 4.5. a) J_{sc}, b) V_{oc}, c) FF, and d) η versus W_{sub} for the simulated 75-Ω/sq HE cell.

4.2.2 Dark *J-V* analysis

A total dark saturation current density $J_{0,tot}$ of ~1010 fA/cm^2 has been extrapolated from the simulated dark *J-V* characteristics of the screen-printed 75-Ω/sq HE solar cell. Table 4.2 reports in detail the results of the dark loss analysis in terms of emitter saturation current density ($J_{0,e}$), base saturation current density ($J_{0,b}$), and BSF saturation current density ($J_{0,BSF}$), each separated into different contributions due to the Auger recombination, the bulk SRH recombination, the surface SRH recombination at passivated interfaces, and the surface recombination at metallized interfaces.

[fA/cm^2]	**Auger**	**SRH**	**Surface SRH**	**Metal**	**Total**
$J_{0,e}$	62.6	0.1	196.6	25.1	284.4
$J_{0,b}$	2.3	131.9	--	--	134.2
$J_{0,BSF}$	3.3	573.7	--	13.9	590.9
$J_{0,tot}$	68.2	705.7	196.6	39.0	1009.5

Table 4.2. Dark current components for the simulated 75-Ω/sq HE cell.

The simulated 75-Ω/sq HE solar cell exhibits a $J_{o,e} \approx 284$ fA/cm^2, in good agreement with the experimental values reported in [4.17]. In particular, the recombination losses inside the emitter region are dominated by the Auger and the surface SRH recombination mechanisms, due to the high doping concentration in the emitter bulk and at the front passivated surfaces. On the contrary, the bulk SRH mechanism strongly dominates the recombination losses in the lowly-doped *Cz*-Si base region and in the highly Al-doped BSF region, as already discussed in Section 3.3.3. It is worth pointing out that, using Altermatt's parameterization for modeling the degradation of the SRH lifetime in the Al-BSF [4.1], a $J_{0,BSF} \approx 590$ fA/cm^2 has been extracted, similar to the typically measured values in industrial screen-printed *c*-Si solar cells [4.1].

Therefore, the results reported in Table 4.2 reveal that the total recombination losses in conventional screen-printed *c*-Si solar cells, featuring an homogeneously diffused front-side emitter and a full-area metallized Al-alloyed p^+-BSF, are dominated by the recombination losses at the rear side. In this regard, it has been demonstrated that the optimization of the rear contact design with the adoption of local rear point contacts can significantly reduce these losses at rear side, thus leading to higher conversion efficiencies [4.18]. However, the recombination losses in the front-side emitter are also significant and, therefore, need to be reduced. Two alternative concepts have been recently developed to reduce the emitter recombination losses, one based on the use of high sheet resistance ($R_{sq} > 80$ Ω/sq) and, hence, lowly-doped homogeneous emitters combined with advanced metallization techniques for contacting them [4.19], [4.20], and the other one on the adoption of a selective emitter design [4.21].

4.2.3 Cell losses analysis

A photogenerated current density J_{ph} of 37.85 mA/cm^2 has been calculated for the simulated 75-Ω/sq HE solar cell featuring the maximum efficiency (i.e., at W_{sub} = 2.2 mm) by using Eq. 3.36. As expected, it has been found that $J_{sc} < J_{ph}$ since a fraction of the photogenerated carriers inside the device is not collected at the electrodes due to recombination losses. The effect of the recombination losses as a function of the wavelength λ of the radiation can be observed in the quantum collection efficiency η_c curve (shown in Fig. 4.6), computed by using Eq. 2.77 as the ratio between the short-circuit current density J_{sc} (λ) and the photogenerated current density J_{ph} (λ) within the wavelength range 300-1200 nm.

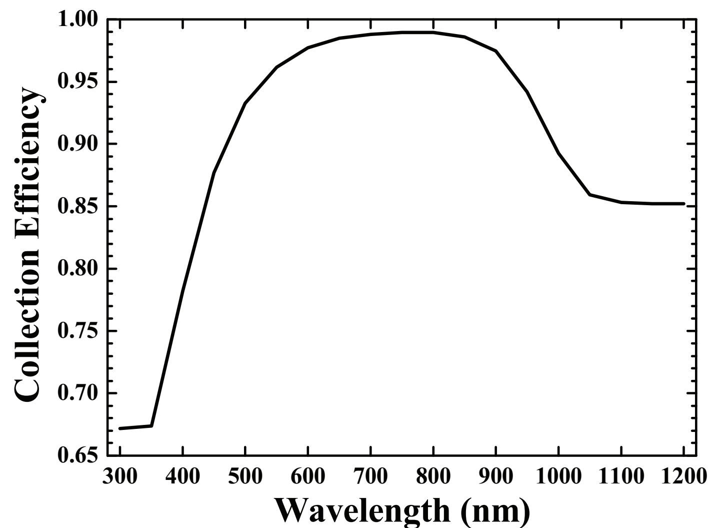

Figure 4.6. Quantum collection efficiency curve within the wavelength range 300-1200 nm for the simulated 75-Ω/sq HE cell.

Fig. 4.6 shows that conventional solar cells, featuring an homogeneous front-side emitter and a full-area metallized BSF, are not very effective in collecting carriers photogenerated close to the front and the back surfaces. In particular, a low η_c can be observed for the carriers photogenerated close to the front surface, thus corresponding to absorbed photons of the blue region of the spectrum (at short wavelengths), as a result of the relatively high recombination losses in the emitter region. Similarly, the collection efficiency of the carriers photogenerated close to the back surface, thus corresponding to the absorbed long-wavelength photons, is affected by the recombination losses at the rear side of the solar cell. Conversely, at intermediate wavelengths, the carriers photogenerated near the depletion region show a very high η_c, close to unity, since they have a higher probability of getting separated by the electric field of the *p-n* junction and, then, collected at the cell electrodes.

It is worth noting that, as already discussed in Section 2.2.5, the quantum collection efficiency is not suited to investigate the effect of the optical losses because it refers to the

efficiency whereby the solar cell collects the carriers under short-circuit conditions, once they are generated in the device. Therefore, η_c only accounts for the effect of the recombination losses inside the device. A more comprehensive analysis of the impact of the different loss mechanisms (including both optical and electrical losses) affecting the cell performance has been made by following this approach: first, the considered 75-Ω/sq HE solar cell has been simulated in ideal conditions by disabling all the loss mechanisms; then, the different loss mechanisms have been gradually introduced in the simulation, starting from the optical losses. The results of such analysis are summarized in Table 4.3. In the ideal case, both optical and electrical losses are not accounted for. In particular, the reflection losses at the front surface have been disabled by setting to zero the front external reflectivity ($R_{ext,front}$ = 0), while the transmission losses at the back surface have been not accounted for by setting to one both the internal back reflectivity ($R_{int,back}$ = 1) and the internal front reflectivity ($R_{int,front}$ = 1). This means that all the incident sunlight at the front surface is transmitted and, then, trapped into the solar cell. Moreover, the area losses due to the shadowing by the front metal grid, the recombination losses and the parasitic resistive losses (including the shunt resistance and the series resistance due to the emitter and the front metal grid) have been neglected in the ideal case, leading to a maximum conversion efficiency of 27.31% for the simulated 75-Ω/sq HE solar cell (see Table 4.3). The reflection and transmission losses cause a reduction of the J_{ph} and, consequently, of the J_{sc} of about 6%, thus decreasing the efficiency to 25.59%. In addition, the area losses contribute to a further decrease of the J_{ph} of about 6.8% (in agreement with the front metal coverage), thus leading to a cell efficiency of 23.78%. It is worth noting in Table 4.3 that, until the recombination mechanisms are disabled in the simulation, all the photogenerated carriers inside the device are collected at the electrodes and, therefore, $J_{sc} = J_{ph}$. Indeed, recombination losses strongly affect both J_{sc} and V_{oc}, as shown in Table 4.3, leading the efficiency below 19%. However, note that also the *FF* is reduced by the recombination losses, according to the empirical expression of Eq. 2.66 that relates *FF* and V_{oc}. Finally, the resistive losses significantly reduce the *FF*, thus resulting in a further decrease of the efficiency down to 18.22%.

		J_{ph} [mA/cm^2]	J_{sc} [mA/cm^2]	V_{oc} [mV]	*FF* [%]	η [%]	$\Delta\eta_{abs}$* [%]
Ideal case	No optical and electrical losses	43.25	43.25	741.1	85.20	27.31	---
+ Optical losses	+ reflection and transmission	40.63	40.63	739.4	85.18	25.59	-1.72
	+ area losses	37.85	37.85	737.6	85.15	23.78	-3.53
+ Electrical losses	+ recombination losses	37.85	35.83	628.6	83.30	18.76	-8.55
	+ resistive losses	37.85	35.83	628.3	80.91	18.22	-9.09

Table 4.3. Analysis results of the impact of the different loss mechanisms on the performance of the simulated 75-Ω/sq HE cell. *$\Delta\eta_{abs}$ is calculated with respect to the ideal case.

4.3 Simulation of double screen-printed *c*-Si solar cells

The design of the front contact grid layout in a solar cell is the result of a trade-off between two opposite requirements: improving the current carrying capability of the contacts (i.e., decreasing the resistive losses) by increasing the overall cross-section of the front metallized lines, and increasing the light collection by reducing the shadowed area on the front surface. In order to achieve a better trade-off between these competing effects, advanced metallization techniques have been recently developed, such as the double screen-printing technology.

4.3.1 Double screen-printing technology

Double screen-printing (DP) technology, in contrast with the conventional single screen-printing (SP) process, is based on the screen-printing of a second layer of metal paste over the first one with high alignment accuracy; in this way, larger aspect ratios (i.e., the ratio of the finger height to the finger width) of the metal fingers can be achieved with respect to the SP process (according to Fig. 4.7), thus reducing the shadowed area, without significantly increasing the resistive losses of the front metal grid. In particular, two generations of double printing have been recently developed [4.15].

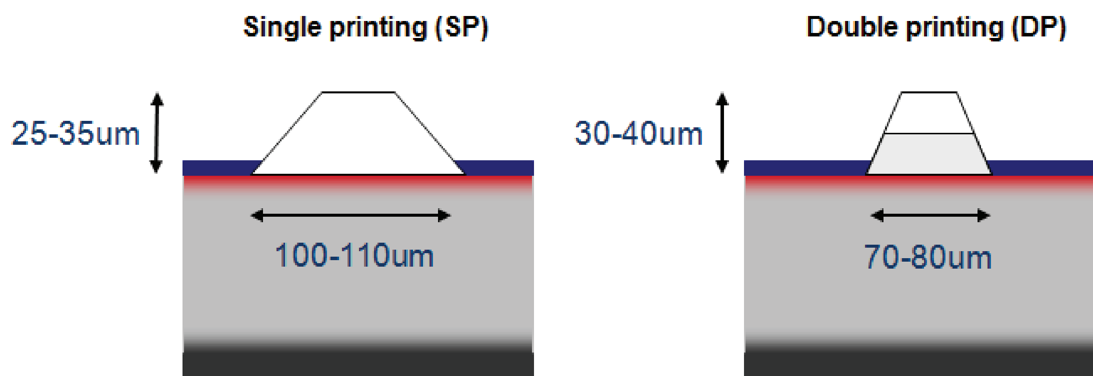

Figure 4.7. Comparison between single screen-printing (SP) and double screen-printing (DP) technologies in terms of typical finger geometrical parameters.

The first-generation concept for the DP process (known as DP-I) is based on (see Fig. 4.8a):

- a first print of silver (Ag) paste using only the finger pattern on the front side with the edge alignment;
- a second print of the same Ag paste with the full H-pattern (fingers + busbars), ensuring the alignment on the same features of the first printing.

The first-generation of the DP process allows to print higher aspect ratio front contacts, thus increasing the cell efficiency, while reducing the paste consumption as compared to the conventional SP process. However, it also shows some limitations, such as the possible shunting under the busbars and the non-optimized conductivity of the upper layer. The second-generation of the DP process (known as DP-II) allows to overcome these limitations, by differentiating the metal pastes for the first and the second print (according to Fig.4.8b): an optimized paste to contact the emitter for the first layer, and a more conductive and non-contacting paste for the upper layer and for the busbars (see Fig. 4.8b). In this way, the overall conductivity of the front contacts is increased, and the busbars shunting is prevented because of the use of the non-contacting paste in the second print (i.e., there is no contact under busbars). The reduction of the front-side contacted area also decreases the recombination losses at front metallized surfaces, thus leading to an increase of Voc compared to the DP-I process. Furthermore, DP-II allows an improved process control, resulting in a finer line printing with a lower finger roughness [4.15].

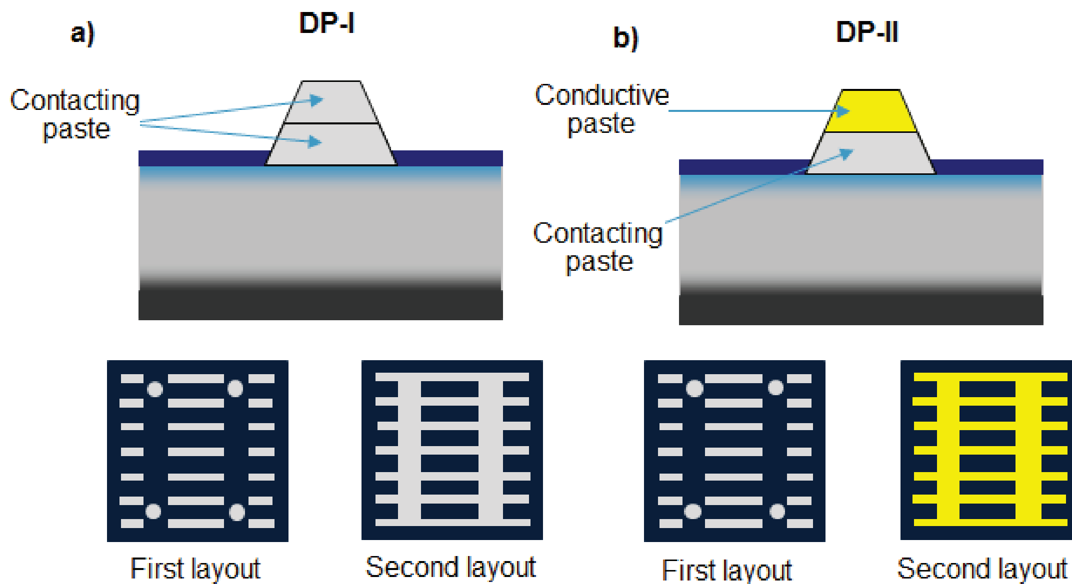

Figure 4.8. Comparison between a) the first-generation (DP-I) and b) the second-generation (DP-II) of the double screen-printing process.

4.3.2 Simulation results

The impact of the double screen-printing technology has been investigated by simulating the 75-Ω/sq HE *c*-Si solar cell described in Section 4.1, considering different front metallization parameters for the SP and DP-II processes, according to the experimental values reported in Table 4.4 [4.13], [4.15]. These parameters confirm that DP-II allows a higher aspect ratio of the front fingers due to the reduced finger width, and a lower finger resistivity thanks to the high-conductive upper layer. Moreover, DP-II shows an improved shunt resistance, which can be ascribed to the reduced front-side contacted area because of the smaller finger width and the non-contacting busbars.

Parameter	SP	DP-II	Units
Front Ag finger resistivity (ρ_m)	3×10^{-6}	2.7×10^{-6}	Ωcm
Front Ag/Si contact resistivity (ρ_c)	2×10^{-3}	2.6×10^{-3}	Ωcm^2
Shunt resistance (R_{sh})	56.5	104.3	Ω
Finger width (W_m)	100	75	μm
Finger height (H_m)	34	33	μm
Aspect ratio	0.34	0.44	-
Finger area factor (F)	0.6	0.5	-

Table 4.4. Experimental front metallization parameters for SP and DP-II processes.

Fig. 4.9 reports the simulation results for both SP and DP-II solar cells as a function of the front contact pitch (W_{sub}). As expected, due to the lower shadowing on the front surface and, hence, to the larger photogenerated current, the J_{sc} is appreciably higher in the DP solar cell for a given W_{sub} (see Fig. 4.9a). The DP solar cell also shows a slight improvement of the V_{oc} in Fig. 4.10b, due to a corresponding small reduction of the dark saturation current density (according to Eq. 2.65). In fact, as reported in Table 4.5, the DP solar cell features a slightly lower value of $J_{0,tot}$ (~1007 fA/cm^2) with respect to the SP solar cell (~1010 fA/cm^2). From the comparison between the values reported in Table 4.2 and Table 4.5, it is possible to observe that the decrease of $J_{0,tot}$ shown by the DP cell arises from the lower recombination losses at the metallized front surface, due to the reduced front-side contacted area in the case of DP. On the contrary, Fig. 4.9c reports that, for a given W_{sub}, the FF is lower in the case of DP due to the following effects. First, higher contact and finger resistances are associated to the DP process, due to the higher contact resistivity and the smaller finger cross-section, respectively, according to the values reported in Table 4.4. Second, for a given W_{sub}, the distance between two adjacent front fingers increases in the DP solar cell due to the narrower fingers, thus resulting in an increased emitter resistance. From the comparison between the efficiency curves of the SP and DP cells, reported in Fig. 4.9d, it is important to observe that the peak efficiency moves toward lower W_{sub} for the DP solar cell because of the higher emitter resistance and the reduced

shadowing effect. In particular, the DP solar cell shows a peak efficiency of 18.38% at W_{sub} = 2.0 mm (Fig. 4.9d). The comparison between the SP and DP cells featuring the maximum efficiency is summarized in Table 4.6. The DP cell shows an increase in terms of J_{sc} and V_{oc} of 0.3 mA/cm^2 and 0.5 mV, respectively, a slight *FF* decrease of 0.02%$_{abs}$, and an efficiency gain of 0.16%$_{abs}$. It is worth noting that the DP process also allows a lower front metal coverage, thus leading to a considerable reduction of the paste consumption of about 20-30% [4.15]. Moreover, it can be observed in Fig. 4.9d that the DP cell exhibits a lower dependence of the efficiency on the front contact pitch, i.e., a lower sensitivity of the optimum point.

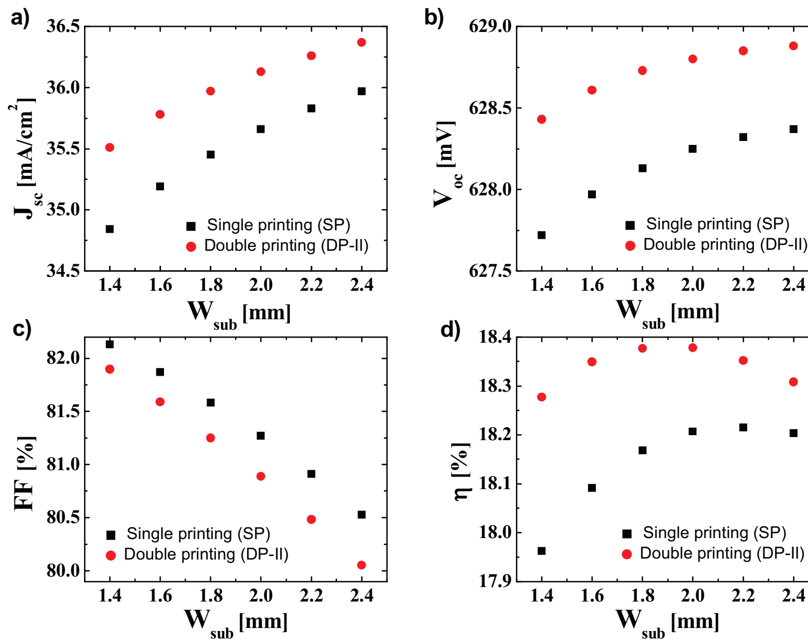

Figure 4.9. a) J_{sc}, b) V_{oc}, c) *FF*, and d) η versus W_{sub} for the simulated 75-Ω/sq HE solar cells featuring SP and DP-II front metal fingers, respectively.

[fA/cm^2]	Auger	SRH	Surface SRH	Metal	Total
$J_{0,e}$	62.9	0.1	199.2	18.8	281.0
$J_{0,b}$	2.3	132.0	--	--	134.3
$J_{0,BSF}$	3.3	574.0	--	13.9	591.2
$J_{0,tot}$	68.5	706.1	199.2	32.7	1006.5

Table 4.5. Dark current components for the simulated DP solar cell.

	DP-II	SP	Δ
Front contact pitch [mm]	2.0	2.2	---
Front metal coverage [%]	6.15	6.95	-0.8
J_{sc} [mA/cm^2]	36.13	35.83	+0.30
V_{oc} [mV]	628.8	628.3	+0.50
FF [%]	80.89	80.91	-0.02
η [%]	18.38	18.22	+0.16

Table 4.6. Comparison between the simulated SP and DP-II solar cells featuring the maximum efficiency.

In Table 4.7, the effect of the different parasitic resistances has been individually evaluated, finding that the shunt resistance slightly influences the efficiency of both considered cells. Consequently, the efficiency gain of the DP cell over the SP cell shows only a small reduction when the R_{sh} is not taken into account. On the contrary, the series resistances strongly impact on the efficiency gain, which potentially rises to 0.24%$_{abs}$ when the series resistances are not considered in the post-processing. In particular, it can be observed in Table 4.7 that the finger resistance is more effective than the front resistance contact in reducing the efficiency gain shown by the DP cell. As a matter of fact, the efficiency gain rises to 0.19%$_{abs}$ when the front contact resistance is not included, and to 0.21%$_{abs}$ when the finger resistance is not taken into account.

R_{sh}	R_{fc}	R_{fm}	DP-II	SP	Δ
Y	Y	Y	18.38	18.22	+0.16
N	Y	Y	18.40	18.25	+0.15
Y	N	N	18.64	18.40	+0.24
Y	N	Y	18.47	18.28	+0.19
Y	Y	N	18.54	18.33	+0.21

Table 4.7. Separate analysis of the effect of the different parasitic resistances on the conversion efficiency of the simulated SP and DP-II solar cells.

References

[4.1] P. P. Altermatt et al., “Highly Predictive Modelling of Entire Si Solar Cells for Industrial Applications”, *Proc. of 24th European Photovoltaic Solar Energy Conference* (*EU PVSEC*), pp. 901-906, 2009.

[4.2] D. Fenning, M. Bertoni, T. Buonassisi, “Predictive modeling of the optimal phosphorus diffusion profile in silicon solar cells”, *Proc. of 24th European Photovoltaic Solar Energy Conference* (*EU PVSEC*), pp. 1893-1896, 2009.

[4.3] T. Janssens et al., “Advanced Phosphorous Emitters for High Efficiency Si Solar Cells”, *Proc. of 34th IEEE Photovoltaic Specialists Conference* (*PVSC*), pp. 878-882, 2009.

[4.4] S. Solmi, A. Parisini, R. Angelucci, “Dopant and carrier concentration in Si in equilibrium with monoclinic SiP precipitates”, *Physical Review B*, Vol. 53, No. 12, pp. 7836-7841, 1996.

[4.5] A. Kimmerle et al., “Modelling carrier recombination in highly phosphorus-doped industrial emitters”, *Energy Procedia*, Vol. 8, pp. 275-281, 2011.

[4.6] Sentaurus Device User Guide, Synopsys, Mountain View, CA.

[4.7] A. Schenk, “Finite-temperature full random-phase approximation model of band gap narrowing for silicon device simulation”, *Journal of Applied Physiscs*, Vol. 84, No. 7, pp. 3684-3695, 1998.

[4.8] P. P. Altermatt, “Models for numerical device simulations of crystalline silicon solar cells – a review”, *Journal of Computational Electronics*, Vol. 10, No. 3, pp. 314-330, 2011.

[4.9] D. B. M. Klaassen, “A unified mobility model for device simulation: I. model equations and concentration dependence”, *Solid-State Electronics*, Vol. 35, No. 7, pp. 953-959, 1992.

[4.10] D. B. M. Klaassen, “A unified mobility model for device simulation: II. temperature dependence of carrier mobility and lifetime”, *Solid-State Electronics*, Vol. 35, No. 7, pp. 961-967, 1992.

[4.11] S. W. Glunz et al., “Minority carrier lifetime degradation in boron-doped Czochralski silicon”, *Journal of Applied Physiscs*, Vol. 90, No. 5, pp. 2397-2404, 2001.

[4.12] P. P. Altermatt et al., “Reassessment of the intrinsic carrier density in crystalline silicon in view of band-gap narrowing”, *Journal of Applied Physiscs*, Vol. 93, No. 3, pp. 1598-1604, 2003.

[4.13] P. Magnone et al., “Understanding the Impact of Double Screen-Printing on Silicon Solar Cells by 2-D Numerical Simulations”, *Proc. of 37th IEEE Photovoltaic Specialists Conference* (*PVSC*), pp. 2177-2180, 2011.

[4.14] D. K. Schroder, “Solar Cell Contact Resistance – A Review”, *IEEE Transactions on Electron Devices*, Vol. 31, No. 5, pp. 637-647, 1984.

[4.15] M. Galiazzo et al., “ Double Printing of Front Contact Ag in c-Si Solar Cells”, *Proc. of 25th European Photovoltaic Solar Energy Conference* (*EU PVSEC*), pp. 2338-2340, 2010.

[4.16] P. Magnone et al., “A Methodology to Account for the Finger Non-Uniformity in Photovoltaic Solar Cell”, *Energy Procedia*, Vol. 27, pp. 191-196, 2012.

[4.17] International Technology Roadmap for Photovoltaics (ITRPV) - Results 2011, Third Edition, March 2012.

[4.18] M. Zanuccoli et al., “Performance Analysis of Rear Point Contact Solar Cells by Three-Dimensional Simulation”, *IEEE Transaction on Electron Devices*, Vol. 59, No. 5, pp. 1311-1319, 2012.

[4.19] M. M. Hilali, A. Rohatgi, S. Asher, “Development of Screen-Printed Silicon Solar Cells With High Fill Factors on 100 Ω/sq Emitters”, *IEEE Transactions on Electron Devices*, Vol. 51, No. 6, pp. 948-955, 2004.

[4.20] A. Ebong et al., “High efficiency silicon solar cells with ink jetted seed and plated grid on high sheet resistance emitter”, *Proc. of 35th IEEE Photovoltaic Specialists Conference* (*PVSC*), pp. 1363-1367, 2010.

[4.21] G. Hahn, “Status of Selective Emitter Technology”, *Proc. of 25th European Photovoltaic Solar Energy Conference* (*EU PVSEC*), pp. 1091-1096, 2010.

Chapter 5

Simulation of High-Efficiency Silicon Solar Cells

Industrial screen-printed *Cz*-Si solar cells, featuring a standard 75-Ω/sq homogeneously phosphorus-doped front-side n^+-emitter and a full-area metallized Al-alloyed p^+-back surface field (BSF), are currently limited to a conversion efficiency around 18.5%. As discussed in Chapter 4, the fundamental performance limitations of these conventional cells can be mostly ascribed to the recombination losses occurring at the front and rear sides. Several technological solutions have been proposed to optimize both cell sides and, therefore, improve the cell performance. In particular, two alternative approaches have been recently developed for the improvement of the front-side emitter, such as the development of advanced front metallization techniques for contacting emitters with a high sheet resistance (R_{sq} > 80 Ω/sq), or the use of a selective emitter design. In addition, the optimization of the rear contact design with the adoption of local point contacts can significantly reduce the recombinations losses at the rear side, thus leading to a further increase of the solar cell performance.

In this chapter, these advanced technological solutions for high-efficiency silicon solar cells have been investigated by means of multi-dimensional electro-optical numerical simulations. First, a two-dimensional (2-D) modeling approach is adopted to analyze the impact of different emitter doping profiles in selective emitter solar cells. Then, the optimization of the rear point contact geometry in a PERC-type solar cell, featuring also a high sheet resistance (140 Ω/sq) phosphorus-doped emitter contacted by means of an advanced front metallization scheme with narrow and highly-conductive electro-plated Ti/Cu contacts, is performed through a rigorous three-dimensional (3-D) modeling approach.

5.1 Simulation of selective emitter solar cells

The selective emitter (SE) design, featuring lower doped areas between the front contact fingers, and higher doped areas underneath the front metallization, is crucial to improve the performance at the front side of silicon solar cells. One of the most interesting and promising low-cost SE process consists of the screen-printing of a phosphorus-doped paste [5.1], [5.2]. A particularly important feature of this SE process is that to allow a separate optimization of the doping profiles in the metallized and non-metallized front-side areas. Therefore, by referring to

this kind of process, in this thesis, a simulation study with a decoupled analysis of the effect of the lowly-doped and highly-doped profiles on the performance of a SE solar cell has been performed by means of two-dimensional (2-D) electro-optical numerical device simulations [5.3]. Moreover, by exploiting the 2-D modeling approach, the effect of the alignment tolerance used in the SE diffusion process for the subsequent metallization process has been also investigated. Numerical results show that the adoption of an optimized design for the SE solar cell can lead to an efficiency improvement above $0.4\%_{abs}$ as compared to a 75-Ω/sq homogeneous emitter (HE) reference cell. Finally, the effect of the combined use of double screen-printing technology and SE concept has been investigated.

5.1.1 Introduction to SE solar cells

The improvement in the front-side emitter is currently a challenging issue for the optimization of the silicon solar cell technological process. The emitter requires high lateral conductance to achieve a low series resistance contribution at the front side, and high surface doping concentration to realize a good ohmic metal-semiconductor front contact. Nevertheless, emitter recombination losses limit cell performance, as shown in Chapter 4, and become increasingly dominant with the improvement of the rear side due to the forthcoming adoption of a rear point contact design with passivated rear surfaces in most of the industrial Si solar cells [5.4]. Since transport and recombination mechanisms are strongly coupled in the semiconductor equations, the emitter design then results in a strategic trade-off between these physical phenomena for the performance of a solar cell. The development of technological solutions to contact emitters with a high sheet resistance (R_{sq} > 80 Ω/sq), such as the optimization of the silver (Ag) pastes [5.5]-[5.7], and/or the so-called seed-and-plate approach [5.8]-[5.10], is a current task in photovoltaic (PV) industry for further optimization of the emitter, but it could be limited by a narrower firing window or by the application of an additional (plating) step [5.11]. However, such technological solutions for contacting high sheet resistance emitter are not industrially available yet.

An alternative and promising approach to improve the emitter performance is the realization of a selective emitter (SE) design. SE solar cells, in contrast with conventional screen-printed industrial *c*-Si solar cells based on an homogeneously diffused emitter (HE), feature different doping profiles in the metallized and non-metallized front-side areas (see Fig. 5.1): while a deep highly-doped (HDOP) profile under the metal-contacted regions ensures a good ohmic metal-semiconductor contact (achieving a low contact resistance) and an adequate lateral conductivity, a shallow lowly-doped (LDOP) profile in the illuminated passivated regions between the front contact fingers leads to a reduction of Auger and surface recombination losses and, consequently, to an enhanced spectral response in the blue region of

the spectrum [5.11]-[5.13]. However, an efficiency trade-off exists between these advantages and the increased emitter resistance that affects the SE solar cells due to the lower doping concentration in the non-metallized areas.

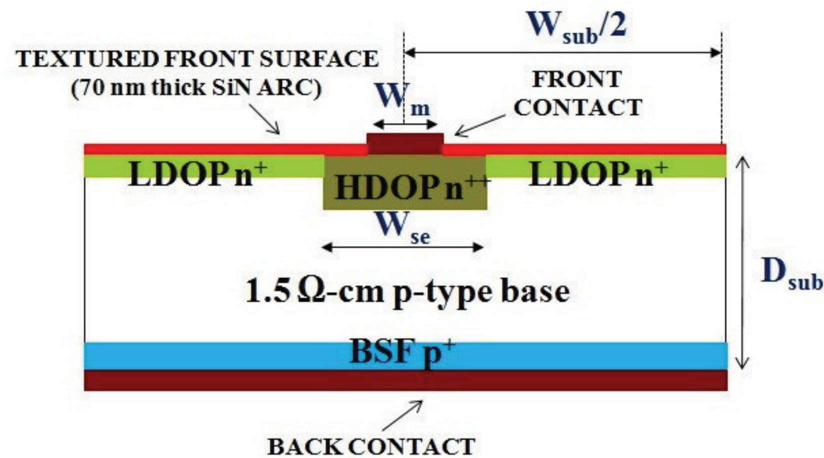

Figure 5.1. 2-D cross-section of the simulated SE solar cell.

The use of SE has become one of the most interesting low-cost concepts to boost efficiency of Si solar cells. Indeed, it has already been demonstrated that a wide variety of process schemes, which are ready for industrial implementation, can be adopted to form a SE and, then, to enhance the performance of a *c*-Si solar cell without a relevant increase in production costs [5.11]. Among these methods, it is worth mentioning the selective laser doping from phosphorus silicate glass [5.12], the etch-back process [5.14], the diffusion masking [5.15], etc. One of the most interesting and promising low-cost SE process is based on the use of a screen-printable phosphorus-doped paste [5.1], [5.2]. An important advantage of using this technique is its ability to selectively form HDOP regions without the need for laser patterning, diffusion mask or etch-back process. Indeed, this process consists of the screen-printing of a dopant paste with the same pattern as the metallization, the firing of the paste and, then, the subsequent printing of the front metallization over the HDOP regions (requiring a good alignment). Moreover, as demonstrated in [5.2], this SE process provides additional degrees of freedom to optimize the LDOP and HDOP emitters independently, achieving an efficiency improvement in the range of 0.3-0.7$\%_{abs}$ compared with the baseline process.

5.1.2 Simulation setup

By considering the promising low-cost SE process based on the screen-printing of a phosphorus-doped paste which allows a separate optimization of the doping profiles in the metallized and non-metallized front-side areas, this thesis presents a simulation study with a decoupled analysis of the influence of the LDOP and HDOP profiles on the performance of a *c*-Si SE solar cell [5.3], [5.16]. Unlike some previous works [5.13], [5.17], [5.18], [5.19], where the impact of the emitter doping profile was analyzed by using a one-dimensional (1-D) analytical or numerical modeling, two-dimensional (2-D) numerical simulations has been performed using a state-of-the-art numerical TCAD simulator [5.20] coupled to an optical simulator that provides the 2-D map of the optical generation rate inside the solar cell. The 2-D approach is mandatory to account for the shadowing losses underneath the front metallization, to distinguish the front-side passivated and metallized areas and, in case of SE design, to differentiate the local front-side doping properties. This allows to better model the physical mechanisms occurring inside the device (and, in particular, in the emitter region), mainly in terms of doping-dependent bulk and surface recombination and of 2-D lateral carrier transport. The comparison with a reference 75-Ω/sq HE solar cell allows to quantitatively evaluate the expected performance improvements. Moreover, thanks to the 2-D modeling, the effect of the alignment tolerance used in the SE diffusion process for the subsequent metallization process, which leads to broad HDOP dopant lines, has been also investigated, by estimating the benefit achievable by reducing the HDOP lateral width in the SE cell.

The simulated 2-D planar SE solar cell is depicted in Fig. 5.1. Similarly to the HE solar cell analyzed in Chapter 4, a two-busbar 12.5×12.5 cm^2 SE cell has been considered with the following characteristics: a 1.5 Ω·cm, 180-µm-thick boron-doped *p*-type substrate with a full-area metallized aluminum-alloyed back surface field (Al-p^+ BSF) modeled with a typical 10-µm-deep profile reported in [5.21]; a front surface covered with a 70-nm-thick silicon nitride (SiN_x) anti-reflective coating (ARC) layer; a silver front finger with a width (W_m) of 100 µm. The front side of the SE solar cell is also characterized by the lateral width of the HDOP region (W_{se}), as shown in Fig. 5.1. It is worth mentioning that, by exploiting the symmetry of the device, the lateral size of the 2-D simulation domain has been limited to the half of the front contact pitch (W_{sub}), i.e., to the half of the depicted structure in Fig. 5.1. Moreover, in addition to the mesh refinements performed for the HE solar cell (explained in Section 4.1.1), it is worth noting that the SE cell requires an additional refinement along the horizontal axis in the transition region between the HDOP and LDOP areas, where a doping gradient is present along the horizontal direction.

All the simulated emitter phosphorus doping profiles are modeled by an analytical double error function (i.e., two error function-like curves with different peak position and depth), in

order to reproduce the typical "kink-and-tail" shape [5.22]. Furthermore, a cut-off at an activation limit of ~2×10^{20} cm^{-3} [5.23] has been assumed to calculate the electrically active concentration profiles from the generated doping profiles (refer to Fig. 4.2b), assuming full dopant ionization below the activation limit and neglecting shifts between the carrier and the dopant profiles [5.24]. In the following, C_{peak} represents the surface peak doping concentration of the chemical profile, J_{depth} is the junction depth, and R_{sq} is the sheet resistance extracted from the electrically active profiles by applying the Klaassen mobility model [5.25], [5.26].

Similarly to Chapter 4, the optical generation rate profiles have been calculated with a mono-dimensional simulation of plane-waves propagation in silicon, assuming direct illumination with a standard AM1.5G spectrum (1000 W/m^2) and ideal shadowing under front metal fingers, and accounting for a random pyramids textured SiN_x-passivated front surface. Moreover, it is worth pointing out that the electrical simulation of the SE solar cell have required the same ad-hoc refinement of the TCAD physical models and parameters, as already discussed in Section 4.1.2 for the simulation of the HE solar cell. Accordingly, refer to Table 4.1 for the main geometrical and physical parameters of the simulated SE solar cell. Likewise, the post-processing analysis described in Section 4.1.3 has been performed on the simulated *J-V* characteristics of the SE cell for the extraction of the electrical and optical performance parameters.

5.1.3 Analysis of the effect of the lowly-doped profile

The effect of the LDOP profile in the passivated front-side areas has been evaluated following the procedure suggested in [5.27]: for a given HDOP profile (50 Ω/sq with C_{peak} = 5×10^{20} cm^{-3} and J_{depth} = 0.6 µm), several LDOP profiles (see Table 5.1) have been simulated by assuming a HDOP lateral width W_{se} = 250 µm (i.e., 150 µm wider than the finger width) as a function of the front contact pitch W_{sub} (ranging from 1.4 mm to 2.4 mm with a step of 200 µm) in order to highlight the trade-off between the emitter resistance, the illuminated area and the recombination losses in the LDOP regions. The different LDOP profiles are obtained by changing the surface peak doping concentration from 1×10^{20} to 4×10^{19} cm^{-3} for a fixed J_{depth} = 0.25 µm, corresponding to a sheet resistance range between 90 Ω/sq and 188 Ω/sq (according to Table 5.1). The simulated SE solar cells have been compared with the reference 75-Ω/sq HE solar cell analyzed in Chapter 4, featuring a doping profile with C_{peak} = 4×10^{20} cm^{-3} and J_{depth} = 0.35 µm (Table 5.1).

Doping profile	**C_{peak} [cm^{-3}]**	**J_{depth} [µm]**	**R_{sq} [Ω/sq]**
L90	1×10^{20}	0.25	89.7
L100	9×10^{19}	0.25	100.2
L113	8×10^{19}	0.25	112.6
L127	7×10^{19}	0.25	127.1
L144	6×10^{19}	0.25	144.3
L165	5×10^{19}	0.25	164.5
L188	4×10^{19}	0.25	187.8
HE75	4×10^{20}	0.35	75.0

Table 5.1. Parameters of the simulated LDOP and HE profiles.

J_{sc} and V_{oc} curves versus W_{sub} for some of the simulated LDOP profiles and for the HE solar cell are reported in Fig. 5.2. For a given front contact pitch value, both J_{sc} and V_{oc} of the SE solar cells are larger with respect to the HE cell due to the lower doping concentration and, hence, lower Auger and surface recombination losses in the illuminated non-metallized areas. In fact, the highest J_{sc} and V_{oc} values are obtained by the SE solar cell featuring the LDOP profile with the lowest doping concentration and, consequently, the highest sheet resistance (i.e., 188 Ω/sq) within the considered range. Moreover, in all the simulated cells, the increase of the front contact pitch (W_{sub}), leading to larger illuminated areas, results in an increasing trend of both J_{sc} and V_{oc}.

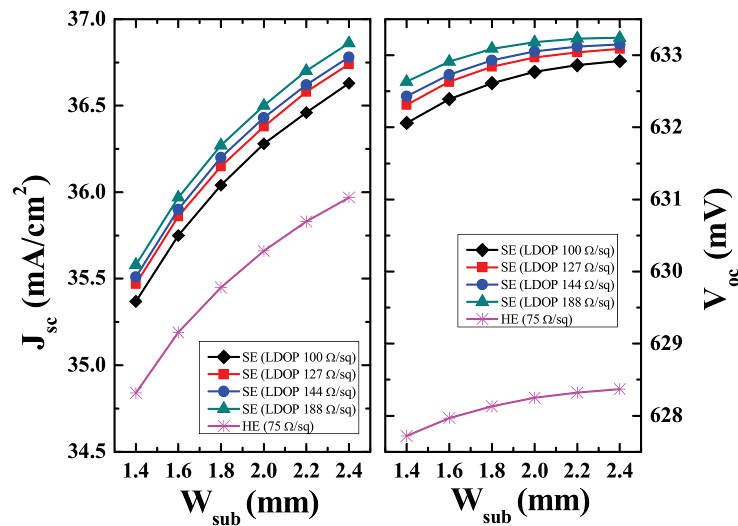

Figure 5.2. (Left) Short-circuit current density J_{sc}, and (right) open-circuit voltage V_{oc} versus front contact pitch W_{sub} for the SE cell at different simulated LDOP profiles and for the 75-Ω/sq HE cell.

An opposite trend can be observed in Fig. 5.3, where the *FF* versus W_{sub} curves are reported. Simulation results highlight the strong dependence of the *FF* on the emitter resistance. Indeed, the increase of the front contact pitch, leading to larger emitter resistances, results in a steep decrease of the *FF*, particularly for the SE cells featuring a high sheet resistance LDOP profile. Therefore, for a given front contact pitch, among the investigated SE cells, the highest *FF* is obtained for the LDOP profile with the lowest sheet resistance (i.e., 90 Ω/sq). The efficiency trade-off between the emitter resistance, the illuminated area and the emitter recombination losses can be better appreciated in Fig. 5.3, where the efficiency versus W_{sub} curves show a typical bell shape.

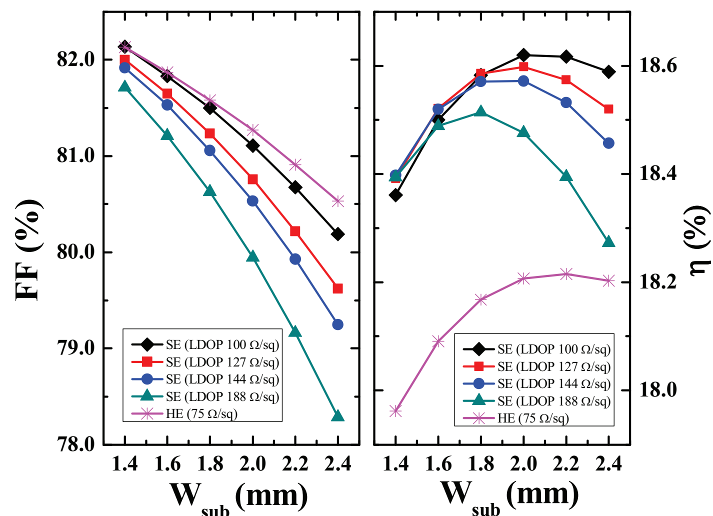

Figure 5.3. (Left) Fill factor *FF*, and (right) efficiency η versus front contact pitch W_{sub} for the SE cell at different simulated LDOP profiles and for the 75-Ω/sq HE cell.

On one hand, for lower W_{sub} values, the efficiency increases with the front contact pitch due to the increase of both J_{sc} and V_{oc}. On the other hand, for higher W_{sub}, the emitter resistance losses dominate and, hence, the efficiency decreases. Moreover, it can be observed in Fig. 5.3 that the position of the efficiency peak changes depending on the sheet resistance of the LDOP profile for the simulated SE cells: in particular, the efficiency peak moves toward lower W_{sub} for the cells featuring a higher emitter sheet resistance.

The maximum efficiency (18.62%) is obtained by the SE cell featuring a 100-Ω/sq LDOP profile at W_{sub} = 2 mm, while the 75-Ω/sq HE cell shows a peak efficiency of 18.22% at W_{sub} = 2.2 mm. The comparison between the HE and SE cells featuring the maximum efficiency is reported in Table 5.2. The SE cell shows an increase in terms of J_{sc} and V_{oc} of 0.45 mA/cm^2 and 4.5 mV, respectively, a FF increase of 0.2%$_{abs}$ and an efficiency gain of 0.4%$_{abs}$.

	W_{sub} [mm]	J_{sc} [mA/cm^2]	V_{oc} [mV]	FF [%]	η [%]
HE CELL	2.2	35.83	628.3	80.91	18.22
SE CELL	2.0	36.28	632.8	81.11	18.62

Table 5.2. Comparison between the simulated HE (W_{sub} = 2.2 mm, 75 Ω/sq) and SE (W_{sub} = 2.0 mm, W_{se} =250 µm, 100-Ω/sq LDOP, 50-Ω/sq HDOP) solar cells featuring the maximum efficiency.

In terms of total dark saturation current density $J_{0,tot}$, the SE cell shows a lower value (~861 fA/cm^2 in Table 5.3) with respect the HE cell (~1010 fA/cm^2 in Table 4.2), according to the higher performance. The decrease of $J_{0,tot}$ shown by SE cell is a consequence of the reduction of the recombination losses in the emitter: as a matter of fact, the emitter saturation current density $J_{0,e}$ decreases from ~284 fA/cm^2 for HE to ~135 fA/cm^2 for SE. The careful analysis of the loss mechanisms in the emitter region shows that the $J_{0,e}$ decrease can be ascribed to a moderate reduction of Auger recombination losses ($J_{0,e(Auger)}$ decreases from ~63 fA/cm^2 for HE to ~36 fA/cm^2 for SE), and to a strong reduction of the surface recombination losses ($J_{0,e(Surf)}$ decreases from ~197 fA/cm^2 for HE to ~81 fA/cm^2 for SE).

[fA/cm^2]	**Auger**	**SRH**	**Surface SRH**	**Metal**	**Total**
$J_{0,e}$	36.1	0.1	80.8	18.1	135.1
$J_{0,b}$	2.3	131.4	--	--	133.7
$J_{0,BSF}$	3.3	574.7	--	13.9	591.9
$J_{0,tot}$	41.7	706.2	80.8	32.0	860.7

Table 5.3. Dark current components for the simulated SE solar cell (W_{sub} = 2.0 mm, W_{se} =250 µm, 100-Ω/sq LDOP, 50-Ω/sq HDOP) featuring the maximum efficiency.

5.1.4 Analysis of the effect of the highly-doped profile

The impact of the HDOP profile in the metallized front-side areas on SE cell performance has been investigated according to [5.3], [5.6]. Various HDOP profiles have been examined at three different phosphorus dose concentrations (6×10^{15}, 3×10^{15}, and 1.5×10^{15} cm^{-2}), by varying the C_{peak} from 5×10^{20} to 1×10^{20} cm^{-3} and, consequently, the junction depth of the doping profile (see Table 5.4). Accordingly, the sheet resistance of the simulated HDOP profiles ranges from ~12 Ω/sq to ~64 Ω/sq. It is worth noting that only the HDOP profiles whose junction is deeper than that of the previous LDOP profiles have been considered in Table 5.4. The effect of the different HDOP profiles in the SE cell has been evaluated by using the optimal 100-Ω/sq LDOP profile at W_{sub} = 2.0 mm, derived from the analysis reported in the previous section, and by assuming the same HDOP lateral width (W_{se} = 250 μm).

	Dose = 6×10^{15} cm^{-2}		**Dose = 3×10^{15} cm^{-2}**		**Dose = 1.5×10^{15} cm^{-2}**	
C_{peak} [cm^{-3}]	**J_{depth} [μm]**	**R_{sq} [Ω/sq]**	**J_{depth} [μm]**	**R_{sq} [Ω/sq]**	**J_{depth} [μm]**	**R_{sq} [Ω/sq]**
1×10^{20}	2.93	11.9	1.48	23.8	0.75	47.6
2×10^{20}	1.53	13.8	0.78	27.6	0.41	54.9
3×10^{20}	1.05	16.2	0.55	32.3	0.30	64.0
4×10^{20}	0.80	19.0	0.42	37.9	--	--
5×10^{20}	0.66	21.9	0.35	43.3	--	--

Table 5.4. Parameters of the simulated HDOP profiles.

Concerning the specific front contact resistivity, it is worth considering that it depends on the surface concentration, according to the theoretical model proposed by Schroder and Meier in [5.28], and, consequently, on the different HDOP profiles considered in the SE cell. The following surface concentration dependent model for the specific front contact resistivity is typically adopted [5.29]:

$$\rho_c = \rho_{c0}\ \boldsymbol{exp}\left(\frac{C_1\Phi_b}{\sqrt{N_s}}\right) \tag{5.1}$$

where ρ_{c0} is the specific contact resistivity for an infinite active surface doping concentration, C_1 is a constant (~7×10^{10} cm$^{-3/2}\cdot$eV^{-1} for Si), N_s is the surface doping concentration, and Φ_b is the barrier height between the metal and the semiconductor (0.78 eV at Ag contact/n^+-Si interfaces).

However, it has been demonstrated in [5.30] and [5.31] that the contact resistivity of screen-printed silver contacts depends not only on the surface doping concentration, but also on

several other process-dependent factors related to the contact formation. In particular, ρ_c is limited by the number and the size of the silver crystals grown into the emitter, i.e. by the silver crystal covered surface area and by the current paths from the silver crystals to the bulk of the finger [5.31]. In addition, it has been reported that the surface texture, leading to a pyramidal shape of the silver crystal, influences the contact resistance on emitters with high sheet resistance [5.30]. The values reported by Schroder and Meier in [5.28] are referred to planar contacts formed by evaporated metals on silicon and, hence, are significantly lower than the typically measured values for screen-printed silver contacts on industrial emitters [5.32]. Vinod in [5.29] suggests $\rho_c < 1$ m$\Omega\cdot$cm^2 for phosphorus surface concentrations $N_s \geq 2\times10^{19}$ cm^{-3} in case of screen-printed Ag contacts after sintering and annealing.

In this work, by considering that the contact resistivity of industrial screen-printed silver contacts is mainly limited by the process conditions of contact formation, as shown by Schubert *et al.* in [5.30] and [5.31], and by assuming that the process of contact formation does not depend on the emitter surface concentration, a constant $\rho_c = 2\times10^{-3}$ $\Omega\cdot$cm^2 has been considered for all the simulated HDOP profiles in the SE solar cell. Moreover, it is worth noting that, whereas the simulated emitter profiles at the metal/n^+-Si interface feature surface concentrations $N_s \geq 1\times10^{20}$ cm^{-3} both in HE and SE cells, the adoption of the typical surface concentration dependent model for the specific front contact resistivity (see Eq. 5.1) would result in ρ_c values well below 1 m$\Omega\cdot$cm^2, according to Vinod's data [5.29], which do not practically affect the simulation results. Therefore, the impact of the different HDOP surface doping concentrations on the ρ_c is quite negligible in the SE solar cell.

The trend of V_{oc} versus C_{peak} for the three different doses is reported in Fig. 5.4. It can be observed that, for a given dose, a lower C_{peak} and, hence, a deeper junction is slightly beneficial for the V_{oc} because of the following combined effects: 1) a lower peak doping leads to a lower surface recombination velocity in the illuminated HDOP area outside the front metal finger and 2) a deeper junction is beneficial for the reduction of the emitter saturation current density in the metallized regions $J_{0,e(met)}$, as already demonstrated in [5.13], due to the shielding effect of the minority carriers in the emitter, i.e. the holes, from the metal-semiconductor interface. As matter of fact, for a dose of 3×10^{15} cm^{-2}, ranging the C_{peak} from 5×10^{20} to 1×10^{20} cm^{-3}, the $J_{0,e(Surf)}$ decreases from ~80 fA/cm^2 to ~70 fA/cm^2 due to the lower surface recombination velocity in the exposed HDOP region, while the $J_{0,e(met)}$, weighted on the metallized area, decreases from ~333 fA/cm^2 to ~157 fA/cm^2 due to the better shielding effect of the deeper junction. In order to further highlight this effect, the simulation of a cell with $W_{se} = 0$ (i.e., no HDOP region), featuring the 100-Ω/sq emitter profile (L100 in Table 5.1) with a shallow junction of 0.25 μm, has been performed. As expected, this cell exhibits a low value of emitter dark saturation current ($J_{0,e} \approx 132$ fA/cm^2) because of reduced Auger and surface recombination losses. However, the same cell shows a higher value of $J_{0,e(met)} = 588$ fA/cm^2 due to the shallower

junction that causes an increased recombination at the metal/semiconductor interface, according to [5.13]. Nevertheless, simulation results reported in Fig. 5.4 only reveals a weak dependence of the V_{oc} on the HDOP profile: the maximum variation of the V_{oc} is limited to ~0.75 mV (~0.12%). On the contrary, a stronger impact of the HDOP profile on the J_{sc} is highlighted in Fig. 5.4, where a maximum change of 0.75 mA/cm^2 (~2.1%) has been observed. For a given dose, a higher C_{peak} leads to larger J_{sc} (see Fig. 5.4), despite higher Auger and surface recombination losses in the exposed HDOP area, because of the shallower junction.

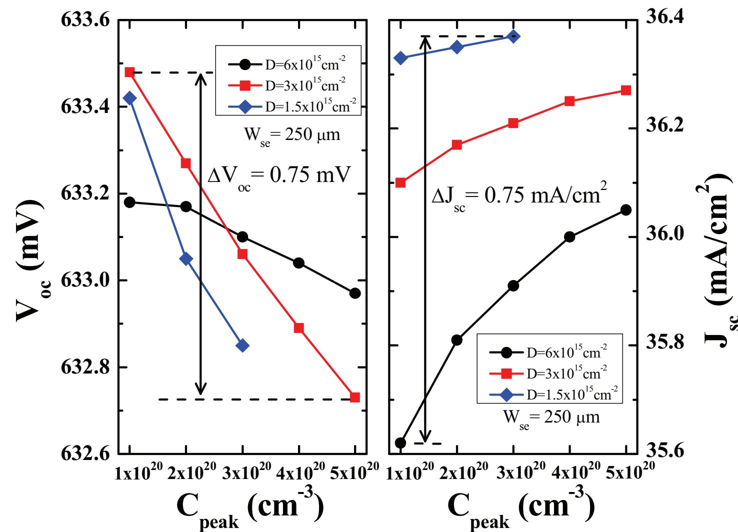

Figure 5.4. (Left) Open-circuit voltage V_{oc}, and (right) short-circuit current density J_{sc} versus peak doping concentration C_{peak} at three different dose concentrations (6x10^{15}, 3x10^{15}, and 1.5x10^{15} cm^{-2}) for the simulated HDOP profiles, by assuming a HDOP lateral width W_{se} of 250 µm.

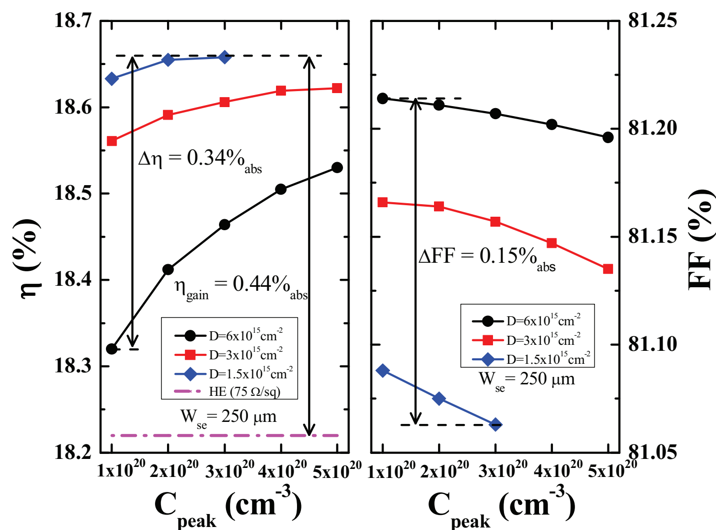

Figure 5.5. (Left) Efficiency η, and (right) fill factor FF versus peak doping concentration C_{peak} at three different dose concentrations (6x10^{15}, 3x10^{15}, and 1.5x10^{15} cm^{-2}) for the simulated HDOP profiles, by assuming a HDOP lateral width W_{se} of 250 µm.

The dominant impact of the HDOP profile on J_{sc} is confirmed by the efficiency graph in Fig. 5.5, where a similar trend can be found. Fig. 5.5 shows that an improper HDOP diffusion may result in an efficiency loss up to $0.34\%_{abs}$. It is worth noting that, the lower is the dose, the lower is the impact of the HDOP profile. This is due to the fact that, at low doses, by varying the C_{peak}, the change in the junction depth of the corresponding HDOP profiles is lower than that observed at higher values of dose and, hence, the effect on J_{sc} is similar for the HDOP profiles at such doses.

The analysis also shows in Fig. 5.5 a slight effect of the HDOP profile on the *FF* with a maximum variation of $0.15\%_{abs}$, due to the fact that the emitter resistance of the SE cell is dominated by the LDOP regions. A higher value of *FF* is observed by increasing the dose and, for a given dose, by decreasing the peak concentration, due to the reduction of the HDOP sheet resistance (see Table 5.4).

5.1.5 Investigation on the alignment tolerance

The analysis performed in the previous section, which has been carried out by considering a large lateral width of the highly-doped region (W_{se}) equal to 250 µm (i.e., 150 µm wider than the finger width), clearly shows a strong impact of different HDOP profiles on the J_{sc} and, then, on the efficiency of the SE solar cell, particularly at low sheet resistances (hence at high dose concentrations) of the HDOP profile. In order to understand the impact on the SE cell performance of the alignment tolerance used in the SE diffusion process for the subsequent metallization process, the previous analysis has been repeated for other two values of W_{se}, 400 µm and 150 µm. The relative efficiency curves are reported in Fig. 5.6.

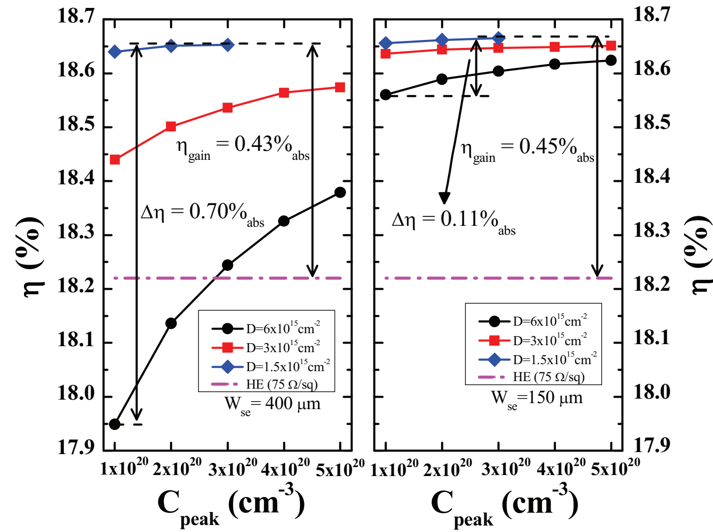

Figure 5.6. Efficiency η versus peak doping concentration C_{peak} at three different dose concentrations ($6x10^{15}$, $3x10^{15}$, and $1.5x10^{15}$ cm^{-2}) for the simulated HDOP profiles, by assuming a HDOP lateral width W_{se} of (left) 400 µm, and (right) 150 µm.

This further investigation reveals a strong influence of the HDOP lateral width on the J_{sc} and, consequently, on the efficiency of the SE cell, especially at low sheet resistance HDOP profiles. In fact, as long as the alignment tolerance (and, then, the exposed HDOP area) decreases, the efficiency of the SE cell becomes less dependent on the dose and the peak doping concentration. This is because the exposed HDOP region (outside the front metal finger) is a source of large variation on J_{sc}, due to a J_{depth} dependent effect (as discussed in Section 5.1.4). Indeed, while for a W_{se} = 400 µm a large efficiency variation of $0.70\%_{abs}$ is observed, a smaller W_{se} = 150 µm results in a much lower variation ($0.11\%_{abs}$), as shown in Fig. 5.6. This means that an improved alignment process and, consequently, a smaller alignment tolerance can reduce the dependence of the SE performance on the HDOP profile and, hence, makes less critical the SE diffusion process, allowing a wider process window and, consequently, a better control of

the diffusion process. Obviously, a reduced W_{se} also enhances the cell performance. This results in an increased gain efficiency of 0.45%$_{abs}$ for the SE cell with respect to the 75-Ω/sq HE cell (Fig. 5.6). It is particularly important to note (focusing on the lower dose curves in Figs. 5.5 and 5.6) that a lower dopant dose and, hence, a higher sheet resistance leads to a reduction of the benefit achievable from a decreased alignment tolerance. This means that the alignment tolerance becomes a less critical issue when the HDOP regions feature a higher sheet resistance.

The SE (W_{sub} = 2 mm, 100-Ω/sq LDOP, 50-Ω/sq HDOP) and HE (W_{sub} = 2.2 mm, 75 Ω/sq) solar cells have been also compared in Fig. 5.7 in terms of collection efficiency of the photogenerated electron-hole pairs, which is calculated as the ratio between the short-circuit current density J_{sc} and the photogenerated current density J_{ph} as a function of the wavelength λ of the radiation, within the wavelength range 300-1200 nm.

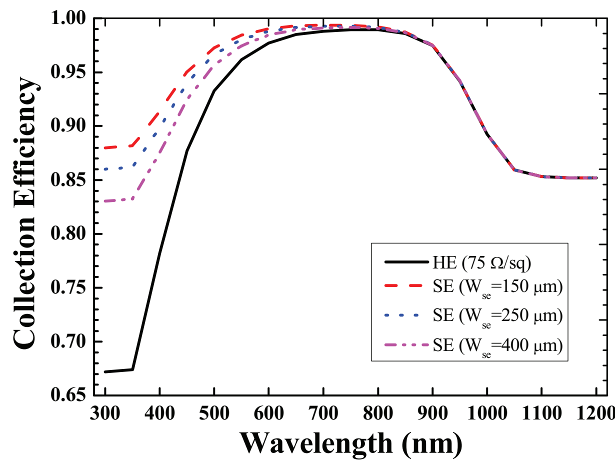

Figure 5.7. Collection efficiency η_c within the wavelength range 300-1200 nm for the simulated HE (W_{sub} = 2.2 mm, 75 Ω/sq) and SE (W_{sub} = 2.0 mm, 100-Ω/sq LDOP, 50-Ω/sq HDOP) solar cells.

As expected, the SE cell shows a better spectral response in the blue region of the spectrum, resulting in a higher short-circuit current density and open-circuit voltage (as already discussed previously). In addition, the simulation results in terms of collection efficiency (see Fig. 5.7) show an improved blue spectral response at W_{se} = 150 μm, confirming that the reduction of the alignment tolerance is beneficial for the SE cell. The benefit of the SE cell in terms of blue spectral response with respect to the HE cell is mainly due to the lower doping concentration in the LDOP emitter regions, leading to reduced Auger and surface recombination losses, as well as to the shallower LDOP junction which improves the collection of minority carriers generated close to the front surface mainly contributed by photons at lower wavelengths (i.e., in the range 300-600 nm).

In Table 5.5, the effect of Auger and surface recombination losses has been individually evaluated in the simulated cells, by disabling alternately the two mechanisms in the simulation. When Auger recombination mechanism is not taken into account, the efficiency gain of SE over HE slightly reduces from 0.40%$_{abs}$ to 0.34%$_{abs}$. On the other hand, by disabling the front surface recombination, the efficiency gain of SE over HE reduces to only 0.06%$_{abs}$. Therefore, numerical simulations show that the decrease of the surface recombination losses is the main advantage of the SE design compared with the standard HE solar cell, as already highlighted by the dark analysis results reported in Section 5.1.3. Furthermore, in Table 5.5, it has been demonstrated that by neglecting both the recombination mechanisms, the HE cell becomes more efficient than the SE cell, due to the reduced emitter resistance and, then, to the higher *FF*.

AUGER	**SURFACE SRH**	**SE CELL** η [%]	**HE CELL** η [%]	Δ_{abs}
Y	Y	18.62	18.22	+0.40
N	Y	18.71	18.37	+0.34
Y	N	18.92	18.86	+0.06
N	N	19.05	19.12	-0.07

Table 5.5. Efficiency values for the HE (W_{sub} =2.2 mm, 75 Ω/sq) and SE (W_{sub} =2.0 mm, W_{se} =250 µm, 100-Ω/sq LDOP, 50-Ω/sq HDOP) solar cells under different assumptions for the Auger and surface recombination losses: Y indicates that the recombination mechanism is taken into account, while N is used for the opposite case.

5.1.6 Effect of DP process over SE design

The improvement of the front-side of solar cells, both in terms of emitter region and front metallization, is a relevant task in PV industry. The SE design represents a promising and low-cost concept which allows to enhance the front-side performance by reducing the emitter recombination losses, as shown in the previous analysis. In addition, it has been already demonstrated in Chapter 4 that advanced front metallization techniques, like the double screen-printing (DP), can further enhance the cell performance, leading to increased aspect ratios of the front metal fingers and, consequently, to reduced shadowing effects. It is worth noting that DP and SE are complementary processes. Therefore, an increased efficiency gain is expected when the DP front metallization is implemented over a SE design. The process scheme based on the combined use of the DPII (second-generation) and SE techniques is described in Fig. 5.8, consisting of:

- the realization of the SE design with the formation of the HDOP regions, using the same pattern of the front metal fingers;
- the first print of the optimized paste for contacting the emitter, using only the finger pattern and ensuring a good alignment with the HDOP areas;
- the second print of the more conductive paste with the full H-pattern (fingers + busbars), ensuring the alignment on the features of the first printing.

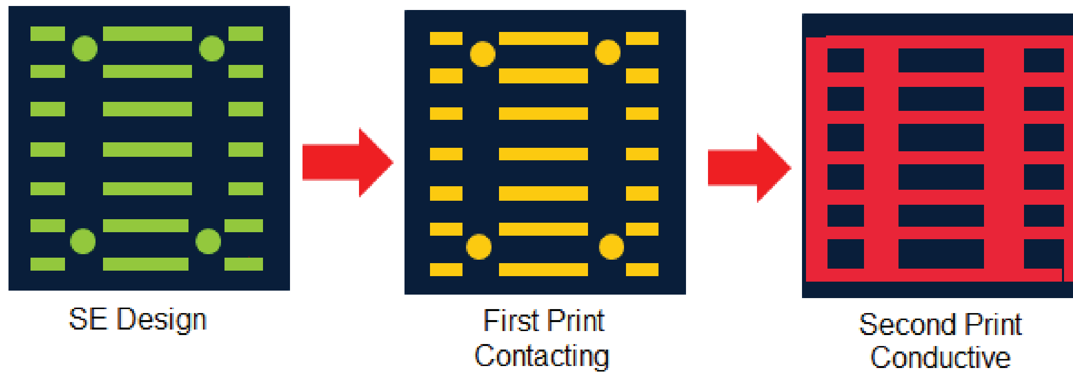

Figure 5.8. Process scheme for the combined use of second-generation double screen-printing (DPII) and selective emitter (SE) techniques.

In this work, in order to investigate the effect of the use of double screen-printing technology in combination with SE concept (i.e., SE-DP), the analysis of the impact of different LDOP profiles (refer to Table 5.1) at different front contact pitch values (ranging from 1.4 mm to 2.4 mm with a step of 200 µm) has been repeated for a SE solar cell featuring DPII front metal fingers (refer to Table 4.4 for the parameters of DPII fingers). The comparison with the conventional single screen-printing (SP) technology has allowed to estimate the expected performance improvements.

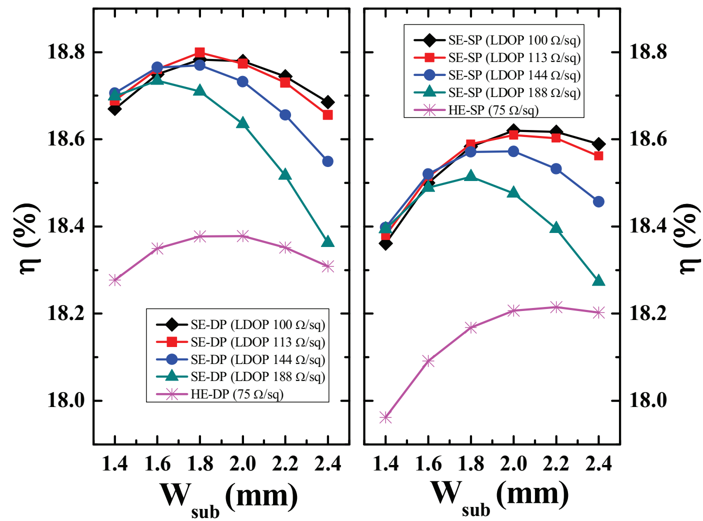

Figure 5.9. Efficiency η versus front contact pitch W_{sub} for the (left) SE-DP, and (right) SE-SP solar cells at different simulated LDOP profiles, and for the 75-Ω/sq (left) HE-DP, and (right) HE-SP solar cells.

The corresponding efficiency versus W_{sub} curves for the considered SE-DP cells are reported in Fig. 5.9. For comparison, Fig. 5.9 also reports the efficiency curves for the simulated SE-SP cells, already shown in Fig. 5.3. Note that, for a given LDOP sheet resistance, the peak efficiency moves toward lower W_{sub} for the DP cells because of the reduced shadowing effect and the increased emitter resistance, according to what already discussed in Section 4.2.2. As a matter of fact, in case of SE-DP cell, the maximum efficiency (18.80%) is reached with the 113-Ω/sq LDOP profile at W_{sub} = 1.8 mm. The full comparison between all the simulated configurations of solar cells (i.e., HE-SP, HE-DP, SE-SP and SE-DP) featuring the maximum efficiency is summarized in Table 5.6.

	W_{sub} [mm]	R_{sq_LDOP} [Ω/sq]	J_{sc} [mA/cm^2]	V_{oc} [mV]	FF [%]	η [%]	$J_{0,tot}$ [fA/cm^2]	$J_{0,e}$ [fA/cm^2]
HE-SP	2.2	--	35.83	628.3	80.91	18.22	1009.5	284.4
HE-DP	2.0	--	36.13	628.8	80.89	18.38	1006.5	281.0
SE-SP	2.0	100	36.28	632.8	81.11	18.62	860.7	135.1
SE-DP	1.8	113	36.60	633.4	81.10	18.80	856.4	130.7

Table 5.6. Comparison between the simulated HE-SP, HE-DP, SE-SP, and SE-DP solar cells featuring the maximum efficiency.

As expected, simulation results clearly demonstrate that the use of DP technology in combination with the SE design allows to enhance the cell performance. Moreover, in Table 5.6, it is shown that a small additional efficiency gain can be obtained through the combined use of the two advanced processes. In fact, the efficiency gain of DP over SP slightly increases from 0.16%$_{abs}$ in case of HE cell up to 0.18%$_{abs}$ in case of SE cell. Accordingly, the efficiency gain of

the SE cell with respect to the 75-Ω/sq HE cell rises from 0.40%$_{abs}$ in case of SP metallization up to 0.42%$_{abs}$ in case of DP metallization. In order to better understand the source of this additional efficiency gain, it is worth noting that these comparative results are influenced by the different emitter resistance, illuminated area and emitter recombination losses in the considered cells, as a result of the different front contact pitch values (see Table 5.6) and/or front metallization width. In addition, the two considered SE cells are also characterized by different LDOP profiles (see Table 5.6). Therefore, the observed additional efficiency gain shown by the SE-DP cell can be mainly ascribed to the sum of the benefits of the SE design and the DP technology in terms of reduced shadowing effects (leading to larger J_{sc}) and recombination losses (leading to lower saturation current density and, consequently, higher V_{oc}), in combination with a proper optimization of the doping profiles in the SE solar cell.

5.2 Simulation of rear point contact solar cells

The adoption of rear point contact (RPC) schemes in high-efficiency monocrystalline silicon solar cells is one of the most promising approaches to reduce the recombination losses at the rear side of the device. However, the reduction of the rear contact area results in an increase of series resistance losses, thus leading to a degradation of the fill factor. In this work, rigorous three-dimensional (3-D) numerical simulations, compared with experimental measurements of a reference cell, have been performed to optimize the rear contact design of a RPC solar cell, featuring also a high sheet resistance (140 Ω/sq) phosphorus-doped emitter and a front-side metallization with narrow and highly-conductive electro-plated copper lines (40-µm-wide) on lowly resistive Ti contacts [5.33]. Simulation results show that an optimization of the rear point contact design potentially leads to a conversion efficiency above 20%.

5.2.1 Introduction to rear point contact solar cells

Conventional screen-printed solar cells, featuring a uniformly contacted rear surface, are affected by significant recombination losses at the rear side, as discussed in Chapter 4. An effective strategy to increase the performance of monocrystalline silicon solar cells is the realization of a rear point contact design, which is typically implemented in high-efficiency PERC (Passivated Emitter Rear Cell) and PERL (Passivated Emitter Rear Locally diffused) solar cells [5.34], [5.35] (Fig. 5.10). The main advantage of the RPC design is given by the reduction of the effective rear surface recombination velocity because of the passivation of the non-contacted rear areas. In addition, the rear passivation leads to increase the effective internal bottom reflectivity due to the larger reflectivity of *c*-Si/dielectric/metal stack interface (typically around 0.90, depending upon the dielectric) with respect to the *c*-Si/metal one (around 0.65) [5.4], [5.36]. Aside from considerations on increased manufacturing complexity and costs, the main drawback of RPC cells derives from the increase of the parasitic series resistances, such as the base spreading resistance (due to the current crowding at rear local point contacts) and the back contact resistance (due to the reduction of the rear contact area).

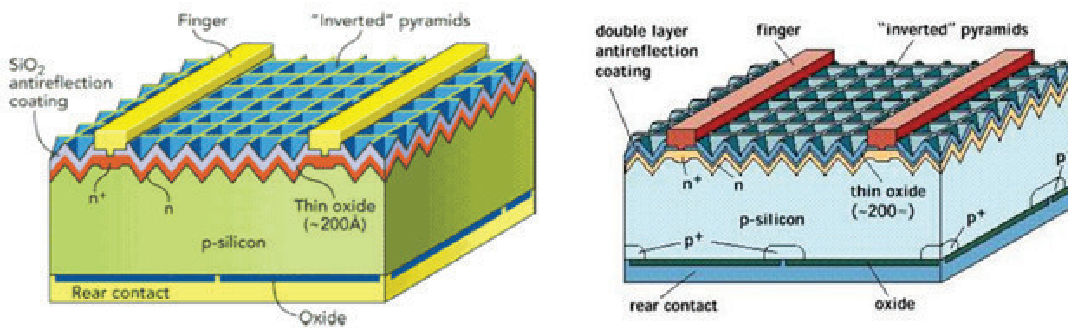

Figure 5.10. Rear point contact (RPC) solar cells: (left) PERC (Passivated Emitter Rear Cell) and (right) PERL (Passivated Emitter Rear Locally diffused) solar cells

Low-cost and high-volume manufacturing processes for RPC solar cells typically involve the use of the Laser Firing Contact (LFC) technique, which leads to the formation of a local back-surface field (BSF) p^+-diffusion at rear point contacts [5.37], [5.38]. In particular, LFC technique allows to fabricate rear holes featuring laser spot diameters within the range 25-50 μm and relatively low specific contact resistivity (0.05-3 mΩ·cm^2) for a wide substrate resistivity range (0.01-100 Ω·cm) [5.38]. In RPC solar cells (see Fig. 5.10), the non-contacted rear-side areas are typically passivated by dielectrics, like silicon nitride (Si_3N_4) and/or silicon dioxide (SiO_2), leading to low surface recombination velocities, within 1-100 cm/s range, depending on the process quality and the substrate resistivity. Moreover, the future trend toward thin *c*-Si solar cells has pushed for the development of low-cost and efficient rear surface passivation processes, as one based on the amorphous hydrogenated silicon nitride (*a*-SiN_x:H) deposited by low-temperature Plasma Enhanced Chemical Vapour Deposition (PECVD) [5.39].

5.2.2 Simulation setup

Due to the complexity of the RPC geometry, a careful analysis and optimization of the RPC solar cells require a rigorous 3-D modeling approach [5.40]-[5.42], in order to properly account for the trade-off between the several competing physical mechanisms occurring in these cells, such as the different internal bottom optical reflectivity and surface recombination velocity at the passivated and metallized rear surfaces, the base spreading series resistance effects due to the 3-D current crowding paths at rear local point contacts, and the back contact resistance. Nevertheless, several authors have adopted 1-D numerical modeling combined with semi-empirical models to approximately account for 3-D effects on the electrical transport and recombination losses [5.43], [5.44], or have limited the analysis to simplified 2-D spatial domains [5.45], [5.46]. In [5.47], the optimization of a PERL-type solar cell was performed with a simplified 3-D Finite Difference simulation method, assuming low injection conditions and an ideal emitter. In [5.48], a 3-D simulation method based on the numerical solution through the Fast Fourier Transform of the minority and majority carrier transport equations in the base of a PERC-type solar cell was proposed. Moreover, an extensive simulation study based on 3-D electro-optical numerical device simulations has been reported in [5.42], aiming at highlighting the dependence of the conversion efficiency of PERC- and PERL-type solar cells on the main geometrical and technological parameters, such as the pitch and the size of rear local point contacts, and the substrate resistivity. In this thesis, 3-D numerical TCAD-based device simulations have been performed to optimize the rear point contact geometry of a reference PERC-type solar cell, which also features a 140-Ω/sq phosphorus-doped front emitter and electro-plated Ti/Cu front contacts (40-μm-wide), thus leading to further improvements, as shown in [5.49]. Indeed, introducing a high sheet resistance emitter with a low surface concentration is beneficial to reduce surface and Auger recombination losses at the front side. In addition, by replacing the relatively wide screen-printed silver front-side fingers with narrower, denser and better conducting Ti/Cu electro-plated lines, front contact shadowing and resistive losses can be reduced. The optimization of the rear point contact design has been carried out by changing the rear contact pitch, and by considering a constant rear contact diameter of 35 μm. It is worth noting that the size of the rear contacts is set consistently with the technological limitation of the laser rear patterning process used to form local contact holes [5.49], [5.50].

The reference PERC cell (size 12.5×12.5 cm^2) features a 1.3 Ω·cm, 150-μm-thick *p*-type *Cz*-Si substrate and a random pyramid textured front surface with a 80-nm-thick SiN_x anti-reflective coating (ARC) layer. The front-side electro-plated Ti/Cu contacts are 40-μm-wide with a thickness of 9 μm and a pitch of 1.53 mm. The rear-side metallization consists of local Al contact holes with a diameter of 35 μm and a pitch of 550 μm, while the rear passivation layer features a SiO_2/SiN_x stack. A local Al-BSF is formed in the openings by firing the rear Al layer.

Further details on the process and the design of the reference PERC-type cell are reported in [5.50]. The performance of this reference cell has been measured and summarized in Table 5.7. The related illuminated *J-V* curve is shown in Fig. 5.11.

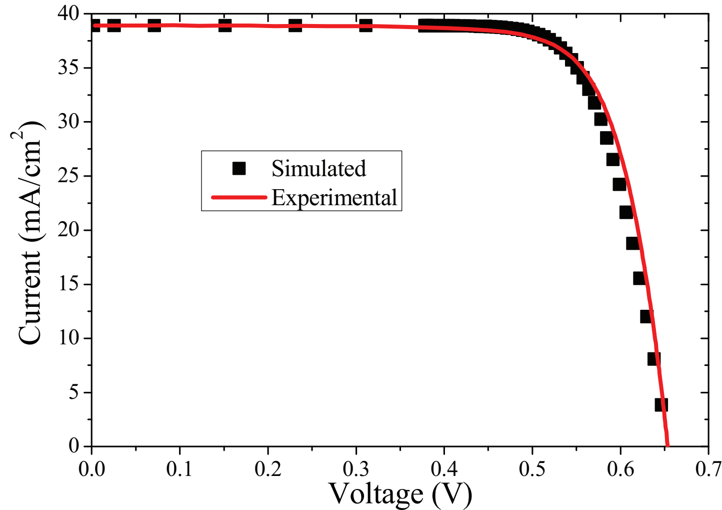

Fig. 5.11. Experimental and simulated *I-V* curves for the reference PERC solar cell.

Cell type	J_{sc} **[mA/cm^2]**	V_{oc} **[mV]**	***FF*** **[%]**	η **[%]**
Measured	38.9	653.7	77.0	19.6
Simulated	38.9	653.6	77.1	19.6

Table 5.7. Comparison between the performance of the experimental and simulated PERC solar cells.

The simulated 3-D structure, built and configured on the basis of the characteristics of the reference cell, is shown in Fig. 5.12, representing a quarter of the 3-D symmetric element. Indeed, the simulation domain has been selected by following these criteria [5.41]:

- the length L_x (along the x-axis) is half of the front contact pitch (W_{sub}), assuming that the front contact pitch is larger than the rear contact pitch (p);
- the width L_z (along the z-axis) is half of the rear contact pitch and, consequently, only half of the rear hole contact has been placed along this direction (see Fig. 5.12);
- the height W is equal to the substrate thickness (W).

In order to preserve the symmetry of the rear contacts along the x-direction, the rear contact pitch of the simulated structure has been set to 510 μm to make sure that the ratio between the front contact pitch (1.53 mm) and the rear hole pitch is an integer number. Furthermore, an automatic procedure has been developed to ensure the correct placement of the rear point contacts and the local rear BSF p^+-diffusion along the x-axis, starting from the lower-left corner of the simulation domain, according to the considered front contact pitch, rear contact pitch and rear contact size.

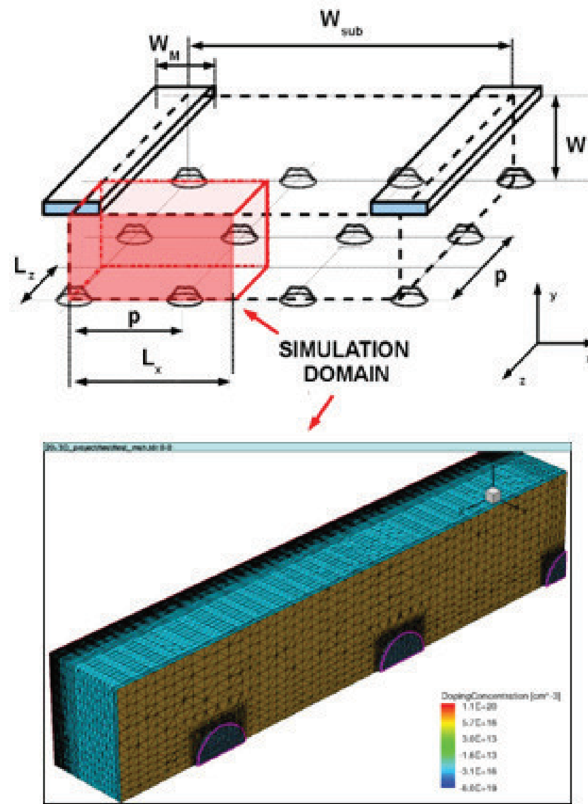

Fig. 5.12. (Top) 3-D sketch of the simulated RPC solar cell. W_{sub} is the front contact pitch, W the substrate thickness, W_M the finger width, and p the rear contact pitch, respectively. The considered simulation domain is highlighted in red ($L_x = W_{sub}/2$, $L_z = p/2$, $L_y = W$).
(Down) Back view of the 3-D simulated structure.

The definition of the discretization grid mesh is quite critical in these inherent 3-D structures. In particular, an accurate mesh refinement is required around the rear point contacts to improve the simulation accuracy (see Fig. 5.13), due to the local BSF diffusion and the 3-D current crowding in these regions.

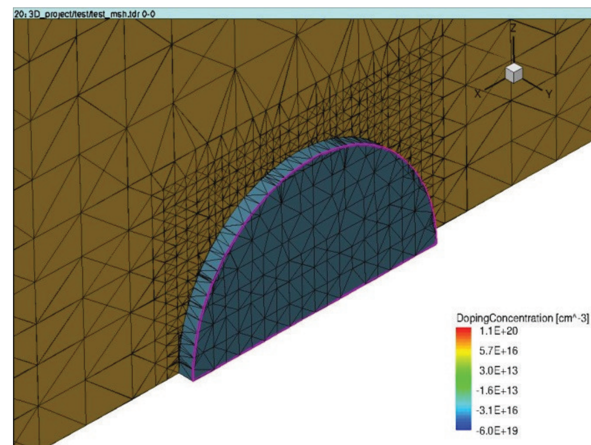

Fig. 5.13. Mesh refinement around the rear hole point contact in order to improve the simulation accuracy.

An ad-hoc calibration of the physical parameters and models has been performed to obtain realistic predictions in the optimization procedure. The adopted models include the Schenk band-gap narrowing model to account for the effective intrinsic density [5.51], [5.52], and the doping-dependent front surface recombination velocity (SRV) model according to [5.53]. The main critical parameters of the simulated reference PERC solar cell are summarized in Table 5.8. The SRV at the rear passivated surfaces is set to 330 cm/s, while the front/rear contact SRV at electrodes is assumed to be $2x10^6$ cm/s, similarly to that used in [5.49], [5.50]. It is worth noting that the assumed values for the SRV at rear-side passivated and metallized surfaces and the rear metallization fraction strongly impact on the effective rear surface recombination velocity and, consequently, on the performance of a locally contacted rear surface passivated solar cell, as well described in [5.44].

Parameter	*value*	*units*
Substrate thickness	150	μm
Substrate resistivity	1.3	Ω·cm
Front ARC thickness	80	nm
Front contact width	40	μm
Front contact thickness	9	μm
Front contact pitch	1530	μm
Front finger length	12.3	cm
Rear contact size (diameter)	35	μm
Rear contact pitch	510	μm
Rear contact fraction	0.37	%
Rear passivation SRV	330	cm/s
Front/rear contact SRV	2×10^6	cm/s
Bulk lifetime	500	μs
Front metal resistivity	1.8×10^{-6}	Ω·cm
Front contact resistivity	5×10^{-4}	$\Omega\cdot cm^2$
Rear contact resistivity	1×10^{-3}	$\Omega\cdot cm^2$

Table 5.8. Parameters of the simulated PERC solar cell.

The optical simulation has been performed at 1-sun illumination condition with the Ray-Tracer tool which is implemented in the TCAD simulator [5.20], accounting for the front texturing and ARC layer, and for the different optical generation profiles at rear passivated and metallized surfaces, according to their different interface reflectivity [5.54]. In particular, the internal bottom reflectivity at rear-side metallized and passivated surfaces has been set to 0.65 and 0.90, respectively. Accordingly, the optical generation profile placement has been

performed by dividing the device into three different types of regions (see Fig. 5.14): the region underneath the front contact, where there is no optical generation due to the assumed ideal shadowing, the regions whose rear surface is covered with the rear point contacts, and the regions whose rear surface is passivated.

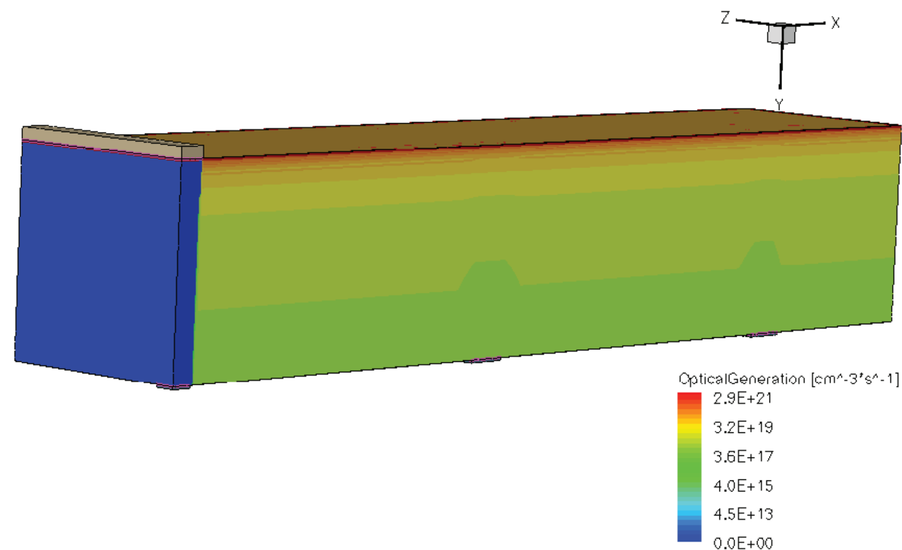

Fig. 5.14. Map of the optical generation inside the simulated 3-D structure.

The 140 Ω/sq phosphorus-doped emitter has been modeled by a Gaussian function with a peak concentration of 2×10^{19} cm^{-3} and a junction depth of 0.6 µm. All the series parasitic resistance losses (including the front and the back contact resistance, and the front metal resistance) have been accounted by a post-processing analysis. The shunt resistance and the busbars resistance have been neglected. It is worth noting that the non-ideal resistive-limited enhanced recombination effects (giving a local non-ideal factor $n_2 > 2$) [5.50] have been not taken into account.

The performance and the illuminated *J-V* curve of the simulated reference solar cell are reported in Table 5.7 and Fig. 5.11, respectively. A good agreement can be observed between experimental and simulated results.

5.2.3 Optimization of the rear point contact design

The optimization of the PERC cell has been performed in terms of rear contact pitch, keeping the diameter of the rear hole contacts constant (35 μm). The simulation results for the short-circuit current density (J_{sc}), the open-circuit voltage (V_{oc}), the fill factor (FF) and the efficiency (η) as a function of the rear contact fraction (CF_{rear}), defined as the ratio of the rear contacted area to the total cell area, are plotted in Fig. 5.15.

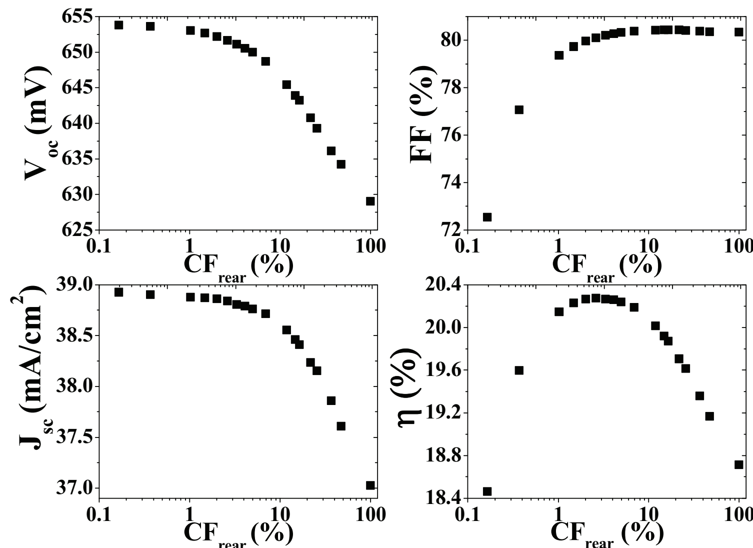

Fig. 5.15. Simulation results for the optimization of the rear point contact geometry in terms of short-circuit current density J_{sc}, open-circuit voltage V_{oc}, fill factor FF and efficiency η as a function of the rear contact fraction CF_{rear}.

As expected, by decreasing the CF_{rear}, both J_{sc} and V_{oc} increase due to the reduction of the effective rear surface recombination velocity and to the increase of the effective internal bottom reflectivity. On the contrary, an opposite trend can be observed for the FF: by decreasing the CF_{rear}, the base spreading resistance and the back contact resistance increase, leading to a strong degradation of the FF at $CF_{rear} < 1\%$. The efficiency trade-off due to these opposite trends leads to an optimal value of CF_{rear} within the range 2-3%. It is worth noting that the obtained optimum value of CF_{rear} is influenced by several factors: among them, the assumed SRV values at rear metallized and passivated surfaces, the substrate resistivity and the size of the rear point contacts. Concerning the hole contact diameter, it has already been shown in [5.42] that the optimization of PERC-type solar cells depends on the size of the rear point contacts. In particular, for a given rear contact fraction, a smaller hole diameter means a smaller distance between adjacent rear contacts, thus leading to higher efficiency because of a reduced base spreading resistance. Moreover, a smaller hole contact diameter leads to a lower optimum value of CF_{rear}, as shown in [5.42].

In Table 5.9, the simulation results obtained for the reference cell (CF_{rear} = 0.37%), for the optimal cell (CF_{rear} = 2.63%, equivalent to a rear contact pitch of 191.25 μm) and for the rear full-metallized cell (CF_{rear} = 100%) are compared. The simulation results show that the optimization of the rear point contact design for the considered PERC-type solar cell can potentially lead to an efficiency improvement of 0.68%$_{abs}$ with respect to the reference cell, and of 1.57%$_{abs}$ with respect to the case of full-metallized rear side, thus resulting in a conversion efficiency above 20%.

Cell type	**CF_{rear} [%]**	**J_{sc} [mA/cm^2]**	**V_{oc} [mV]**	**FF [%]**	**η [%]**
Reference	0.37	38.90	653.63	77.07	19.60
Optimal	2.63	38.84	651.64	80.11	20.28
Rear full-metallized	100	37.03	629.06	80.34	18.71

Table 5.9. Simulation results for the reference, the optimal and the rear full-metallized solar cells.

References

[5.1] M. Edwards et al., "Screen-Print Selective Diffusions for High-Efficiency Industrial Silicon Solar Cells", *Progress in Photovoltaics: Research and Applications*, Vol. 16, No. 7, pp. 31-45, 2008.
[5.2] P. Kumar et al., "Industrial Selective Emitter Processes for Czochralski-Silicon Solar Cells", *Proc. of 26th European Photovoltaic Solar Energy Conference* (*EU PVSEC*), pp. 1334-1339, 2011.
[5.3] R. De Rose et al., "Understanding the Impact of the Doping Profiles on Selective Emitter Solar Cell by Two-Dimensional Numerical Simulation", *IEEE Journal of Photovoltaics*, DOI:10.1109/JPHOTOV.2012.2214376, pp. 1-9, 2012.
[5.4] T. Dullweber et al., "Towards 20% efficient large-area screen-printed rear-passivated silicon solar cells", *Progress in Photovoltaics: Research and Applications*, Vol. 20, No. 6, pp. 630-638, 2012.
[5.5] M.M. Hilali, A. Rohatgi, S. Asher, "Development of Screen-Printed Silicon Solar Cells With High Fill Factors on 100 Ω/sq Emitters", *IEEE Transactions on Electron Devices*, Vol. 51, No. 6, pp. 948-955, 2004.
[5.6] M.M. Hilali et al., "Understanding and development of Ag pastes for silicon solar cells with high sheet-resistance emitters", *Proc. of 19th European Photovoltaic Solar Energy Conference* (*EU PVSEC*), pp. 1300-1303, 2004.
[5.7] A. Ebong et al., "Understanding the role of glass frit in the front Ag paste for high sheet resistance emitters", *Proc. of 22nd European Photovoltaic Solar Energy Conference* (*EU PVSEC*), pp. 1734-1737, 2007.
[5.8] A. Ebong, D.S. Kim, A. Rohatgi, W. Zhang, "Understanding the mechanism of light induced plating of silver on screen-printed contacts for high sheet resistance emitters with low surface phosphorous concentration", *Proc. of 33rd IEEE Photovoltaic Specialists Conference* (*PVSC*), pp. 1-5, 2008.
[5.9] A. Ebong et al., "High efficiency silicon solar cells with ink jetted seed and plated grid on high sheet resistance emitter", *Proc. of 35th IEEE Photovoltaic Specialists Conference* (*PVSC*), pp. 1363-1367, 2010.
[5.10] M. Hörteis, S. W. Glunz, "Fine line printed silicon solar cells exceeding 20% efficiency", *Progress in Photovoltaics: Research and Applications*, Vol. 16, No. 7, pp. 555-560, 2008.
[5.11] G. Hahn, "Status of Selective Emitter Technology", *Proc. of 25th European Photovoltaic Solar Energy Conference* (*EU PVSEC*), pp. 1091-1096, 2010.
[5.12] T. Röder et al., "0.4% Absolute Efficiency Gain of Industrial Solar Cells by Laser Doped Selective Emitter ", *Proc. of 34th IEEE Photovoltaic Specialists Conference* (*PVSC*), pp. 871-873, 2009.
[5.13] U. Jäger et al., "Influence of Doping Profile of Highly Doped Regions for Selective Emitter Solar Cells ", *Proc. of 35th IEEE Photovoltaic Specialists Conference* (*PVSC*), pp. 3185-3189, 2010.
[5.14] B. Raabe et al., "The Development of Etch-Back Processes for Industrial Silicon Solar Cells", *Proc. of 25th European Photovoltaic Solar Energy Conference* (*EU PVSEC*), pp. 1174-1178, 2010.
[5.15] F. Book, B. Raabe, G. Hahn, "Two diffusion step selective emitter: comparison of mask opening by laser or etching paste", *Proc. of 23rd European Photovoltaic Solar Energy Conference* (*EU PVSEC*), pp. 1546-1549, 2008.
[5.16] R. De Rose et al., "2-D numerical analysis of the impact of the highly-doped profile on selective emitter solar cell performance", *Proc. of 37th IEEE Photovoltaic Specialists Conference* (*PVSC*), pp. 2556-2559, 2011.
[5.17] A. Rohatgi et al.,, "Self-Aligned Self-Doping Selective Emitter for Screen-Printed Silicon Solar Cells", *Proc. of 17th EU PVSEC*, pp. 2001.
[5.18] N. Stem, M. Cid, "Physical limitations for homogeneous and highly doped n-type emitter monocrystalline silicon solar cells", *Solid-State Electronics*, Vol. 48, No. 2, pp. 197-205, 2004.
[5.19] A. Cuevas, D.A. Russell, "Co-optimisation of the Emitter Region and the Metal Grid of Silicon Solar Cells", *Progress in Photovoltaics: Research and Applications*, Vol. 8, No. 6, pp. 603-616, 2000.
[5.20] Sentaurus Device User Guide, Synopsys, Mountain View, CA.

[5.21] P. P. Altermatt et al., "Highly Predictive Modelling of Entire Si Solar Cells for Industrial Applications", *Proc. of 24th European Photovoltaic Solar Energy Conference* (*EU PVSEC*), pp. 901-906, 2009.
[5.22] D. Fenning, M. Bertoni, T. Buonassisi, "Predictive modeling of the optimal phosphorus diffusion profile in silicon solar cells", *Proc. of 24th European Photovoltaic Solar Energy Conference* (*EU PVSEC*), pp. 1893-1896, 2009.
[5.23] S. Solmi, A. Parisini, R. Angelucci, "Dopant and carrier concentration in Si in equilibrium with monoclinic SiP precipitates", *Physical Review B*, Vol. 53, No. 12, pp. 7836-7841, 1996.
[5.24] A. Kimmerle et al., "Modelling carrier recombination in highly phosphorus-doped industrial emitters", *Energy Procedia*, Vol. 8, pp. 275-281, 2011.
[5.25] D. B. M. Klaassen, "A unified mobility model for device simulation: I. model equations and concentration dependence", *Solid-State Electronics*, Vol. 35, No. 7, pp. 953-959, 1992.
[5.26] D. B. M. Klaassen, "A unified mobility model for device simulation: II. temperature dependence of carrier mobility and lifetime", *Solid-State Electronics*, Vol. 35, No. 7, pp. 961-967, 1992.
[5.27] M. Zanuccoli et al., "2-D numerical simulation and modeling of monocrystalline selective emitter solar cells", *Proc. of 35th IEEE Photovoltaic Specialists Conference* (*PVSC*), pp. 2262-2265, 2010.
[5.28] D. K. Schroder and D. L. Meier, "Solar Cell Contact Resistance – A Review", *IEEE Transactions on Electron Devices*, Vol. 31, No. 5, pp. 637-647, 1984.
[5.29] P. N. Vinod, "SEM and specific contact resistance analysis of screen-printed Ag contacts formed by fire-through process on the shallow emitters of silicon solar cells", *Journal of Material Science*, Vol. 20, pp. 1026-1032, 2009.
[5.30] G. Schubert et al., "Silver thick film contact formation on lowly doped phosphorus emitters", *Proc. of 20th European Photovoltaic Solar Energy Conference* (*EU PVSEC*), pp. 934-937, 2005.
[5.31] G. Schubert, J. Horzel, S. Ohl, "Investigations on mechanism behind the beneficial effect of a forming gas anneal on solar cells with silver thick film contacts", *Proc. of 21st European Photovoltaic Solar Energy Conference* (*EU PVSEC*), pp. 1460-1466, 2006.
[5.32] S. Kontermann, "Characterization and modeling of contacting crystalline silicon solar cells", *Ph.D. dissertation*, *Department of Physics*, *University of Konstanz*, *Germany*, 2009.
[5.33] R. De Rose et al., "Optimization of Rear Point Contact Geometry by Means of 3-D Numerical Simulation", *Energy Procedia*, Vol. 27, pp. 197-202, 2012.
[5.34] M. A. Green, "Silicon Solar Cells: Advanced Principles & Practice", *Centre for Photovoltaic Devices and Systems*, University of New South Wales, 1995.
[5.35] J. Zhao et al., "24% efficient PERL silicon solar cells: recent improvements in high efficiency silicon cell research", *Solar Energy Materials and Solar Cells*, Vol. 41/42, No. 26, pp. 87-99, 1996.
[5.36] S. W. Glunz, "High-efficiency crystalline silicon solar cells", *Advances in OptoElectronics* , Vol. 2007, pp. 1-15, 2007.
[5.37] M. Tucci et al., "Laser fired back contact for silicon solar cells", *Thin Solid Films*, Vol. 516, No. 20, pp. 6767-6770, 2008.
[5.38] P. Ortega et al., "Laser-fired contact optimization in c-Si solar cells", *Progress in Photovoltaics: Research and Applications*, Vol. 20, No. 2, pp. 173-180, 2012.
[5.39] W. Brendle et al., "20.5% efficient silicon solar cell with a low temperature rear side process using laser-fired contact", *Progress in Photovoltaics: Research and Applications*, Vol. 14, No. 7, pp. 653-662, 2006.
[5.40] G. Heiser et al., "Optimisation of rear contact geometry of high efficiency silicon solar cells using three dimensional numerical modeling", *Proc. of 13th European Photovoltaic Solar Energy Conference* (*EU PVSEC*), pp. 447-450, 1995.
[5.41] M. Zanuccoli et al., "Numerical Simulation and Modeling of Rear Point Contact Solar Cells", *Proc. of 37th IEEE Photovoltaic Specialists Conference* (*PVSC*), pp. 1519-1523, 2011.

[5.42] M. Zanuccoli et al., “Performance Analysis of Rear Point Contact Solar Cells by Three-Dimensional Numerical Simulation”, *IEEE Transaction on Electron Devices*, Vol.59, No. 5, pp. 1311-1319, 2012.
[5.43] H. Plagwitz et al., “Analytical model for the optimization of locally contacted solar cells”, *Proc. of 31st IEEE Photovoltaic Specialists Conference* (*PVSC*), pp. 999-1002, 2005.
[5.44] P. Saint-Cast et al., “Advanced analytical model for the effective recombination velocity of locally contacted surfaces”, *Journal of Applied Physiscs*, Vol. 108, No. 1, pp. 13705-13711, 2010.
[5.45] A. G. Aberle, G. Heiser, M. A. Green, “Two dimensional numerical optimization study of the rear point contact geometry of high efficiency silicon solar cells”, *Journal of Applied Physiscs*, Vol. 75, No. 10, pp. 5391-5405, 1994.
[5.46] J. Dicker et al., “Analysis of one-sun monocrystalline rear-contacted silicon solar cells with efficiencies of 22.1%”, *Journal of Applied Physiscs*, Vol. 91, No. 7, pp. 4335-4343, 2002.
[5.47] S. Sterk and S. W. Glunz, “Simulation in high efficiency solar cell research”, *Simulation of Semiconductor Devices and Processes* , Vol. 5, pp. 393-396, 1993.
[5.48] K. Kotsovos and K. Misiakos, “Three-dimensional simulation of carrier transport effects in the base of rear point contact silicon solar cells”, *Journal of Applied Physiscs*, Vol. 89, No. 4, pp. 2491-2496, 2001.
[5.49] K. Van Wichelen et al., “Towards 20.5% efficiency PERC cells by improved understanding through simulation”, *Energy Procedia*, Vol. 8, pp. 78-81, 2011.
[5.50] C. Allebé et al., “Large-Area PERC Cells with a Ti-Cu Based Metallization Leading to Efficiencies Above 19.5%”, *Proc. of 26th European Photovoltaic Solar Energy Conference* (*EU PVSEC*), pp. 2276-2279, 2011.
[5.51] A. Schenk, “Finite-temperature full random-phase approximation model of band gap narrowing for silicon device simulation”, *Journal of Applied Physiscs*, Vol. 84, No. 7, pp. 3684-3695, 1998.
[5.52] P. P. Altermatt et al., “Reassessment of the intrinsic carrier density in crystalline silicon in view of band-gap narrowing”, *Journal of Applied Physiscs*, Vol. 93, No. 3, pp. 1598-1604, 2003.
[5.53] P. P. Altermatt et al., “Numerical modeling of highly doped Si:P emitters based on Fermi-Dirac statistics and self-consistent material parameters”, *Journal of Applied Physiscs*, Vol. 92, No. 6, pp. 3187-3197, 2002.
[5.54] Synopsys, “Optimization of Rear Contact Design in Monocrystalline Silicon Solar-Cell Using 3D TCA Simulations”, *TCAD Sentaurus application note*, July 2010.

Chapter 6

Simulation Methodology to Account for the Finger Non-Uniformity

The numerical device simulation of entire large-area solar cells would lead to a very large discretization mesh that cannot be handled by state-of-the-art computers. Therefore, by exploiting the symmetry of the device, and by neglecting the edge effects and the resistivity of the front metal grid, the simulation domain is typically reduced to only a small repetitive portion of the structure representing an irreducible section of the device. However, while such restricted simulation domain is sufficient for the analysis of bulk and surface properties, a full analysis of the losses occurring in the solar cell, like the parasitic resistive losses resulting from the front metal grid, would require a full-scale modeling of the solar cell.

In previous chapters, the effects of the parasitic series resistances due to the front-side metallization have been included by means of an analytical post-processing. However, such simplified approach does not allow to account for the non-uniformities in the front metal grid. In this chapter, a simulation methodology based on a mixed-mode simulation approach, which combines device simulations and circuit simulations, is proposed to investigate the impact of the non-uniformities in the front-side metallization. First, the effect of the finger roughness on the solar cell performance is studied as a function of the finger height, finger width and finger resistivity for both conventional single screen-printing (SP) and double screen-printing (DP) techniques. Then, the proposed methodology is applied to evaluate the impact of the finger interruptions on the solar cell performance as a function of the interruption size, interruption position, number of interruptions and finger resistivity for typical fingers realized with DP technology.

6.1 Analysis of the impact of the finger roughness

The design of the front-side metallization of solar cells plays an important role for increasing the cell efficiency and reducing the cell manufacturing costs [6.1]-[6.6]. The front metal grid layout must achieve a good trade-off between contrasting requirements: improving the current carrying capability of the contacts by increasing the overall cross-section of the front metallized lines and increasing the photogeneration inside the device by reducing the shaded area on the front surface. For a typical industrial solar cell, the main contribution to the series resistance arises from the finger metal resistance, which accounts for about 40% [6.6]. Double screen-printing (DP) technology, as already discussed in Chapter 4, is a well-established industrial process which allows to increase the finger aspect ratio and to reduce the silver paste consumption. Furthermore, this technique allows an improved control of the width and the height of the finger, thus resulting in lower finger non-uniformity [6.3]-[6.5]. In fact, the morphology of screen-printed fingers strongly depends on the process parameters and, particularly, on the screen characteristics (mesh count, open area,…). In general, the finger roughness is detrimental for the finger conductivity, as the local reduction of the finger height and cross-section area causes an increase of the effective series resistance. Therefore, in order to properly estimate the finger series resistance, the roughness along the finger has to be carefully considered. Proper modeling tools to quantitatively evaluate the impact of the finger roughness on the series resistance are then mandatory to guide the design and the optimization of the front-side metallization. In this section, a simulation methodology is proposed for evaluating the impact of the finger roughness on the solar cell performance [6.7]. Then, the proposed methodology is applied to typical finger profiles realized with conventional single screen-printing (SP) and double screen-printing (DP) technology.

6.1.1 Simulation methodology

The proposed methodology is based on a mixed-mode simulation approach, which allows to evaluate the solar cell properties by performing both numerical device simulations and circuit simulations. The adopted tool flow is described in Fig. 6.1. Numerical device simulation of a 2-D domain of the solar cell which does not account for the conduction through the finger, referred as Simulation Block (SB) in Fig. 6.2, has been performed by means of TCAD simulator [6.8]. A 180-μm-thick mono-crystalline solar cell with a uniform boron-doped base of 10^{16} cm^{-3} (1.5 Ω·cm) and a 65-Ω/sq phosphorous-doped n^+-type homogeneous emitter has been considered [6.5]. A standard AM1.5G spectrum and a textured front surface have been taken into account for the calculation of the optical generation rate profile in the optical simulation.

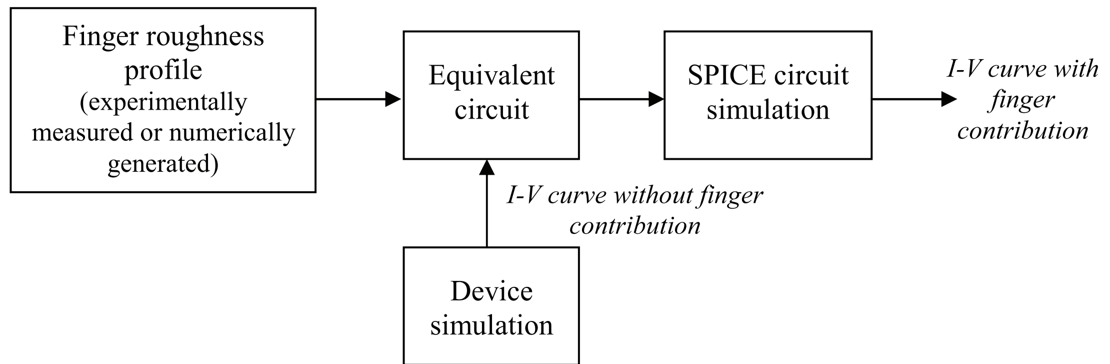

Fig. 6.1. Tool flow for the proposed mixed-mode simulation methodology.

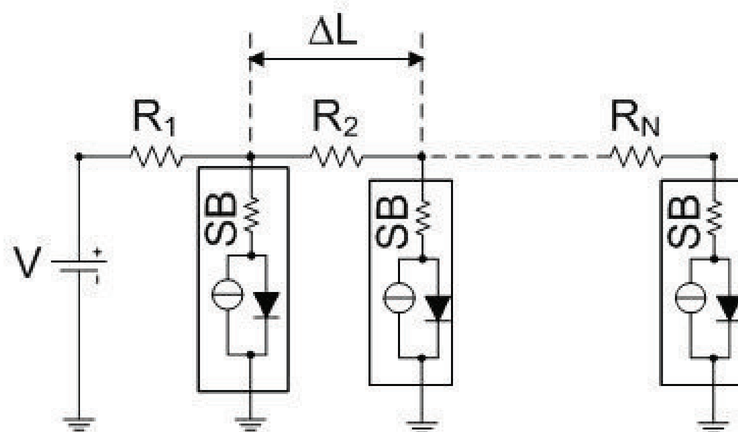

Fig. 6.2. Equivalent circuit for the solar cell. The Simulation Block (SB) is obtained from numerical device simulations. The i-th resistance is calculated according to Eq. 6.1.

In order to account for the losses due to the finger resistance, an equivalent circuital network of the solar cell has been built by discretizing the finger in elementary blocks, as

schematized in Fig. 6.2. Note that the assumed equivalent circuit represents the solar cell area under a single finger (finger length times the distance between two adjacent fingers). The associated resistance to the *i*-th elementary block of the discretized finger is given by:

$$R_i = \rho_f \frac{\Delta L}{A_i} \tag{6.1}$$

$$A_i = H_i \cdot W_f \cdot F \tag{6.2}$$

$$\sigma_A = \sigma_H \cdot W_f \cdot F \tag{6.3}$$

where ΔL is the length of the elementary block, W_f is the finger width, H_i and A_i are the finger height and cross-section area of the i-th elementary block, ρ_f is the finger resistivity and F is a correction factor that takes into account for the non-rectangular shape of the finger cross-section. By assuming a constant width along the finger, the standard deviation of the cross-section area σ_A has been accounted for by considering only the standard deviation of the finger height σ_H (according to Eq. 6.3). Then, circuit simulations have been performed with a SPICE circuit simulator. It is worth noting that the parameters of the equivalent circuital network have to be set according to the considered finger roughness profile (according to Fig. 6.1). In this work, in order to fully understand the impact of finger roughness on the solar cell performance, several finger roughness profiles have been analyzed. In particular, the different finger profiles have been numerically generated. For this purpose, an average height H_m and an autocorrelation function for representing the height fluctuations must be defined [6.9]. Gaussian and exponential types of autocorrelation function have been considered. The power spectrum for the Gaussian autocorrelation function is given by:

$$S_E(k) = \sqrt{\pi}\, \sigma_H^2 \xi \, exp\left(-\frac{k^2 \xi^2}{4} \right) \tag{6.4}$$

while, for the exponential function, it is given by:

$$S_E(k) = \frac{2\sigma_H^2 \xi}{1 + k^2 \xi^2} \tag{6.5}$$

where ξ is the correlation length, which defines an average period of the oscillations of the finger height, and $k = I\,(2\pi/N \cdot \Delta L)$, where N is the number of elementary blocks and $0 < I < N/2$.

Fig. 6.3 shows two typical experimental 3-D finger profiles measured with a laser profilometer in the case of SP and DP technologies. These profiles have been used to calculate the cross-section area and the finger height as a function of the longitudinal position. In Table 6.1, the corresponding average values of the finger width (W_f), height (H_m) and area (A_m), as well as the standard deviation of the height and area fluctuations, are reported. It has been found that the same correction factor F satisfies both Eqs. 6.2 and 6.3. This means that the major source of fluctuations of the cross-section area is related to the finger height, in agreement with Eq. 6.3. Moreover, the correlation length ξ has been evaluated for both SP and DP profiles.

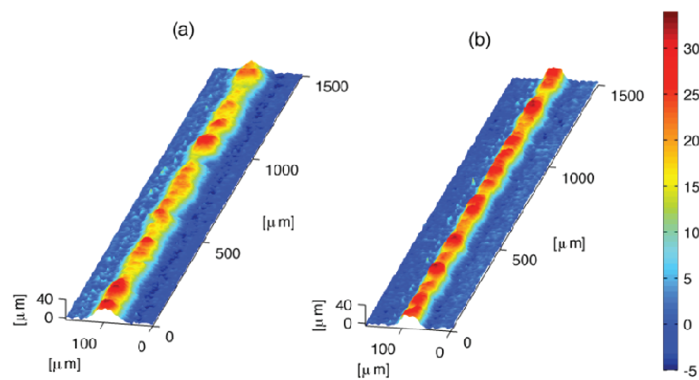

Fig. 6.3. Measured finger profiles for (a) single screen-printing and (b) double screen-printing technologies.

	W_f [µm]	H_m [µm]	A_m [µm^2]	σ_H [µm]	σ_A [µm^2]	F	ξ [µm]
SP	95	20.7	1002.9	5.1	247.0	0.51	36.2
DP	75	23.9	932.1	3.9	140.4	0.52	24.6

Tab. 6.1. Experimental parameters for the considered SP and DP finger profiles of Fig. 6.3.

The results reported in Table 6.1 confirm that the DP technology allows to reduce the finger roughness, resulting in a lower standard deviation of the finger height and, consequently, of the finger cross-section area. An example of the autocorrelation function of the finger height, related to the experimental SP finger profile, is reported in Fig. 6.4. It is possible to observe that the Gaussian function better matches the experimental data with respect to the exponential model. For this reason, in this work, only the Gaussian autocorrelation function has been used for the numerical generation of the finger roughness profiles.

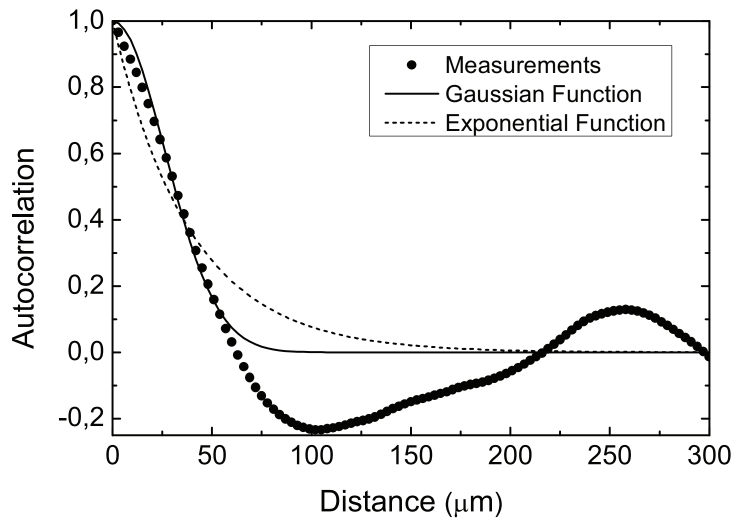

Fig. 6.4. Fitting of the autocorrelation function related to the measured roughness profile of the SP finger with two types of function: Gaussian and exponential.

As described in Fig. 6.1, the SPICE simulation provides the *I-V* curve which accounts for the finger contribution to the series resistance of the solar cells. By comparing this *I-V* curve resulting from the circuit simulation with the *I-V* curve represented by the SB in Fig. 6.2 (i.e., the *I-V* curve provided by the device simulation without the finger contribution), the equivalent finger series resistance R_{fm} can be calculated as:

$$R_{fm} = \frac{\Delta V}{I_0} \tag{6.6}$$

where ΔV is the voltage difference between the two *I-V* curves, evaluated at the same current value I_0. In particular, since R_F can depend on the specific value of I_0, Eq. 6.6 has been applied at the bias point corresponding to the calculated maximum power point when the finger contribution is considered.

6.1.2 Simulation results

The proposed simulation methodology has been applied to investigate the impact of the finger roughness on the solar cell performance as a function of the standard deviation of the finger height, the average finger height and the finger resistivity for both SP and DP technologies. As previously stated, the different analyzed finger roughness profiles have been numerically generated by considering a Gaussian autocorrelation function for representing the height fluctuations.

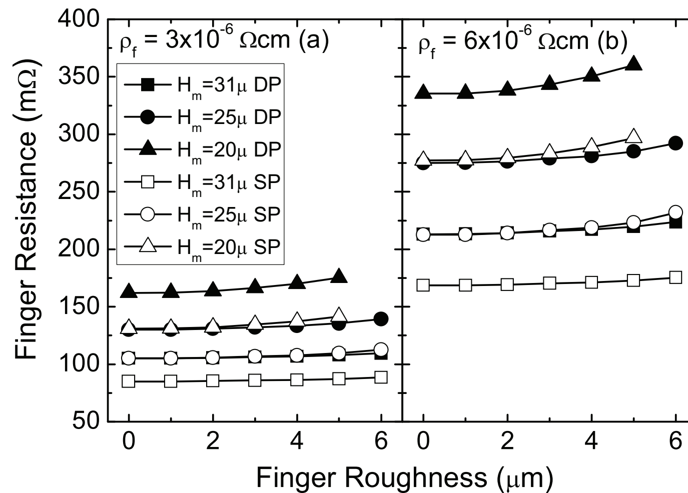

Fig. 6.5. Finger resistance as function of the roughness at different finger height H_m and finger resistivity ρ_f for SP and DP technologies.

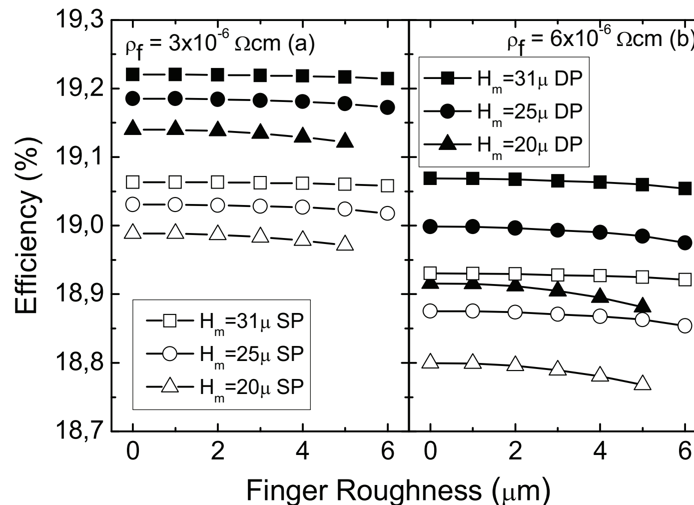

Fig. 6.6. Conversion efficiency as function of the roughness at different finger height H_m and finger resistivity ρ_f for SP and DP technologies.

Figs. 6.5 and 6.6 report the finger resistance and cell efficiency dependencies, respectively, on the finger roughness (represented by the standard deviation of the finger height

σ_H), on the average finger height H_m, and on the finger resistivity ρ_f (two different values have been considered: 3×10^{-6} and 6×10^{-6} Ω·cm) in case of SP (W_f = 95 µm, F = 0.51) and DP (W_f = 75 µm, F = 0.52) processes for a fixed correlation length ξ of 25 µm. The finger resistance has been calculated according to Eq. 6.6. The finger length has been set to 5.05 cm. It is worth noting that the contact and the busbar resistances have been neglected. Similar trends can be observed for the series resistance and the conversion efficiency in Figs. 6.5 and 6.6. As expected, an increase of the roughness results in an increase of the finger series resistance and, consequently, in a degradation of the efficiency. For example, in case of SP with $\rho_f = 6\times10^{-6}$ Ω·cm and H_m = 20 µm, the efficiency degradation at σ_H = 5 µm is $\Delta\eta = 0.03\%_{abs}$ with respect to the zero roughness case (i.e., σ_H = 0 µm). The degradation typically increases when the finger resistivity is higher, since the fluctuations in the resistance of each elementary block are proportional to the metal resistivity. Therefore, the higher the finger conductivity, the smaller the impact of the finger roughness on the cell performance. Another important observation from Fig. 6.6 is that the impact of roughness on the efficiency is higher when the average height H_m decreases. In fact, for a given finger roughness, the reduction of H_m increases the probability to find elementary blocks with a very small height and, hence, very large resistance, which act as bottleneck. Moreover, for a given finger average height and roughness, the efficiency gain of DP over SP increases when reducing the metal resistivity. As a matter of fact, by considering H_m = 25 µm and σ_H = 6 µm, the efficiency gain of DP reduces from $0.15\%_{abs}$ for $\rho_f = 3\times10^{-6}$ Ω·cm to $0.12\%_{abs}$ for $\rho_f = 6\times10^{-6}$ Ω·cm. Finally, by considering the experimental parameters reported in Table 6.1, the efficiency gain of DP over SP is $\Delta\eta = 0.19\%_{abs}$ for $\rho_f = 3\times10^{-6}$ Ω·cm and $\Delta\eta = 0.17\%_{abs}$ for $\rho_f = 6\times10^{-6}$ Ω·cm. Accordingly, the simulation results confirm that the DP technology is less affected by the finger roughness as compared to the conventional SP technology, thus showing an increased efficiency gain when the finger roughness is taken into account.

Therefore, the main results of the performed analysis on the impact of the finger roughness can be summarized as follows:

- an increase of the finger roughness causes an increase of the finger resistance and, consequently, a degradation of the cell efficiency;
- the impact of the finger roughness reduces when the metal resistivity is decreased (i.e., the finger conductivity is increased);
- taller fingers are less affected by the height fluctuations;
- the advantage of DP technology over SP is higher in case of smaller metal resistivity and, in general, when the finger roughness is taken into account in the simulations;
- finally, by calibrating the finger properties with the experimental data of SP and DP (see Table 6.1), simulation results reveal an efficiency gain of DP over SP of $0.19\%_{abs}$.

6.2 Analysis of the impact of the finger interruptions

The interruption of the fingers in the front-side metallization is a critical problem that affects the performance, the reliability and the yield of solar cells. The efforts of photovoltaic (PV) industry are currently focused on improving the screen-printing process, aiming also at reducing the presence of finger interruptions. In this regard, some technological solutions, such as the electroless silver plating (ESP) [6.10] or the double screen-printing (DP) technique [6.3], show a capability to partially recover insufficiently screen-printed cells. The SEM image of a typical finger interruption due to insufficient screen-printing is shown in Fig. 6.7. Moreover, the finger disruption can also occurs after the metallization process, due to usury or accidental damage. The size of the finger interruption S depends on the cause of disruption. Typically, $S <$ 10 μm is found for finger disruptions due to usury, 10 μm $< S <$ 1 mm for insufficient screen-printing and $S >$ 1 mm for accidental damage.

Proper modeling tools to quantitatively evaluate the impact of the finger interruptions on the solar cell performance are mandatory to understand their implications in terms of yield and reliability. In this section, by following the same approach which has been already discussed in the previous section, a mixed-mode simulation methodology is applied to account for the impact of the finger interruptions on the solar cell performance as a function of the interruption size, interruption position, number of interruptions and finger resistivity in typical finger profiles realized with DP technology [6.11].

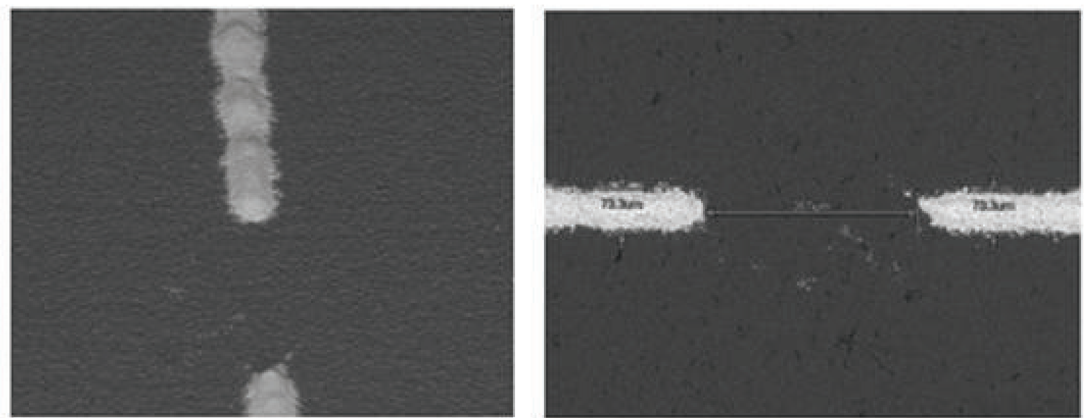

Fig. 6.7. Lateral (left) and top (right) view of a typical finger interruption due to insufficient screen-printing.

6.2.1 Simulation methodology

The simulation methodology is based on a mixed-mode simulation approach, which combines numerical device simulations and circuit simulations (see Fig. 6.1), as already discussed in Section 6.1.1. The assumed equivalent circuit of the elementary finger simulation domain, representing the solar cell area under a single finger (finger length times the distance between two adjacent fingers) and including a finger interruption is shown in Fig. 6.8. The Photovoltaic Block (PVB), obtained by means of TCAD device simulations [6.8], represents a 2-D domain of the cell which does not account for the conduction through the finger. The 15.6×15.6 cm^2 simulated mono-crystalline (*c*-Si) solar cell consists of a 180-μm-thick boron-doped *p*-type base with a uniform concentration of 10^{16} cm^{-3} (1.5 Ω·cm) and a 65-Ω/sq phosphorous-doped n^+-type homogeneous emitter, modeled with an error function doping profile featuring a peak concentration of 1.26×10^{20} cm^{-3} and junction depth of 0.4 μm [6.5]. The optical simulation has been performed by assuming a standard AM1.5G spectrum and a textured front surface.

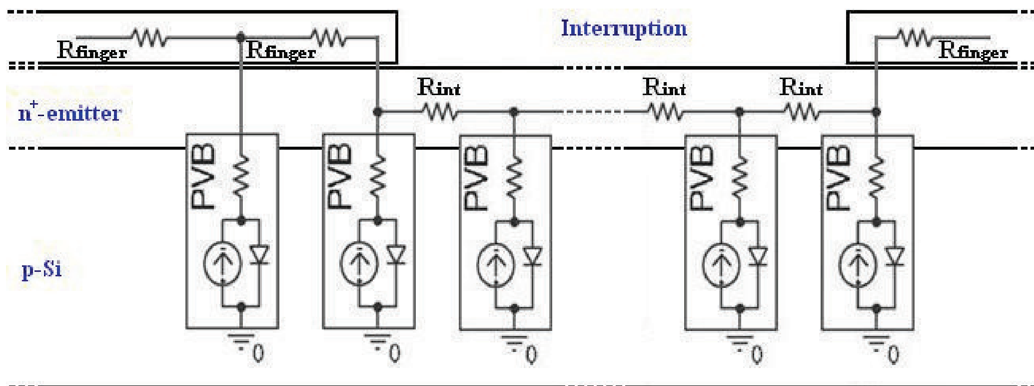

Fig. 6.8. Equivalent circuit for the elementary finger simulation domain, representing the solar cell area under a single finger and including a finger interruption.

In addition to the electro-optical device simulations, circuit simulations have been performed with a SPICE circuit simulator in order to account for the losses due to the finger resistance, as schematized in Fig 6.8. Similarly to Section 6.1.1, the finger has been discretized in elementary blocks, whose associated resistance is given by Eq. 6.1, and the finger roughness due to height fluctuations has been modeled by assuming a Gaussian autocorrelation function (see Eq. 6.4) with the two parameters, standard deviation σ_H and correlation length ξ, extracted by measurements of experimental finger roughness profiles (refer to Table 6.1). Moreover, it is worth noting that the contact resistance at metal/Si interface and the busbar resistance have been neglected in the circuit simulations.

Note that, in correspondence of the finger interruption, the current flows through the emitter layer, which certainly offers a higher resistance with respect to the metallization.

Therefore, the resistance of the *i*-th elementary block in the region where the finger is interrupted has been modeled using the following expression:

$$R_{int} = \frac{R_{sq}}{W_f} \cdot \Delta L \tag{6.7}$$

where R_{sq} is the emitter sheet resistance. In practice, Eq. 6.7 is used instead of Eq. 6.1 when an interruption occurs and, hence, the resistance of the metallization becomes much higher than the resistance of the emitter layer.

From the output *I-V* characteristics provided by SPICE simulations, the main figures of merit of the solar cell, such as efficiency, fill-factor and series resistance, have been extracted in correspondence of the maximum power point. By simply adding the *I-V* curves corresponding to the solar cell areas under all the fingers, the overall *I-V* curve for the whole cell area can be obtained.

6.2.2 Simulation results

As a figure of merit for evaluating the impact of the finger interruption on the solar cell performance, the efficiency degradation $\Delta\eta$ has been considered, which is calculated as the difference between the efficiency in the case of interruption η_{with_int} and the reference efficiency $\eta_{without_int}$ (without finger interruption):

$$\Delta\eta = \eta_{with_int} - \eta_{without_int} \tag{6.8}$$

It is worth noting that $\Delta\eta$ refers to the local efficiency degradation in a single elementary finger simulation domain. Fig. 6.9 shows the schematic representation of such domain with a single interruption between the two busbars. Note that, in this work, it has been assumed that the interruption can occur only between two busbars (the case for which the interruption occurs between a busbar and the edge of the cell has been neglected).

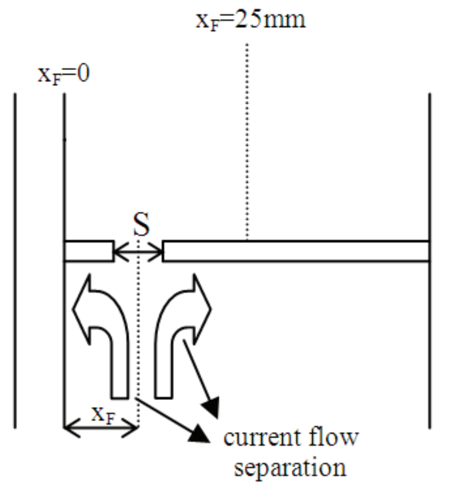

Fig. 6.9. Schematic representation of the area within a single elementary finger domain with a single interruption between the two busbars. *S* denotes the interruption size, while x_F indicates the interruption position Note that x_F =0 corresponds to the busbar position and x_F = 25 mm corresponds to the position in the middle of the two busbars.

The finger roughness profiles have been numerically generated according to the procedure described in Section 6.1.1, i.e., by assuming a Gaussian autocorrelation function for representing the height fluctuations. Table 6.2 reports the considered geometric parameters for the double screen-printed finger profile. In particular, the average value of the finger width W_f and height H_m, the standard deviation σ_H and the correlation length ξ of the height fluctuations and the finger length (from busbar to busbar) L_f are reported.

W_f [μm]	H_m [μm]	σ_H [μm]	F	ξ [μm]	L_f [cm]
95	30	4	0.52	24	5.05

Tab. 6.1. Geometric parameters of the considered DP finger profile.

Fig. 6.10 reports the efficiency degradation corresponding to a single elementary finger domain induced by a single finger interruption as a function of the interruption size S for different interruption position (x_F = 0 corresponds to the busbar position and x_F = 25 mm corresponds to the position in the middle of two adjacent busbars, as described in Fig. 6.9), in case of metal resistivity of 3×10^{-6} Ω·cm and 6×10^{-6} Ω·cm, respectively.

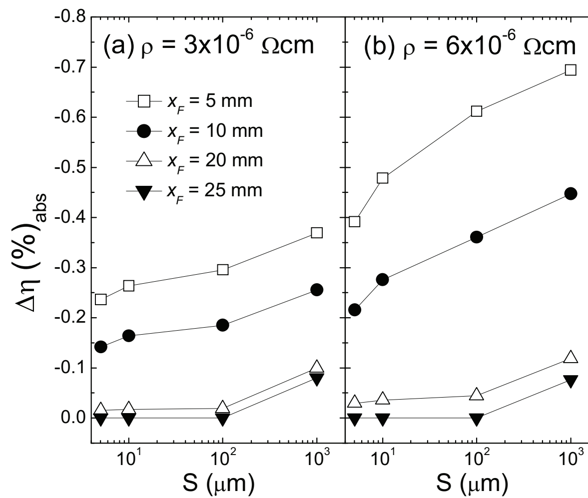

Fig. 6.10. Efficiency degradation corresponding to the area under a single finger induced by a finger interruption as a function of the interruption size S for different interruption position x_F and finger resistivity ρ_f.

The observed qualitative trends are quite clear: $\Delta\eta$ worsens by increasing the interruption size, by moving the interruption from the centre between two adjacent busbars to the busbar position and by increasing the resistivity. In particular, $\Delta\eta$ ranges from -0.079%$_{abs}$ to -0.369%$_{abs}$ by moving the interruption from x_F = 25 mm (centre between the two adjacent busbars) to x_F = 5 mm (close to the busbar position) in case of metal resistivity of 3×10^{-6} Ω·cm for an interruption size of 1 mm. This arises from the fact that, in this modeling approach, the current generated at a given side of the interruption is assumed to be practically collected only by the busbar on the same side, as illustrated in Fig. 6.9, because of the large resistance in the interruption region. On one hand, when the interruption is in the middle of the two busbars, the collected current by the two busbars is divided in half (that is also the case in absence of interruption). Therefore, in this case, the effect of the interruption is very limited. On the other hand, if the interruption moves close to the busbars, the current separation becomes asymmetric, leading to an increase of the current path and, consequently, of the series resistance. Moreover, it is worth noting that the

efficiency degradation almost doubles in case of metal resistivity of 6×10^{-6} Ω·cm. This phenomenon can be understood by considering that the efficiency degradation is due to an increase of the current path through the finger. This causes an increase of series resistance, which is proportional to the metal resistivity. As a matter of fact, similar trends have been obtained in terms of fill factor and series resistance degradation induced by a single finger interruption in a single finger domain, as shown in Figs. 6.11 and 6.12, respectively.

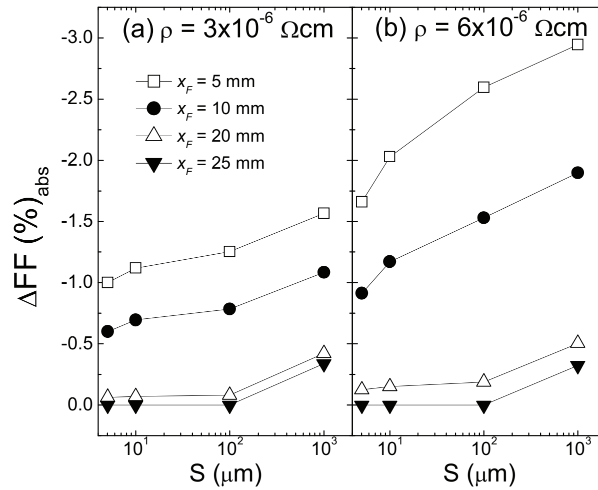

Fig. 6.11. Fill factor degradation corresponding to the area under a single finger induced by a finger interruption as a function of the interruption size *S* for different interruption position x_F and finger resistivity ρ_f.

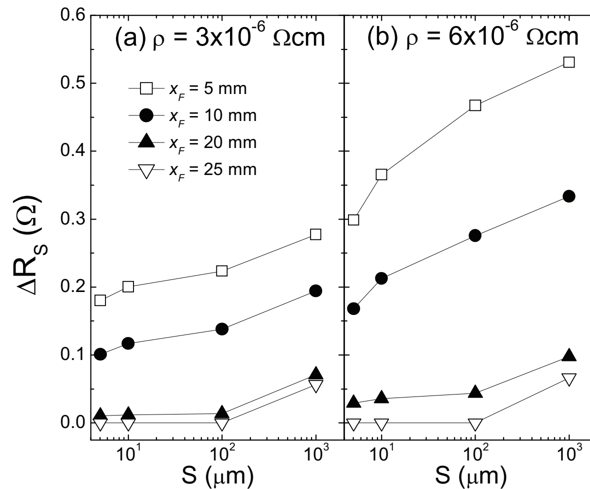

Fig. 6.12. Series resistance degradation corresponding to the area under a single finger induced by a finger interruption as a function of the interruption size *S* for different interruption position x_F and finger resistivity ρ_f.

Fig.6.13 shows the efficiency degradation weighted over the whole solar cell area, by considering 75 (number of fingers) × 3 (number of busbars) = 225 elementary finger simulation domains. $\Delta\eta$ is plotted as a function of the number of finger interruptions with an interruption size of 100 μm for different interruption position and finger resistivity. In this kind of analysis,

it has been assumed that all the different interrupted finger domains feature a single interruption in the same position. However, it is worth noting that the developed tool is able to simulate the case in which the interruptions occur in different positions on the different fingers. In Fig. 6.13, the observed efficiency degradation increases almost linearly with the number of interruptions and with the finger resistivity. In particular, $\Delta\eta$ reaches about -0.30%$_{abs}$ (-0.15%$_{abs}$) in presence of 100 interrupted fingers at x_F = 5 mm in case of a metal resistivity of 6×10^{-6} Ω·cm (3×10^{-6} Ω·cm). On the other hand, the simulation results reveal that, in case of fewer interruptions, the efficiency degradation is not so relevant. This can be ascribed to the fact that, in such analysis, only a single interruption per finger domain has been considered. Indeed, it is expected that the presence of two or more interruptions on the same finger leads to a stronger impact on the solar cell performance, because, in this case, the entire portion of the finger between two interruptions is isolated from the front metal grid and, consequently, does not contribute to the cell output current.

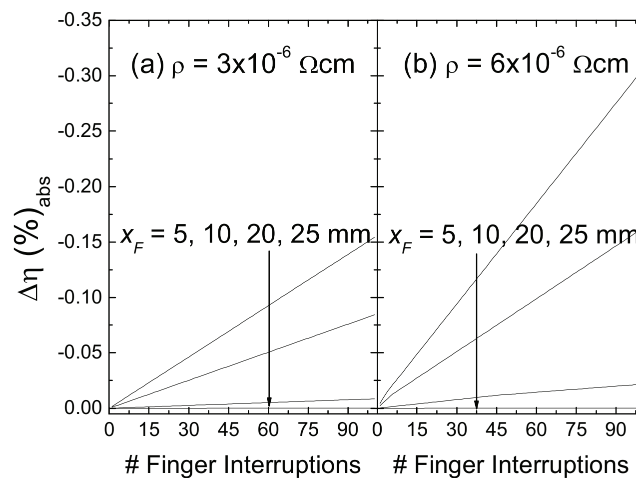

Fig. 6.13. Efficiency degradation corresponding to the whole solar cell area as a function of the number of finger interruptions with a size S = 100 μm for different interruption position and finger resistivity.

Therefore, simulation results of the performed analysis on the impact of the finger interruptions show that:

- the effect of the finger interruptions on the solar cell performance depends on the interruption size, the number of interruptions, the finger resistivity and is position-related ;
- in particular, the efficiency degradation induced by finger interruptions worsens by increasing the interruption size, by moving the interruption position from the middle of two adjacent busbars to the busbar position and increases almost linearly with the number of finger interruptions and with the finger resistivity.

References

[6.1] T. E. Rardin and R. Xu, "Printing Process Used to Manufacture Photovoltaic Solar Cells", *The Journal of Technology Studies*, Vol. 37, pp. 62-68, 2011.
[6.2] L. A. Dobronaski et al., "Investigation of the screen printed contacts of silicon solar cells using Transmission Line Model", *Journal of Achievements in Materials and Manufacturing Engineering*, Vol. 41, No. 1-2, pp. 57-65, 2010.
[6.3] M. Galiazzo et al., "Double Printing of Front Contact Ag in c-Si Solar Cells", *Proc. of 25th European Photovoltaic Solar Energy Conference* (*EU PVSEC*), pp. 2338-2340, 2010.
[6.4] M. Galiazzo et al., "Esatto Technology Upgrade: Feasibility and Advantages in c-Si Solar Cell Metallization", *Proc. of 26th European Photovoltaic Solar Energy Conference* (*EU PVSEC*), pp. 2044-2047, 2011.
[6.5] P. Magnone et al., "Understanding the Impact of Double Screen-Printing on Silicon Solar Cells by 2-D Numerical Simulations", *Proc. of 37th IEEE Photovoltaic Specialists Conference* (*PVSC*), Seattle, Washington, USA, pp. 2177-2180, 2011.
[6.6] C. Vazquez et al., "Towards the Limits of Efficiency of Screen Printed Solar Cells: New Techniques for the Front Side Contacts", *Proc. of 25th European Photovoltaic Solar Energy Conference* (*EU PVSEC*), pp. 1816-1819, 2010.
[6.7] P. Magnone et al., "A Methodology to Account for the Finger Non-Uniformity in Photovoltaic Solar Cell", *Energy Procedia*, Vol. 27, pp. 191-196, 2012.
[6.8] Sentaurus Device User Guide, Synopsys, Mountain View, CA.
[6.9] A. Asenov, S. Kaya, A. R. Brown, "Intrinsic Parameter Fluctuations in Decananometer MOSFETs Introduced by Gate Line Edge Roughness ", *IEEE Transactions on Electron Devices*, Vol. 50, No. 5, pp. 1254-1260, 2003.
[6.10] P. R. Wefringhaus et al., "Electroless silver plating of screen printed front grid fingers as a tool for enhancement of solar cell efficiency", *Proc. of 22nd European Photovoltaic Solar Energy Conference* (*EU PVSEC*), pp. 1050-1052, 2010.
[6.11] R. De Rose et al., "A methodology to account for the finger interruptions in solar cell performance", *Microelectronics Reliability*, Vol. 52, pp. 2500-2503, 2012.

Conclusions

One of the most challenging goal in PV industry and research is the manufacturing of low-cost, high-efficiency and reliable solar cells. The improvement of PV solar cells in terms of reducing production costs and increasing conversion efficiency requires a careful device and process optimization. To this purpose, modeling of PV devices turns out to be a powerful and helpful tool to aid the design of solar cells. Furthermore, solar cell modeling becomes increasingly strategic for PV industry in view of the forthcoming adoption of advanced solar cell architectures and concepts. In this context, this Ph.D. thesis concerns the electro-optical numerical simulation of *c*-Si solar cells by means of a state-of-the-art TCAD computer program, able to solve numerically the fully coupled set of semiconductor differential equations within the drift-diffusion approximation, accounting also for the Fermi-Dirac statistics.

The first part of the thesis consists of an outline about the physics of solar cells. In particular, the main physical mechanisms which limit the conversion efficiency of solar cells have been explained. Later on, the basis of the numerical modeling of solar cells, including both device, optical and circuit simulations, has been discussed with particular emphasis on the main issues and limitations of most of the state-of-the-art tools used for the electro-optical numerical simulation of PV devices. In addition, in order to set up a specific simulation framework for silicon solar cells by the adopted state-of-the-art TCAD simulator, the calibration of some of the most relevant physical models implemented in the TCAD program, such as those for the intrinsic carrier density, the Auger recombination, the SRH recombination, and the surface recombination, has been discussed.

The second part of the thesis concerns the analysis of silicon solar cells by means of the fine-tuned TCAD-based simulation framework. First, conventional screen-printed *c*-Si solar cells, featuring a standard 75 Ω/sq homogeneously phosphorus-doped front-side n^+-emitter and a full-area metallized Al-alloyed p^+-back surface field (BSF), have been investigated by 2-D electro-optical numerical simulations. This analysis has shown that the fundamental performance limitations of these conventional solar cells are mostly related to the recombination occurring both at front and rear sides. Moreover, the impact of improved front metallization architectures due to the double screen-printing (DP) technology on the performance of conventional silicon solar cells has been evaluated by means of numerical simulations.

Then, some advanced technological solutions aimed at improving both sides of silicon solar cells have been investigated. More specifically, 2-D numerical simulations has been performed to analyze the impact of different emitter doping profiles in selective emitter (SE) solar cells, featuring lightly-doped (LDOP) areas between the front contact fingers, and highly-doped (HDOP) areas underneath the front metallization. Moreover, by exploiting the 2-D

modeling approach, the effect of the alignment tolerance used in the SE diffusion process for the subsequent metallization process has been also investigated. Numerical results have confirmed that the SE design can be very effective to improve the performance at the front side of silicon solar cells. In particular, simulation results has shown that the adoption of an optimized design for the SE solar cell can lead to an efficiency improvement above $0.4\%_{abs}$ as compared to a 75-Ω/sq homogeneous emitter (HE) reference cell. In addition, the effect of the combined use of DP and SE concepts has been investigated, revealing that the sum of the benefits of the SE design and the DP technology, in combination with a proper optimization of the doping profiles, allows to achieve an additional efficiency gain.

Afterwards, a rigorous 3-D modeling approach has been adopted to optimize the rear point contact (RPC) geometry of a reference PERC-type silicon solar cell, featuring also a high sheet resistance (140 Ω/sq) phosphorus-doped front-side emitter contacted by means of an advanced front metallization scheme with narrow and highly-conductive electro-plated Ti/Cu contacts. Numerical results have confirmed that the adoption of RPC schemes in high-efficiency silicon solar cells is one of the most promising approaches to reduce the recombination losses at the rear side of the device. In particular, it has been shown that the optimization of the considered PERC-type solar cell in terms of the rear point contact design can potentially lead to a conversion efficiency above 20%.

Finally, a simulation methodology based on a mixed-mode simulation approach, which combines numerical device simulations and circuit simulations, has been adopted to investigate the impact of the non-uniformities in the front-side metallization on the performance of silicon solar cells. First, the effect of the finger roughness has been studied as a function of the finger height, width and resistivity for both conventional Single Screen-Printing (SP) and Double Screen-Printing (DP) metallization technologies. This analysis has revealed that: 1) an increase of the finger roughness leads to an increase of the finger resistance and, consequently, to a degradation of the solar cell efficiency; 2) the impact of the finger roughness reduces when the metal resistivity is decreased (i.e., the finger conductivity is increased), and when the finger height is increased; 3) the advantage of DP technology over SP is higher when the finger roughness is taken into account. Then, the proposed mixed-mode simulation methodology has been applied to evaluate the impact of the finger interruptions on the solar cell performance as a function of the interruption size, interruption position, number of interruptions and finger resistivity for typical fingers realized with DP technology. This analysis has shown that the effect of the finger interruptions depends on the interruption size, the number of interruptions, the finger resistivity and is position-related. In particular, the efficiency degradation induced by finger interruptions worsens by increasing the interruption size, by moving the interruption position from the middle of two adjacent busbars to the busbar position, and increases almost linearly with the number of finger interruptions and with the finger resistivity.